TECHNISCHE UNIVERSITÄT WIEN
Vienna University of Technology

Diese Dissertation haben begutachtet:

Prof. Dr. C.W. Fabjan   Prof. Dr. João Varela

D I S S E R T A T I O N

Time resolution in scintillator based detectors for positron emission tomography

Ausgefürt zum Zwecke der Erlangung des akademischen Grades eines Doktors der technischen Wissenschaften unter der Leitung von

Univ. Prof. DI Dr. Christian Fabjan

Atominstitut der Technischen Universität Wien (E141)

eingereicht an der Technischen Universität Wien Fakultät für Physik von

Dipl.-Ing. Stefan Gundacker

Matrikel Nr. 0325764

Siebenhöf 22, 3921 Langschlag, Österreich

26.03.2014
Datum   Unterschrift

Abstract

Highest time resolution in scintillator based detectors is becoming more and more important in applications for high energy physics and medical physics. In the domain of medical photon detectors L(Y)SO scintillators are commonly used for positron emission tomography (PET). The interest for time of flight (TOF) in PET is increasing since measurements have shown that new crystals like L(Y)SO coupled to state of the art photodetectors, e.g. silicon photomultipliers (SiPM), can reach coincidence time resolutions (CTRs) of far below 500ps FWHM. Several commercial whole-body TOF-PET scanners further demonstrated that already a clear improvement in image signal to noise ratio (SNR) and contrast can be achieved with time resolutions of the order of 500ps. However, CTRs smaller than 100ps FWHM are necessary to benefit of the image SNR improvement to such a level where scanning times and radiation exposure to the patient can be significantly reduced. To achieve these goals it is important to study and understand the individual processes and the associated time evolution in the whole detection chain, i.e. the high energy particle or gamma interaction in the crystal, the scintillation process itself, the light propagation in the crystal with the light transfer to the photodetector, and the electronic readout.

In this thesis time resolution measurements for a PET like system are performed in a coincidence setup utilizing the ultra fast amplifier discriminator NINO. We found that the time-over-threshold energy information provided by NINO shows a degradation in energy resolution for higher SiPM bias voltages. This is a consequence of the increasing dark count rate (DCR) of the SiPM with higher bias voltages together with the exponential decay of the signal. To overcome this problem and to operate the SiPM at its optimum voltage in terms of timing we developed a new electronic board that employs NINO only as a low noise leading edge discriminator together with an analog amplifier which delivers the energy information. With this new electronic board we indeed improved the measured CTR by about 15%. To study the limits of time resolution in more depth we measured the CTR with 2x2x3mm^3 LSO:Ce codoped 0.4%Ca crystals coupled to commercially available SiPMs (Hamamatsu S10931-050P MPPC) and achieved a CTR of 108±5ps FWHM at an energy of 511keV. We determined the influence of the data acquisition system and the electronics on the CTR to be 27±2ps FWHM and thus negligible.

To quantitatively understand the measured values, we developed a Monte Carlo simulation tool in MATLAB that incorporates the timing properties of the photodetector and electronics, the scintillation properties of the crystal and the light transfer within the crystal as simulated by SLITRANI. The simulations enabled us to predict the expected time resolution in each step of the detection process and hence explain the results from our measurements to a high degree and to explore the nature of all parameters affecting the time resolution. In agreement with previous works we then confirm that the time resolution is inversely proportional to the square root of the number

of photoelectrons detected (n') and proportional to the square root of the scintillation decay time (τ_d), i.e. $CTR \propto \sqrt{\tau_d/n'}$. The influence of the scintillation rise time (τ_r) on the CTR is strongly correlated with the single photon time resolution ($SPTR$) of the SiPM and the photon travel time spread (PTS) in the crystal. We could show that the CTR is proportional only to the square root of any of these three parameters if the influence of the other two parameters is negligible, e.g. $CTR \propto \sqrt{SPTR}$ if $\tau_r = 0$ and $PTS = 0$ or $CTR \propto \sqrt{\tau_r}$ if $SPTR = 0$ and $PTS = 0$. In practice, however, due to the irreducible, non-zero, photon travel time spread in the crystal the CTR is less dependent on τ_r and the $SPTR$, if these two quantities are small and in the range of the PTS.

In a further step we have measured the CTR as a function of crystal length under the same experimental conditions. While the 2x2x3mm³ LSO:Ce codoped 0.4%Ca crystal showed a CTR of 108±5ps FWHM, an increase in crystal length to 5mm deteriorates the CTR to 123±7ps FWHM, 10mm to 143±7ps FWHM and 20mm to 176±7ps FWHM. This degradation in CTR is caused by a gradually decreasing light transfer efficiency and a steady increase in photon travel time spread in the crystal. We showed that for increasing crystal length the deterioration in CTR is dominated by the loss in light transfer efficiency, i.e. the ratio of photons reaching the photodetector and the total amount of photons generated. On the other hand, the influence of the photon travel time spread is partly compensated by the gamma absorption delay time in the crystal. Although in our simulation the photon travel time spread does not increase significantly with crystal length, its overall influence still seems to be high. If we "turn off" in the simulation the PTS contribution for the 2x2x3mm³ crystal the CTR would improve from 110ps to 90ps.

In PET, however, crystals with 20mm length or more are necessary in order to ensure an efficient detection of the 511keV annihilation gammas. To improve the CTR for longer crystals we tested the readout of a 2x2x20mm³ crystal on both extremities. After depth of interaction (DOI) corrections we obtained a CTR of 154±10ps FWHM. This method produces a CTR improvement of 22ps or 14% if compared to the single sided readout. The improvement is almost fully explained by a superior light collection with the double sided readout and supports our assumption that a loss in light transfer efficiency is the main cause for deteriorating the CTR with increasing crystal length.

With our developed Monte Carlo simulation tool we also investigated a new type of SiPM, the fully digital SiPM. In this type of SiPM the time of detection of every single photoelectron is recorded. We showed that the fully digital readout of a SiPM with optimized time estimators can reach the intrinsic limit of the time resolution calculated from pure statistical considerations, i.e. the Cramér-Rao lower bound. In addition we pointed out that the best CTR achievable in analog SiPMs with microcell signal pile-up and leading edge discrimination can also be close to the intrinsic limit in time resolution. Our simulations further revealed that this CTR equality between analog and digital readout of SiPMs even holds for different crystal lengths, i.e. 3mm, 5mm, 10mm and 20mm. Consequently there is no preference for either a fully digital or analog readout of SiPMs for the sake of achieving highest time resolution. However, the best CTR in the analog SiPM is observed in a rather small range of optimal threshold values, whereas the fully digital SiPM provides stable CTR after roughly 20 incorporated photoelectron time stamps in the time estimator. This feature could make the digital readout immune to instrumental and SiPM noise in contrast to the leading edge time estimator used in analog SiPMs.

Kurzfassung

Die Zeitauflösung von Szintillator basierende Detektoren für Anwendungen in der Hochenergie- und Medizinphysik gewinnt an mehr und mehr Bedeutung. Im Bereich der medizinischen Gammastrahlungsdetektion und insbesondere für Positronen-Emissions-Tomographie (PET) werden L(Y)SO Szintillatoren häufig eingesetzt. Das Interesse für Flugzeitbestimmung (TOF) in PET steigt, seitdem Messungen gezeigt haben, dass mit Szintillatoren wie L(Y)SO gekoppelt an kürzlich entwickelten Photodetektoren, z.B. Silicon Photomultiplikatoren (SiPM), Koinzidenz Zeitauflösungen (CTR) deutlich unter 500ps FWHM erreicht werden können. Desweiteren demonstrierten mehrere kommerzielle Ganzkörper TOF-PET Geräte, dass bereits mit Zeitauflösungen im Bereich von 500ps eine deutliche Verbesserung im Signal-Rauschabstand (SNR) des Bildes sowie im Bildkontrast zu erkennen ist. Jedoch sind Zeitauflösungen unter 100ps nötig um von den Verbesserung im Bild Signal-Rauschabstand derart zu profitieren, dass die Aufnahmezeiten und die Strahlenbelastung des Patienten deutlich verringert werden kann. Um dieses Ziel zu erreichen ist es wichtig den kompletten Detektionsvorgang und die verbundenen Zeitentwicklungen zu studieren und im Detail zu verstehen, das heißt die hochenergetische Teilchenstreuung im Kristall, den Szintillationsprozess, die Lichtausbreitung im Kristall mit der Übertragung zum Photodetektor und die dazugehörende Ausleseelektronik.

In dieser Arbeit wird die Zeitauflösung in einer Koinzidenz Anordnung gemessen, welche in ihrem Aufbau dem realen PET System gerecht wird. Als Ausleseelektronik wird der Schwellenwertdiskriminator NINO verwendet. Unsere Messungen haben gezeigt, dass der von NINO generierte Ausgangspuls, welche Länge eine Funktion der Gamma-Energie ist, eine Verschlechterung der Energieauflösung für höhere SiPM Betriebsspannungen aufweist. Das ist eine direkte Konsequenz der höheren Dunkelzählrate (DCR) des SiPMs, wenn dieser mit höheren Vorspannungen betrieben wird, zusammen mit dem exponentiellen Abfall des Signals. Um dieses Problem zu lösen und um den SiPM mit optimalen Betriebsspannungen zu betreiben haben wir eine neue Elektronikplatine entwickelt, welche NINO als rauscharmen Schwellenwertdiskriminator nur dazu verwendet um die Zeitinformation zu ermitteln und einen analogen Verstärker dazu um die Energie Information zu messen. Mit dieser neuen Elektronik verbesserten wir die gemessenen CTR Werte um 15%. Um die Grenzen der Zeitauflösung genauer zu studieren führten wir Messungen mit einem 2x2x3mm^3 LSO:Ce kodotierten 0.4%Ca Kristall durch, welcher mit kommerziell erhältlichen SiPMs (Hamamatsu S10931-050P MPPC) gekoppelt wurde. Mit diesem Messaufbau erzielten wir eine CTR von 108±5ps FWHM, für Gamma-Energien von 511keV. Der Einfluss der Elektronik und des Datenerfassungssystems auf die Zeitauflösung wurde zu 27±2ps FWHM ermittelt, und ist deshalb vernachlässigbar.

Um die gemessenen Werte auch quantitativ zu verstehen haben wir eine komplette Monte

Carlo Simulationsumgebung in MATLAB entwickelt, welche den Photodetektor und die Elektronik sowie die Szintillation und Lichtausbreitung im Kristall mit SLITRANI simuliert. Die Simulationen erlaubten uns die einzelnen Schritte im Detektionsprozess in Hinsicht auf deren Einfluss zur Zeitauflösung zu untersuchen und somit auch die Resultate unserer Messungen vorherzusagen. In einen weiteren Schritt erforschten wir den Einfluss aller Parameter auf die Zeitauflösung des Detektors. In Übereinstimmung mit früheren Arbeiten bestätigten wir, dass die Zeitauflösung invers proportional zu der Wurzel der detektierten Photoelektronen (n') und proportional zu der Wurzel der Szintillationsabklingzeit (τ_d) ist, dass heißt $CTR \propto \sqrt{\tau_d/n'}$. Der Einfluss der Szintillationsanstiegszeit (τ_r) ist dagegen stark korreliert mit der Einphotonen-Zeitauflösung (SPTR) des SiPMs und der Photonen-Transport-Zeitstreuung (PTS) im Kristall. Wir konnten zeigen, dass die Zeitauflösung nur proportional zu der Wurzel eines dieser Parameter ist, wenn der Einfluss der anderen Parameter vernachlässigbar wird, z.B. $CTR \propto \sqrt{SPTR}$ wenn $\tau_r = 0$ und $PTS = 0$ oder $CTR \propto \sqrt{\tau_r}$ wenn $SPTR = 0$ und $PTS = 0$. In der Praxis jedoch, aufgrund von der nicht reduzierbaren Photonen-Transport-Zeitstreuung im Kristall, ist die Zeitauflösung nur gering abhängig von τ_r und der $SPTR$, wenn diese zwei Parameter bereits klein sind und im Bereich der PTS.

Der nächste Schritt war unter gleichbleibenden experimentellen Bedingungen den Einfluss der Kristalllänge auf die Zeitauflösung zu untersuchen. Mit dem 2x2x3mm^3 LSO:Ce kodotierten 0.4%Ca Kristall erreichten wir eine CTR von 108±5ps FWHM, wenn der Kristall auf 5mm verlängert wird verschlechterte sich die CTR auf 123±7ps FWHM, 10mm auf 143±7ps FWHM und 20mm auf 176±7ps FWHM. Die Verschlechterung in der Zeitauflösung wird prinzipiell verursacht durch eine graduelle Abnahme in der Lichtübertragunseffizienz und durch eine Zunahme in der Photonen-Transport-Zeitstreuung. Wir zeigten das die Verschlechterung der Zeitauflösung mit steigender Kristalllänge zum Großteil durch die Abnahme in der Lichtübertragungseffizienz verursacht wird, dass heißt durch das Verhältniss der Photonen welche den Photodetektor erreichen zu der Gesamt-heit an Photonen produziert. Die Photonen-Transport-Zeitstreuung ist im Gegensatz teilweise kompensiert durch den Gamma-Absorptions-Zeitverzug im Kristall. Wenngleich unsere Simulationen zeigen das die Photonen-Transport-Zeitstreuung nicht wesentlich zunimmt für längere Kristalle, ist ihr Einfluss dennoch groß. Wenn wir in der Simulation die PTS für den 2x2x3mm^3 Kristall "abschalten", würde sich die CTR von 110ps auf 90ps verbessern.

In PET, Kristalllängen von 20mm oder länger sind nötig um eine ausreichende Detektionseffizienz der 511keV Gamma-Photonen zu erreichen. Um die CTR für länger Kristalle zu verbessern haben wir an beiden Enden eines 2x2x20mm^3 Kristalls einen SiPM montiert und erreichten nach Interaktionstiefen-Korrekturen (DOI) eine Zeitauflösung von 154±10ps FWHM. Dieses Resultat stellt eine CTR Verbesserung von 22ps oder 14% dar, verglichen mit der einseitigen Messung des Kristalls. Die CTR Verbesserung ist fast ausschließlich erklärbar mit einer höheren Lichtausbeute der Zweiseiten-Messung und bekräftigt unseren zuvor gefundene Zusammenhang, dass die Abnahme in der Lichtübertragungseffizienz die Hauptursache für die CTR Verschlechterung mit längeren Kristallen ist.

Mit der Hilfe der entwickelten Monte Carlo Simulation untersuchten wir auch einen neuen Typ von SiPM, den vollständigen digitalen SiPM. In dieser Variante von SiPM kann die Zeit jedes einzelne detektierte Photoelektrons gemessen werden. Wir haben gezeigt, dass mit optimierten

Zeit-Schätzern dieser digitale Ansatz in der Lage ist das intrinsische Limit der Zeitauflösung zu erreichen, welches mit reinen statistischen Überlegungen, wie dem "Cramér-Rao lower bound", berechnet werden kann. Darüber hinaus sind wir zu dem Ergebniss gekommen, dass der analoge SiPM, in welchem die Mikrozellen-Signale überlagert werden, auch in der Lage ist das intrinsische CTR Limit zu erreichen. Von unseren Simulationen lernten wir desweiteren, dass die Gleichheit in der erzielten Zeitauflösung für den digitalen und analogen SiPM auch für verschiedene Kristallängen gültig ist, das heißt für 3mm, 5mm, 10mm und 20mm Länge. Folglich kann keine Präferenz zwischen analogen und digitalen SiPM gegeben werden, wenn es nur darum geht beste Zeitauflösung zu erhalten. Jedoch soll bemerkt werden, dass der analoge SiPM die beste Zeitauflösung in einen eher kleinen Schwellenwerte-Bereich liefert, wohingegen der digitale SiPM eine stabile Zeitauflösung nach ungefähr 20 in den Zeit-Schätzer eingebundenen Photoelektronen zeigt. Dieses Merkmal könnte den vollständig digitalen SiPM stabiler gegen elektronisches Rauschen und im SiPM künstlich erzeugte korrelierte und unkorrelierte Photoelektronen machen.

Acknowledgments

To acknowledge everyone who gave support and help on my exciting journey towards the end of this thesis is a huge, maybe even impossible, task. There were so many people who supported me in a professional way and at least as many who gave me support and love on the various roads besides my carrier as a physicist. To me it seems difficult to acknowledge all of them in a manner they would deserve and most importantly not to lose sight of anyone. In the next paragraphs I will try to do my best in order to give all of you my highest gratitude, although I can say already now, the text below should be longer, much longer.

I beginn with my supervisor Prof. Christian Fabjan, who supported and guided me during my PhD and I as well want to thank him for his final proofreads. I want to thank Dr. Paul Lecoq and Dr. Etiennette Auffray for giving me the chance to work in their group on such an exciting subject as TOF-PET and for their encouragement during the last three years. Additionally they proofread my thesis and helped to refine it to the current version. Speaking about corrections I immediately have to think of Dr. Thomas Meyer, who helped me immensely with my written English and the physical discussions we had, I do not want to miss. Next I want to thank Dr. Pierre Jarron with whom I had as well some interesting discussions about, most of the times, not quite trivial problems. My gratitude goes as well to Benjamin Frisch and Kristof Pauwels who introduced me to the diverse experimental setups in our group and to the numerous organizational tricks at CERN. Thank you for always having an ear for my sometime too many concerns. At this point I also want to mention François Powolny, who was my "short term" mentor at the very first months of my stay at CERN. He and Tom familiarized me to the concept of TOF-PET and the setup from which I could start to develop my own work, as will be presented in this thesis. I also want to mention Arno Knapitsch with whom I not only shared an office but had as well a lot of discussions about light propagation in crystals and as well light ray tracing simulations. Further I want to mention Nicolas Di Vara and Marco Pizzichemi for their help here and there. I as well want to thank our two technicians Dominique Deyrail and Alain Machard for helping with various kinds of mechanical problems like cutting/polishing crystals, building crystal holders, constructing light tight boxes and so on. Last but not least I want to mention Mythra, Pawel, Marco, Zheng, Rita, Alessio, Rosana, Faraah, Giulia, Katayoun and all the other persons at CERN which were accompanying me and made my stay so much more pleasant.

Aber, das ist bei weitem noch nicht das Ende! Ich will auch meiner Familie, Verwandten und all meinen Freunden in Österreich danken wie Armin, Maria, Lukas, Luzi, Chris, Heli, Julia, Stefan, Birgit, Markus, Daniela,... Wenn ich nach längerer Zeit wieder nach Österreich zurückkehre, habt

ihr immer Zeit um gemütlich zu quatschen, Spaß zu haben und einfach nur zu entspannen. Ich habe immer eine gute Zeit mit euch, und möchte keinen von euch missen!

Am Ende dieser Zeilen ist es mir ein Anliegen meine Eltern, Karl und Leopoldine, voranzuheben. Sie stehen mir immer zur Seite und haben mich mit ihrer Liebe und Aufmerksamkeit schon durch so einige düstere Tage geleitet. Ohne eurer Zuneigung und Unterstützung hätte ich meine Ziele sicherlich nicht erreichen können. Danke für alles!

My sincere thanks goes to all of you,
family, friends, and colleagues!

Stefan Gundacker

It is not the nature of things for any one man to make a sudden, violent discovery; science goes step by step and every man depends on the work of his predecessors. When you hear of a sudden unexpected discovery - a bolt from the blue - you can always be sure that it has grown up by the influence of one man or another, and it is the mutual influence which makes the enormous possibility of scientific advance. Scientists are not dependent on the ideas of a single man, but on the combined wisdom of thousands of men, all thinking of the same problem and each doing his little bit to add to the great structure of knowledge which is gradually being erected.

Sir Ernest Rutherford

Contents

Chapter 1

Introduction

Positron emission tomography (PET) is commonly used in oncology for the diagnosis of cancerous cells in the body. In PET the β^+-decay of a radioactive biomarker (tracer) produces a positron resulting, from the annihilation with an electron, in the emission of two almost anti-parallel 511keV gammas. These 511keV photons are detected in gamma detectors placed around the patient. The connecting line of an opposite detector pair forms the line of response (LOR) along which the emission took place. If many of such LORs are recorded, a three dimensional image of the tracer concentration in the body can be drawn. A commonly used tracer is Fluorodeoxyglucose (FDG) which has a comparable metabolism like glucose. Because most cancer cells show a higher glucose metabolism than normal cells the biomarker uptake will predominantly take place in cancerous cells and thus enhance the positron emission rate in these zones.

Without precise time information in PET all points along the LOR have the same probability of being the origin of the β^+-emission, i.e. originating from the tumor. If, on the other hand, timing information from the individual arrival time of the coincident gammas is included in the reconstruction algorithm, their true emission point along the LOR could be confined with a precision that depends only on the achievable time resolution of the apparatus. While it is not possible to reach with current CTRs (of the order of a few hundreds of picoseconds) a tumor delineation in the millimeter range along the LOR, uncorrelated background can nonetheless be significantly reduced with the effect of greatly improving image reconstruction and -quality to the benefit of the patient [1, 2]. This makes TOF an increasingly attractive feature and hence playground for future research in PET. Today commercial, state of the art, full-body TOF-PET scanners achieve a coincidence time resolution (CTR) of around 500ps FWHM [3–5]. More advanced research solutions aim at a CTR of around 200ps FWHM [6], corresponding to a zone of ~3cm around the point of emission, sufficient to reduce coincidence events not originating from the zone of interest. An improvement of the CTR to ~100ps would further suppress such background and isolate the emission point to better than 1.5cm. A gain in SNR by a factor of ~5 can be achieved this way, corresponding to a sensitivity gain of 25 [1]. Therefore, to achieve a CTR of 100ps FWHM is a plausible target for a fully integrated TOF-PET system of the future.

Scintillator based detectors are commonly used to detect the 511keV gammas produced by the electron-positron annihilation. Such detectors consist of a scintillating crystal, a photodetector

and electronics to read out and process the signals. On absorption in the scintillator, the 511keV gammas are transformed to visible photons which are transfered to the photodetector. The photodetector, e.g. a photomultiplier tube (PMT) or silicon photomultiplier (SiPM), detects this visible light and produces an electrical signal. The high energy of the gammas makes it necessary to use dense and high-Z materials, e.g. Lutetium, with lengths of 20mm or longer in order to ensure high detection efficiency.

New photodetectors like SiPMs are promising candidates towards achieving excellent time resolution [7, 8]. Coupled to LSO:Ce doped scintillators with dimensions of $3x3x5mm^3$ it is for example possible to achieve CTRs of 147ps FWHM. This value, however, degrades to 186ps FWHM if crystals of $3x3x20mm^3$ were used [9]. Hence, the photon travel spread and absorption in the crystal is not negligible and has to be taken into account for a full understanding of the system's time resolution [10, 11]. The research performed on SiPMs so far highlights their strong advantages in terms of timing. On the other hand, their drawbacks are a high dark count rate (DCR), high temperature dependence and the need for fast and low noise electronics to amplify and read out the signals generated by one pixel.

The objective of this thesis is to describe the whole 511keV gamma detection chain in terms of timing, from the gamma absorption and the scintillation process with its characteristic photon emission leading to the total amount of photons produced to the light transfer from the crystal to the SiPM together with its readout electronics. We have been using commercially available SiPMs from Hamamatsu (S10931 MPPC) and the NINO amplifier-discriminator chip to read out the generated signals. A large effort was made to optimize and understand the measurement setup in all its facets. The SiPMs, readout electronics, data acquisition system and used scintillators were fully characterized to provide realistic input to specially developed Monte Carlo (MC) simulations. The simulation tool is able to describe the whole scintillator based detector such that the predicted CTR values could be compared with CTR measurements for different crystal lengths. The various measurements that we had performed, together with the simulation tool, enabled us to analyze each step of the detection chain in terms of its influence to the time resolution of the whole gamma detector. In this thesis special emphasis was placed on TOF-PET applications. Therefore the nominal gamma energy used throughout this study was 511keV. Nonetheless, the arguments and results developed in this work can be extrapolated to other interaction energies in the crystal.

The thesis is organized in the following way:

- The second chapter will give a short introduction to PET, the basic principles, its challenges and the expected benefit from applying time of flight in PET. We conclude with a table of crystals suitable for TOF-PET applications.

- In chapter three follows a detailed description of the scintillator based detector divided into three main parts. The first part describes the gamma ray interaction in the crystal and the basic mechanisms of scintillation. We will discuss limiting factors in the light transfer of a crystal and make a simple approach to estimate the time resolution of the first photons

emitted in the scintillation process. The second part of chapter three describes the silicon photomultiplier. Its composition will be discussed as well as its basic properties and operational parameters. In the third part we will give a short overview of the time-over-threshold amplifier-discriminator NINO that was used for the timing measurements.

- In chapter four the SiPM is characterized in terms of its timing performance using femtosecond laser pulses. We tested three commercially available types of SiPM (Hamamatsu S10931 MPPC) with the same active area of 3x3mm^2 but different microcell sizes, i.e. 25μm, 50μm and 100μm. We measured the single photon time resolution (SPTR) as a function of SiPM overvoltage. Additionally we tested the timing performance of the SiPM for higher light fluxes as a function of bias overvoltage and NINO threshold. This allowed to estimate the timing contribution of the electronics, i.e. NINO.

- Chapter five reports on coincidence time resolution measurements as a function of SiPM bias overvoltage and NINO threshold voltage. We tested the three different types of SiPMs given above, always using the same type of crystal in order to probe only the SiPM performance. The results were compared with the femtosecond laser tests. Additionally, we show CTR measurements with different crystal cross sections and wrapping. The influence of the dark count rate (DCR) of the SiPM to the CTR will be discussed and different SiPM production batches of the same manufacturer tested.

- In chapter six the time-over-threshold energy encoding of NINO is investigated in more detail. We present a newly developed NINO board using NINO as a fast, low noise leading edge discriminator and a separate analog amplifier to determine the gamma energy with higher accuracy than the NINO time-over-threshold energy encoding. CTR measurements using the new NINO board are presented and the improvements discussed.

- To obtain a deeper understanding of the interplay of photon detection, scintillation statistics and light transfer in the crystal we developed a Monte Carlo simulation comprising the whole detection chain, to be presented in chapter seven. The simulation developed in MATLAB incorporates the scintillation properties of the crystal, light transfer within the crystal as simulated by SLITRANI, and the timing properties of the photodetector and electronics. We compare the simulated CTR values with measurements and conclude by investigating the influence of various factors to the time resolution, like scintillation rise and fall time, number of detected photons, SPTR, DCR, optical crosstalk, electronic noise and photon travel time spread in the crystal.

- In chapter eight we investigate in more detail the scintillation light transfer in the crystal. We present CTR measurements for crystals with a common cross section of 2x2mm^2 but different lengths, i.e. 3mm, 5mm, 10mm and 20mm. We compare the measurements with the Monte Carlo predictions and examine the influence of the scintillation light transfer efficiency and photon travel time spread to the CTR as a function of crystal length.

- Chapter nine reports on the effects of double sided readout using 2x2x20mm^3 crystals. We

compare the measured CTR of a double sided readout crystal with a single sided readout crystal and discuss the improvements. A possible CTR dependence on parallax effects in PET will be mentioned as well.

- In chapter ten the limits of the CTR are being explored. We discuss the best achievable time resolution in an analog SiPM and indicate ways for improvements. We show lower bound calculations and discuss the influence of the scintillation rise time and SPTR to the time resolution. This chapter also discusses CTR simulations on a fully digital SiPM where we test different time estimators and compare the results with lower bound calculations. The chapter finishes with a comparison of the analog and digital SiPM. For both types of SiPM we show simulations of the best achievable time resolution for different crystal lengths.

- In chapter eleven the thesis closes with a short summary, final remarks and conclusions and an outlook to future research interests.

Chapter 2

Positron emission tomography

2.1. Introduction

Positron emission tomography (PET) is a functional imaging method in medicine which uses radioactive tracers to obtain a three dimensional image of metabolism processes in the body. In the case of PET these tracers or radiopharmaceuticals are labeled with radioactive isotopes disintegrating via β^+-decay and produce two (nearly) collinear 511keV gammas by annihilation with an electron. The collinear gammas are recorded by detectors placed around the patient giving the input data for the image reconstruction. The carrier molecules can be designed to match particular characteristics of the targeted cells or metabolism. This makes PET extraordinary in the discipline of medical imaging as it maps physiological processes on the microscopic level. For instance X-ray computed tomography (CT) maps only macroscopic anatomical features, i.e. the X-ray attenuation coefficient. PET is able to detect single β^+-disintegrations and thus is theoretically sensitive to tiniest tracer molecule concentrations in the cells at the picomolar level which is unbeatable by any other imaging method in medicine. In this chapter the basic principles of PET will be explained, i.e. radioactive tracers, image reconstruction, noise, spatial resolution, sensitivity and parallax error. Time of flight PET will be introduced discussing the advantage expected by the additional time information. We will conclude this chapter with scintillating crystals suitable for PET before we will talk about the radiation detector components in chapter 3 in more detail.

2.2. PET principle

The idea of PET is to measure the distribution of biomarkers in the body or in organs of interest. In order to do that the biomarkers are labeled with a radioactive isotope which disintegrates via a β^+-decay. The emitted positron will annihilate with an electron in the tissue and be converted into two almost collinear gammas ($e^+ + e^- \rightarrow 2\gamma$). The cross section of electron-positron annihilation is highest for low center mass velocity. This means that the positron will undergo collisions in the tissue until being thermalized with the environment. The mean distance the positron will be spread is called the positron range and is around 0.2mm for ^{18}F. This spread leads to a spatial smearing of the tracer distribution in the reconstructed image. The positron range depends

strongly on the initial kinetic energy and thus on the type of used radioactive isotope (see table 2.1). Despite the higher probability of annihilation after thermalization the momentum of the electron-positron pair is not zero at the time of annihilation (mostly due to thermal fluctuations). Because of conservation of momentum the two gamma rays emitted are not exactly collinear. The angular variation can be described by a Gaussian distribution with a full width half maximum (FWHM) of about 0.5 degrees [12]. This acollinearity leads to an additional spatial resolution degradation in the order of 2mm for a whole body PET scanner with a ring diameter of 80cm.

The pair of gammas can be detected by placing radiation detectors around the patient. In figure 2.1 the schematics of a whole body PET scanner is shown. In the center of the field of view (FOV) the patient lies on a bed, which can be moved through the PET ring. If two detectors in figure 2.1 measure a gamma almost simultaneously, within a short coincidence time window, such a positron decay was detected. The line joining these two detectors forms the line of response (LOR). Recording many of such LORs allows to reconstruct a 3-D image of the tracer distribution in the whole body of the patient.
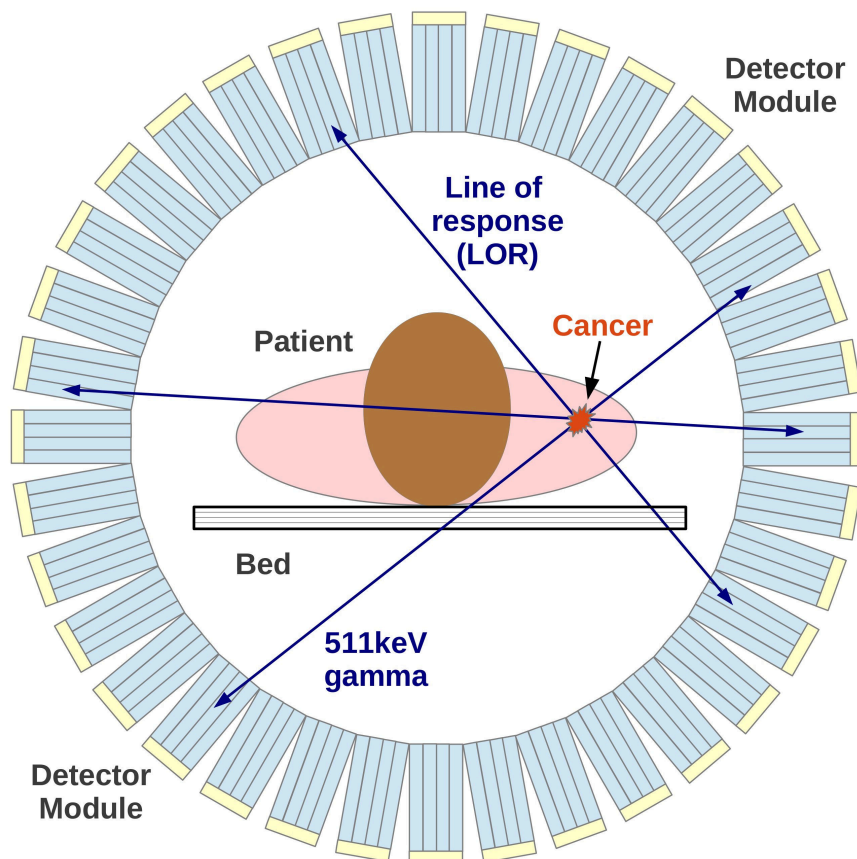

Figure 2.1.: Schematic illustrating the principle of a PET system. The crossing of the line of responses (LORs) determines the position of the cancer. One detector module is build of several single crystals with dimensions of about $2x2x20mm^3$ arranged in matrices.

2.2.1. Radioactive tracers

The most common tracer is Fluorodeoxyglucose (FDG) which is a glucose molecule labeled by a positron emitting Fluorine ^{18}F. The chemical structure of FDG can be seen in figure 2.2. This glucose molecule has a comparable metabolism like sugar but is not degraded in the cells contrary to normal glucose. It will therefore concentrate in cells where the glucose metabolism is the highest, drawing a radioactive map of glucose metabolism in the body. Because most cancer cells show a higher glucose metabolism as compared to somatic cells FDG is suitable for oncology. However it should be noted that some cancer types are not sensitive to FDG, e.g. lymphoma or neuroendocrine tumors. As well inflammation of non-cancerous cells can increase the FDG uptake and lead to false positive results [13].
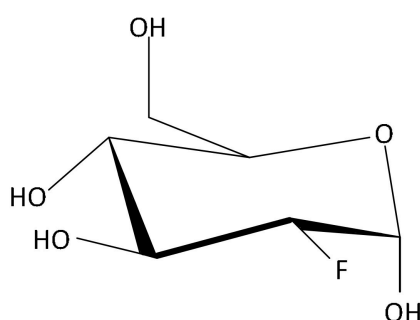
Figure 2.2.: Skeletal chemical formula of FDG [14].

The radiopharmaceutical does not necessarily has to be labeled with ^{18}F. There are many other types of β^+ radioactive isotopes, e.g. ^{11}C, ^{13}N, ^{15}O, ^{68}Ga and ^{82}Rb. They have different physical properties as can be seen on some examples in table 2.1.

Table 2.1.: Common radioisotopes and their physical properties [15]. Both full width half maximum (FWHM) and full width tenth maximum (FWTM) of the positron range are given in order to point out the exponential tails.

Isotope	half-life (min)	average kinetic energy (keV)	maximum kinetic energy (keV)	positron range FWHM (mm)	positron range FWTM (mm)
^{11}C	20.4	385	960	0.28	1.86
^{15}O	2.0	735	1732		
^{18}F	109.8	242	633	0.22	1.09
^{82}Rb	1.3	1320	4390	2.60	13.20

Among the different radioisotopes ^{18}F has the longest half life of 110 minutes. Because the half life of all radioisotopes is too small for storage they must be produced directly at the hospital or be delivered within a rather small delay. A common way to produce radioisotopes is through bombardment of a stable mother target with high energetic protons from a cyclotron. Fluorine ^{18}F is produced in this way: $^{18}O + p \rightarrow ^{18}F + n$.

2.2.2. Image reconstruction

A line of response shown in figure 2.1 can be fully characterized by its angle θ relative to the horizontal direction (x-axis) and by the shortest distance between the center of the PET detector ring and the LOR $d_{center,LOR}$. Any LOR sums the activity along its path as in a classical PET, without time of flight information, β^+-decays along the LOR cannot be distinguished. Thus, the detection in PET maps the tracer distribution into a space described by line integrals of the activity. One can find that this transformation observed in PET is described by the so called Radon transformation after the Austrian mathematician Johann Radon, who introduced the mathematical description already in 1917. The definition of the Radon transformation can be seen in equation 2.2.1 which describes the measured activity $A(\mathbf{L})$ in the space of straight lines $\mathbf{L}$. This lines are equal to the predefined LORs.

$$A(\mathbf{L}) = \int_{\mathbf{L}=LOR} S(\mathbf{x}|\mathbf{L})\varrho(\mathbf{x})|d\mathbf{x}| \qquad (2.2.1)$$

The tracer distribution as a function of the coordinate space $\mathbf{x}$ is given by the term $\varrho(\mathbf{x})$. In addition a weighting factor $S(\mathbf{x}|\mathbf{L})$ is used to describe the sensitivity of the detector for a given point of emission $\mathbf{x}$ under the condition of a certain LOR ($\mathbf{L}$). In figure 2.3 an example of the Radon transformation is given. On the left a tracer distribution showing two points and a straight line. On the right in figure 2.3 one can see the respective Radon transformation. A point in the center of the PET ring will be transformed to a horizontal line. If the point is off-centered then the transformation gives a sine wave like function. This is why the graph on the right in figure 2.3 is as well called sinogram. The value of every point in the sinogram represents the integral activity of the LOR defined by $d_{center,LOR}$ and θ.
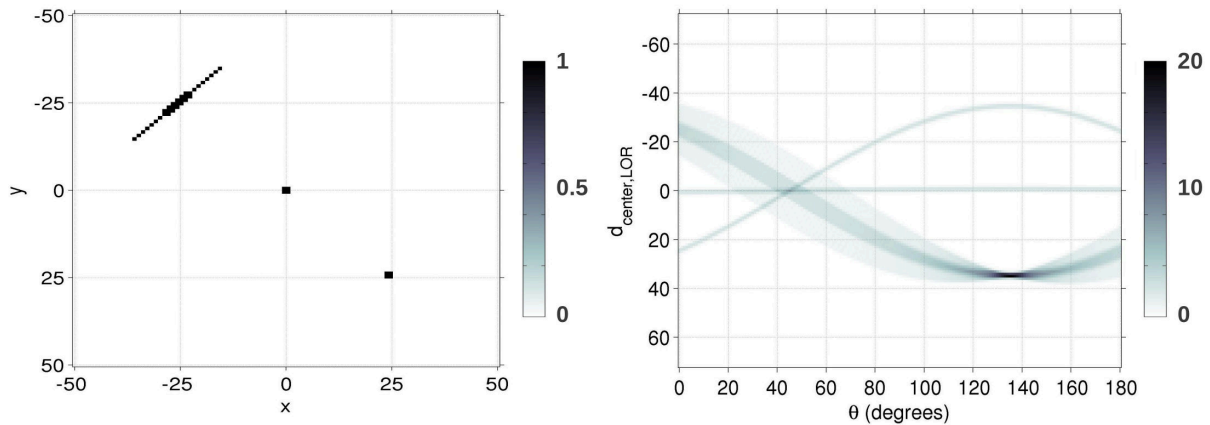
**Figure 2.3.:** Illustration of the Radon transformation. Left: image in the coordinate space and right: sinogram of the respective Radon transformation.

There are two main ways of transforming the sinogram back to the original image in the coordinate space: back-projection and iterative image reconstruction.

In the back projection one assumes that all pixels in the LOR have contributed equally to the

measured activity. Overlapping all lines represented by the sinogram with constant value along the LOR gives the back projected image. In other words the measured activity of a detector pair will be projected as constant value along the LOR defined by the detector pair. The density of overlapped lines is highest for the center and decreases with larger distance from the center. This corresponds to a convolution of the image data with a cone shaped filter function $s = (x^2 + y^2)^{-1/2}$. In the filtered back projection one accounts for this by an appropriate inverse filter to the image or projection data. Filtered back projection has been the choice in PET for many years because of its simpleness and relatively low computational needs. However this method has disadvantages if the recorded data is noisy. Hence iterative image reconstruction methods are most of the times better suited [16].

The iterative methods start with an assumed tracer distribution image in the body. With this distribution the expected projection according to equation 2.2.1 is calculated. The calculated sinograms will then be compared with the measured ones. The differences are the input for an update in the tracer distribution function $\varrho(\mathbf{x})$. With the updated tracer distribution the expected projection is again calculated and so on. The algorithm stops when a predefined criteria is met or until a fixed number of iterations is reached. In this method noise can be included fairly easily in the reconstruction, e.g. in so called maximum likelihood expectation maximizations [17].

2.2.3. True, random and scattered coincidence events

A coincidence event is observed when two gamma signals in the PET ring are detected within a short predefined coincidence time interval. Gammas of 511keV interact with matter mainly via photoelectric absorption or Compton scattering. A detailed description of these processes will be given in the next chapter 3. The attenuation length in tissue (λ_{tissue}) is about 10cm and therefore a noticeable amount of gammas will be absorbed before reaching the gamma detectors which lowers the event rate. In addition Compton scattering can change the path of the gammas. All these processes lead to noise in PET because not all coincidence events are true ones in the sense that they originated from the same point or the gamma trajectories remained unchanged. In figure 2.4 the different types of noise in PET are illustrated.

Random coincidence events denote the detection of two 511keV gamma in a short time interval although they were not generated from the same β^+-decay (to be seen on the top of figure 2.4). This can be caused by a decay of two radioisotopes at the same time where only one gamma of each pair reaches the detector ring and the other is absorbed in the tissue. Such an event cannot be distinguished from a real coincidence event and a wrong LOR will be associated. The random coincidence rate R_{random} is proportional to the coincidence time window Δt and the square of the single count rate S ($R_{random} \propto \Delta t \cdot S^2$) [18]. Thus a shorter time window Δt given by a better time resolution of the gamma detectors can reduce the rate of random coincidences effectively.

Another type of noise is caused by scattered coincidence events when gammas underly Compton scattering. This can be seen on the left in figure 2.4. Compton scattering is the inelastic scattering

of gamma photons with weakly bound or free electrons. Depending on the scattering angle θ, defined by the deviation from the original path of the gamma, a noticeable amount of energy is transfered to the electron. The higher the deviation angle the higher is the energy transfer. Thus scattered coincidences can be filtered by measuring the gamma energy and applying an energy threshold which requires detectors with a good energy resolution. For small scattering angle θ the energy resolution is in the most cases too small to apply such a threshold. The accepted scattered coincidence events are associated with a wrong LOR and thus will contribute to a reduction of the image resolution. The fraction of Compton scattered events can reach up to 50% of the total amount of detected events [19] and is therefore important in PET.
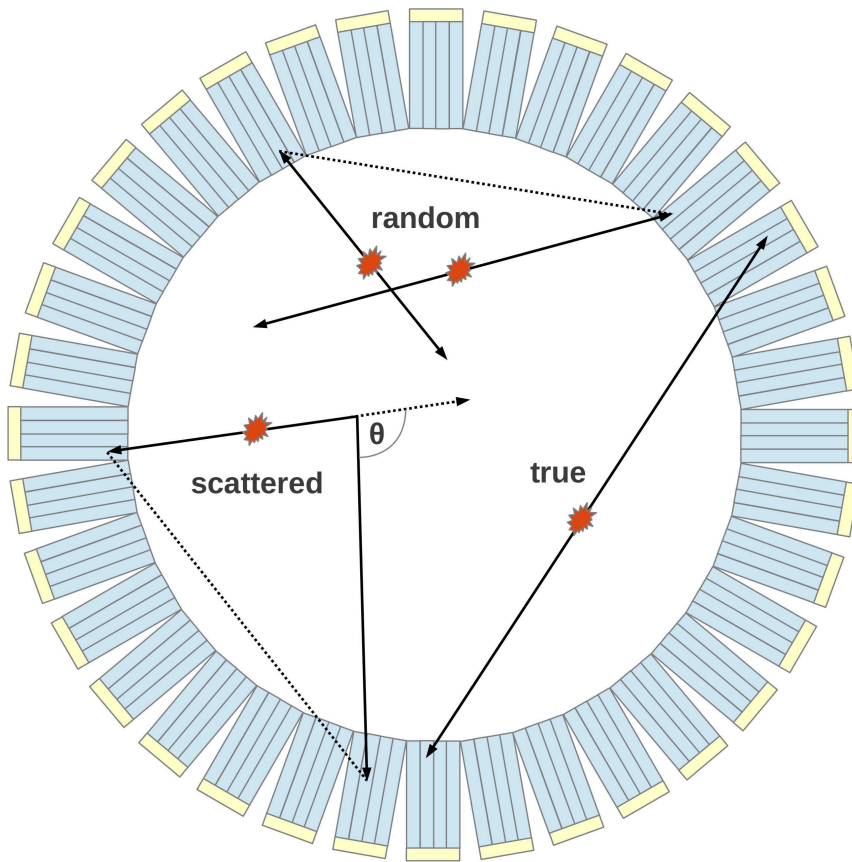
Figure 2.4.: Illustration of true, random and scattered coincidence events in a whole body PET.

Only true coincidence events deliver LORs where the actual point of emission is contained. The other false coincidence events add to background noise in the reconstructed image and are reducing the signal to noise ratio (SNR) of the image, contrast and image resolution. The SNR is a function of the count rate of true coincidence events R_{true}, random coincidence events R_{random} and scattered coincidence events $R_{scattered}$ as can be seen in equation 2.2.2 [2].

$$SNR \propto \sqrt{\frac{R_{true}^2}{R_{true} + R_{random} + R_{scattered}}} \tag{2.2.2}$$

2.2.4. Sensitivity

The sensitivity of a PET system is defined as the number of detected true coincidence events normalized to the tracer activity. It is one of the most important system parameters since the SNR is proportional to the number of detected true coincidence events (see equation 2.2.2). The true coincidence event rate and thus the sensitivity depends on the gamma detector efficiency ($\eta_{detector}$), solid angle coverage of the detector (η_Ω) and gamma attenuation in the tissue with the attenuation length λ_{tissue}. In equation 2.2.3 the true coincidence event rate R_{true} is expressed by these factors. D is the thickness of the patient and R_0 the tracer activity in positrons per second.

$$R_{true} = R_0 \cdot \eta_{detector}^2 \cdot \eta_\Omega^2 \cdot \exp\left(-\frac{D}{\lambda_{tissue}}\right) \qquad (2.2.3)$$

The gamma detector efficiency $\eta_{detector}$ and solid angle coverage of the detector η_Ω are squared since the two 511keV gamma have to be detected in coincidence in two detectors. This shows the need for materials with a high gamma stopping power in order to keep $\eta_{detector}$ high. For this purpose commonly scintillating crystals with high effective Z and density are used as will be discussed in chapter 3.

2.2.5. Parallax error

If coincidence events take place at the margin of the field of view (FOV) the volume of response increases. This is illustrated in figure 2.5. The volume of response (VOR) is the three dimensional extension of the line of response. It is defined as the volume in which every β^+-decay can cause an observation of two true coincident gamma events in a chosen detector pair. If the coincidence event is located in the center of the PET ring the VOR is determined by the cross section of the crystals. Coincidence events which are taking place off-centered do not travel parallel to the crystal axis and the VOR can be calculated by the projection of the whole crystal dimensions. Hence parallax effects become more pronounced with increasing crystal lengths.

Parallax errors can be suppressed if the depth of interaction (DOI) of the 511keV gamma in the crystal is known. Several techniques can be used to determine the DOI information. One method is double sided readout where a photodetector is placed at each end of the crystal. Because of scintillation light absorption in the crystal the photodetector closest to the gamma impact point will measure a higher amount of scintillation light. With this approach it is possible to determine the DOI in the crystal to a few millimeter in precision [14, 20]. Another technique is the so called phoswich detector. Two scintillating crystals with different emission properties, e.g. LSO and LuAP, are stacked on each other and readout by one single photodetector [21, 22]. The characteristics of the scintillation light detected, e.g. scintillation decay time, indicates which crystal absorbed the 511keV gamma. This method is limited in the DOI resolution by the number of different crystals applicable. A third interesting concept is the AX-PET where crystals are oriented axially and thus avoid the problem of parallax completely [23].
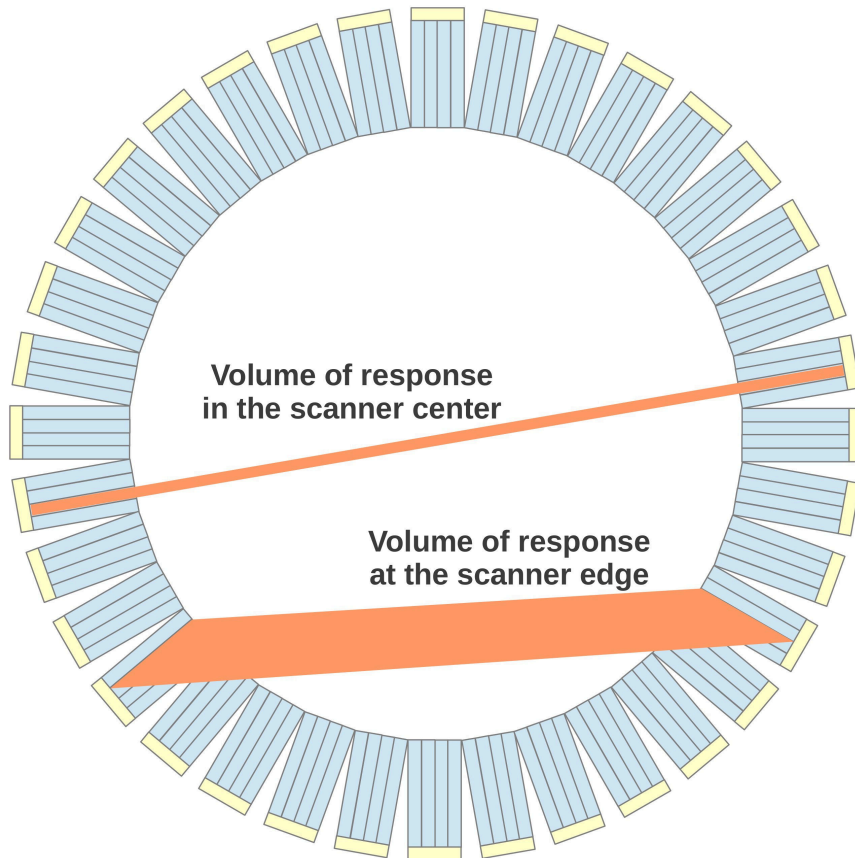
Figure 2.5.: Parallax effect in a whole body PET.

2.3. Time of flight information

In a PET system the image quality determined by the signal to noise ratio, can be drastically improved by using time of flight (TOF) information [2]. This additional time information improves the prior information on the exact localization of the positron emission point in the LOR and thus contributes to the rejection of background events outside the region of interest, reducing the noise in the reconstructed image and increasing the image contrast. In figure 2.6 the concept of time of flight in a whole body PET system can be seen. Without any time information all points along the LOR have the same probability of being the origin of the β^+ emission, i.e. being emitted by the cancer cells. Including the time of flight information a certain region of the LOR can be identified to have the highest probability of being the origin of the β^+ emission as illustrated in figure 2.6. If in addition the time resolution of the detector was sufficient to determine the point of emission of every β^+ decay exactly, true 3D image reconstruction based on single events would be possible.

The image SNR gain of a TOF-PET system compared to a non-TOF-PET system can be expressed by equation 2.3.1, as described in [2]. It should be noted that equation 2.3.1 gives only an estimate for practical systems with a finit amount of acquired coincidence events and is only a

good approximation for analytical reconstruction algorithms.

$$G = \frac{SNR_{TOF}}{SNR_{non-TOF}} = \sqrt{\frac{2 \cdot D}{c \cdot CTR}} \tag{2.3.1}$$

The term D denotes the diameter of the volume to be examined (the patient dimensions), c is the speed of light in vacuum and CTR denotes the coincidence time resolution achieved by the system. Examples of the gain of a whole body TOF-PET system compared to non-TOF is listed in table 2.2. The patient diameter D is assumed to be 40cm (D=40cm).

Table 2.2.: Signal to noise ratio gain of a TOF-PET system compared to non-TOF for an examination volume (patient diameter) of D=40cm.

|	
CTR=1ns	G=1.6
CTR=500ps	G=2.3
CTR=100ps	G=5.2
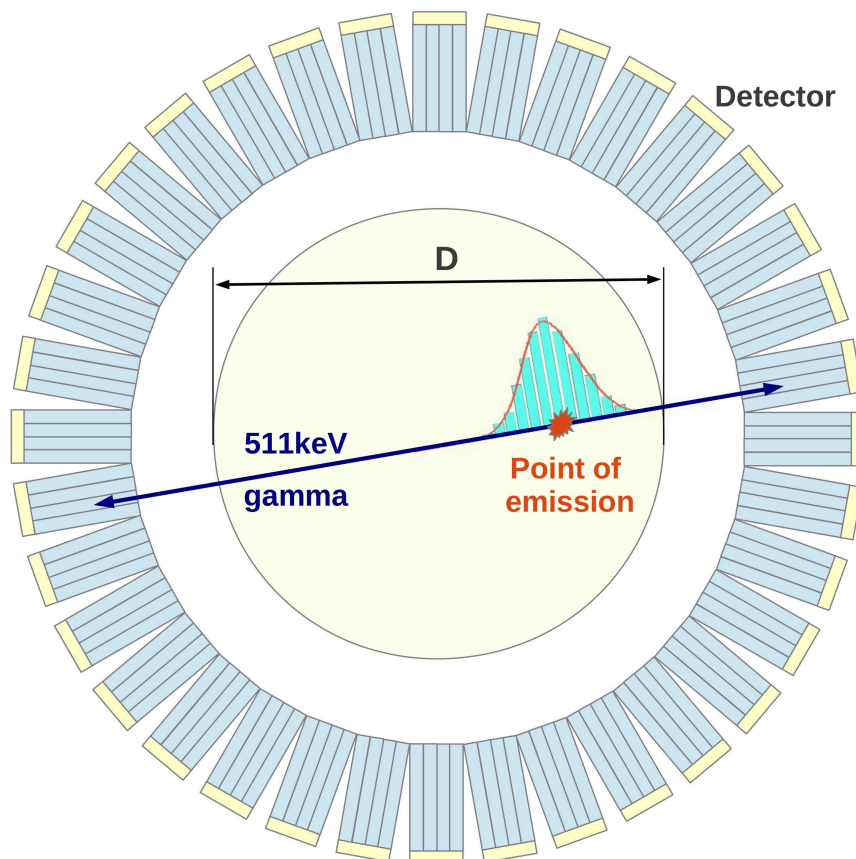
Figure 2.6.: Time of flight information in PET constraints the positron emission region along the LOR, leading to an improved SNR.

A CTR=100ps FWHM corresponds to 1.5cm position resolution and a SNR gain of 5 or a PET sensitivity gain of about a factor 25 if compared to a non-TOF-PET system [1,2]. Thus, for constant image quality, a TOF-PET system with 100ps CTR can give a tremendous reduction of the patient examination time or can lower highly the radiation dose to the patient. It should be noted that the gain in SNR of a TOF-PET system compared to non-TOF rises with the patient diameter D (see equation 2.3.1). Hence corpulent patients would benefit the most from time of flight information in PET. This is interesting because the SNR for corpulent patients is normally worse because of a lower sensitivity due to gamma absorption in the tissue.

Currently commercial full-body PETs achieve a CTR of ∼500ps FWHM [3–5]. More advanced research solutions aim at a CTR of 200ps FWHM [6], corresponding to a zone of ∼3cm around the point of emission, sufficient to remove coincidence events outside the organ of interest. To further improve the CTR towards 100ps requires detailed studies and knowledge of the full photodetection chain comprising the scintillating crystal, the photodetector and the electronics which will be presented in the following chapters of this thesis.

In figure 2.7 the SNR gain of a clinical TOF-PET system (Philips Gemini TF) with a time resolution of 600ps compared to non-TOF is shown. The TOF system with rather poor time resolution leads already to a noticeable improvement in contrast and SNR [24].
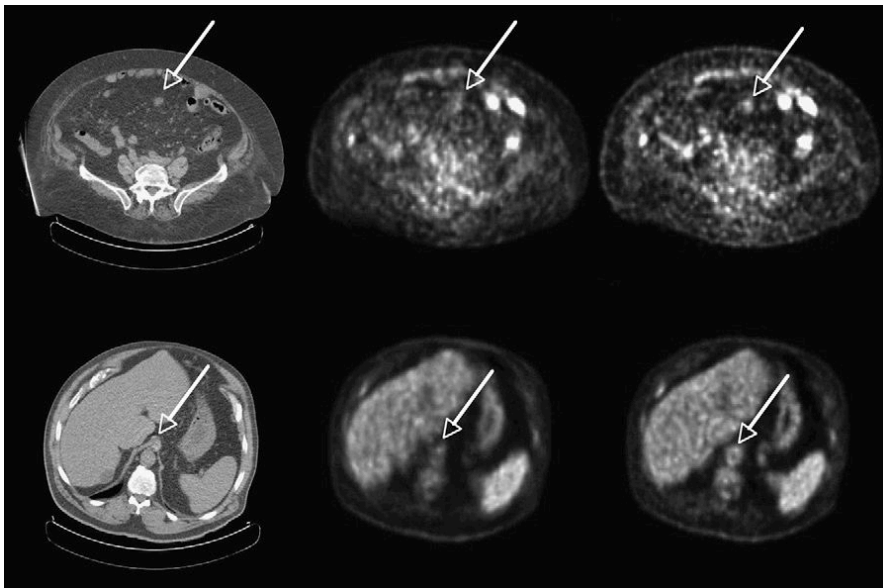
Figure 2.7.: Representative transverse sections of two different patients: low dose CT (left), non-TOF (middle), and TOF (right). (Top) Patient 1 with colon cancer (119 kg, BMI 5 46.5) shows a lesion in abdomen more clearly in TOF image than in non-TOF image. (Bottom) Patient 2 with abdominal cancer (115 kg, BMI 53.8) shows structure in the aorta more clearly in TOF image than in non-TOF image. Taken from [24]

2.4. Scintillators suitable for PET

Scintillators suitable for PET must have a high gamma attenuation, high light yield, fast decay time and the probability of photoelectric effects should be high. In table 2.3 an overview of scintillator

properties of different compositions is shown. The relative light output is given in percent and normalized to the value obtained with LSO. I_0 is defined as the relative light output divided by the scintillation decay time normalized to the decay time of LSO. This value is the most important in view of time of flight PET. A high I_0 results in a better time resolution obtainable. Along all the different scintillators to be considered LSO shows the best compromise between all the different parameters. In principle lanthanum bromide (LaBr$_3$) [25] is a good candidate for time of flight PET because of its high I_0 value. However this crystal is hygroscopic and has a low effective atomic number Z_{eff}, density and high attenuation length which makes this crystal ineffective in detecting gamma rays if compared to LSO. Therefore using LaBr$_3$ one has to resort to longer crystals as compared to LSO if the PET sensitivity should be kept constant. This has several disadvantages on timing (see chapter 8) and would as well increase parallax errors. In addition the emission wavelength of LaBr$_3$ is in the UV which relativizes its high light output because photodetectors have normally a lower detection efficiency in this wavelength range. This is as well the reason why LuAP is less suitable for TOF-PET applications when compared to LSO. In the next chapter we will describe the gamma interaction mechanisms and scintillation processes in LSO doped Cerium crystals in more detail.

Table 2.3.: Properties of common scintillators used in PET detectors. Data from [15] and [26].

Scintillator	BGO	NaI	LSO	LaBr$_3$	LuAP
Composition	$Bi_4Ge_3O_{12}$	$N_aI : Tl$	$Lu_2SiO_5 : Ce$	$LaBr_3 : Ce$	$LuAlO_3 : Ce$
Density (g/cm^3)	7.1	3.67	7.4	5.3	8.34
Z_{eff}	75	51	66	46	65
Refractive index	2.15	1.85	1.82	1.9	1.94
Attenuation length for 511keV (mm)	10.4	29.1	11.4	22.3	11
Probability of photoelectric effect (%)	40	17	32	14	32
Relative light output to LSO (%)	30	137	100	200	40
I_0 relative to LSO (%/ns)	4	24	100	500	90
Decay time (ns)	300	230	40	16	18
Scint. emission wavelength (nm)	480	410	420	360	365
Hygroscopic	no	yes	no	yes	no

Chapter 3

Components of the radiation detector

3.1. Introduction

For medical applications gamma photon energies are usually in the range of tens to hundreds of keV. This thesis is focused on TOF-PET where only gamma ray energies of around 511keV are to be considered. These energetic photons do interact only weakly with light materials, e.g Silicon, and thus it is difficult to transfer their energy directly to electric charges accessible to electronic readout. The common approach to detect such energetic photons is via scintillating crystals. A schematic of the radiation detector can be seen in figure 3.1. A heavy inorganic scintillator (e.g. lutetium oxyorthosilicate) is coupled to a photodetector. The density and length of the scintillator are chosen to ensure to stop gamma photons efficiently. The absorbed energy is converted via scintillation to visible light with a wavelength around 420nm. These visible photons can be detected by a photodetector coupled to the crystal, e.g. a silicon photomultiplier (SiPM), an avalanche photodiode (APD) or a classical photomultiplier tube (PMT). The photodetector is then generating an electronic signal which is further treated by the readout electronics. A reason for using scintillators is that in medical applications it is important to minimize the radiation dose to the patient by increasing the sensitivity of the PET system. Therefore the radiation detector must have a high detection efficiency, i.e. the gamma absorption coefficient must be high. In this chapter the three building blocks of the radiation detector, which can be seen in figure 3.1, will be discussed.
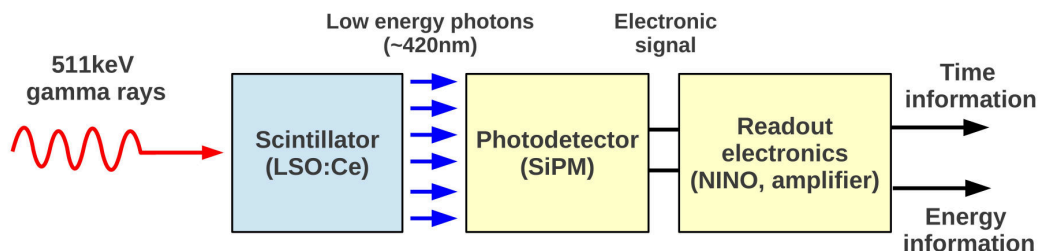
Figure 3.1.: Schematic of the scintillator based detector. An inorganic scintillator, e.g. L(Y)SO, is coupled to the photodetector (SiPM) and readout with NINO and an amplifier.

3.2. Scintillator

3.2.1. Gamma ray interaction

There are three interaction mechanisms of a gamma ray with the scintillator: photoelectric absorption, Compton scattering and pair production. These processes lead to partial or complete transfer of the gamma energy to electrons in the scintillator material. In these processes the gamma ray is either absorbed completely or its trajectory is changed abruptly into other directions. In this section an overview of the most important gamma ray interactions in the crystal is given, following the publication [27]. The arguing will be adapted to the special case of lutetium oxyorthosilicate (Lu_2Si0_5 or LSO) crystals [28] and to energies around 511keV as used in positron emission tomography.

Photoelectric absorption:

In the photoelectric absorption a gamma ray with energy E_γ is absorbed completely by an electron bound to an atom. Due to conservation of momentum and energy this process is not possible for free electrons. However the recoil energy of the atom involved is very small and usually can be neglected. The absorbed gamma energy is used to free the electron from its bound state with the binding energy E_b and leaves the electron with the kinetic energy E_{e^-} as shown in figure 3.2 and described in formula 3.2.1.
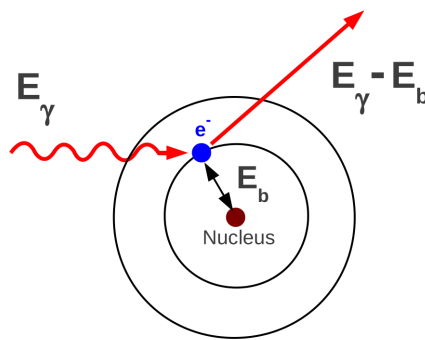
Figure 3.2.: Illustration of the photoelectric absorption of a gamma.

$$E_{e^-} = E_\gamma - E_b \qquad (3.2.1)$$

The photoelectric absorption is predominant for low gamma energies and an enhancement in the cross section can as well be seen in materials with high atomic number Z. A rough approximation of the photoelectric cross-section (σ_{pe}) is given by formula 3.2.2.

$$\sigma_{pe} = constant \cdot \frac{Z^n}{E_\gamma^{3.5}} \qquad (3.2.2)$$

In equation 3.2.2 the exponent *n* varies between 4 and 5 for gamma energies used in clinical detector applications. Therefore high atomic number materials, e.g. Lutetium, are preferred in gamma-ray detector systems.

Photoelectric absorption is likely to happen with the most tightly bound K-shell electron, if the gamma ray energy is sufficient. As a consequence the interaction creates an ionized atom with a vacancy in one of its shells. This vacancy will be filled through capture of other bound or free electrons generating one or more characteristic X-ray photons. These low energy X-ray photons will be in general reabsorbed close to the primary photoelectric event. However, if the scintillator dimensions are small, then such photons can escape the detector and cause an escape peak in the response. In some cases Auger electrons can as well carry away the atomic excitation energy.

Compton scattering:

Compton scattering is the inelastic scattering between the incoming gamma and a weakly bound or free electron in the material. The gamma photon with an energy E_γ will be deflected by an angle θ with respect to its incoming direction as can be seen in figure 3.3. A portion of the gamma photon energy and momentum is transfered to the recoil electron. All angles of scattering are possible which means that the energy transfer can vary from zero to a large fraction of the gamma energy.
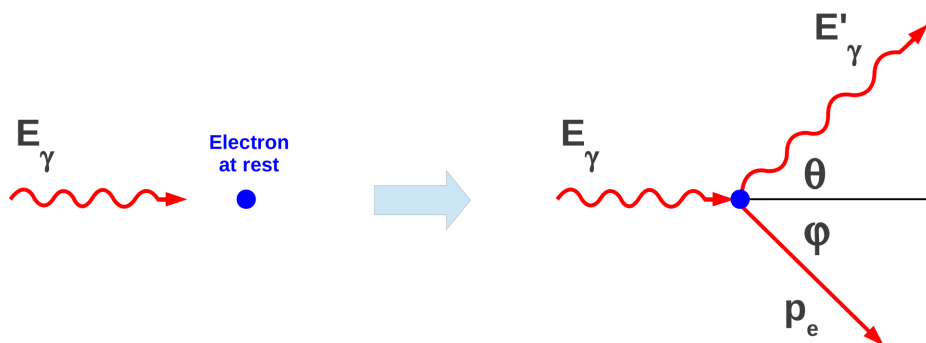

Figure 3.3.: Illustration of Compton scattering on a free electron.

Using the conservation law of momentum and energy one can derive the gamma energy after scattering E'_γ, shown in equation 3.2.3. The term $m_e c^2$ describes the rest mass of the electron (511keV). It is interesting to notice that even for the extreme case $\theta = \pi$ some of the initial energy is kept by the incident gamma photon. For an incident gamma with energy E_γ =511keV this retained energy is E'_γ =170keV, i.e. one third of 511keV. Consequently in a detector the Compton edge is observed at an energy 511keV-170keV=341keV, for an incident gamma energy of 511keV.

$$E'_\gamma = \frac{E_\gamma}{1 + \frac{E_\gamma}{m_e c^2}(1 - \cos\theta)} \tag{3.2.3}$$

The angular distribution can be described by the Klein-Nishina formula [27] as shown in equation 3.2.4. It is linearly dependent on the atomic number Z, as the probability of Compton scattering depends on the number of electrons available. In figure 3.4 the Klein-Nishina distribution according to equation 3.2.4 is shown. The plot illustrates that Compton scattering tend to be more and more forward directed if the gamma photon energy is increasing.

$$\frac{d\sigma_{cpt}}{d\Omega} = Z \cdot \frac{e^2}{4\pi\varepsilon_0 m_e c^2} \cdot \frac{1}{2} \cdot \frac{E'_\gamma}{E_\gamma} \left(1 - \frac{E'_\gamma}{E_\gamma} \cdot \sin^2\theta + \left[\frac{E'_\gamma}{E_\gamma}\right]^2\right) \tag{3.2.4}$$
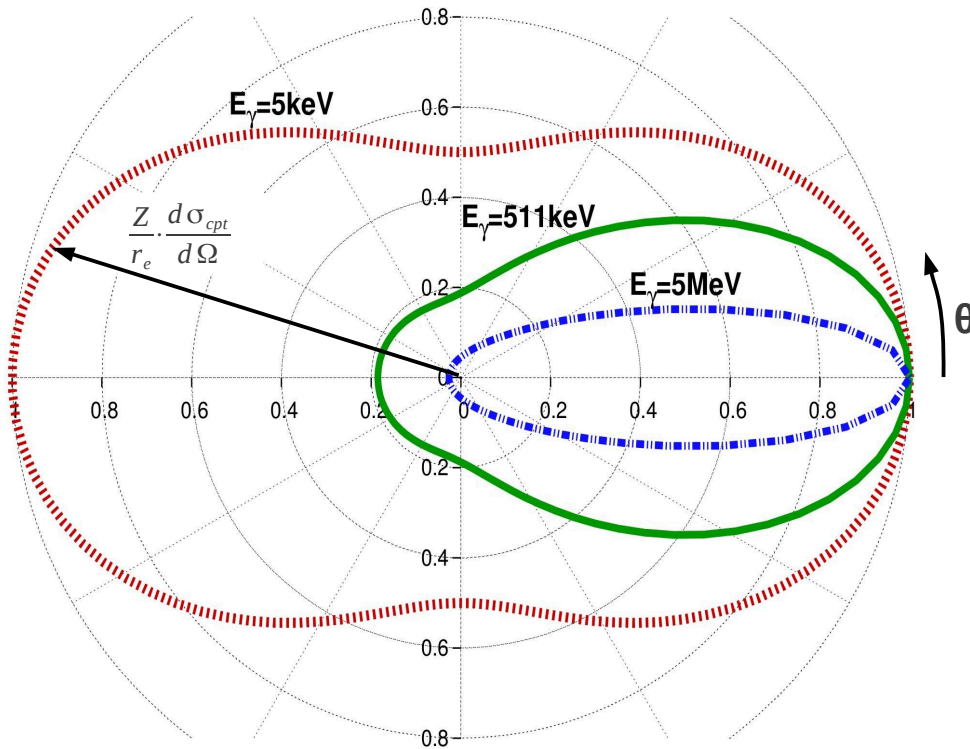

Figure 3.4.: Normalized Klein-Nishina formula plotted in polar coordinates. The classical electron radius r_e is defined in equation 3.2.5. For high gamma energies almost only forward scattering is observed.

The integral cross section can be calculated by integrating formula 3.2.4 over the solid angle $d\Omega$. Two extreme cases can be identified: (a) the gamma energy E_γ is low compared to the electron rest mass $m_e c^2$ and (b) the gamma energy is high compared to the electron rest mass $m_e c^2$. If E_γ is low compared to the electron rest mass $m_e c^2$ then the integral cross section is constant and proportional to the classical electron radius r_e, as can be seen in equation 3.2.5. If E_γ is high compared to the electron rest mass the integral cross section σ_{cpt} is proportional to $\ln(E_\gamma)/E_\gamma$ as shown in equation 3.2.6.

$$\sigma_{cpt}(E_\gamma << m_e c^2) = \int \frac{d\sigma_{cpt}}{d\Omega} d\Omega = Z \cdot \frac{8\pi}{3} r_e^2 \quad with \quad r_e = \frac{e^2}{4\pi\epsilon_0 m_e c^2} \tag{3.2.5}$$

$$\sigma_{cpt}(E_\gamma >> m_e c^2) = \int \frac{d\sigma_{cpt}}{d\Omega} d\Omega = Z \cdot \frac{m_e c^2}{E_\gamma} \pi r_e^2 \left(\frac{1}{2} + \ln \left[\frac{2E_\gamma}{m_e c^2} \right] \right) \quad with \quad r_e = \frac{e^2}{4\pi\epsilon_0 m_e c^2}$$

$$(3.2.6)$$

Pair production:

In the electromagnetic field of the detector atoms pair production is possible if the incident gamma energy exhibit values higher than twice the rest mass of an electron, i.e. 1.02MeV. A sketch of this process can be seen in figure 3.5. The probability of this reaction compared to Compton scattering and Photoelectric absorption still remains very low until the gamma energy approaches several MeV. In medical imaging applications such energies are not reached, especially in PET where the gamma energy is bound to 511keV. Therefore pair production will be neglected in the further discussions.
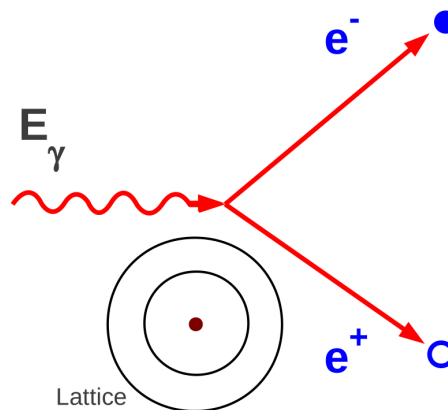

Figure 3.5.: Illustration of pair production in the electromagnetic field of the detector atoms.

Rayleigh scattering:

Another type of scattering which neither excites or ionizes the atom can happen as well, the so called Rayleigh scattering. It is a type of coherent scattering involving all the electrons of an absorber atom. The gamma photon retains its original energy and is only subject to changes in its direction. This type of coherent scattering is dominant for low gamma energies and an order of magnitude lower than the photoelectric effect. Hence, for PET applications it can be neglected.

In figure 3.6 an overview of the relative importance of the photoelectric effect, Compton scattering and pair production is shown. For LSO with an effective atomic number Z_{eff} of 66 and gamma energies of 511keV only Compton scattering and photoelectric absorption are important and have approximately the same relative weight.
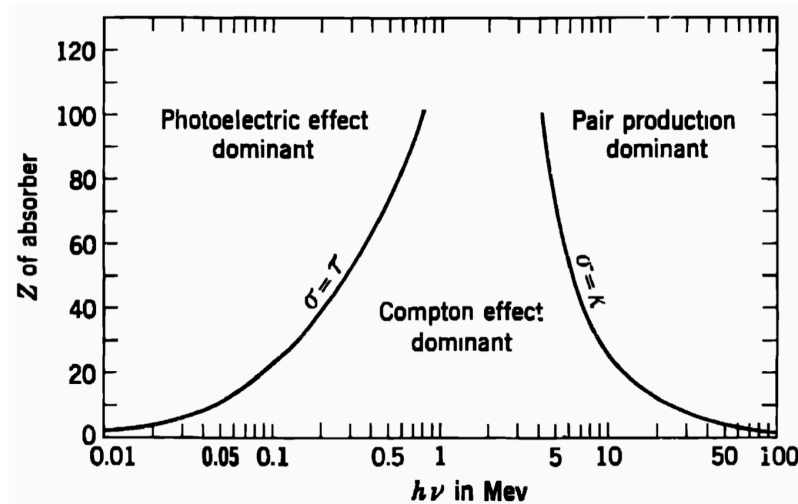
Figure 3.6.: Relative importance of the three major types of gamma-ray interactions, i.e. photoelectric, Compton and pair production. Solid lines show where two neighboring interactions are equal as a function of Z values and gamma energies. Picture is a reprint taken from [29].

Detection efficiency:

The detection efficiency of a scintillator describes its ability to stop gamma rays, e.g. 511keV gamma photons. The detection efficiency can be expressed by the gamma ray attenuation length λ as defined according to equation 3.2.7. When gamma radiation of intensity I_0 is incident on a crystal with thickness L, then the transmitted intensity I is given by a simple exponential law (see equation 3.2.7).

$$I = I_0 \cdot \exp\left(-L/\lambda\right) \tag{3.2.7}$$

Lower attenuation length (λ) values represent a higher gamma absorption of the scintillation detector and are preferential in PET applications. In the case of the photoelectric effect the gamma absorption is proportional to Z^n with n in the range between 4 and 5 (see equation 3.2.2). Equation 3.2.5 shows that the Compton scattering and thus the according gamma absorption is linearly dependent on the charge number Z.

In figure 3.7 the repartition of the different types of gamma interactions are shown for lutetium oxyorthosilicate (LSO). The y-coordinate is given in the mass attenuation coefficient [30] (see equation 3.2.8). With N_A the Avogadro's number ($6.02 \cdot 10^{23}\,\text{mol}^{-1}$) and A the atomic weight of the absorber.

$$\frac{\mu}{\varrho} = \frac{N_A}{A}\sigma_{tot} = \frac{N_A}{A}\left(\sigma_{pe} + \sigma_{cpt} + \sigma_{pair} + \sigma_{Rayleigh}\right) \tag{3.2.8}$$

The total mass attenuation of LSO is $11.8 * 10^{-2}\,\text{cm}^2/\text{g}$ for a gamma energy of $E_\gamma = 511keV$. Thus, the gamma ray attenuation length $\lambda = 1/\mu$ can be determined to 11.5mm using the density

of LSO equal ϱ =7.4g/cm^3 [28]. In equation 3.2.8 it can be noticed that a detector material with a higher number of atoms per unit volume shows a larger gamma absorption and thus a lower attenuation length λ.

Additionally in figure 3.7 one can notice the K-edge of Lutetium ($_{71}$Lu) which can be seen at a characteristic energy of 63KeV. As well at an energy around 10keV the L-edges of Lutetium can be recognized.
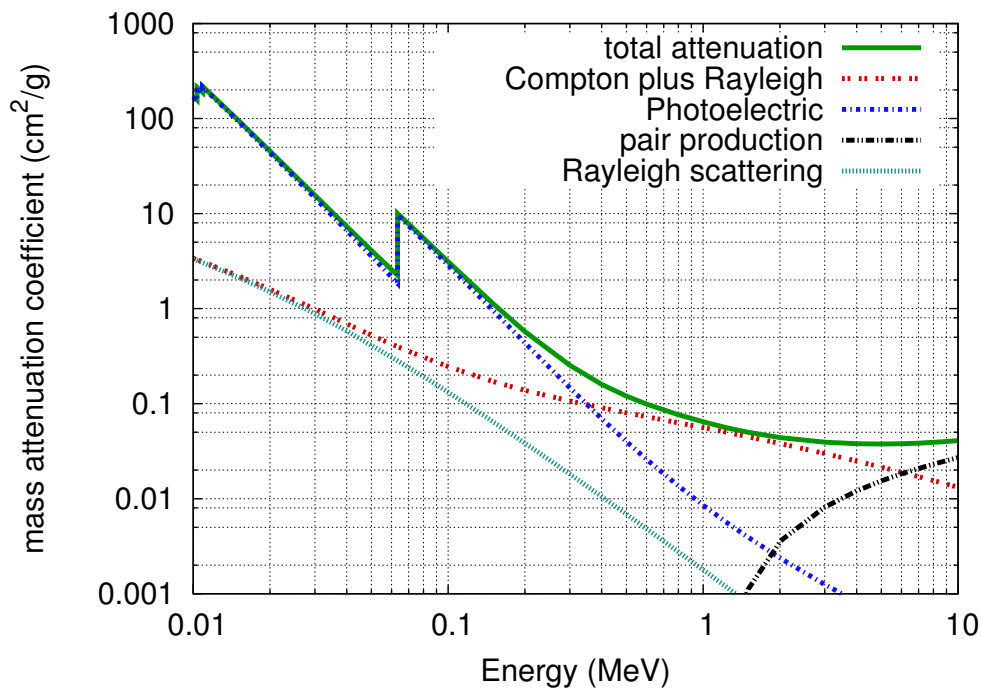

Figure 3.7.: Gamma-ray interaction processes in LSO. Data taken from [31].

Typical energy spectrum measured with ^{22}Na:

All the previous discussed gamma ray interactions can be seen in the measured energy spectrum if irradiating a scintillator with gamma rays from a radioactive source. In figure 3.8 a typical ^{22}Na energy spectrum measured with a LSO crystal is shown. The isotope ^{22}Na decays into ^{22}Ne under emission of a positron. The excited state of ^{22}Ne can give rise to an additional gamma with an energy of 1274keV. The 511keV and 1274keV photopeaks and associated Compton edges and plateaus can be seen in figure 3.8. Left to the 511keV peak the Lutetium ($_{71}$Lu) escape peak can be recognized at an energy of 511keV-63keV=448keV. The ^{22}Na energy response is on top of the Lutetium background. Lutetium naturally contains 2.6% ^{176}Lu, which beta decays to ^{176}Hf whilst emitting three gamma rays with energy 88keV, 202keV and 307keV. The total activity of this background is 40cps/g [32] for LSO, i.e. for a 2x2x20mm^3 LSO crystal this gives a background activity of 23 counts per second. This background activity is in fact the largest disadvantage in using LSO for PET applications. However other properties like fast decay time, high light output,

high gamma detection efficiency make LSO the preferred choice in PET. In addition, by selecting the 511keV photopeak this background can be suppressed to a large extent.
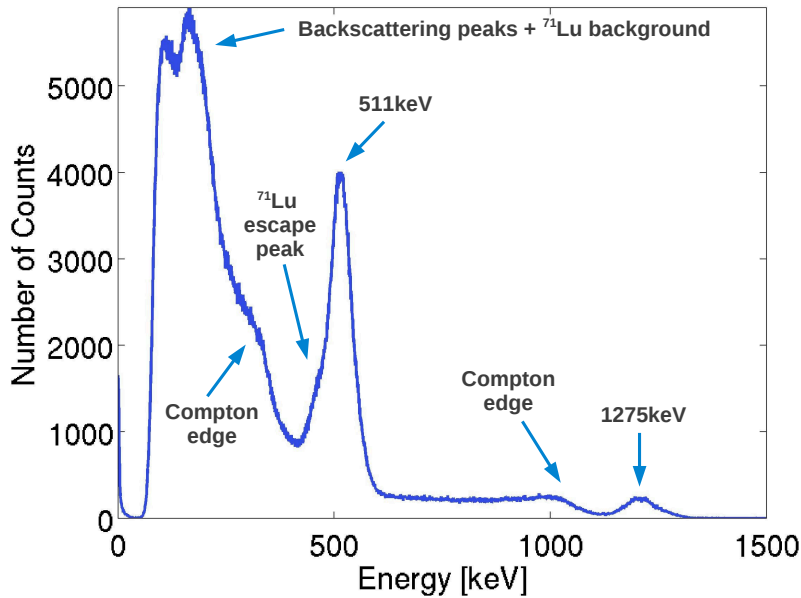

Figure 3.8.: Typical energy spectrum of ^{22}Na measured with LSO.

3.2.2. Scintillation mechanism

One can divide in two categories of scintillators: organic and inorganic. In organic scintillators transitions of free valence electrons that occupy molecular orbits lead to luminescence. Inorganic scintillators can exhibit intrinsic luminescence or via doping with a luminescent ion. In PET inorganic scintillators are used because of their good radiation stopping power as discussed in section 3.2.1. The different inelastic gamma ray interactions create a hot electron-hole pair as can be seen on the very left in figure 3.9. The scintillation process can then be described by four subsequent steps [33–35]:

The first step is the multiplication process. The hot electron is subject to electron-electron scattering and Auger processes in the material. This creates other electron-hole pairs via inelastic scattering with electrons from the scintillator matrix until the energy is falling below the ionization threshold, i.e. twice the bandgap. A significant number of electrons and holes are produced which will be available for scintillation. However, they still have a too high kinetic energy in order to occupy the luminescence centers.

The second step is the thermalization of the electron-hole pairs via phonon scattering in the crystal matrix and intra-band transitions. At the end of the thermalization process all electrons are at the bottom of the conduction band and all holes at the top of the valence band.

In the third step the electron-hole pairs may be trapped by the luminescence centers which in the case of LSO doped Cerium crystals is the trivalent Ce^{3+} ion present in the crystal lattice. Electron-hole pair recombination can as well happen through non radiative processes (thermal

quenching). They additionally can be trapped by defects or impurities in the crystal. These non-radiative processes are in competition with the light producing scintillation.

In the fourth and last step the recombination of electron-hole pairs can start. The processes described above are delaying the start of the scintillation and are responsible for the rise time of the scintillation emission rate. For practical purposes the rise time can be modeled by one or more exponential time components τ_r. As can be seen in figure 3.9 the scintillation rise time is fast, in the range of 100ps. For Cerium doped crystals, e.g. LSO:Ce, the radiative transition or recombination of electron-hole pairs takes place between the lowest 5d and two split 4f levels. The Ce^{3+} 4f level lies just above the valence band and the 5d level just below the conduction band. Because the transition is parity allowed it is rather fast with a decay time ranging from 20ns to 100ns depending on the host lattice. The radiative transitions can be described in a phenomenological way by one ore more exponential decay times τ_d.
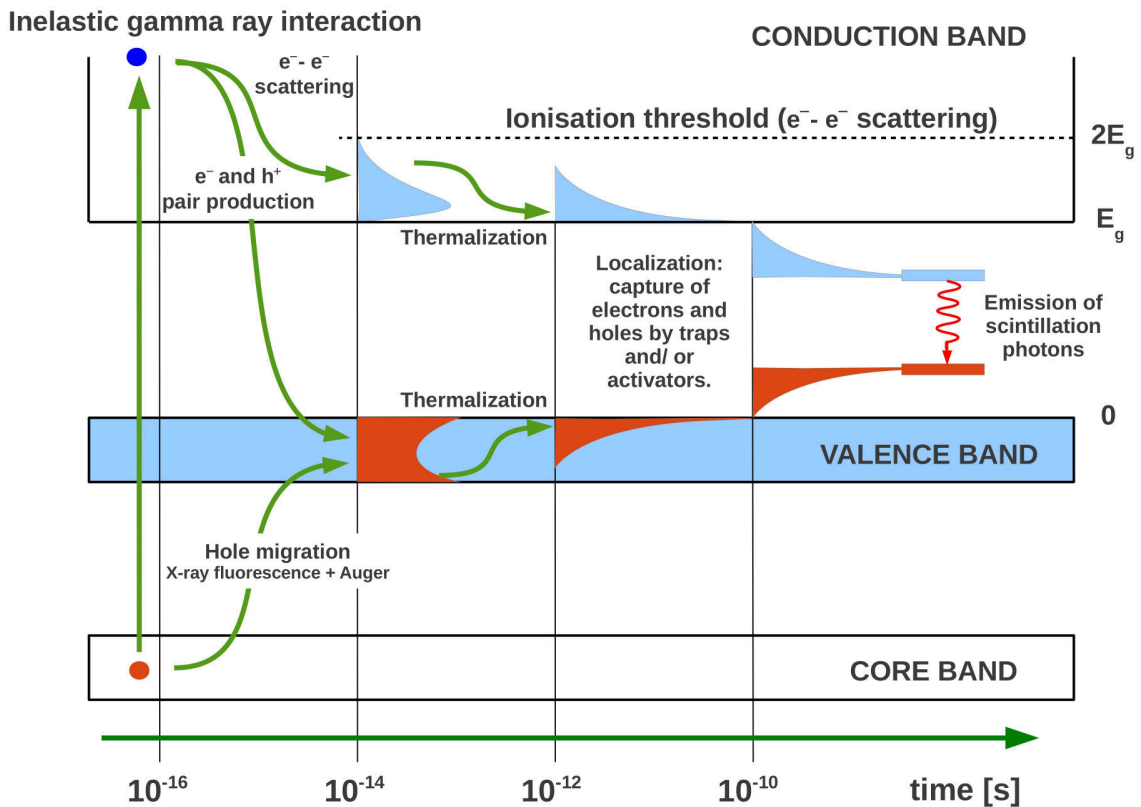

Figure 3.9.: Relaxation of hot electron-hole pair excitations in a scintillator.

The total scintillation photon emission rate can be described by a convolution of two decaying exponentials, according to equation 3.2.9. The time constant τ_r represents the thermalization and filling of the luminescence center after electron hole pair production. In equation 3.2.9 this time constant represents the scintillation rise time τ_r and is in the order of several tens of picoseconds. The time constant τ_d describes the emission decay of scintillation photons given by the radiative transition properties of the luminescence center, i.e. by the Cerium doping.

$$\widehat{f}(t) = \int_{-\infty}^{\infty} \exp\left(-\frac{t'}{\tau_r}\right) \exp\left(-\frac{t-t'}{\tau_d}\right) \Theta(t')\Theta(t-t')dt' \tag{3.2.9}$$

The radiative decay time τ_d is limited by quantum mechanics [36] as can be seen in equation 3.2.10. In the equation λ is the transition wavelength in nanometers, n_{sc} the refractive index of the scintillator and f_{osc} the oscillator strength of the transition, summed over the final quantum states and averaged over the initial states.

$$\tau_d = \frac{2}{3} \cdot 10^{-5} \cdot \frac{9\lambda^2}{f_{osc} \cdot (n_{sc}^2 + 2)^2 \cdot n_{sc}} \tag{3.2.10}$$

Solving the integral in equation 3.2.9 yields to the normalized scintillation photon emission rate or photon emission probability density function (PDF) as stated in equation 3.2.11.

$$\widehat{f}(t) = \frac{\exp\left(-\frac{t}{\tau_d}\right) - \exp\left(-\frac{t}{\tau_r}\right)}{\tau_d - \tau_r} \cdot \Theta(t) \tag{3.2.11}$$

By multiplying $\widehat{f}(t)$ in equation 3.2.11 with the number of photons emitted n we obtain the average photon emission rate of the scintillation $f(t) = \widehat{f}(t) \cdot n$. The term $F(t) = \int_0^t f(t')dt'$ defines the average number of photons having already been emitted until the time t, as can be seen in equation 3.2.12.

$$F(t) = \int_0^t f(t')dt' = n \cdot \left[1 - \frac{\tau_d \exp\left(-\frac{t}{\tau_d}\right) - \tau_r \exp\left(-\frac{t}{\tau_r}\right)}{\tau_d - \tau_r} \right] \cdot \Theta(t) \tag{3.2.12}$$

3.2.3. Scintillation efficiency

For LSO the emission peak is at a wavelength around 420nm [28] which corresponds to a transition energy of 2.95eV and the absolute light yield of such scintillator materials is in the order of 40000 photons per MeV [37]. The ratio of the energy of the produced scintillation light to the gamma ray energy can be calculated according to equation 3.2.13.

$$\eta_{Sc} = \frac{E_{scintillation}}{E_\gamma} = \frac{40000 \cdot 2.95eV}{1 \cdot 10^6 eV} = 11.8\% \tag{3.2.13}$$

Thus only a small fraction of the gamma ray energy is converted to scintillation photons. The scintillation efficiency describes how effective the gamma ray energy can be converted to scintillation photons detectable by a photodetector and is a product of three efficiencies: conversion (β), transfer (S) and luminescence (Q) [36]. The scintillation efficiency described in 3.2.13 can be expressed by these three quantities as can be seen in equation 3.2.14.

$$\eta_{Sc} = \frac{1}{2.3} \cdot \beta \cdot S \cdot Q \quad with \quad 0 \le \beta, S, Q \le 1 \tag{3.2.14}$$

The first parameter β describes the conversion efficiency of the gamma ray energy (E_γ) to produce electron-hole pairs. It has been stated in the work of [36] that at least an energy of 2.3

times the bandgap energy E_g is necessary to produce an electron-hole pair. Thus the maximum number of electron-hole pairs produced is $E_\gamma/(2.3\,E_g)$. The conversion efficiency β is defined as $\beta = \frac{n_{e-h}}{E_\gamma/(2.3\,E_g)}$ with n_{e-h} the number of electron-hole pairs produced [36]. The second parameter S describes the probability that the activator, e.g. Cerium, excited state will be filled by an electron from the valence band. Possible losses can be caused by trapping of electrons or holes and during the thermalization process. The parameter Q is the activator luminescence efficiency which describes the fraction of radiative emission during the electron-hole recombination [38] and is given by equation 3.2.15.

$$Q = \frac{P_r}{P_r + P_{nr}} \tag{3.2.15}$$

The term P_r denotes the probability of radiative emission and P_{nr} the probability of non-radiative de-excitation. Non-radiative recombination can provoke a faster decay time of the scintillation pulse (non-radiative quenching), although at the expense of a lower light production.

3.2.4. Stokes shift and thermal quenching

As already indicated not all electron-hole pairs created will combine in a radiative way and thus produce scintillation light. A fraction will de-excite via non-radiative relaxation under emission of phonons. One possible non-radiative decay channel is caused by thermal quenching. The principle of thermal quenching can be seen in figure 3.10. The parabolic curves shown in the figure represents the potential energies of the ground state and excited state. The energy is plotted against the mean inter-atomic distance between the luminescence center and neighboring atoms. The positions A and C representing the minimum potential energy and are shifted by ΔQ. This shift is called Stokes shift and depends on the electron-phonon coupling in the crystal. The ground state of the luminescence center A can be excited via the line AB in figure 3.10. Because the process is fast compared to atomic or ionic movements this excitation is vertical (Franck-Condon principle). The state B is not in equilibrium and will dissipate the extra energy thermally until being again in equilibrium at the position C. The excited state will decay to the ground state after a certain time depending on the optical transition probability of CD. In the ground state the point D is not in equilibrium and will dissipate thermally to the point A. It is interesting to notice that the transition CD emits at lower energies than the transition AB needs for excitation. This represents a positive effect of the Stokes shift as it makes the crystal transparent for its own emission. However, due to thermal fluctuations represented by the horizontal lines in figure 3.10 self-absorption can be observed as well. In this case the emission wavelength overlaps with the absorption wavelength and part of the luminescence light emitted will be re-absorbed by the luminescence centers. A direct consequence is an increase of the scintillation decay time. Additionally a certain amount of light loss can be observed, although the loss can be assumed to be small as almost all the light will be re-emitted again.

As can be seen in figure 3.10 the ground state and the excited state can intersect at a certain point. If the thermal energy gets high enough in the range of E_q the state can de-excite non-radiatively producing only phonons (heat). This process is called thermal quenching and is in

competition with the normal photon emission by radiative luminescence. The luminescence efficiency Q (see equation 3.2.15) in the case of thermal quenching can be calculated according to equation 3.2.16. Using the probability of non-radiative emission $P_{nr} = A \cdot \exp\left(-\frac{E_q}{k_B T}\right)$.

$$Q = \frac{P_r}{P_r + P_{nr}} = \frac{1}{1 + C \cdot e^{-\frac{E_q}{k_B T}}} \qquad (3.2.16)$$

The probability of non-radiative emission increases with temperature, consequently reducing the light yield as well as the decay time. In some PET applications where the operational temperature is given by external circumstances the temperature dependence of self quenching has to be considered.
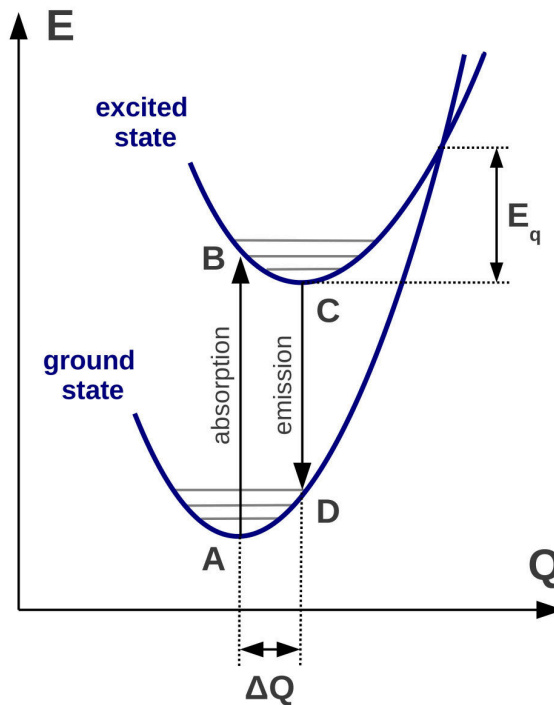

Figure 3.10.: The ground state and excited state in the configurational coordinate diagram. The minima of the excited state is shifted described by the Stokes shift in an inorganic scintillator.

3.2.5. Scintillation light output

Not all the light produced by the scintillation will eventually reach the photodetector. This is because of inefficiencies in the scintillation light transfer within the crystal which is strongly dependent on the geometry and surface finish of the crystal itself. The scintillation light transfer efficiency (LTE) can be defined as the fraction of scintillation light reaching the photodetector to the total amount of light produced by the scintillation process. In this paragraph a short description of light reflections within the crystal is given in order to estimate in a simplified manner the light transfer efficiency.

Considering Snell's law one can define three classes of emission directions [39]: (a) angles

where light can couple directly into the photodetector, (b) angles where the scintillation light escapes the crystal and (c) angles where the scintillation light will be trapped in the crystal due to internal total reflection. Normally the photodetector is coupled via optical coupling agents to the scintillator, as can be seen in figure 3.11. Commonly a refractive index of $n_{ca} = 1.41$ is chosen for the optical coupling agent. This values is similar to the refractive index of the entrance window of the photodetector. For LSO type scintillators the refractive index is $n_{sc} = 1.82$.
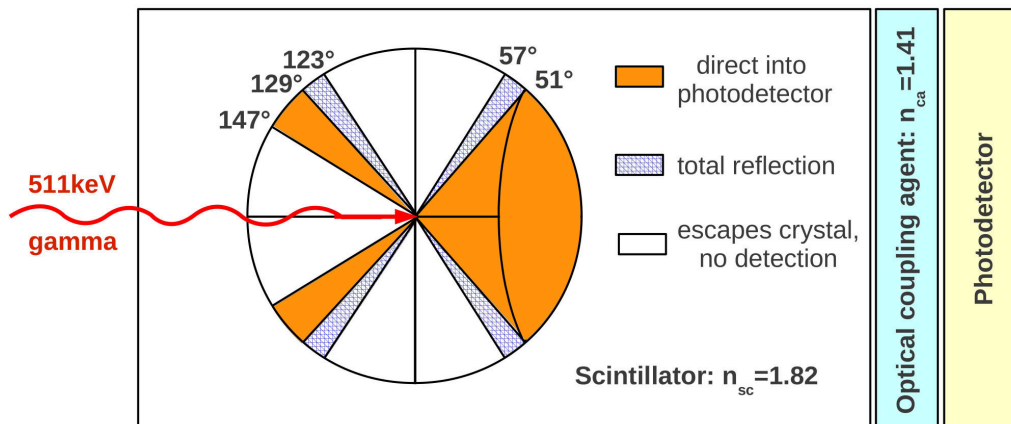

Figure 3.11.: Schematic of a scintillator coupled to a photodetector. From the Snell's law angles of extraction can be calculated.

Using Snell's law we can identify the different types of emission regions (in terms of the angle θ) summarized in table 3.1. For the stated calculations the crystal was unwrapped and the surface is supposed to be perfectly polished.

Table 3.1.: Different cases of scintillation photon emission regions in terms of the angle θ.

emission range (θ)	description
$0° < \theta < \arcsin(1.41/1.82) = 51°$	photons couple directly into the photodetector
$51° < \theta < 90° - \arcsin(1/1.82) = 57°$	total internal reflection, photons cannot escape crystal
$57° < \theta < 90° + \arcsin(1/1.82) = 123°$	photons escape on the lateral surface and will be lost
$123° < \theta < 180° - \arcsin(1.41/1.82) = 129°$	total internal reflection, photons cannot escape crystal
$129° < \theta < 180° - \arcsin(1/1.82) = 147°$	photons are reflected on the surface opposite the detector by total internal reflection and can be detected
$147° < \theta < 180°$	photons escape the crystal and will be lost

It should be noted that the regions stated in table 3.1 are calculated for the two dimensional

case, however, are easily expandable to three dimensions using the solid angle ($\Omega = 2\pi(1 - \cos(\theta))$). Considering that the surface of a sphere with unit radius is 4π one can normalize the solid angle Ω and obtain the probability of emission in a given region compared to the total amount of photons emitted by the scintillation. In the special case of an unwrapped crystal mounted with optical grease to the photodetector the probability of scintillation light transfered directly to the photodetector P_{direct} can be calculated analytically to 29%, shown in equation 3.2.17. Here n_{air} denotes the refractive index of air and is unity, i.e. $n_{air} = 1$.

$$
\begin{aligned}
P_{direct} &= 2 \cdot \frac{2\pi}{4\pi}\left\{1 - \cos\left(\arcsin\left[\frac{n_{ca}}{n_{sc}}\right]\right)\right\} - \frac{2\pi}{4\pi}\left\{1 - \cos\left(\arcsin\left[\frac{n_{air}}{n_{sc}}\right]\right)\right\} = \\
&= 0.5 - \cos\left(\arcsin\left[\frac{n_{ca}}{n_{sc}}\right]\right) + 0.5\cos\left(\arcsin\left[\frac{n_{air}}{n_{sc}}\right]\right) = 29\%
\end{aligned}
\tag{3.2.17}
$$

In equation 3.2.17 it was shown that without wrapping only about 30% of the scintillation light produced can couple into the photodetector. In the discussion above Fresnel reflections are neglected. However, it can be shown that a full incorporation of Fresnel reflections into the simple model would only provoke small corrections, in the range of a few %. The situation becomes much more complex if wrapping of the crystal as well as surface roughness and diffusion is considered. A direct consequence is that light being in a total reflection mode can couple to the photodetector by means of scattering. In general it can be stated that surface effects play the dominant role in the light transfer of scintillators with dimensions used in PET systems, e.g. 2x2x20mm^3. In this case analytical solutions are very difficult, if not even impossible, and sophisticated Monte Carlo simulations become increasingly important. A more detailed investigation can be found in chapter 7.

3.2.6. Energy resolution

The energy resolution is defined as the ratio of the measured energy peak fluctuation ΔE in FWHM to the full energy peak value E. According to [40, 41] it results from the contribution of several terms shown in equation 3.2.18.

$$
\left(\frac{\Delta E}{E}\right)^2 = (\delta_{sc})^2 + (\delta_{st})^2 + (\delta_p)^2 + (\delta_n)^2
\tag{3.2.18}
$$

The term δ_{sc} represents the intrinsic energy resolution of the scintillating material, δ_{st} is the statistical contribution, δ_p is the scintillation light transfer and photodetectors conversion resolution and δ_n is the photodetectors dark noise contribution. The statistical contribution (δ_{st}) is inverse proportional to the square root of the number of detected photons or photoelectrons (p.e.), i.e. $\delta_{st} \sim 1/\sqrt{N_{p.e.}}$. The last two terms δ_p and δ_n are dependent on the detector design, e.g. crystal dimensions and shaping as well on the photodetector itself.

The first component, the intrinsic energy resolution δ_{sc}, represents a fundamental limit on the overall energy resolution $\Delta E/E$. It is mainly associated with the non-linear responses and fluctuations to secondary gamma and X-ray quanta as well as secondary electrons produced in

the stopping process of the incoming radiation. In this aspect LSO as well as NaI and CaI$_2$ show particularly poor values, as can be seen in figure 3.12. However the measured energy resolution for LSO doped Cerium is in the range of 10% and thus acceptable for PET detectors.
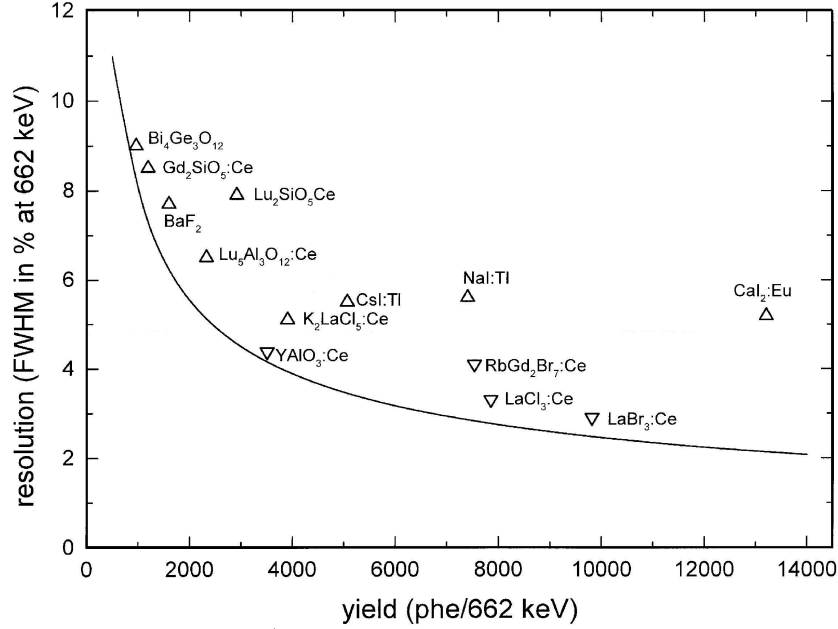

Figure 3.12.: Energy resolution of different scintillating materials. LSO shows a particular poor intrinsic energy resolution as its total energy resolution value is much higher than one would expect by pure statistical considerations $(1/\sqrt{N_{pe}})$. Picture modified from [42].

3.2.7. Analytical considerations of the time resolution

The cumulative photon emission rate $F(t)$ introduced in equation 3.2.12 can be simplified using a second order series expansion (see equation 3.2.19). The series expansion is only valid if $(t/\tau_r) \ll 1$ and $(t/\tau_d) \ll 1$, i.e. for photon emission times t small compared to the time constants τ_r and τ_d. Hence, equation 3.2.19 is valid for the very first photons emitted of the photon emission rate with n being the total number of photons.

$$F(t) = n \cdot \left[1 - \frac{\tau_d \exp\left(-\frac{t}{\tau_d}\right) - \tau_r \exp\left(-\frac{t}{\tau_r}\right)}{\tau_d - \tau_r} \right] \simeq \frac{n\,t^2}{2\tau_r \tau_d} \tag{3.2.19}$$

According to the work of [43] and with the cumulative photon emission rate defined in equation 3.2.19 the probability of the kth scintillation photon emitted in the time interval $t, t + dt$ can be expressed by $W_k(t)$ in equation 3.2.20.

$$W_k(t)dt = \frac{F(t)^{k-1} e^{-F(t)}}{(k-1)!} \frac{dF(t)}{dt} dt \simeq \frac{2a^k t^{2k-1} e^{-at^2}}{(k-1)!} dt \quad with \quad a = \frac{n}{2\tau_r \tau_d} \tag{3.2.20}$$

The variance of the kth photon emitted can be calculated via the standard mathematical defini-

tion of the variance and is presented in equation 3.2.21. The normalization term $\int_0^\infty W_k(t)dt$ is unity per definition.

$$var(k) = \frac{1}{\int_0^\infty W_k(t)dt} \int_0^\infty t^2 W_k(t)dt - \left[\frac{1}{\int_0^\infty W_k(t)dt} \int_0^\infty t\, W_k(t)dt \right]^2 \qquad (3.2.21)$$

In table 3.2 the analytical solution for the variance stated in equation 3.2.21 and the related coincidence time resolution (CTR) is shown for the first three photons emitted. The factor $2 * \sqrt{2 * ln(2)} * \sqrt{2} = 3.33$ in table 3.2 converts to coincidence time resolution FWHM.

Table 3.2.: Calculated variance of the kth photon emitted and corresponding coincidence time resolution of a scintillation photon emission rate with rise time τ_r, decay time τ_d and photons emitted n.

rank k^{th} photon	variance $var(k)$	coincidence time resolution
1	$var(1) = \frac{4-\pi}{2} \frac{\tau_r \tau_d}{n}$	$3.33 \cdot \sqrt{0.429 \frac{\tau_r \tau_d}{n}}$
2	$var(2) = \frac{32-9\pi}{8} \frac{\tau_r \tau_d}{n}$	$3.33 \cdot \sqrt{0.466 \frac{\tau_r \tau_d}{n}}$
3	$var(3) = \frac{768-225\pi}{128} \frac{\tau_r \tau_d}{n}$	$3.33 \cdot \sqrt{0.478 \frac{\tau_r \tau_d}{n}}$

It is interesting to notice that in the case of a simple bi-exponential photon emission rate the time resolution is lowest for the 1st photon emitted. This observation strictly holds only in the limit of the variance being lower than the rise time itself, as the series expansion is only valid within this condition. If a Gaussian smearing by the photodetector or photon transport in the crystal is introduced the 1st photon will no longer show the best time resolution. A more detailed discussion of the time resolution will be given in chapter 7. Simulations presented will incorporate as well the timing properties of the photodetector, electronics and scintillation light transport in the crystal.

3.3. Photodetector

The visible photons generated by the scintillator are detected by the photodetector which produces an electrical signal proportional to the photon rate. The photon detection is based on generating free electrons or electron-hole pairs in a medium. Because a minimum energy is necessary for the ionization, photon detection is a threshold phenomenon, i.e. the photon energy $E_{photon} = hc/\lambda$ has to overcome a certain limit. Two main technologies can be distinguished: (a) the vacuum photodetectors and (b) the solid state photodetectors. In vacuum photodetectors electrons are emitted in an external photocathode by photoelectric interaction. These electrons are then accelerated in a high electric field and produce secondary electrons by interaction on so called multiplication stages. Prominent examples of vacuum devices are the photo multiplier tube (PMT) and the micro channel plate (MCP). In solid state photodetectors electron-hole pairs are produced by internal

photon interaction in a semiconductor. The produced electron-hole pairs are accelerated in the electric field and multiplied by impact ionization in the semiconductor itself. The avalanche photodiode (APD) and Geiger-mode APD (G-APD) leading to the silicon photomultiplier (SiPM) are examples of this type of photodetectors. In this section the working principle of the PMT and the SiPM will be described with a focus on the analog SiPM. Additionally a new type of SiPM will be discussed, the digital SiPM.

3.3.1. The photomultiplier tube

Photomultiplier tubes (PMTs) belong to the class of vacuum photodetectors and are being produced since the late 1930s. They have been well described in literature, e.g. [27]. In figure 3.13 the schematic of a PMT can be seen. The soft photons generated by the scintillation enter the vacuum chamber of the PMT through a window which is usually made out of quartz for good UV transparency. The entrance window is covered with a photosensitive compound (usually bialkali such as $C_s - K - S_b$). If this so called photocathode is being hit by a photon an electron will be emitted by photoemission in the bialkali, the so called photoelectron (p.e.). The probability of emitting an electron per incident photon gives the quantum efficiency (QE) of the photosensitive compound. The QE is strongly dependent on the material and the incident photon wavelength. The bialkali photocathodes show highest values for all commercially used materials around 25%. This is already the highest disadvantage of PMTs as the photon detection efficiency is limited by the QE.
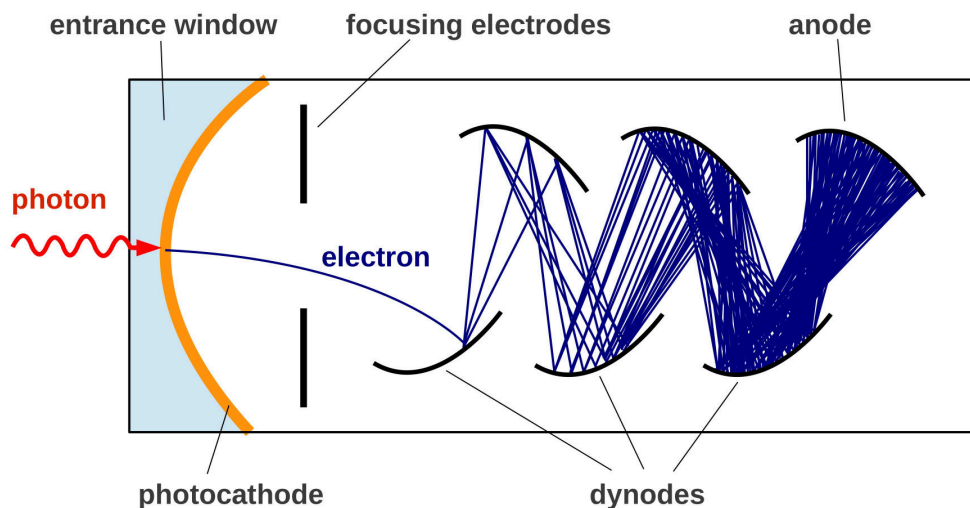

Figure 3.13.: Working principle of a photomultiplier tube (PMT).

The free electrons generated by photoemission are accelerated and focused onto the first dynode of the PMT via the focusing electrodes, as can be seen in figure 3.13. Secondary emission in the dynode frees other electrons which are then accelerated and focused on the second dynode and so on. Each further dynode is biased with increasing positive voltage in order to create an accelerating electric field. The secondary emission yield is dependent on the material and accelerating voltage

of the primary electrons. For bialkali the secondary emission yield is in the range of 10 for 200V. Thus a single photoelectron yields up to 10^6 electrons collected at the anode if 6 dynodes are being used. This gives a signal which is well above the electronic background noise and can easily be detected with rather simple electronics. A big advantage of PMTs is their linear response from one initial photoelectron to several thousands. However saturation effects may occur if the number of secondary electrons becomes high enough in order to produce a noticeable space charge between the last dynode and the anode. Thus the accelerating field will be distorted and the anode collection efficiency will degrade.

3.3.2. Working regions of a reverse biased p-n junction photodetector

Solid state photodetectors progressively replace photomultiplier tubes because of several advantages like higher photon detection efficiency, lower power consumption, insensitivity to magnetic fields, compactness and potential cheapness. The quantum efficiency (QE) in solid state devices is defined as the probability of generating an electron-hole pair per incident photon and can reach values of 80% to 90% [44] and is much higher when compared to the values reached with the best photocathodes used in PMTs. This leads to a higher photon detection efficiency and thus to a potentially better energy and time resolution if used in scintillator based gamma detectors. For many LHC experiments where magnetic fields up to B=4T are common it is important that the photodetector is insensitive to these field strengths. Additionally, in a combined PET-MR scanner magnetic fields of B>1T are used and therefore PMTs would be not operational as well.

If a p-n junction diode is biased reversely one can distinguish between three different reverse bias voltage regions. In figure 3.14 these three working regions are shown, i.e. the photodiode region, the APD region and the SiPM region [45].
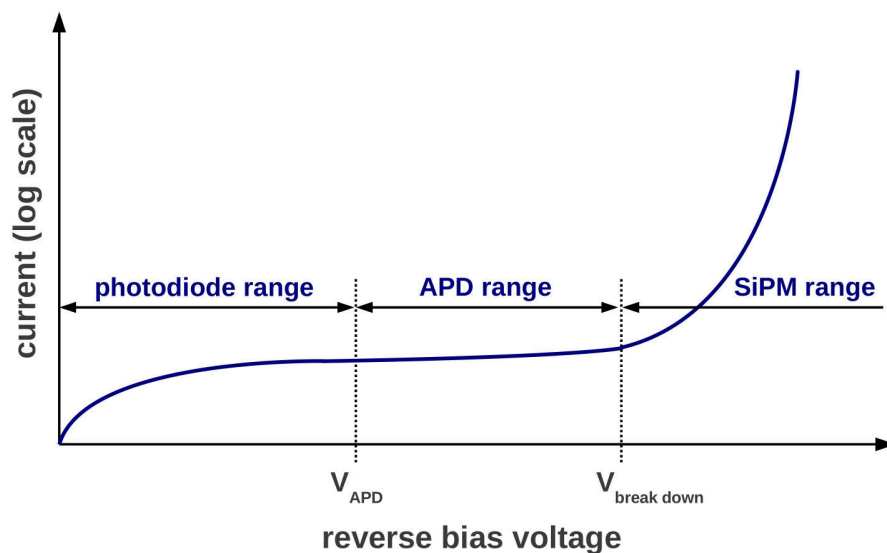

Figure 3.14.: The three different working regions of a p-n junction diode as a function of reverse bias voltage.

At low reverse bias voltages the produced electron-hole pairs are being separated by the applied electric field without any other effects in the solid. The current remains low and is proportional to the input light flux. The minimal detectable signal is in the range of several hundreds (200-300) photoelectrons [44], i.e produced electron-hole pairs. This is the range of standard photodiodes like the PIN diode.

If the reverse bias is increased the electrons gain enough kinetic energy in the electric field in order to produce additional electron-hole pairs in the solid through impact ionization. Because of the higher mobility and ionization coefficient of electrons in Silicon, only electrons add to the avalanche process, see figure 3.15. The multiplication process is linear, i.e. proportional to the initial produced photoelectrons, and the minimal detectable signal is in the order of several tens (10-20) photoelectrons [44]. In this range one can find the avalanche photodiodes (APDs).

If the reverse voltage is increased further above the so called breakdown voltage the electric field becomes high enough to trigger a self sustained avalanche in the p-n junction. Both electrons and holes will contribute to the avalanche process as illustrated in figure 3.15. Each incoming photon is able to trigger such an avalanche and thus the device is able to detect single photoelectrons. The initiated avalanche has to be quenched externally either by a series resistor or by active quenching. This is the working regime of the Geiger-mode APD (G-APD). Several of such G-APD cells connected in parallel form the so called silicon photomultiplier (SiPM) or multi pixel photon counter (MPPC).
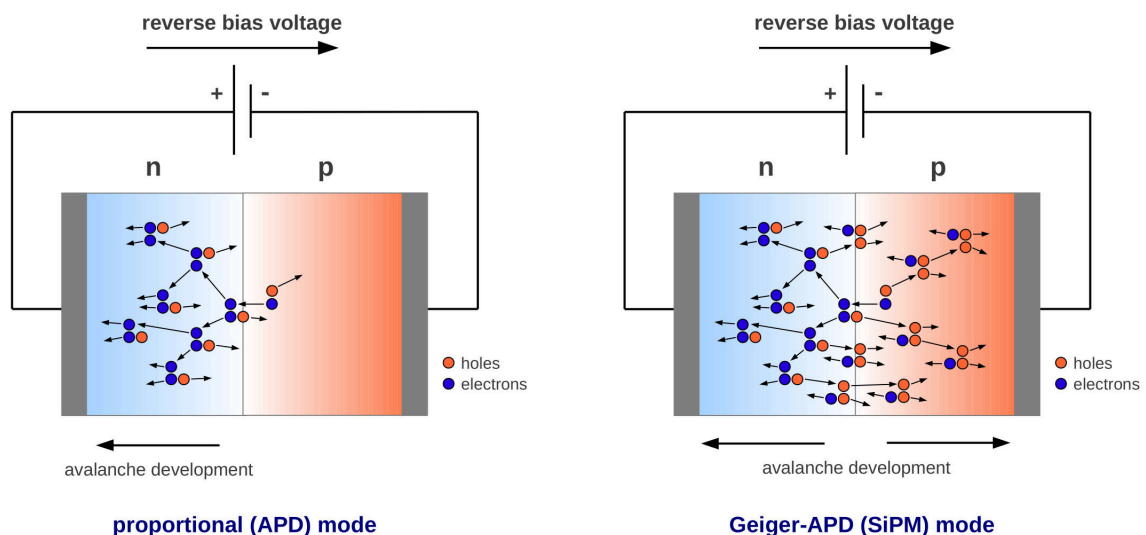

Figure 3.15.: Left: proportional mode of avalanche development in an APD biased below breakdown voltage. Only electrons add to the avalanche development which stops intrinsically. Right: in the Geiger-mode the avalanche development is supported by electrons and holes. The avalanche needs to be quenched externally. Picture modified from [46].

3.3.3. The analog silicon photomultiplier

In the beginning of this millennium the Geiger-mode APD has been further developed [44]. Pioneer work in developing solid state photodetectors operating above the breakdown voltage was carried out by McIntyre and co-workers [47] and by R.H. Haitz and his colleagues in the Schockley research laboratory [48] around the 1960s. The silicon photomultiplier (SiPM) or multi pixel photon counter (MPPC) consists of many such single photon avalanche diodes (SPADs) operating in Geiger-mode and are connected in parallel. Key figures in the development of the SiPM were V. Golovin [49], Z. Sadygov [50] and B. Dolgoshein [51]. The single SPADs or microcells can be seen in figure 3.16.
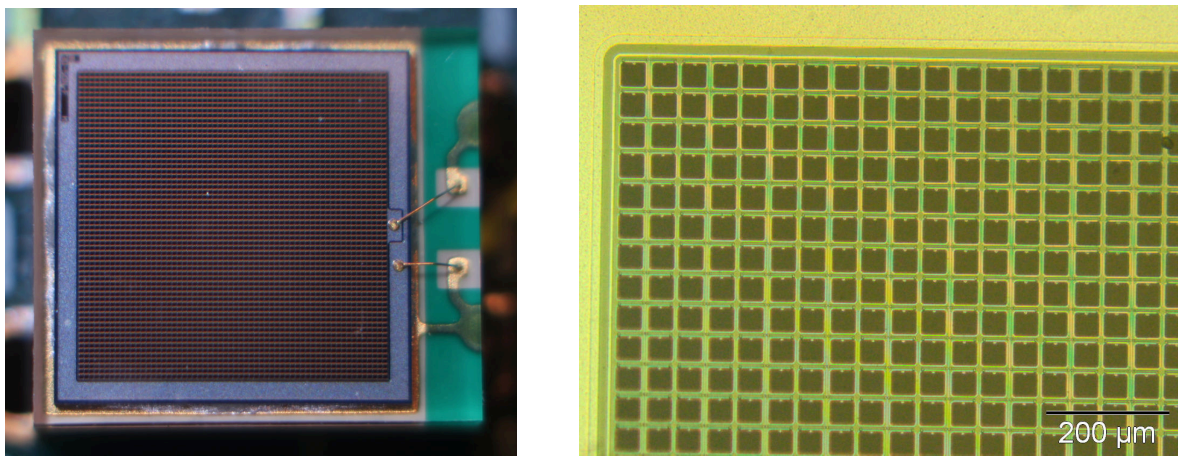
Figure 3.16.: Picture of a SiPM consisting of many single SPADs or microcells. Left: Hamamatsu MPPC S10931-050P with active area of 3x3mm^2 and a SPAD size of 50μm. Right: Zoom on the single SPADs or microcells of the SiPM. Connecting wires can be noticed which reduce the fill factor to 61.5% in the shown case. The fill factor is the ratio between the photosensitive area and total active area of the device.

Because of the high gain due to the internal avalanche this device is able to detect single photons with a resolution better than what can be achieved with the best hybrid photomultiplier tubes [44]. As already mentioned in the preceding chapter the new process in G-APDs is the additional initiation of secondary avalanches triggered by holes in the p-layer. The avalanche becomes self sustained and will not turn off by itself. As a consequence the avalanche process must be quenched by an external quenching resistor (passive quenching) or by an active quenching circuitry. In figure 3.17 the schematics of the parallel connected SPADs with serial quenching resistors R_q (passive quenching) as well as external biasing and analog readout of the summed cell signals is shown. If an avalanche occurs in the microcell a current will start to flow provoking a voltage drop on the serial quenching resistor R_q. With progressing avalanche the voltage drop on R_q is increasing until the point when the operational voltage of the SPAD is below the breakdown voltage, provoking the stop of the avalanche. In the following the structure of the microcells will be described in more detail together with the basic characteristics of a SiPM, following the very good review publication of D. Renker [44].
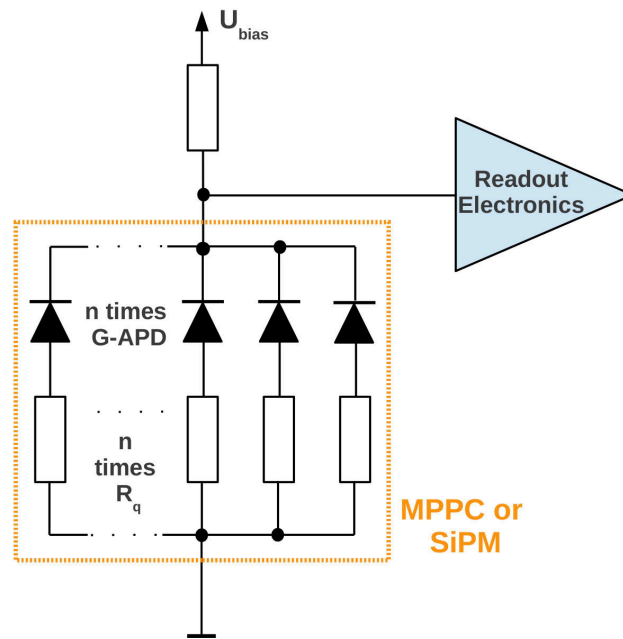
Figure 3.17.: In the analog SiPM all microcells are connected together and readout in parallel. It should be noted that in a real device parasitic capacitances and resistances complicate the equivalent circuit. The parasitic capacitance parallel to the quenching resistor R_q sometimes is even enhanced in order to decrease the signal rise time.

In figure 3.18 and figure 3.19 the structure of a G-APD can be seen in detail [44]. On top of the low resistivity handling wafer (bulk), which is typically 300μm thick the epitaxial layer is located with a thickness of 2μm to 4μm. Into the epitaxial layer a high concentration of dopants is placed by diffusion. Here the epitaxial layer and the heavily doped volume created by diffusion are of the same type either n or p, as can be seen in figure 3.18 and figure 3.19. The p-n junction is formed by ion implantation of opposite charge some 0.5μm below the surface. To distribute the electric field uniformly over the whole sensitive area of the photodiode an extremely thin heavily doped layer is produced on the top surface. The cell is connected via the quenching resistor on the top surface. Normally polycrystalline silicon or polysilicon is used which is not transparent in the visible range and thus lowers the detection efficiency. In a last step the passivation layer (SiO_2) is placed in order to protect the device. The silicon oxide passivation layer has a refractive index of $n_{SiO_2} \approx 1.55$ in the blue, whereas Silicon shows a high refractive index of $n_{Si} \approx 3.5$. Because of the large difference in refractive index Fresnel reflections can occur between the Silicon - SiO_2 interface which can cause severe photon detection losses. However anti-reflection coatings can reduce the reflection losses to values below 10% over the entire visible range [52].

The p on n structure in figure 3.18 is more sensitive for blue light, while the n on p structure in figure 3.19 will be more sensitive in the red. Blue light will be absorbed in the first few μm creating an electron-hole pair. If in the case of the p on n structure the electron-hole pair was created close to the surface the electrons will drift to the high field region of the p-n junction (see figure 3.15) and trigger an avalanche with high probability. Red light has a deeper penetration

depth and therefore will produce electron-hole pairs more likely behind the p-n junction. In this case the holes will drift towards the junction which have a lower probability to trigger an avalanche and consequently the detection efficiency will be reduced. The same arguments, but reversed, holds for the n on p structure where photons with short wavelength have a reduced detection probability. The used photodetectors from the producer Hamamatsu Photonics K.K. (MPPC S10931-025P, S10931-050P and S10931-100P) are p on n type SiPMs as shown in figure 3.18.
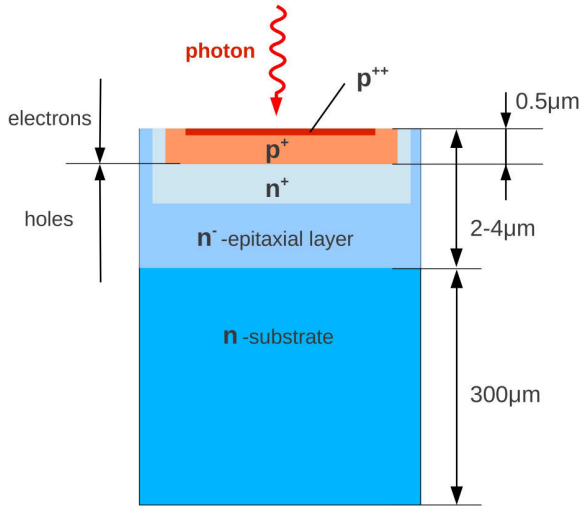
Figure 3.18.: Schematics of a microcell with p on n structure which is predominantly sensitive for blue (e.g. Hamamatsu, Ketek, FBK). Picture modified from [44].
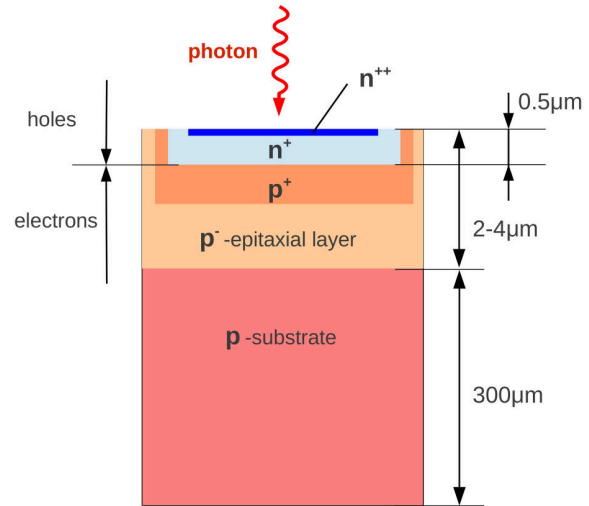
Figure 3.19.: Schematics of a microcell with n on p structure which is predominantly sensitive for red (e.g. Sensl, FBK). Picture modified from [44].

3.3.4. Properties of silicon photomultipliers

In this section the most important properties of SiPMs like gain, recovery time, dark count rate, optical crosstalk, afterpulsing and photon detection efficiency will be discussed.

Gain:

SiPMs produce always the same output signal if any of the microcells goes to a breakdown no matter how many photons initially triggered the avalanche. As is shown in equation 3.3.1, the gain (G) is directly proportional to the cell capacitance (C) and bias overvoltage (U_{ov}), i.e. operating reverse bias voltage minus the breakdown voltage.

$$G = \frac{C \cdot U_{ov}}{q} \tag{3.3.1}$$

The term q denotes the elementary charge $q = 1.602 x 10^{-19} C$. The gain is typically in the

order of 10^5 to 10^7 and produces a single photon signal well above the electronic noise level. Hence, constraints on the readout electronics are not as severe as in the case of APDs and PIN photodiodes. The excess noise factor defined as $F = 1 + \sigma_G/G$ with σ_G the standard deviation of the gain fluctuation is almost unity ($F \approx 1$).

Because of the charge carrier interaction with phonons in silicon the breakdown voltage is strongly dependent on the temperature. For the Hamamtsu devices the bias voltage needs to be increased by ∼50mV when the temperature rises by 1°C if the device should be operated at the same overvoltage [44].

Dark count, optical crosstalk and afterpulsing:

There are different types of uncorrelated and correlated noise in a SiPM, see figure 3.20. Dark count is the random production of free charge carriers in the depleted zone of the SiPM with a thickness of a few μm. The free carriers can produce a breakdown and generate a typical single photoelectron signal which is not distinguishable from a signal which was triggered by an incoming photon. If the dark count rate (DCR) is sufficiently small the generation of a dark count is not dependent on a foregoing dark count and thus this type of noise is uncorrelated. The DCR is in the order of typical 100kHz to several MHz per mm^2 at 25°C [44]. Two main processes produce dark counts, thermally generated electron-hole pairs and the so called field assisted generation of free electrons [44]. The thermally generated DCR reduces by a factor two every 8°C in temperature drop. The field assisted generation of free carriers also called trap-assisted tunneling [53, 54] has normally a low influence to the total DCR. However it can only be reduced by operating the SiPM at lower electric fields and thus lower bias overvoltage or by reducing impurities in the crystal. In figure 3.20 dark count events can be seen on the very left.
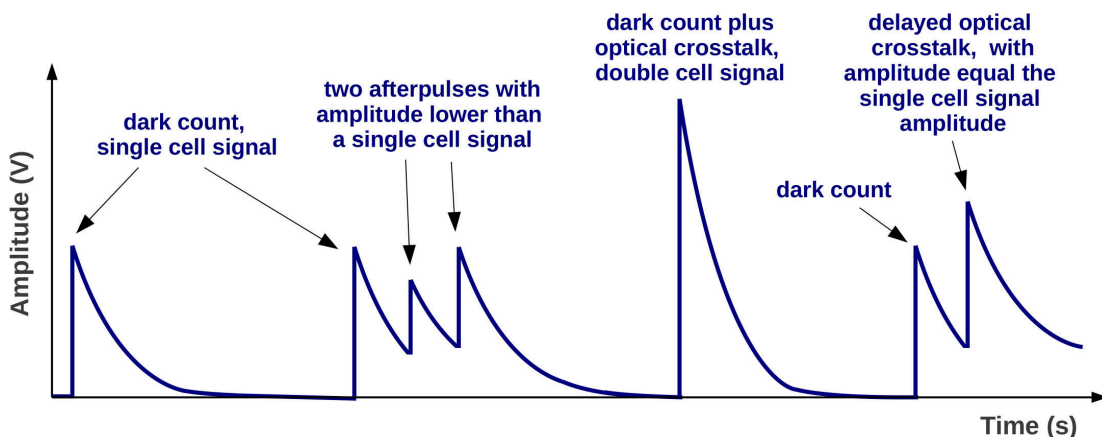

Figure 3.20.: The different kinds of noise observable in SiPMs.

A prominent type of correlated noise in a SiPM is optical crosstalk. In every avalanche breakdown there are on average 30 photons emitted per 10^6 carriers with an energy higher than 1.14eV [55]. The bandgap structure of Silicon does only allow indirect de-excitation, hence the

emission of photons has to be phonon assisted. The secondary emitted photons can travel to neighboring cells and trigger an additional avalanche. This type of optical crosstalk is as well called direct optical crosstalk, the output signal of the SiPM is twice as high in amplitude as can be seen in figure 3.20. If two secondary photons are triggering an avalanche in neighboring cells the output signal is three times higher as a single photoelectron signal. In figure 3.21 the SiPM signal of dark count events, one optical crosstalk events, two optical crosstalk events, ... are overlapped. In figure 3.22 the frequency of dark count events and cross talk events is shown. The probability of triggering N avalanches simultaneously via optical crosstalk decreases exponential with N. Optical crosstalk can be mitigated by inserting optical trenches between the microcells in the SiPM [56]. A drawback of this method is the reduction of fill factor and therefore of the detection efficiency.
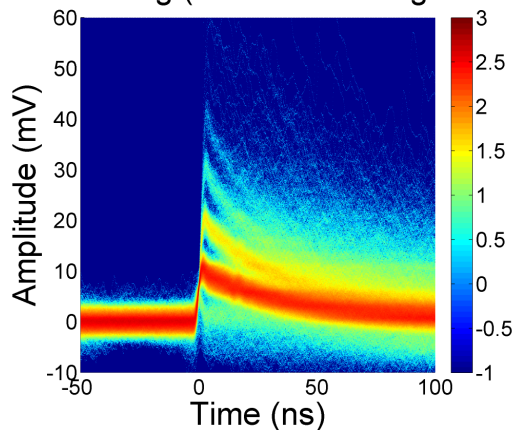
Figure 3.21.: Dark count and direct optical crosstalk events in the SiPM. The color encodes the intensity or number of observed events.
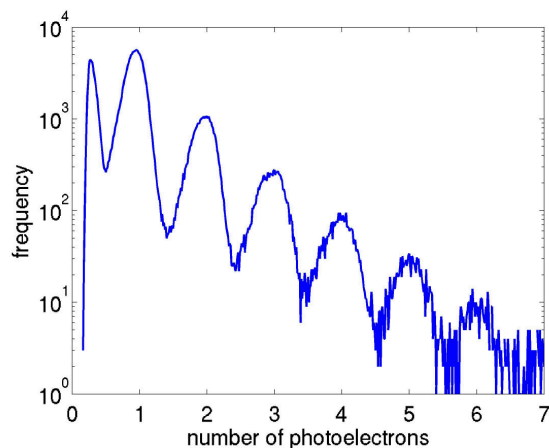
Figure 3.22.: Frequency of dark count events and optical crosstalk in the SiPM. Higher order optical crosstalk decreases rapidly with the number of triggered cells.

Another type of optical crosstalk can be seen on the very right in figure 3.20, the delayed optical crosstalk. It is caused by secondary photons generating an electron-hole pair in the bulk. The charge carriers will diffuse slowly to the active region and trigger an avalanche with a delay of several nanoseconds to microseconds.

The last type of correlated noise in SiPMs is the so called afterpulsing. Carriers trapped during the breakdown discharge will be released several tens to hundreds of nanoseconds later causing afterpulses. Because the microcell is not yet fully recharged, afterpulse events have a lower pulse height than a single photoelectron event, which can be seen in figure 3.20. If the SiPM is operated at lower temperatures the release of the carriers takes longer and therefore the afterpulse time constant increases [57] as can be seen in figure 3.23.
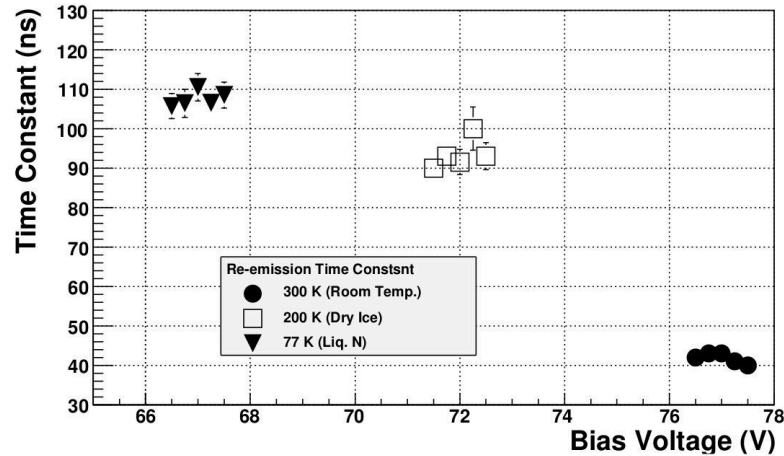
Figure 3.23.: Afterpulse time constant as a function of bias voltage and three different temperatures. Reprinted from [57].

Recovery time:

The time after a breakdown has been quenched until the microcell is charged and ready for the next firing is characterized by the recovery time. The time constant τ is mostly dependent on the quenching resistor R_q and the cell capacitance C, i.e. $\tau = R_q \cdot C$. Hamamatsu has a quenching resistor of about 150kΩ and together with a cell capacitance of about 100fF a recovery time of several tens of nanoseconds. Because the used polysilicon quenching resistor value is strongly dependent on the temperature the recovery time is a function of temperature as well [57]. A high afterpulse rate can prolong the recovery time as the recovery has to start over again for each afterpulse.

Saturation effects:

If the number of impinging photons ($N_{photons}$) times the PDE is small compared to the total amount of microcells (N_{total}) the SiPM output signal ($N_{fired\,cells}$) is proportional to the input photon signal (N_{photon}). If the input photon flux increases SiPMs show saturation effects which are inherently given by their limited number of microcells. An approximation of the input-output transfer function can be seen in equation 3.3.2 [44].

$$N_{fired\,cells} = N_{total} \cdot \left(1 - \exp \left[- \frac{N_{photon} \cdot PDE}{N_{total}} \right] \right) \qquad (3.3.2)$$

In figure 3.24 different gamma source energy spectra measured with a LSO scintillator are shown, i.e. ^{22}Na, ^{57}Co, ^{60}Co, ^{137}Cs. The scintillator was coupled to a Hamamatsu MPPC S10931-025P SiPM. An energy resolution of ~10% for the 511keV can be deduced. For gamma energies above 511keV the number of produced scintillation photons become too high and saturation ef-

fects according to equation 3.3.2 can be observed.
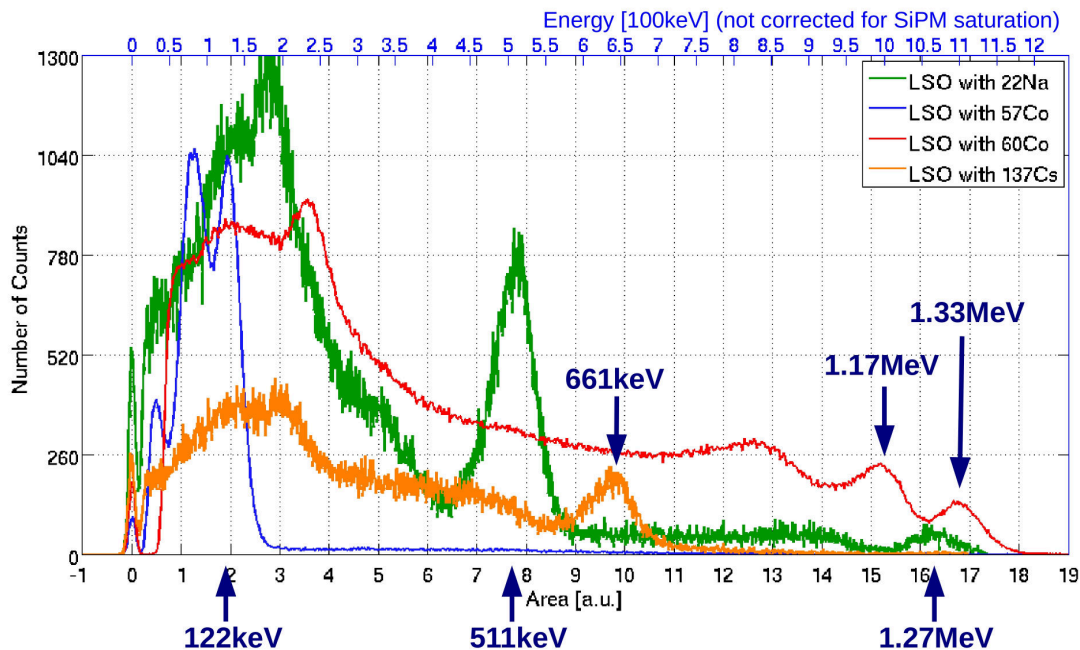
Figure 3.24.: Typical energy spectra of a LSO:Ce scintillator measured with different gamma energies. The scintillator light output was measured with a Hamamatsu MPPC S10931-025P SiPM. At higher gamma energies saturation effects due to the limited number of microcells can be noticed.

Photon detection efficiency:

The photon detection efficiency (PDE) expressed in equation 3.3.3 is a product of three quantities [44]: (1) the quantum efficiency (QE), (2) the geometric fill factor (ε) and (3) the avalanche trigger probability ($P_{trigger}$).

$$PDE = QE \cdot \varepsilon \cdot P_{trigger} \tag{3.3.3}$$

For a p on n type SiPM the quantum efficiency of the active area can reach maximum values up to 90% [44] around the peak wavelength of 450nm. The QE peaks in a narrow wavelength range of only 150nm FWHM around the center which is the consequence of the relatively thin sensitive layer of the p on n structure. It is kind of a preference if the QE as well contains Fresnels reflection losses on the surface, as in the present definition. In any case this influence has to be taken into account but can be minimized to negligible values with proper coating of the SiPM surface.

The geometric fill factor ε is defined by the ratio of photosensitive area to the total active area of the SiPM. On the right in figure 3.16 one can see connection wires leading to each microcell. This area is not sensitive to impinging photons and thus decreases the geometric fill factor. Normally the quenching resistor made out of polysilicon, which is not transparent for wavelengths around 400nm, is located on top of the microcell which as well decreases the value of ε. In order to

obtain a high geometric fill factor one would prefer large microcells over small ones. However this would increase saturation effects and due to the increased microcell volume thermally generated electron-hole pairs would provoke a higher dark count probability in the microcell. In practice there has to be found a compromise between all these factors. In terms of timing this will be discussed more in detail in chapter 5.

The avalanche trigger probability $P_{trigger}$ is the only quantity which is strongly dependent on the bias overvoltage. It denotes the probability of an electron or hole to initiate an avalanche in the microcell and increases with increasing bias overvoltage. Electrons have a better chance to trigger an avalanche than holes [58] as can be seen in figure 3.25. The trigger probability is further dependent on where the charged carrier was generated in the p-n junction (see figure 3.25).
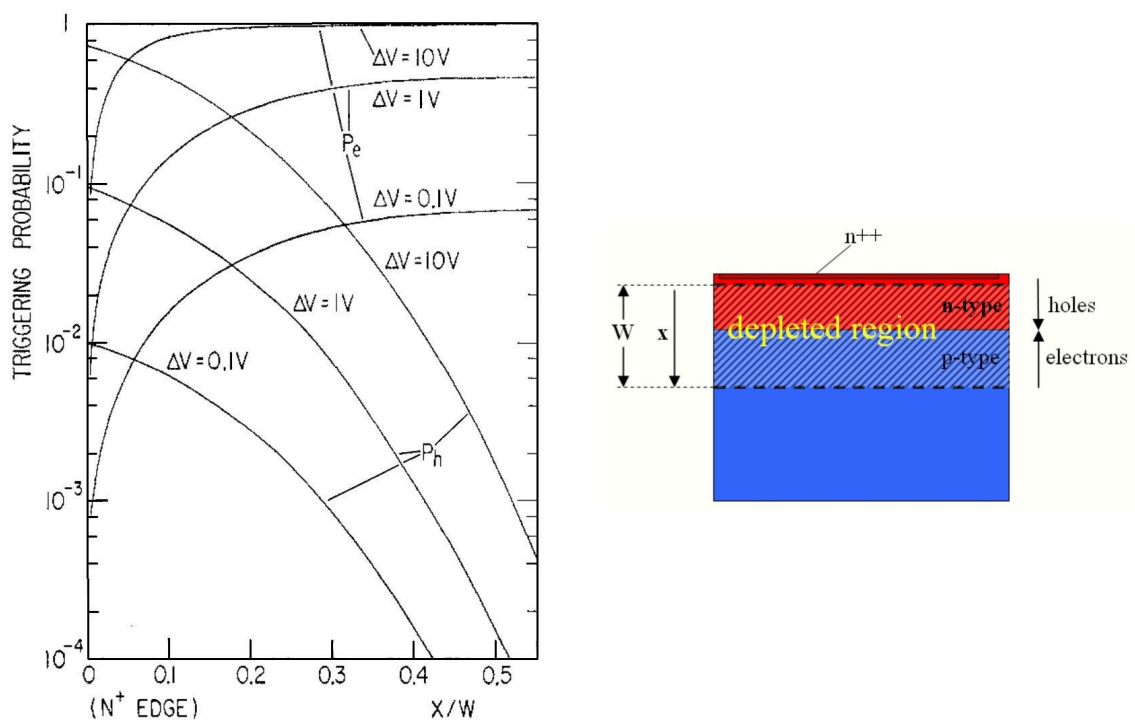
Figure 3.25.: Avalanche trigger probability of electrons P_e and holes P_h as a function of overvoltage and position of charge carrier production in silicon. Pictures are a reprint from [58] and [44].

3.3.5. The digital silicon photomultiplier

The digital silicon photomultiplier is one of the most recent developments along the solid state photodetectors. There are different realizations of d-SiPMs, e.g. using only one time to digital converter (TDC) for all microcells [59], mixed forms with one TDC per column of microcells [60] or the fully d-SiPM as can be seen in figure 3.26. Recently Philips developed a d-SiPM [59] which uses only one TDC per SiPM tile which can be adjusted to trigger on different "levels" of photo-electrons. This approach is very similar to the analog SiPM discussed above. Such a d-SiPM has already been tested successfully in PET systems [23, 61]. In the EndoTOFPET-US project [6, 62] a further step towards a fully digital SiPM is achieved. There several microcell columns are com-

bined and readout by 48 independent TDCs. The fully digital SiPM shown in figure 3.26 is the most complicated to realize because of the need for a high number of readout channels (TDCs), when other factors like PDE especially the geometric fill factor should be kept at acceptable values. In general the fully digital SiPM would deliver the highest amount of information and is thus expected to give the best possible time resolution. An additional complication is the correct combination of the multitude of gathered time stamps in order to reconstruct the gamma absorption time in the coupled scintillator. In chapter 10 we will give an outlook on how to process these time stamps and compare the best achievable time resolution with the analog SiPM.
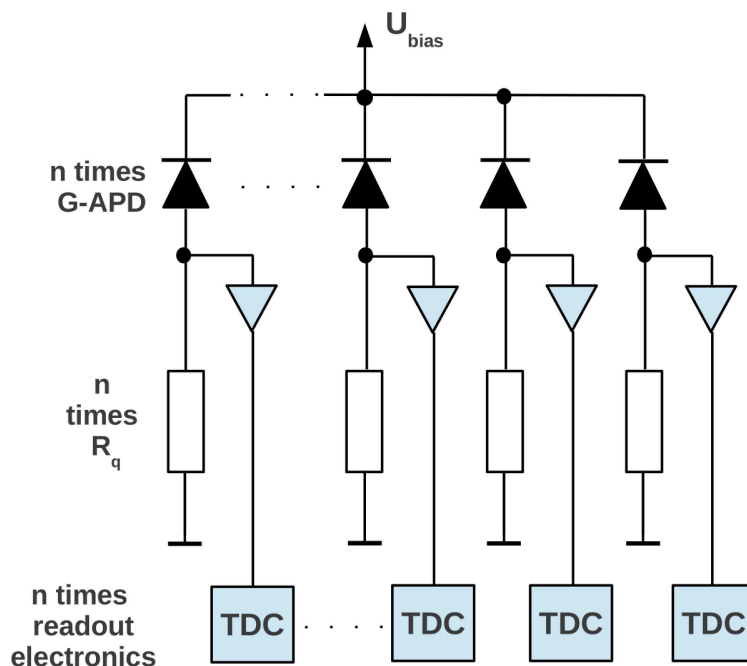
Figure 3.26.: Schematics of the fully digital SiPM. Each microcell of the SiPM is connected to its own readout electronics and a time to digital converter (TDC) which delivers the time of each triggered avalanche.

3.4. Electronics: NINO, a low noise leading edge discriminator

Low noise and fast electronics is needed to readout the small signals generated by the SiPM. For this purpose we use the ultrafast front-end discriminator amplifier NINO [63] developed at CERN. NINO was originally engineered for the ALICE time of flight (TOF) particle identification. The particle identification by means of time of flight demanded a resolution better than 100ps in order to separate e,π,K and p in the momentum range of 1-4GeV/c [63]. Multigap resistive plate chambers (MRPCs) were used because of their very fast charge collection time of $\sim$100ps and relative cheapness. Thus the front-end electronics was required to be very fast, with low noise and a minimum slew rate. In addition a low input impedance was required in order to minimize signal reflections and crosstalk and to meet impedance matching of the transmission lines connecting the detector [63]. All these characteristics primarily developed for the readout of MRPCs are as well

beneficial for SiPM readout. In this section a short overview of the NINO chip and its electronics will be given following the publications of [63] and [45].

In figure 3.27 the layout of the NINO chip is shown. The chip is produced in a 0.25μm CMOS technology and its dimensions are 2x4mm^2. It consists of 8 channels, every channel is designed for full differential signal processing from the input to the output. This differential signal processing gives better stability against pick-up noise and power supply noise. The output signal peaking time is 1ns, the input impedance is adjustable between 40Ω and 75Ω and the power consumption per channel is 30mW. In figure 3.28 a magnified picture of the NINO chip can be seen and in figure 3.29 the NINO chip wire bonded to the printed circuit board (PCB).
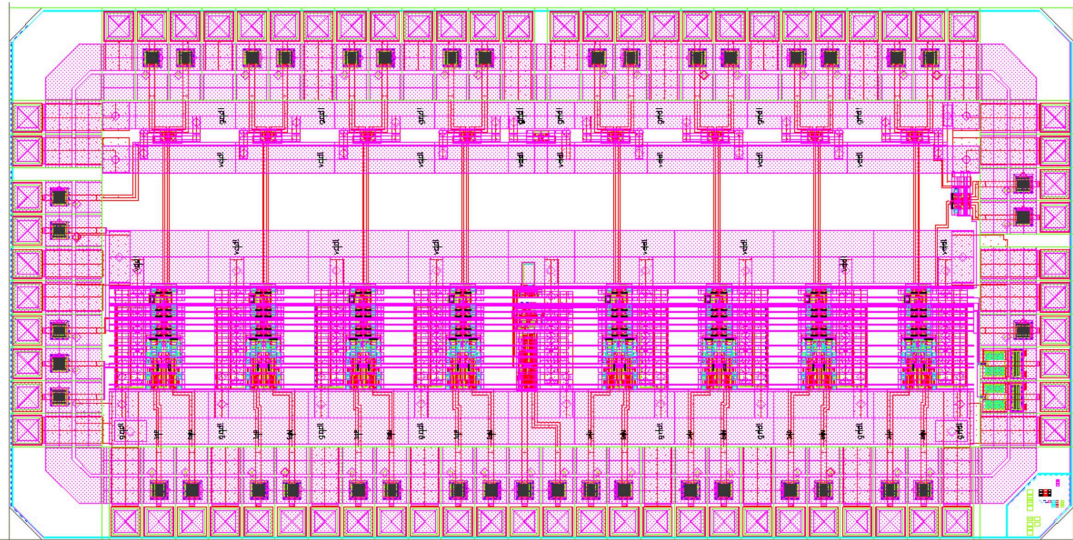
Figure 3.27.: Layout of the NINO chip. Picture is taken out of [45].
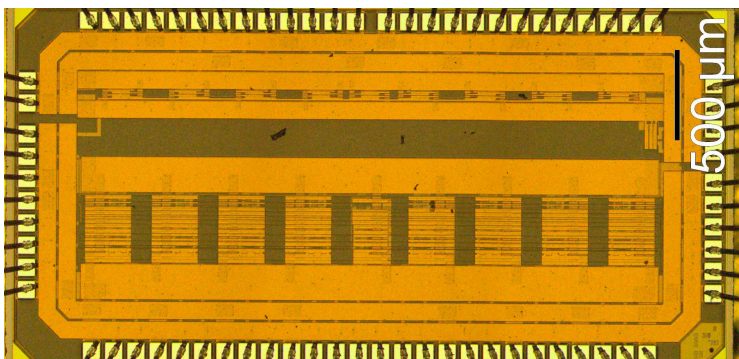
Figure 3.28.: Close up view of the NINO chip.
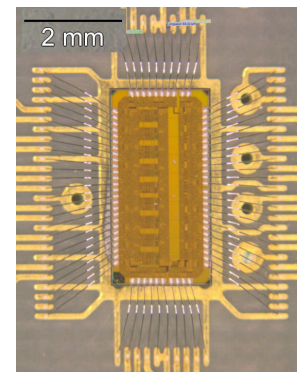
Figure 3.29.: NINO when wire bond to the printed circuit board.

In figure 3.30 we depict the architecture of one NINO channel. The input stage is followed by 4 cascade amplifiers and the output driver is adapting the output signal to the LVDS standard.

The input stage is chosen to be a robust current to voltage converter based on a common gate circuitry [63]. The threshold is applied to the input stage via a voltage difference on the two symmetrical inputs. A small hysteresis can be added by enabling a positive feedback loop. The subsequent cascade amplifiers, optimized for delay and slew rate, provide enough gain (factor six) to operate NINO as a discriminator. In figue 3.31 the input stage and in figure 3.32 the cascade amplifier is shown in more detail.
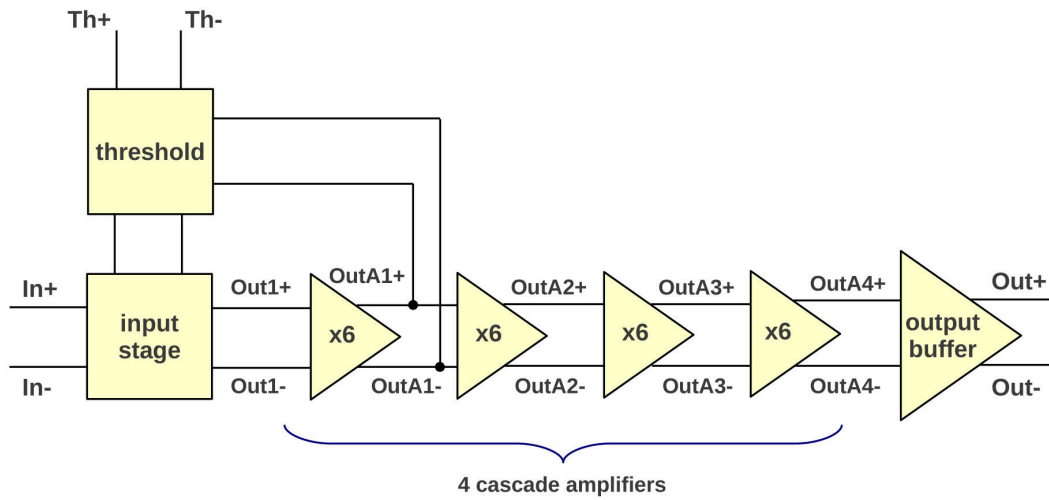

Figure 3.30.: Sketch of the NINO chip [45].

The input stage (see figure 3.31) is a transimpedance amplifier which ensures fast signal processing and low input impedance. The schematic can be separated in four main blocks [45]:

1. Block one in figure 3.31 shows two resistors R which convert the input current into a voltage supplied to the cascade amplifiers. The output voltages are defined as follows:

$$V_{Out1+} = V_{dd} - R\left(I_{source} - I_{th1} + i_{in+}\right)$$
$$V_{Out1-} = V_{dd} - R\left(I_{source} - I_{th2} + i_{in-}\right)$$

(3.4.1)

In equation 3.4.1 the term V_{dd} is the NINO power supply with 2.5V, I_{th1} and I_{th2} are currents injected depending on the applied NINO threshold provoking different DC offsets for the subsequent cascade amplifiers and I_{source} a current provided by the current sources in block four. The NINO input signals are represented by i_{in+} and i_{in-} in equation 3.4.1. The differential output voltage can thus be written as in equation 3.4.2. The current difference $I_{th2} - I_{th1}$ determines the discrimination threshold by generating a DC voltage offset in $V_{Out1+} - V_{Out1-}$ at the first cascade amplifier input. The currents I_{th1} and I_{th2} are determined by the threshold block in figure 3.30 and therefore by the NINO threshold input.

$$\Delta V_{Out1} = V_{Out1+} - V_{Out1-} = R\left(i_{in+} - i_{in-} + I_{th2} - I_{th1}\right)$$

(3.4.2)

2. Block two in figure 3.31 limits the differential voltage output of the input stage in case of

too high input signals.

3. Block three in figure 3.31 is the cascode common gate circuit. It represents a two stage amplifier composed of a common gate amplifier followed by a current buffer. The input impedance of NINO is determined by the transconductance $g_m = \frac{I_{out}}{I_{in}}$ of both common gate input transistor. The transconductance can be estimated to $g_m \approx \frac{I_{source}}{2*V_T}$ with $V_T = 26.6mV$. As example a differential NINO input impedance of 50Ω can be achieved with a current of 2mA.

4. Block four in figure 3.31 shows the current sources delivering I_{source} into each branch of the differential input stage. The current can be adjusted by an external resistor (via BiasN1) to achieve different input impedances of NINO (40-75Ω).

In figure 3.32 the schematic of one of the four cascade amplifiers is shown. It is a simple differential voltage amplifier with gain six and a bandwidth of 1GHz. Putting four of these amplifiers in cascade a squared output pulse of NINO is achieved by saturating the voltage input signal. The width of this squared output pulse is a function of the input charge.


Figure 3.31.: Schematic of the cascode input stage of NINO.

Figure 3.32.: Schematic of the following cascade amplifiers of NINO.

The ultrafast discriminator-amplifier NINO is employing the time-over-threshold (TOT) technique. It produces a squared output pulse with the leading edge determining the time information (leading edge discrimination) and the width being a function of the pulse charge and thus delivering energy information (see figure 3.33). The NINO output thus encodes both energy and time

information in one digital pulse. As already mentioned, NINO uses a common mode configuration with differential input signals coming from the SiPM [64] and hence can actively suppress common ground noise and pick-up.
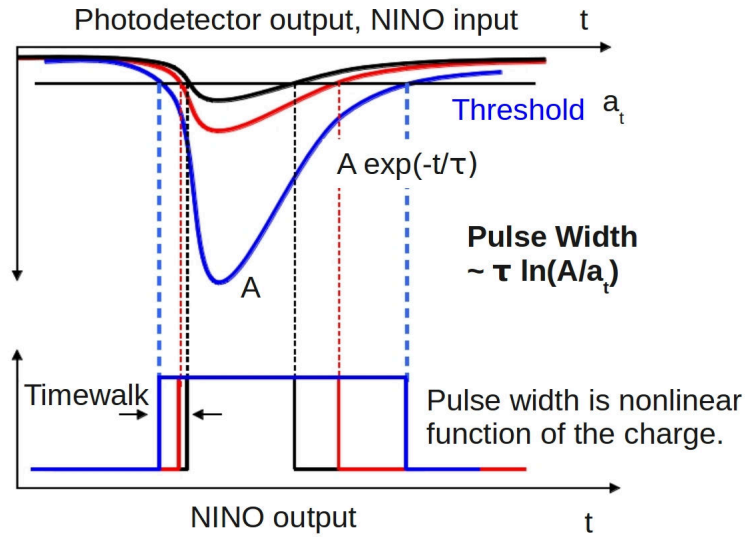

Figure 3.33.: Generation of the squared NINO output pulse from the SiPM input signal. The pulse width is a logarithmic function of the SiPM amplitude. Picture modified from [45].

Chapter 4

Femtosecond laser tests on SiPMs

4.1. Introduction

Time of flight positron emission tomography (TOF-PET) calls for an optimization of all factors affecting the time resolution of the whole photon detection system [8]. Such a system is made of a scintillator, a photo-sensitive detector, and the electronics as discussed in chapter 3. Better time resolution has specially become a prerequisite in PET if improved signal-to-noise ratio images, lower exposure rates for patients, and significantly faster image reconstruction are required [65]. Most of the advantages of time of flight in PET was already discussed in chapter 2. The challenging objective of improving the time resolution can only be achieved through an in-depth understanding and optimization of the light production and light transport mechanisms in the scintillators as well as the best possible control of both, the photodetector and the discrimination threshold [7]. The latest generation of fast photo-sensitive detectors are silicon photomultipliers (SiPMs) which have been introduced in section 3.3 of chapter 3. SiPMs are becoming increasingly attractive as photodetectors, as they combine high speed and gain with compactness and insensitivity to magnetic fields. SiPMs are interesting candidates for dual modality systems, like PET combined with magnetic resonance imaging (MRI). Substantial progress was made in the direction of higher fill factors, better efficiency, and lower noise, though still more understanding of the SiPM device is needed to achieve coincidence timing performance of better than 300ps FWHM currently attained and hence being comparable to the best conventional PMTs [66–68].

Before testing the whole radiation detector described in chapter 3 it is interesting to study the SiPMs without the influence of the scintillation, i.e. the scintillation crystal. A method to do this is to use very short laser pulses and illuminate the SiPM with a tunable number of photons directly. This will give insight on how much the photodetector with the accompanying electronics is contributing to the overall time resolution of the radiation detector. It is thus important to measure the exact timing properties in dependence of the photon flux and the operational parameters of the photodetector and the readout electronics. This chapter reports on the timing of SiPMs as a function of their bias voltage, electronics threshold settings and the number of impinging photons. We used ultrashort laser pulses at 400nm wavelength with pulse duration below 200fs. The studies are focused on different types of SiPMs (Hamamatsu MPPC S10931-025P, S10931-050P

and S10931-100P) with different single photon avalanche diode (SPAD) sizes (25μm, 50μm and 100μm) coupled to the ultrafast discriminator amplifier NINO. The content of this chapter is a revised and adapted version of the publication [69].

4.2. Photodetectors

We have chosen three types of commercial SiPMs of the same active area, 3x3mm^2, but with different fill factors or SPAD sizes, i.e. 25μm, 50μm, and 100μm manufactured by Hamamatsu Photonics K.K. Their pertinent parameters are listed in table 4.1. We measured the Geiger breakdown voltage for each SiPM (see figure 4.1). In figure 4.2 the dark count rate (DCR) of the three different SiPM types can be seen. For these measurements the threshold was set to be low enough to trigger on single photoelectrons (p.e.), i.e. around 0.5 p.e. The 50μm SPAD sized SiPM has the lowest dark count rate, even for high bias overvoltages. In comparison the 100μm type suffers from a rapid increase in DCR with increasing bias overvoltage. To reject ground and supply voltage noise, the SiPMs are connected differentially [64] to the front-end amplifier NINO. In such a scheme, both the anode and cathode of the SiPM feed the avalanche signal to the amplifier with the advantage of effectively suppressing common mode noise picked up in the signal path.

Table 4.1.: Properties of the different photodetectors, HAMAMATSU with 3x3mm^2 active area

| Type: S10931	SPAD size (μm^2)	Number of Cells	Fill Factor (%)	break down (V)
-100P (received June 2010)	100x100	900	78.5	69.3
-050P (received June 2010)	50x50	3'600	61.5	70.5
-025P (received June 2010)	25x25	14'400	30.8	69.2
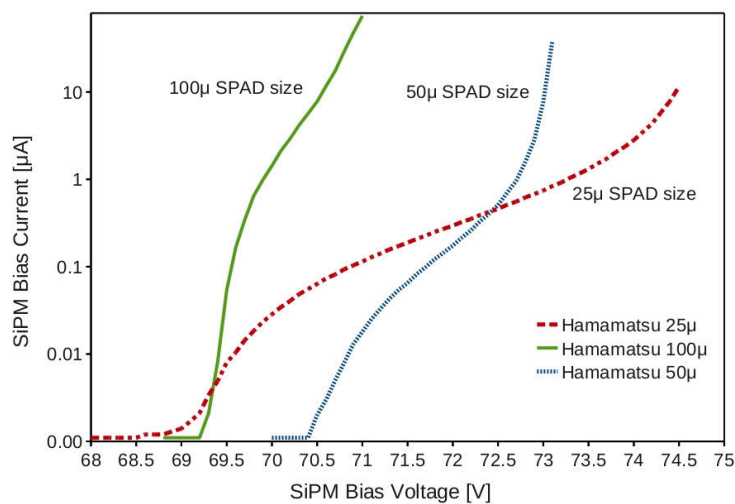
Figure 4.1.: Typical I-V diagram for the three species of different SPAD sized SiPMs showing the respective breakdown voltages.

Dark Count rate vs. Bias overvoltage
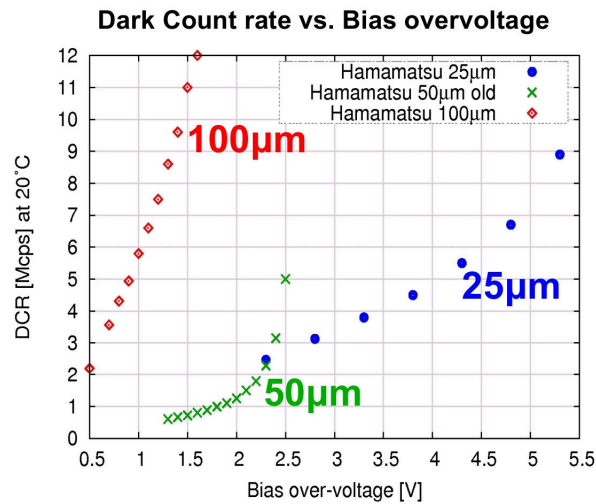
Figure 4.2.: Dark count rate (DCR) versus bias overvoltage for the three different SPAD sized SiPMs (25μm, 50μm and 100μm).

4.3. Setup

The tests comprised a series of systematic studies of SiPM properties in terms of SiPM fill factor or SPAD size, SiPM bias voltage, NINO threshold and optical density (OD) of the light attenuators. The setup can be seen in figure 4.3.
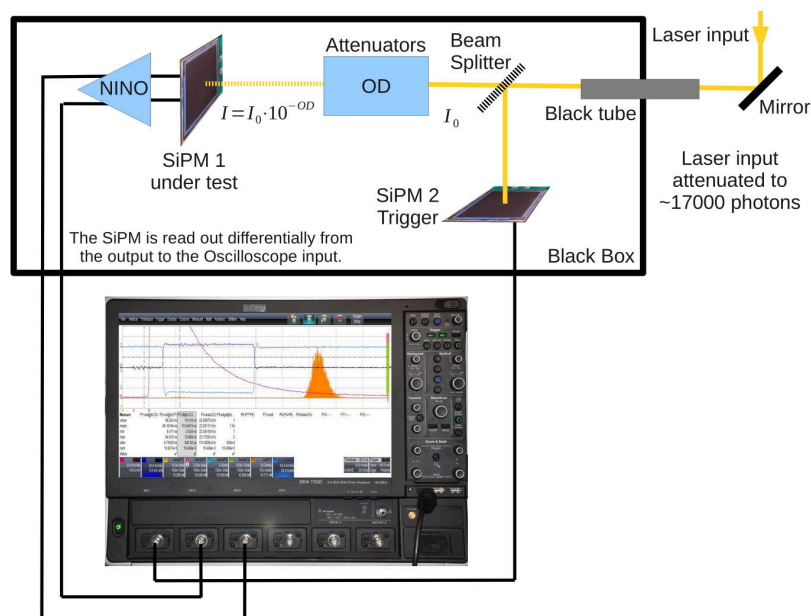

Figure 4.3.: Setup as used for the femtosecond laser tests. The SiPM signals are fed differentially into the ultra-fast discriminator-amplifier NINO. A fast oscilloscope measures the time delay between the differential NINO output and the trigger.

The test were made in collaboration with the University of Geneva (Physical Chemistry Department - Sciences II) were the setup was installed. The SiPMs and electronics were housed in a portable light tight box. The laser beam was coupled into the box via a black tube which ensures to keep stray light to a minimum. The data was acquired with a fast LeCroy Oscilloscope DDA 735Zi 40Gs/s, that achieves ~1ps time resolution by interpolation. The femtosecond laser operated at 400nm wavelength with a pulse width of 200fs and was provided by the University of Geneva. For each attenuation factor, measured in optical density (OD) of the laser beam we scanned the SiPM bias and NINO threshold to find the optimum values. The attenuation given in optical density is defined as $I = I_0 \cdot 10^{-OD}$, e.g. an OD equal one states an attenuation of ten ($I = I_0/10$).

4.4. Time Reference

To establish a precise trigger we split the beam into two, each one illuminating a 25μm - SiPM with approx. 8000 photons. The performance of the trigger was then tested by measuring the time delay between the two 25μm type SiPMs. The signal of the SiPMs was directly fed into the oscilloscope without using any further electronics. We obtained a coincidence time resolution of $\sigma = 4.1ps$. Thus the trigger jitter is about $\sigma = \frac{4.1}{\sqrt{2}}$ps=2.9ps. In figure 4.4 the trigger versus trigger delay time histogram can be seen. Throughout this chapter all time resolution values will be stated in standard deviation of the Gaussian fit and not in FWHM.
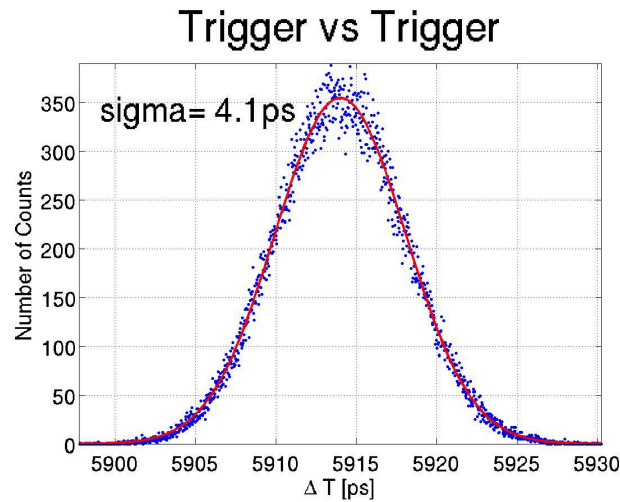

Figure 4.4.: The trigger versus trigger time jitter was measured to have a standard deviation of σ=4.1ps. Thus the time reference jitter is $\sigma = \frac{4.1}{\sqrt{2}}$ps=2.9ps.

4.5. Data analysis

NINO uses the time-over-threshold method and produces a squared output pulse. The leading edge gives the time information, and the pulse width is correlated to the input charge [64]. In figure 4.5 and figure 4.6 we show examples for the measured NINO pulse width histograms and

according time delay histograms versus the trigger, respectively.
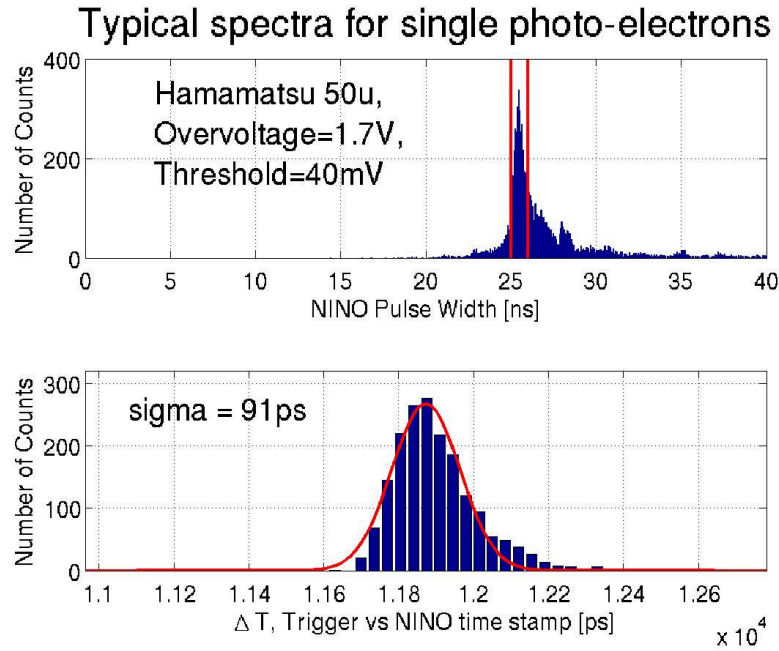
Figure 4.5.: Example of the data analysis for low light fluxes (single photon time resolution measurements). Upper figure: NINO pulse width histogram with selection window on the single photoelectron events. Lower figure: According histogram of the trigger and NINO output time difference for the selected events.
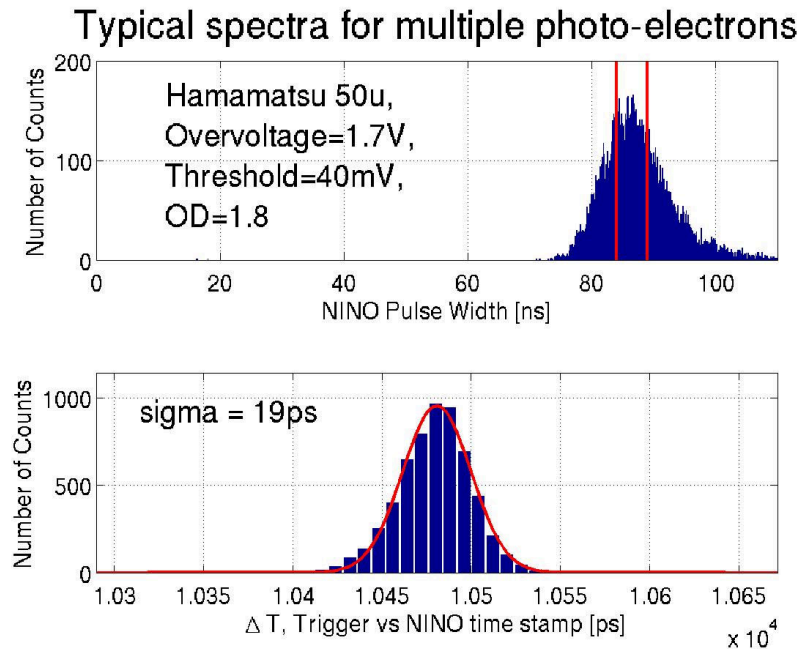

Figure 4.6.: Example of the data analysis for high light fluxes. Upper figure: NINO pulse width histogram with a small selection window around the peak. Lower figure: According histogram of the trigger and NINO output time difference for the selected events. The measurement was performed at an OD=1.8 which corresponds to approximately 22 photoelectrons (p.e.) detected.

For low light fluxes (single photons) we select only events within the single photoelectron peak (see figure 4.5). This ensures to minimize time walk and deterioration caused by optical crosstalk and afterpulse events in the SiPM. The time delay was measured against the trigger which we determined to have a time jitter of $\sigma = 2.9ps$ (see figure 4.4). In the analysis no corrections accounting for the trigger jitter were applied.

In the case of higher photon fluxes, as can be seen in figure 4.6, a small area around the peak of the pulse width histogram was selected and the corresponding delay time spectrum was plotted. With this selection we reduce the influence of time walk and the Poissonian photon flux jitter on the time distribution.

4.6. Single photon time resolution

Single photon time resolution was measured at very low light intensities to ensure single photon hits on the detector, see figure 4.7. An example of the data analysis is shown in figure 4.5. The chosen NINO threshold was set to 40mV. By performing dark count scans, this value was found to be low enough to detect the firing of a single photon avalanche diode (SPAD) for all applied overvoltages and measured SiPM types.
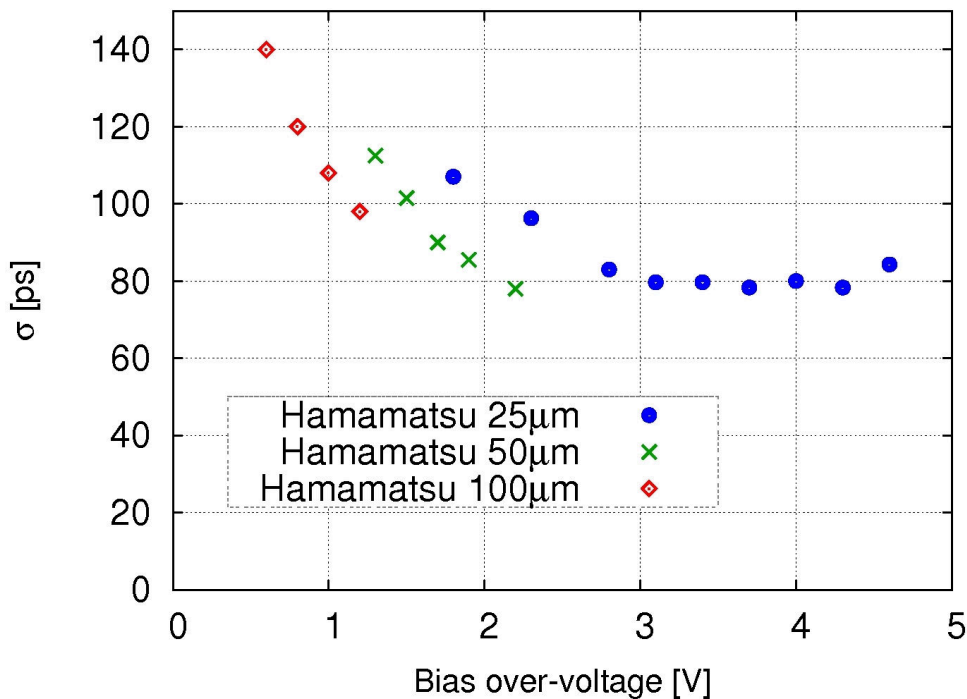

Figure 4.7.: Single photon time resolution of the three different SiPM types. Values are stated in standard deviation (sigma) of the Gaussian fit and not FWHM. The applied NINO threshold was 40mV which ensures to detect the firing of a single SPAD for the three different SiPM types, i.e. around 0.5p.e.

We identify three effects being responsible for the single photon time resolution: (a) electronic

noise of the amplifier NINO, (b) the avalanche generation in a single SPAD with its time profile and (c) non-uniformities of the SPADs together with different signal transmission delays to the SiPM output. With increasing SiPM overvoltage the electronic noise influence gets less important because of an increasing gain of the SiPM. Furthermore with higher overvoltage the avalanche build up gets faster and thus the SPTR value is affected less by this influence.

As can be seen in figure 4.7 the SPTR seems to saturate at 80ps sigma for the 25μm type SiPM. For the 100μm type SiPM operation at higher overvoltages as shown in figure 4.7 was not possible because of the rapid increase in DCR as can be seen in figure 4.2. Further we unfortunately did not investigate the 50μm type SiPM at higher overvoltages because due to the limited time available at the University of Geneva we concentrated our test runs on bias voltage values similar to the ones determined to be best in a TOF-PET system, as will be discussed in chapter 5.

4.7. Time resolution vs. light intensity, threshold and overvoltage

In figures 4.8-4.10 we show the time resolution versus the photon intensity, i.e. the number of photoelectrons (p.e.). We observe that the time resolution follows a $1/\sqrt{N_{p.e.}}$ behavior. This can be explained by pure statistical considerations as the precision of the centroid of a Gaussian is inverse proportional to the square root of the sample number. At high photon intensities the time resolution saturates at around 20ps sigma for low threshold values. This is related to the intrinsic limit of the electronics and because of the very low threshold deteriorated by the SiPMs dark count. For higher threshold values we measure time resolutions of around 8ps sigma as can be seen in the figures 4.11, 4.12 and 4.13. The NINO threshold values and their translation into equivalent photoelectrons or SPADs fired is strongly dependent on the SiPM type and applied overvoltage. It will be discussed in more detail in the following chapter 5 and can be deduced from the figures 5.12 - 5.15.
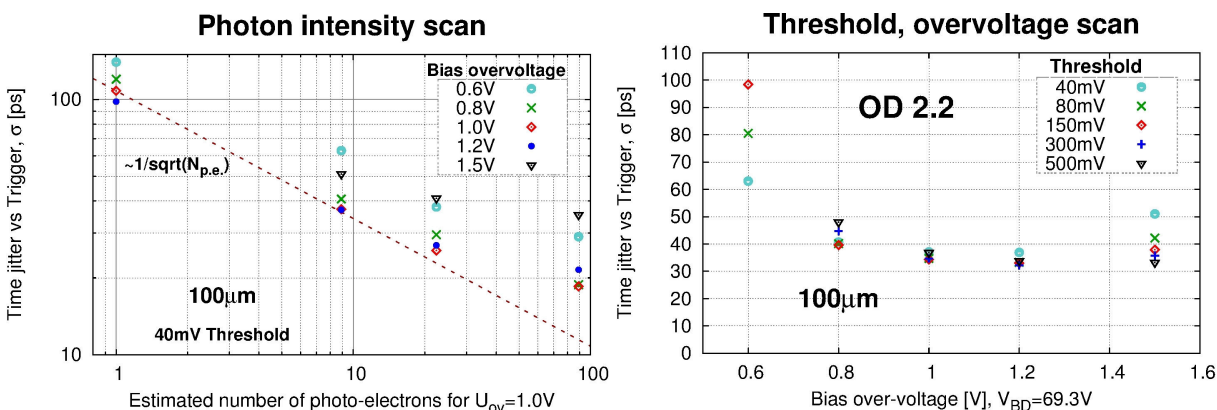

Figure 4.8.: Time resolution performance of the 100μm SPAD sized SiPM when irradiating with femtosecond laser pulses. Left: photon intensity scan versus overvoltage with fixed NINO threshold of 40mV. Right: bias and threshold scans with fixed photon flux of OD=2.2 corresponding to approximately 9p.e. at an overvoltage of 1V.
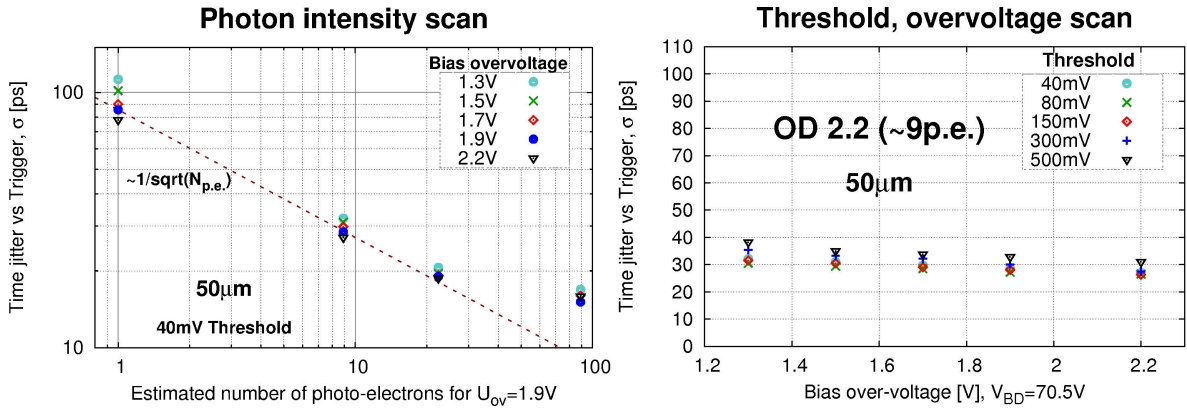
Figure 4.9.: Time resolution performance of the 50μm SPAD sized SiPM when irradiating with femtosecond laser pulses. Left: photon intensity scan versus overvoltage with fixed NINO threshold of 40mV. Right: bias and threshold scans with fixed photon flux of OD=2.2 corresponding to approximately 9p.e. at an overvoltage of 1.9V.
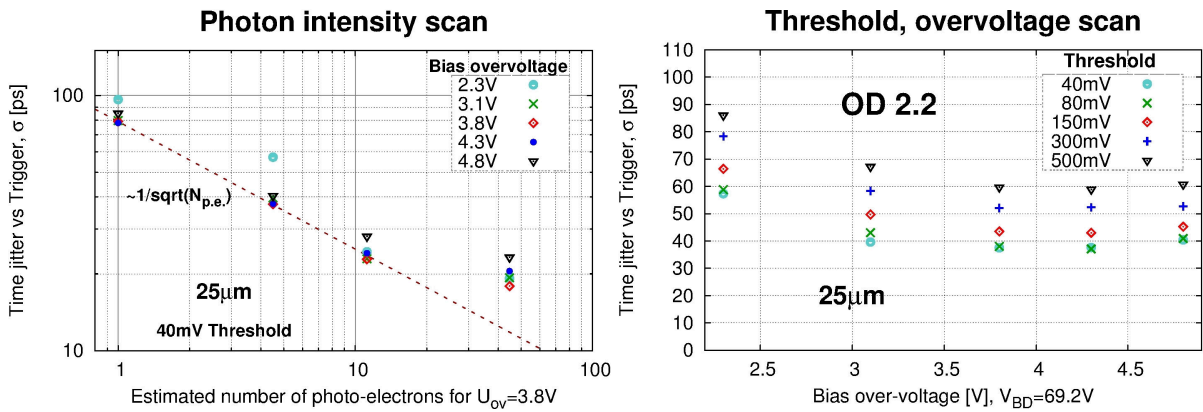
Figure 4.10.: Time resolution performance of the 25μm SPAD sized SiPM when irradiating with femtosecond laser pulses. Left: photon intensity scan versus overvoltage with fixed NINO threshold of 40mV. Right: bias and threshold scans with fixed photon flux of OD=2.2 corresponding to approximately 5p.e. at an overvoltage of 3.8V.
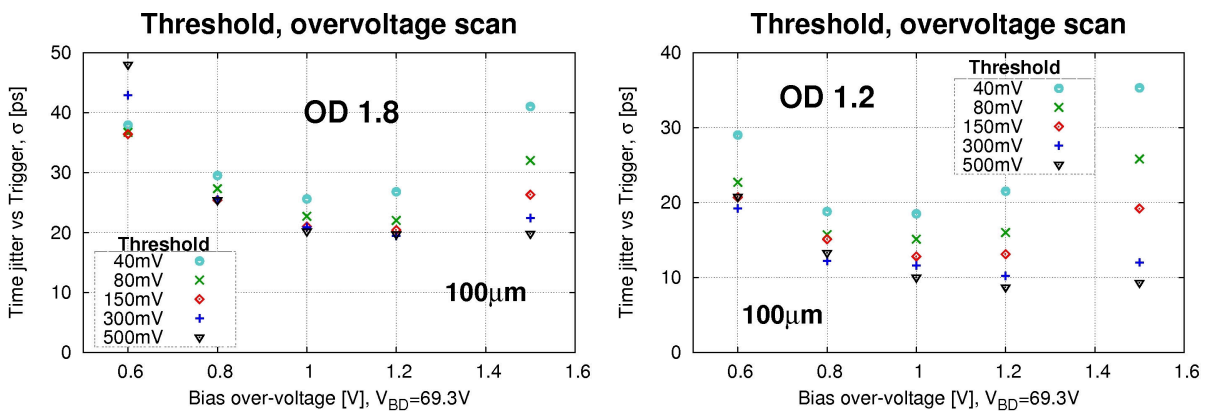

Figure 4.11.: Bias and threshold scans with fixed photon flux for the 100μm SPAD sized SiPM. Left for an optical density of OD=1.8 corresponding to approximately 22p.e. at an overvoltage of 1V and right for OD=1.2 corresponding to approximately 89p.e. at an overvoltage of 1V.
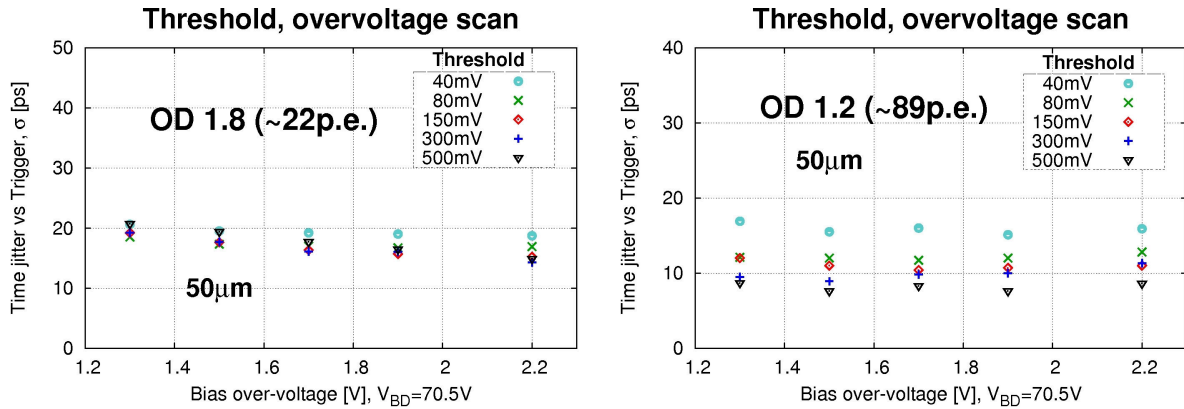
Figure 4.12.: Bias and threshold scans with fixed photon flux for the 50μm SPAD sized SiPM. Left for an optical density of OD=1.8 corresponding to approximately 22p.e. at an overvoltage of 1.9V and right for OD=1.2 corresponding to approximately 89p.e. at an overvoltage of 1.9V.
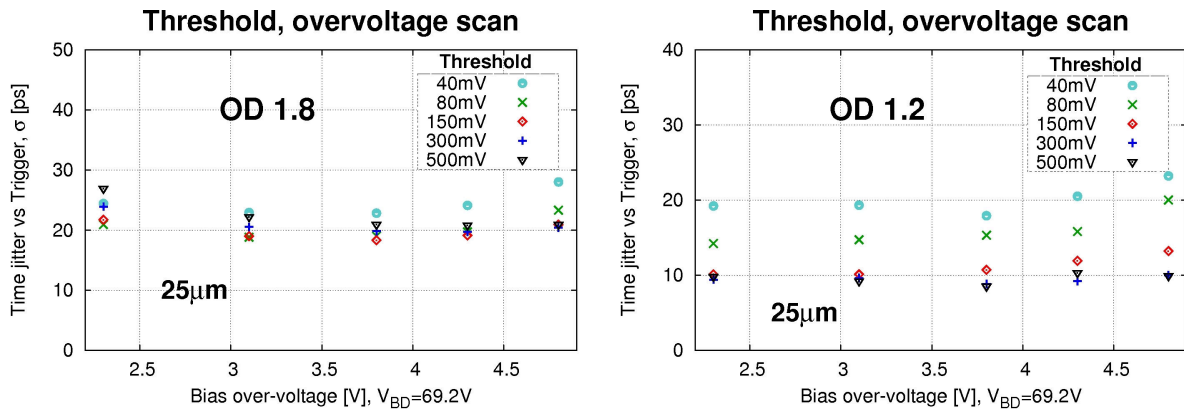

Figure 4.13.: Bias and threshold scans with fixed photon flux for the 25μm SPAD sized SiPM. Left for an optical density of OD=1.8 corresponding to approximately 11p.e. at an overvoltage of 3.8V and right for OD=1.2 corresponding to approximately 45p.e. at an overvoltage of 3.8V.

In figures 4.8-4.10 and figures 4.11-4.13 we see that the measured time jitter versus the bias overvoltages show a minimum for the 25μm and 100μm type SiPM at 3.8V and 1V, respectively. The minimum in time resolution can be explained by an increasing DCR when increasing the bias overvoltage. With increasing bias overvoltage the PDE is increasing as well. As the light flux is kept constant (fixed optical density) the time jitter will slightly decrease with increasing overvoltage because the SiPM will be able to detect more photons. However, the increasing DCR with increasing overvoltage will offset this time jitter improvement at a specific point and gives rise to the observed minimum.

4.8. Summary and Conclusion

Using NINO, we achieved single photon time resolutions (SPTRs) of SiPMs, down to 80ps sigma. Light level scans showed a $1/\sqrt{N_{p.e.}}$ dependence of the measured time resolution. At saturating photon fluxes and high threshold values we even measured a time resolution of less than 10ps

sigma. This approaches the timing limitations of the electronics (NINO) and the acquisition system (oscilloscope). At lower NINO thresholds this value is strongly deteriorated by the SiPM's dark count.

If we measure the time resolution at higher photon fluxes we observe that for the 25μm and 100μm SPAD size type SiPM the time jitter shows an optimum at bias overvoltages of 1V and 3.8V, respectively. This optimum overvoltage values can be explained by an increasing number of detected photons with increasing bias overvoltage, because the light flux is held constant (constant OD). However, the DCR is increasing as well and consequently deteriorates the time resolution with increasing bias overvoltage. The interplay of these two effects then gives rise to the observed minimum in the CTR. On the other hand for the 50μm type this optimum is less evident, leading to the conclusion that for the 50μm type and within the used overvoltage range the DCR is still low enough and does not deteriorate the measured time resolution for this device.

Chapter 5

Optimization of SiPM photodetection for highest time resolution in PET

5.1. Introduction

In this chapter a systematic study of time resolution measurements is reported made with three different commercial silicon photomultipliers (SiPMs) from the producer Hamamatsu (MPPC S10931-025P, S10931-050P, and S10931-100P) coupled to LSO scintillating crystals. The three types of SiPMs are the same as used for the experiments with the femtosecond laser as discussed in the preceding chapter. It is aimed to determine the optimum detector conditions for highest time resolution in a prospective TOF-PET system. Measurements are based on the time-over-threshold method in a coincidence setup using the ultrafast amplifier-discriminator NINO and a fast oscilloscope. Additionally the influence of the crystal cross section and wrapping to the time resolution will be discussed. Parts of the content of this chapter were modified and adapted from the publications [10, 70, 71].

5.2. Measurement setup

A suitable method to optimize the operating conditions of the photodetectors is the measurement of the coincidence time resolution (CTR) with a pair of identical crystals and SiPMs in a back-to-back configuration as shown in figure 5.1. The radioactive β^+ decay of a ^{22}Na source produces a positron which emits two back-to-back 511keV γs by annihilation with an electron. The ^{22}Na source has an activity of 3MBq and a spherical geometry with 1mm diameter. In the scintillating crystal these 511keV gammas are converted into visible photons with wavelength around 420nm. These photons are then detected by the photodetector (SiPM). The SiPM signals are fed into the CERN-developed NINO chip described in chapter 3.4. NINO uses the time-over-threshold technique and thus delivers time and energy information combined in one pulse. The leading edge of the squared NINO output signal delivers the time information and the pulse width the energy information (see figure 3.33 in chapter 3.4).

A high-bandwidth oscilloscope, LeCroy DDA 735Zi (40 GS/s), is recording the dual pulse widths

from the two NINO outputs plus their mutual delay. The logic of the scope is set such that only coincident events are collected irrespective of their energy, i.e. events with the full energy from the photoelectric effect and Compton scattered events. The scope records these events in lists or histograms keeping track of the mutual time delay between coincident photons and the energy of the photons. The energy tag of the photons is needed to eliminate (offline) Compton events, for the refinement of the coincidence time spectrum. To avoid temperature-induced gain fluctuations of the SiPMs, the entire setup was housed in a thermally controlled, insulated dark box. The temperature was held constant at 20±0.1°C.
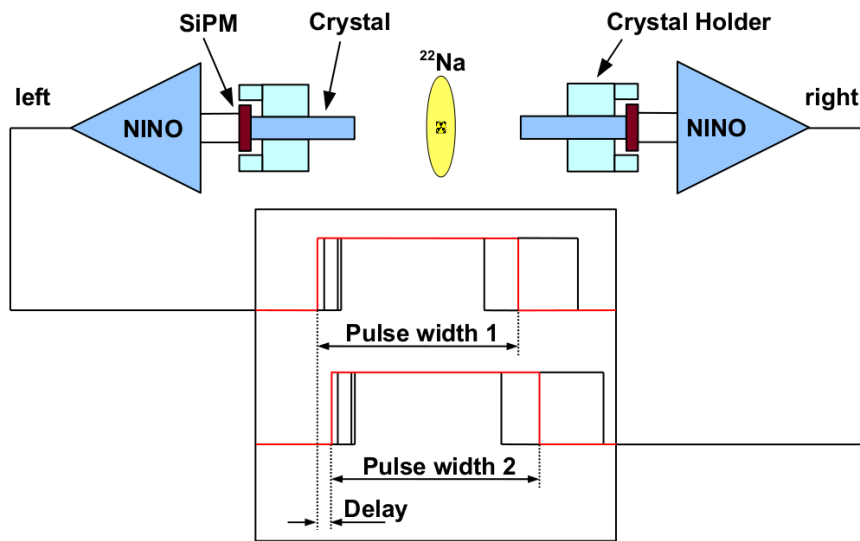

Figure 5.1.: Schematic of the coincidence time measurement setup. The setup is housed in a temperature controlled (20° ± 0.1°C) thermal box.

Tests were grouped into three major packages corresponding to the three investigated photo-detectors, i.e. for 25μm, 50μm, and 100μm SPAD size, and four categories corresponding to: 1) the optimization of the SiPM bias, 2) the optimization of the discriminator threshold, 3) the light collection in the SiPMs, and 4) a study of the dark count rate generated in the devices. Hence, for each SiPM type, the operating parameters of the involved devices were "scanned" in order to identify the optimum set points for both bias and detection threshold, using the coincidence time resolution as the scale of the system's performance. To measure the photoelectron yield of the tested crystals and possibly observe a correlation between photon yield and the corresponding time resolution, the test bench as shown in figure 5.1 was also used, but modified such that only one arm of the coincidence setup was read out where the output of the SiPM was directly fed into the scope not making use of the NINO discriminator. Also, the studies of the dark count rates of the different SiPM types were made in a single arm of the test apparatus. The dark count rate was then recorded as a function of the NINO threshold to detect the threshold values of the first consecutive photoelectrons. This was done to possibly understand the general influence of the dark counts on the time resolution in relation to the PDE.

5.3. Results for 2x2x10mm^3 LSO:Ce crystals

5.3.1. Search for optimum SiPM bias and NINO threshold voltage

Using the coincidence setup shown in figure 5.1, we measured the system's coincidence time resolution as a function of the SiPM bias. We probed their performance in terms of the coincidence time resolution, together with the chosen scintillators and electronics, to be achieved at varying bias and threshold settings. In these coincidence tests, always a pair of same SPAD size SiPMs were used. SiPM properties are known to vary even within a batch of same types. Therefore we have measured the breakdown voltage which is the same for each SPAD size type. Thus we choose the voltage settings to be common to both SiPMs in the system. In figure 5.2 we show the NINO pulse width histograms for the left and right branch of the setup. The time- and energy-encoded data from the time-based readout are fed into a delay time and pulse width scatter plot, shown in figure 5.3. In this plot, axis projections yield horizontally the ^{22}Na energy spectrum as already mentioned (see figure 5.2). Vertical axis projection shows the delay time spectra of the coincident gammas, with and without photopeak selection to be seen on the left-hand side of figure 5.3. In figure 5.4 the delay time spectra of the coincident gammas is depicted if only events within both photopeaks are selected.

The discontinuity in the scatter areas, found in the top and middle plots between 50ns and 200ns pulse width, is an artifact produced by the specific data taking mode of the oscilloscope (gating and averaging the coincident pulse widths while recording the "Trend"). This has no influence on data quality as long as the data are selected in both photopeak regions (bottom part of the scatter plot). The energy spectra of the correlated gammas allow rejection of Compton photons by selecting events associated with the 511-keV photopeak, i.e. at around its mean value. It should be noted that, owing to the time-over-threshold method, signal discrimination in NINO is subject to time walk, predominantly for low input charges [72]. However, as one can see from figure 5.3, the effect is negligible in the domain of the photopeak.
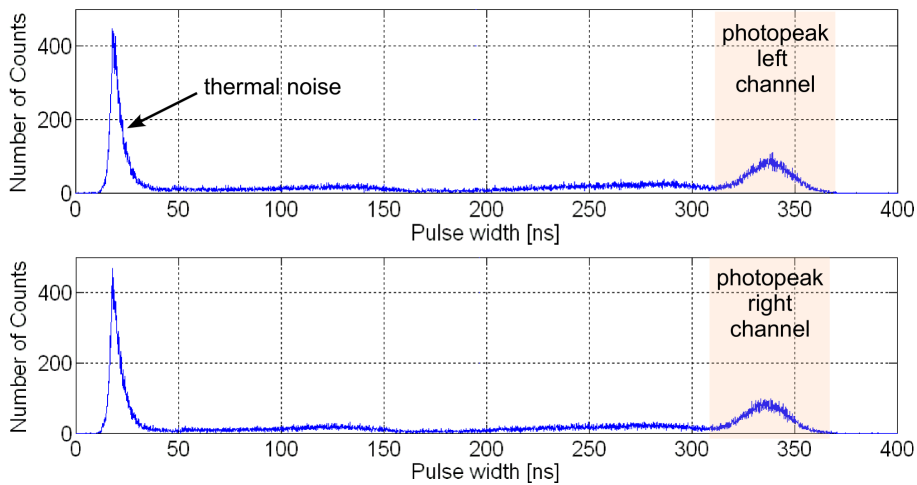

**Figure 5.2.:** Typical energy (pulse width) spectra of two coincident gammas in the timing setup.
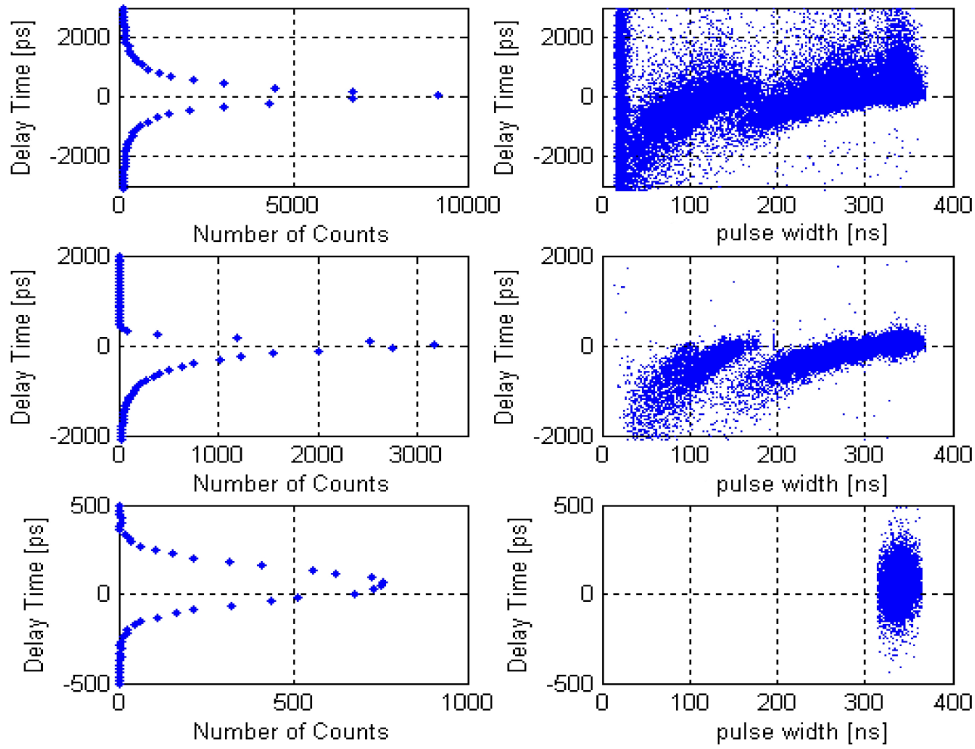
Figure 5.3.: Correlation of pulse width (energy) and time difference for coincident gammas from ^{22}Na. (Top): all events and (middle): single photopeak selection. (Bottom): Double photopeak selection.
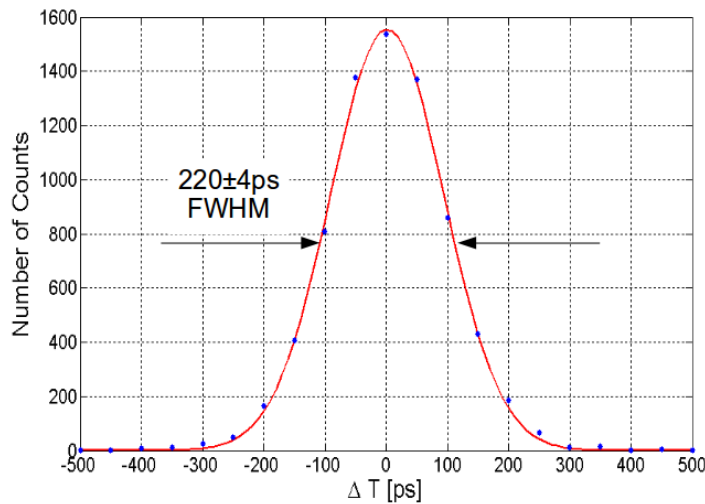

Figure 5.4.: Example of a coincident time distribution of two correlated gammas from ^{22}Na measured with the 50μm SPAD sized SiPM.

We repeatedly measured the coincidence time resolution each time the SiPM bias was changed until a minimum was found. An example of such a refined CTR spectrum is given in figure 5.4. The SiPM bias scan and its effect on coincidence time resolution with two LSO 2x2x10mm^3 crystals

are shown in figures 5.5, 5.6 and 5.7 for the three Hamamatsu SiPMs: S10931-025P, S10931-050P, S10931-100P, respectively. For better readability, the plot entries are slightly displaced horizontally, but measurements at the three different threshold settings were always taken at the same bias values. As expected, the bias scans exhibit a clearly identifiable minimum in coincidence time resolution irrespective of the three different discriminator thresholds. The corresponding voltage, however, does not coincide with the operational voltage that was indicated by the manufacturer separately for each of the three pairs under test. Why this is the case cannot be answered conclusively. However, it should be noticed that the optimum bias overvoltage for best timing must not necessarily be the same as for best energy resolution.
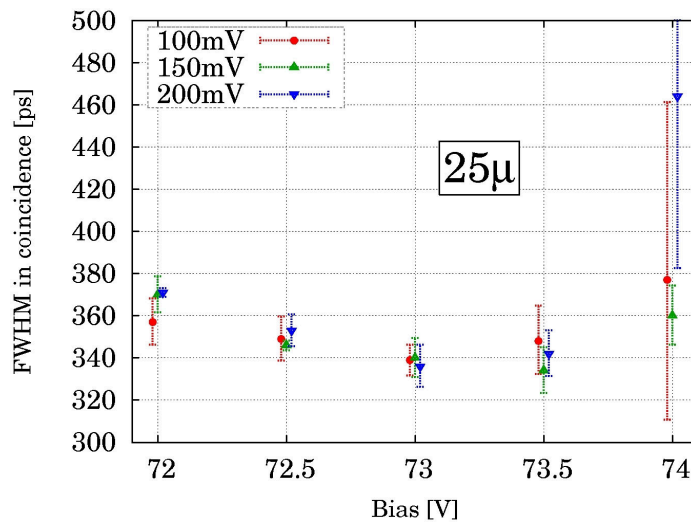

Figure 5.5.: Bias scan of the Hamamatsu S10931-025P MPPC for three NINO threshold settings. Optimum bias point is found at 73 V with 340 ps FWHM and 100-200 mV threshold.
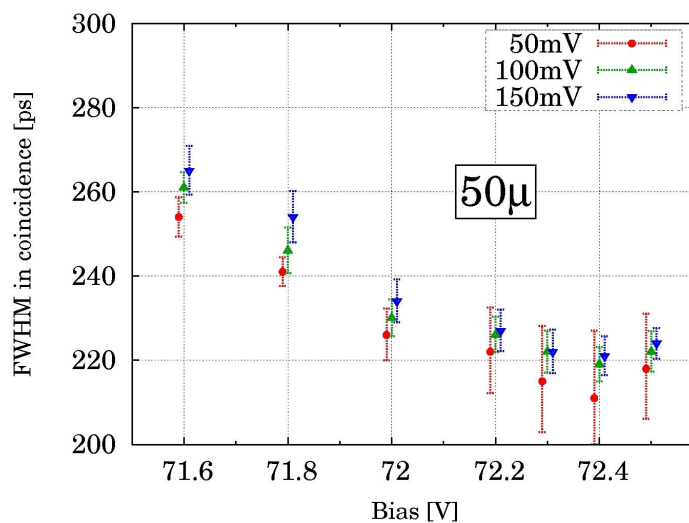

Figure 5.6.: Scan of Hamamatsu S10931-050P for optimum SiPM bias for highest coincidence time resolution. Best value (220 ps FWHM) is achieved at 72.4 V and 100-150 mV NINO threshold setting.
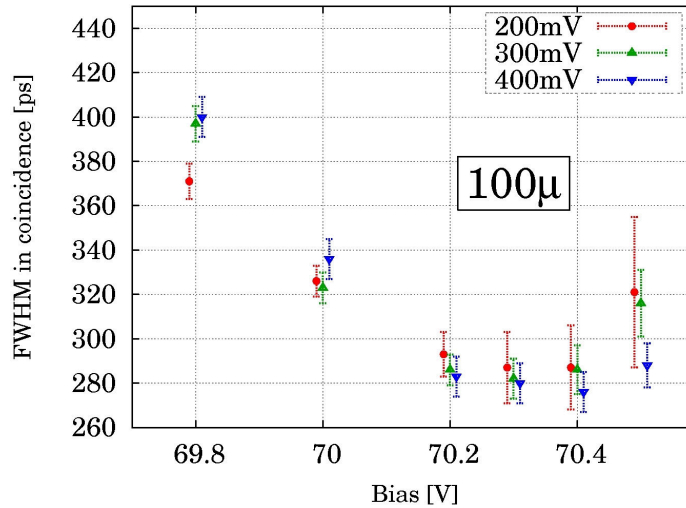
Figure 5.7.: Scan of Hamamatsu S10931-100P for optimum SiPM bias for highest coincidence time resolution. Best value (280 ps FWHM) is achieved at 70.3 V at a NINO threshold setting of 200-400 mV.

The next category of tests comprised a series of coincidence timing measurements at fixed values of SiPM bias, but with varying thresholds of the NINO discriminator. The sum of the NINO threshold scans is given in (a)-(d) of figures 5.8, 5.9 and 5.10 for the three Hamamatsu SiPMs: S10931-025P, S10931-050P, S10931-100P, respectively.

A typical feature of all scans is that, especially for lower SiPM biases, a systematic improvement in time resolution is observed towards lower threshold settings. Larger SiPM bias settings lead to a steady increase in DCR and other excess noise such that the event rate becomes gradually dominated by random noise hits rendering the time resolution increasingly insensitive to the NINO threshold. The effect is more pronounced in the 25μm and 100μm SPAD size SiPMs. The 100μm cell type SiPM, being particularly prone to dark noise, even suffers from a degradation in coincidence time resolution when biased only a tenth of a volt above the optimum bias. From the above test series, we have deduced the best coincidence time resolution for each SiPM type. The results are summarized in table 5.1. Best NINO threshold values consider as well the statistical error of the measured CTR.

Table 5.1.: Summary of optimal settings (best bias) and corresponding time resolution (CTR) for Hamamatsu types: S10931 -025P, -050P and -100C. The voltage V_{OP} denominates the recommended operational SiPM bias stated by the producer Hamamatsu.

| SPAD size (μm)	V_{OP} (V)	Best bias (V)	NINO min. Thr. (mV)	Threshold in equivalent photo-electron amplitude (p.e.)	CTR FWHM (ps)
25	71.47	73.0	$\lesssim 150$	$\lesssim 3$	340±9
50	72.10	72.4	$\lesssim 100$	$\lesssim 1$	220±4
100	70.84	70.3	$\lesssim 300$	$\lesssim 3$	280±9
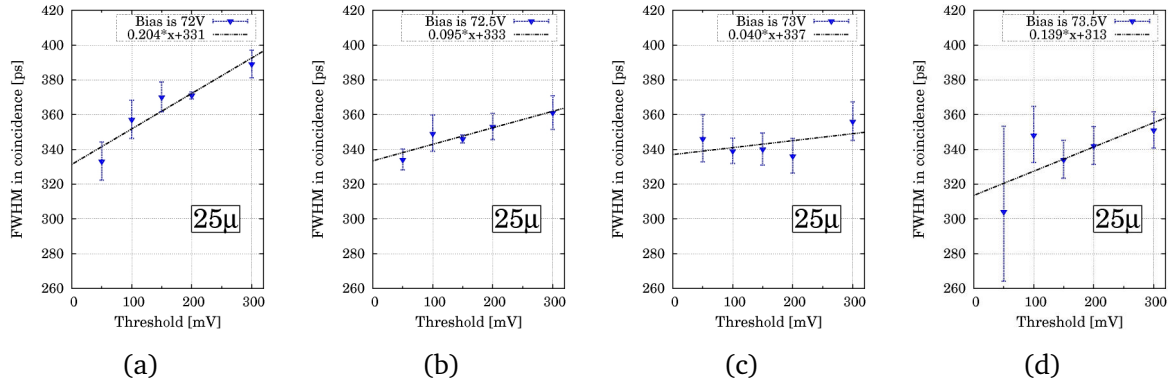
Figure 5.8.: Threshold scan of NINO for four fixed SiPM biases of (a) 72V, (b) 72.5V, (c) 73V, and (d) 73.5V with Hamamatsu S10931-025P MPPC. Best NINO threshold setting considering the CTR measurement error can be deduced to approximate 150mV as can be seen in figure (c).
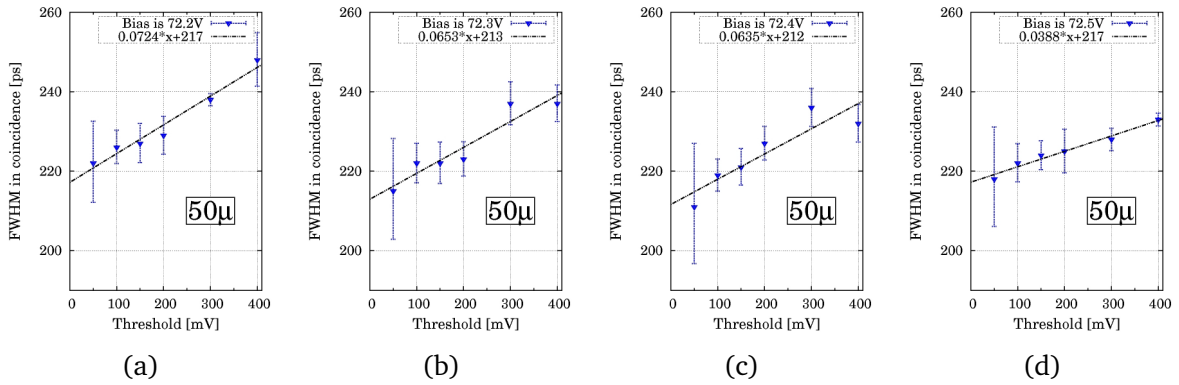

Figure 5.9.: Threshold scan of NINO for four fixed SiPM biases of (a) 72.2V, (b) 72.3V, (c) 72.4V, and (d) 72.5V with Hamamatsu S10931-050P MPPC. Best NINO threshold setting considering the CTR measurement error can be deduced to approximate 100mV as can be seen in figure (c).
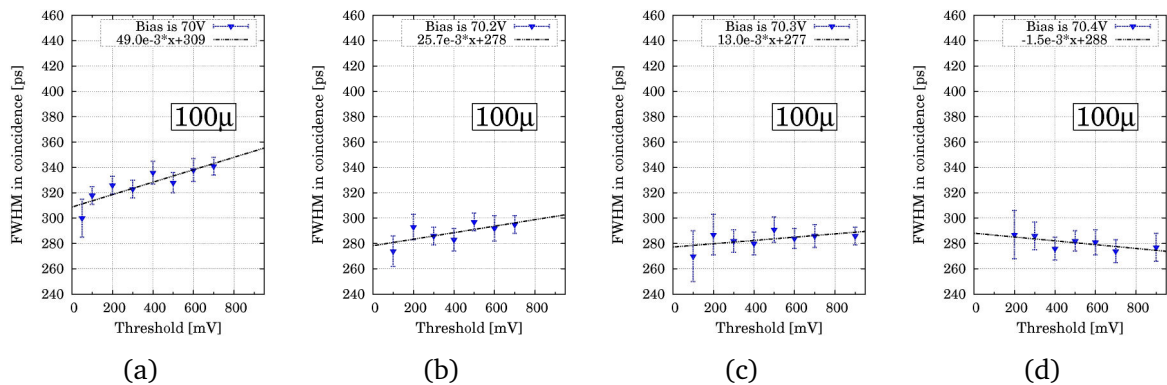

Figure 5.10.: Threshold scan of NINO for four fixed SiPM biases of (a) 70V, (b) 70.2V, (c) 70.3V, and (d) 70.4V with Hamamatsu S10931-100P MPPC. Best NINO threshold setting considering the CTR measurement error can be deduced to approximate 300mV as can be seen in figure (c) and (d).

5.3.2. Charge collection with the three SiPMs at optimum bias voltage

The third category of our test series concerned the investigation of the light output from the LSO crystals subject to irradiation by a number of gamma sources. Figure 5.11 summarizes the collected charge of the used LSO crystals obtained in the three different SiPMs under test. The collected charge, expressed in volt seconds (Vs), is a function of the photoelectron yield and thus of the light output of the crystals. We do not include NINO for this purpose as it is known to be nonlinear in energy response. Using radioactive sources (^{57}Co, ^{60}Co, ^{22}Na, and ^{137}Cs), we covered a wide range of energies from 122keV to 1.33MeV. The charge response curve was then determined for the LSO crystal and the SiPM under test. Despite its smallest SPAD size of only 25μm among the three cell types, this detector already shows noticeable saturation effects at gamma energies above 700 keV. This is attributed to the limited number of SPADs irradiated by a too large number of scintillation photons resulting in double hits [73]. Consequently, these effects are even more pronounced in the other SiPMs with larger and fewer SPADs than the 25μm type. The more important observation, however and in agreement with [74], is that the highest output charge is achieved with the 50μm cell type of Hamamatsu's SiPMs.
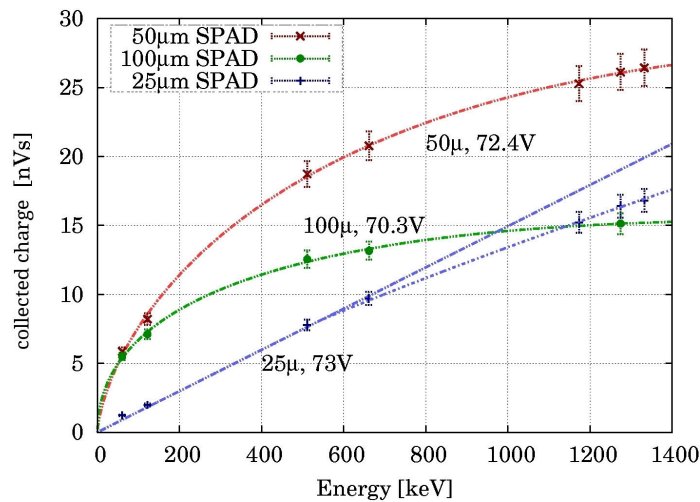

Figure 5.11.: Collected charge for the three different types of SiPMs, Hamamatsu S10931-025P, -050P, and -100P, coupled to a LSO crystal of 2x2x10mm^3 as a function of gamma energy. Linear energy response is seen only for lower gamma energies and only with the Hamamatsu S10931-025P. The variation of the collected charge is as well influenced by the different operational gains of the various SiPM types.

5.3.3. Dark count rates in the three SiPM-types at optimum bias voltage

To gain a better understanding of the achieved time resolution with respect to the dark noise, we measured, in a separate run, the dark count rate (DCR) against the NINO threshold for all three devices (see figure 5.12), always operated at the best bias voltage. Only one arm of the setup was used, and no crystal was coupled to the SiPM. The first plateau in figure 5.12 represents the DCR of the SiPM at a defined bias overvoltage and the consecutive steps at higher NINO threshold values are mainly caused by optical crosstalk in the SiPM (see chapter 3).

All three curves exhibit a clear transition between individual photoelectrons that can be detected with decreasing threshold down to the first photoelectron. The most prominent transitions (steps) are seen in the diagram for the 50-μm SPAD device, with dark noise rates of 1.1 MHz for 1 p.e., 0.25 MHz for 2 p.e., and 0.07 MHz for 3 p.e. The dark counts of the other devices are consistently higher than those of the 50μm sample, with the highest count rates registered for the 100μm SPAD SiPM as was already discussed in chapter 4 (see figure 4.2). Our measurements confirm the trend as stated by the manufacturer that the 50μm device has the lowest dark count rate, followed by the 25μm SPAD size and the 100μm device with the highest dark count rate. From figure 5.12, we find DCR values for the 50μm device of 1.1 MHz, for the 25μm device of about 4.5 MHz and for the 100μm device a value of 6 MHz. Looking at the individual transitions in figure 5.12, we can also deduce the threshold values of detecting the very first photoelectron, which is at 50 mV for the 25μm device, 120 mV for the 50μm SiPM, and 90 mV for the 100μm device. Another important observation is that, e.g. for the 100μm SPAD size, this transition comes at lower values than that for the 50μm type. This is most likely due to the fact that, with regard to optimum timing, the gain of the 100μm is still lower than that for the 50μm type. Because of a rapid noise increase in the 100μm device, it was impossible to operate it at higher bias voltages. This severely limits the operation of the 100μm SPAD-size SiPMs. The same behavior was observed for the laser tests discussed in chapter 4. It appears that only with the 50μm SPAD-size SiPM we were able to trigger on the first photoelectron, whereas the other devices prevented operation at low thresholds due to the rapid increase in dark count events.
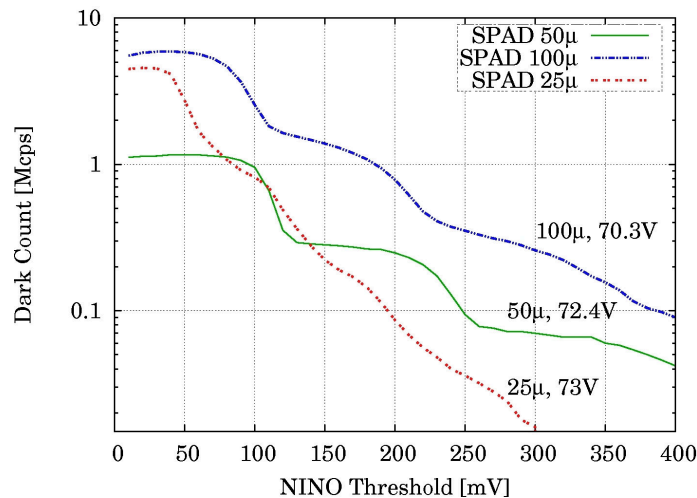

Figure 5.12.: Dark count rate of the three different types of SiPMs, Hamamatsu S10931-025P, -050P, and -100P, as a function of NINO threshold voltage. The transitions from the first photoelectron to the second and the third are clearly seen for all three devices.

5.4. Results for 2x2x5mm^3 LSO:Ce codoped 0.4%Ca crystals

In addition to the previous tests we additionally chose LSO:Ce codoped 0.4%Ca crystals [75] from the producer Agile with dimensions of 2x2x5mm^3 to minimize the influence of time travel jitter

due to different light paths in the crystal, and to be only limited by the scintillation mechanisms. The crystals were wrapped in Teflon and coupled with optical grease (Rhodorsil 47V) to the photodetector. The different SiPMs used are shown in table 4.1. For the 50μm SPAD size type, we in addition compare 2 different batches produced at different times and one selected SiPM with lower DCR (dark count rate).

It is also possible to define a reference detector with this setup. For that purpose we modify one branch of the setup. We glued a 2x2x5mm^2 LSO:Ce:Ca crystal fully wrapped in Teflon on a Hamamatsu 50μm SiPM and always operated it at the same bias and threshold voltage. The reference was determined to have a single time resolution of 107ps FWHM. By measuring a SiPM plus crystal under test versus this reference we obtain CTR^m. Applying the formula $CTR = \sqrt{(CTR^m)^2 - 107^2} * \sqrt{2}$ one can calculate the CTR of the SiPM plus crystal under test.

5.4.1. Optimization of SiPM bias and NINO threshold voltage

We made the same series of systematic measurements changing the SiPM bias and NINO threshold voltage. We always used the same type of scintillator, i.e. LSO:Ce with 0.4% Ca codoping and 2x2x5mm^3 in dimensions, ensuring to investigate only the timing behaviour of the different SiPMs tested. Figures 5.13 to Figure 5.15 show bias and threshold voltage scans made with different SiPMs of 25μm, 50μm and 100μm SPAD size, all from a June 2010 batch. For every case we provide a staircase plot that shows the DCR over NINO threshold. As already mentioned the staircase plots give important information not only of the DCR value but also of the transition threshold between the 1st and 2nd SPADs firing.

All SiPMs have a minimum CTR seen in the bias voltage scans. The PDE of the SiPM is a product of geometrical fill factor, quantum efficiency and the probability of triggering an avalanche. With increasing bias overvoltage the avalanche triggering probability becomes higher, thus increasing the PDE. An increased PDE allows to detect more photons of the scintillation process and thus improves timing by improving statistics. Dark count rate is increasing with bias overvoltage as well. Above a certain bias overvoltage the PDE levels off and dark counts begin to deteriorate the time resolution, giving rise to the observed minimum.
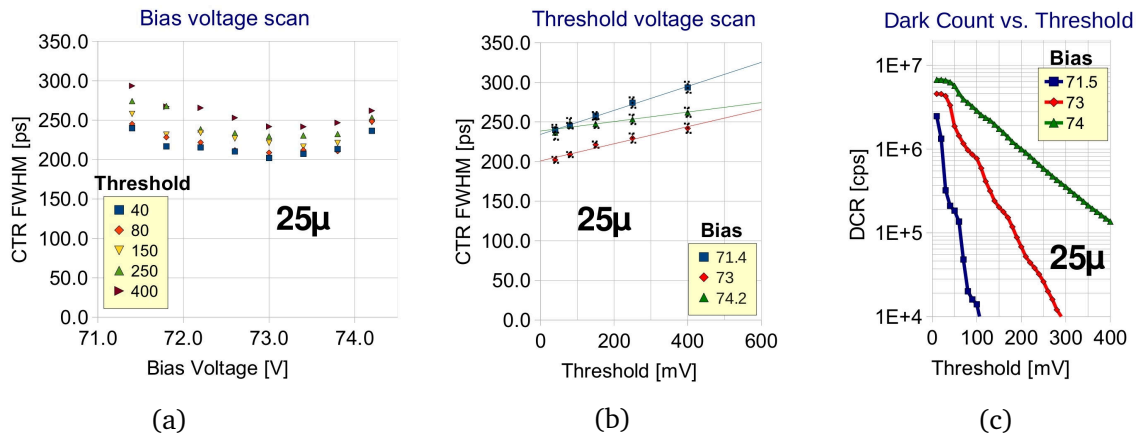

(a) (b) (c)

Figure 5.13.: 25μm SPAD size: (a) bias voltage scan, (b) NINO threshold voltage scan, (c) DCR scan
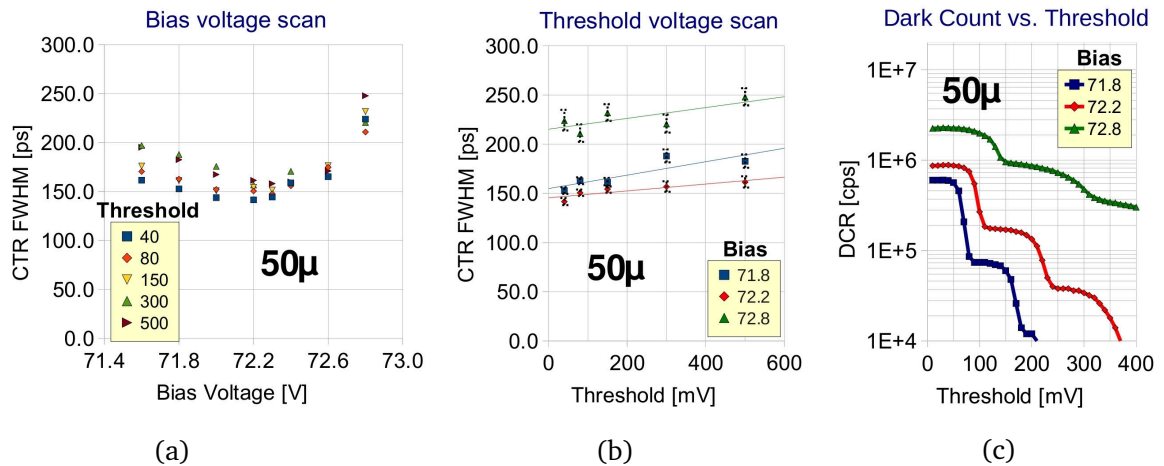
Figure 5.14.: 50µm SPAD size: (a) bias voltage scan, (b) NINO threshold voltage scan, (c) DCR scan
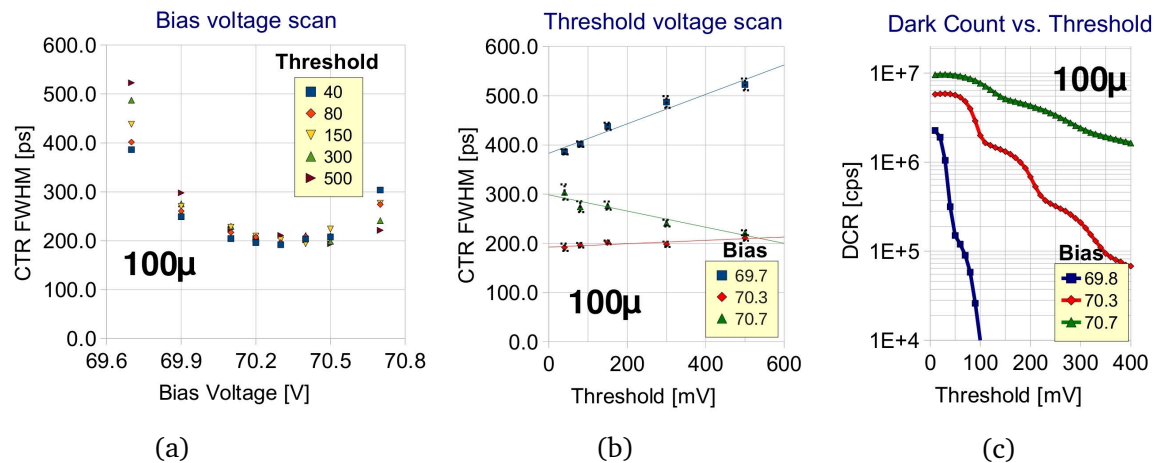

Figure 5.15.: 100µm SPAD size: (a) bias voltage scan, (b) NINO threshold voltage scan, (c) DCR scan

With decreasing NINO threshold the time resolution becomes better as a consequence of triggering at lower ranks of the scintillation's Poisson process. The fact that we do not see an increase in CTR at very low threshold levels implies a very low electronic noise level of NINO. For the 100µm type and high bias voltage values we see an increase in CTR if going to lower threshold values, see figure 5.15,b. This can be explained by the very high DCR of this device adding baseline shifts and subsequently deteriorating the CTR.

Comparing the 3 different types (25µm, 50µm and 100µm) in table 5.2 and figure 5.16 the 50µm gives best results with CTR values of 142ps FWHM at the minimum. Despite its good fill factor of 78.5% the 100µm type is only slightly better than the 25µm type. Obviously the 100µm type cannot be operated at an optimum bias voltage because of its rapid increase in DCR (see figure 4.2). The 25µm type shows a CTR of 202ps FWHM and is thus about a factor $\sqrt{2}$ worse than the 50µm type. This factor could be explained by photon-statistics, because of its fill factor being 30.8% and thus half of the 50µm type.

For the 25µm and 100µm type SiPM the optimal bias voltage values determined in order to find the best CTR are similar to the values obtained when using solely femtosecond laser pulses

as light source (see chapter 4). This observation gives rise to the assumption that in fact the DCR is the driving force in deteriorating the CTR for the 25μm and 100μm type SiPM. However, using laser pulses it is interesting to notice that in chapter 4 for the 50μm SPAD sized SiPM no minimum of the time resolution in dependence of the bias overvoltage can be observed. Looking at figure 4.2 we see that the DCR of the 50μm type SiPM is very low compared to the 25μm and 100μm types. This gives evidence that for the 50μm SPAD sized SiPM and within the used overvoltage range the DCR is not the culprit in deteriorating the coincidence time resolution in the TOF-PET measurements performed in this chapter. Indeed the problem lies in the photopeak selection process. Due to the logarithmic energy encoding performed by NINO the 511keV photopeak events combine with Compton scattered events, subsequently deteriorating the measured CTR. This as well could explain the lower optimal bias voltage value deduced for the 5mm long crystals compared to the 10mm long crystals, as can be noticed by looking at table 5.1 and table 5.2. Because in small crystals the probability of secondary photon escape is higher and thus Compton events gain in frequency as compared to photoelectric absorption. This can worsen the CTR if the photopeak resolution is too low.

Table 5.2.: Minimal CTR achieved for different HAMAMATSU SiPMs with 3x3mm^2 active area coupled to a 2x2x5mm^3 LSO:Ce codoped 0.4% Ca scintillator. Temperature is at 20°C for all measurements.

| Type: S10931	SPAD size (μm^2)	Fill Factor (%)	Break down voltage (V)	NINO threshold (mV)	Bias Voltage (V)	DCR at bias voltage (Mcps)	Best CTR FWHM (ps)
-025P	25x25	30.8	69.2	40	73.0	4.55	202±4
-050P	50x50	61.5	70.5	40	72.2	0.88	142±4
-100P	100x100	78.5	69.3	40	70.3	5.85	192±8
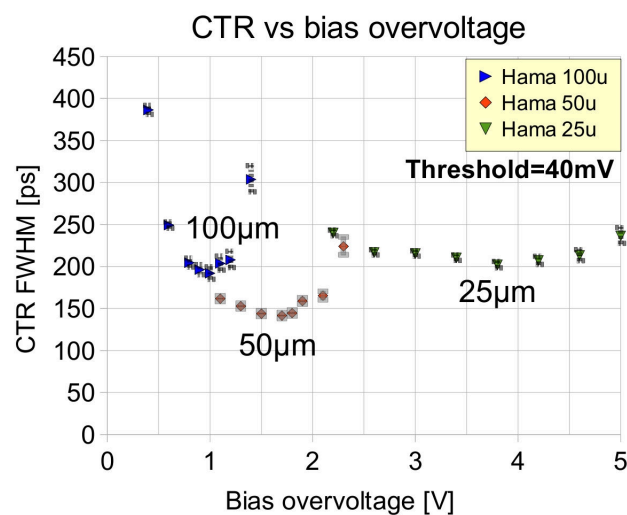
Figure 5.16.: Summary of the three investigated SiPM types. Shown is the bias voltage scan at same NINO threshold of 40mV.

5.4.2. Differences between SiPM production batches

Variation of the timing behaviour between different production batches is an important considera-
tion. We investigated 3 different production batches of the 50μm type received in June 2010, May
2011 and January 2012 (see table 5.3). One special selected device with a lower DCR allowed to
investigate the influence of DCR on the CTR at fixed temperature.

Table 5.3.: Properties of the three different production batches of the 50μm SPAD sized SiPMs with
3x3mm² active area.

Type: S10931	SPAD size (μm²)	Number of Cells	Fill Factor (%)	break down (V)
-050P (received June 2010)	50x50	3'600	61.5	70.5
-050P (received May 2011)	50x50	3'600	61.5	70.9
-050P (impr. DCR, Jan. 2012)	50x50	3'600	61.5	70.6

We observed that the different production batches yielded the same timing behaviour when
coupled to a LSO:Ce codoped 0.4%Ca scintillation crystal with 5mm length (see figure 5.17). In
our setup we did not see any improvement of time resolution despite reducing the DCR by about a
factor 2. This leads to the assumption that for the 50μm type other factors have a higher influence
on time resolution. However it should be noticed that for the 50μm type the DCR is already very
low, even at high overvoltages, suggesting a more refined production process compared to the
25μm and 100μm type.
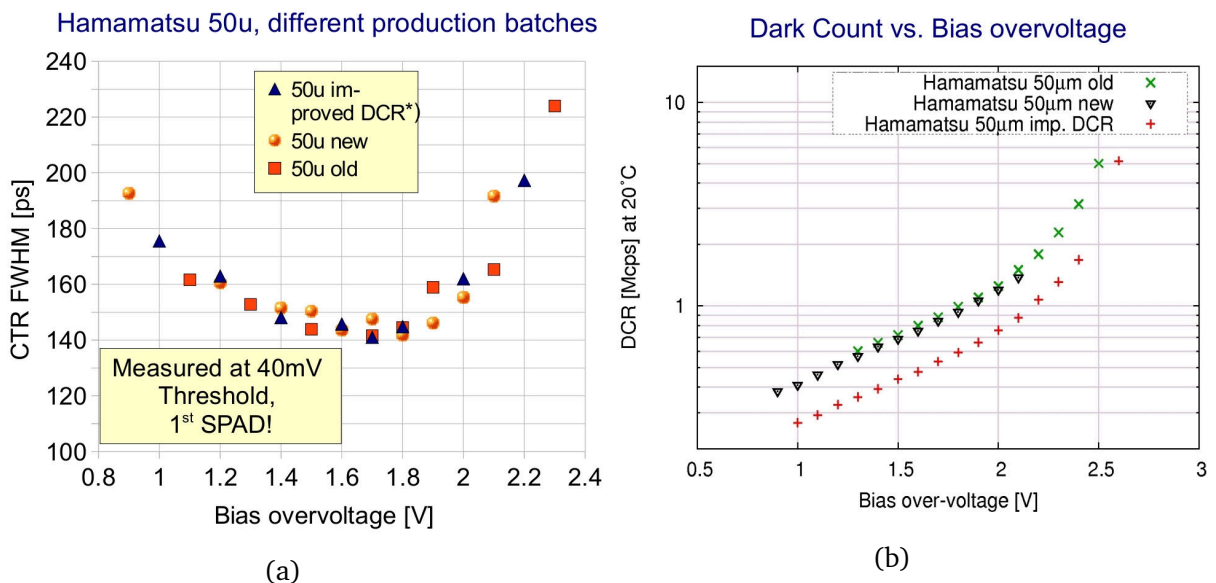
Figure 5.17.: Measurements of three different production batches of the SiPMs: (a) CTR vs. bias overvolt-
age and (b) DCR vs. bias overvoltage

5.5. CTR dependency of crystal cross section and wrapping

In this section the crystal state and wrapping influence are studied in terms of light yield and coincidence time resolution. Small section crystals, also called pixels, are favorable to provide the optimum spatial resolution for a PET system. However, those high aspect ratio crystals show a lower light output because of a higher number of reflections, i.e. on the lateral faces, which the scintillation light has to undergo until reaching the photodetector. To study the influence on the time resolution we have tested LYSO crystals of same length (10mm) but of two different sections, i.e. 2x2mm^2 and 0.75x0.75mm^2, from three different manufacturers. Table 5.4 shows the results of the measurements. We observe that despite a significant drop (∼30%) in light output the CTR is less impaired by the smaller crystal section. The corresponding increases in CTR value range from 4% (CPI crystal) to 7% (Proteus crystal) and 8% (SIPAT crystal). For the time being we assume that light which is being reflected by internal total reflection shows less attenuation per reflection than compared to light being reflected by the Teflon. If this assumption is true, then scintillation light being emitted towards the photodetector or the opposite direction, undergoing only total reflection, will be relatively less attenuated as compared to scintillation light being emitted towards the lateral faces and thus being reflected by the Teflon wrapping. Another assumption necessary to explain this behaviour is that highly delayed scintillation light, i.e. light emitted towards the lateral faces, will not influence the CTR values noticeable. If this two assumptions are fullfield then only direct and back reflected light will mainly determine the CTR and consequently, in a first order approximation, the crystal cross section will not play any role in the achievable time resolution.

Table 5.4.: Light output measured with a Photonis XP2020Q PMT (setup will be discussed in chapter 7.3.7) and CTR in crystals of different cross sections. CTR and light output measurement errors are in the range of 5%. Values were published in [10].

| Crystal | 2x2x10mm^3 | | 0.75x0.75x10mm^3 | |
	light output [kph/MeV]	CTR [ps]	light output [kph/MeV]	CTR [ps]
LYSO (CPI)	17.4	184	13.7	192
LYSO (Proteus)	18.0	175	13.9	188
LYSO (SIPAT)	19.0	206	12.0	223

In the foregoing tests the crystals were conditioned to what is known to give the best results in terms of LY and CTR. This is commonly achieved with "full" wrapping of the scintillator with a reflector, preferably with Teflon. To gain a more detailed insight into the effects of reflective material, light losses and reflections at the different crystal faces, i.e. lateral and top, tests with different reflectors and wrapping methods were performed. In table 5.5 different CTR and light output measurements of three different crystals with four different wrapping configurations are summarized. We wrapped the crystals (a) fully in Teflon, (b) laterally in Teflon and left the top

face free, (c) left the lateral face free and wrapped only the top face in Teflon and (b) did not wrap the crystal at all. As can be seen in table 5.5 the Teflon wrapped configuration gives the highest measured light output normalized to 100% as compared to the lowest for the unwrapped case with 46%. Interestingly the two partially wrapped configurations give almost the same light output of 77%. Nevertheless the configuration where the top face was wrapped with Teflon and the lateral face left unwrapped gives a much better CTR value as compared to the top: none, lateral: Teflon case. This we explain with the same arguments as for the high aspect ratio crystals: highly delayed scintillation light, coming from reflections of the lateral faces, cannot contribute to improve the time resolution.

Table 5.5.: Measured light output and coincidence time resolution for four wrapping scenarios. Light output is referenced and related to the light output as achieved with Teflon wrapping on both the lateral face and top faces (100%). All crystals are 2x2x10mm^3. CTR measurement error is in the range of 5%. Values were published in [10].

Wrapping	Relative light output [%]	CTR FWHM [ps]		
		LSO:Ce:Ca	LSO CTI	LSO PML
top: Teflon; lateral: Teflon	100	170	190	206
top: Teflon; lateral: none	76	177	207	224
top: none; lateral: Teflon	77	195	224	237
top: none; lateral: none	46	252	278	309

In table 5.6 we summarize results in terms of light output and coincidence time resolution for different reflector materials.

Table 5.6.: Measurement of light output and CTR for four different reflectors. CTR corrected for the light output loss is depicted as well. CTR and light output measurement errors are in the range of 5%. Values were published in [10].

Reflector Material	Reflectance [%]	Relative light output [%]	CTR FWHM [ps]	CTR corrected [ps]
Teflon	98 [76]	100	206	$206 * \sqrt{(100/100)} = 206$
ESR Vikuiti	98 [77]	100	209	$209 * \sqrt{(100/100)} = 209$
Al-Mylar	88 [78]	79	230	$230 * \sqrt{(79/100)} = 204$
none	0	46	309	$309 * \sqrt{(46/100)} = 210$

We see a dependency of the light output and CTR on the reflectivity of the material. If the measured CTR is corrected for the light output loss by multiplying with the square root of the loss (see table 5.6, 5th column) we are able to describe the CTR dependence only by photon statistics. It is important to notice that in these tests summarized in table 5.6 we do not change the light propagation modes in the crystal, as the reflectivity of the wrapping is changed for the whole crystal. Thus the CTR is dependent on the light output as predicted by pure Poisson photon

statistics. The CTR measurements summarized in table 5.5 do not show such a simple dependence on the light output as we do change the propagation modes by wrapping the crystals partially different.

5.6. Summary and conclusion

The aim of this chapter was to investigate to what extent time resolution is influenced by instrumental changes in photodetectors, such as commercial silicon photomultipliers, utilizing LSO based scintillating crystals for that purpose.

There are several important factors influencing the time resolution of TOF-PET detection systems, for example, the scintillation process itself and the light transport that is strongly affected by the size and geometry of the crystal. However strong in their effect, these factors were not changed in the tests investigating the instrumental parameters as we always used the same crystals when comparing different types of SiPM with different SPAD sizes. Another known and perhaps the most prominent shortcoming in achieving highest possible time resolution is the Poissonian character of the distribution of photons arriving at the photo detector. In order to at least partially overcome the limitations given by photostatistics the photodetector ought to have the highest possible PDE. Obviously, apart from inherent geometrical inefficiencies of the SiPM (fill factor), another dominant effect on the PDE is inadequate device gain to initiate a Geiger avalanche, whereas the intrinsic quantum efficiency of the silicon substrate can be higher 90% [79]. Also, the dead time of an individual pixel following the avalanche quenching has a detrimental influence on the PDE. These factors then limit the SiPM's PDE to values typically below 35% [80]. Focusing on the first two effects, one would naively expect that higher fill factors implicitly lead to higher PDE and hence to higher time resolution. However, aside from increasing saturation effects due to double hits, larger SPAD (microcell) sizes also imply a growing probability to initiate spontaneous Geiger discharges or dark counts that severely degrade the signal to noise ratio. As a consequence, one is obliged to run at higher detection thresholds. This means that an improvement of the PDE, or Geiger efficiency, with increasing gain is more easily offset in the larger SPAD sizes by a rapid rise in dark noise.

Other gain dependent side effect is photon induced (optical) crosstalk and after pulsing, which can artificially boost the PDE by as much as 20% [81]. Hamamatsu devices are prone to optical crosstalk since their SPAD architecture, in favor of a higher fill factor, provides no optical trenches/barriers between pixels to counteract this effect. As our measurements indicate, it appears that the 50μm SPAD size SiPM can be operated at relatively high bias or overvoltage, which results in a high PDE that seems not to be compromised by excessive dark noise. On the other hand, the smaller 25μm SPAD size SiPM must run at higher bias in order to achieve adequate PDE, however, at the expense of a much higher dark count rate at that bias. The 100μm size SiPM, despite its favorable fill factor also suffers from an excessive dark noise rate (and early saturation), which are inherent in the large area of the microcell itself.

Therefore, both the 25μm and 100μm devices, in contrast to the 50μm SiPM, are affected by there excessive dark count rates causing baseline shifts, provoking additional time jitter. Figure

5.12 together with the outcome of the time resolution runs suggests that the optimum threshold is where the dark count rate lies below 2 MHz. If this is the case, then only the 50μm device is capable of achieving best time resolutions not affected by its dark noise.

Changes in bias voltage have a large impact on time resolution because of a substantial change in PDE (see figure 5.6). The threshold scans were made for four bias voltages around and including the optimum value (highest CTR, minimum of curve) that was found afore in the bias voltage scans. It is noteworthy that the 25μm SiPM exhibits a rather shallow minimum in this respect. In other words, a bias change of 1 V around the minimum leads to a degradation of the CTR of only 20 ps on either side. The other devices, both providing better achievable CTRs than the 25μm device, show a more pronounced minimum, where a smaller bias voltage change leads to the same deterioration of the CTR.

From the threshold scans, we learn that, common to all three SiPM types, pushing the bias voltage to higher values also moves the threshold settings toward higher values in order to achieve best timing. This is expressed by a decreasing slope with growing bias in the linear fits applied to the CTR data. In other words, beyond a certain (optimum) bias, the coincidence time resolution improves only very little with lower threshold settings (within the chosen range). In fact, the 100μm cell type even regresses in time resolution as the threshold approaches the dark noise floor. We attribute this effect to the abundance of dark noise hits obscuring the arrival of the first photoelectrons and additionally provoking huge base line shifts at the input of our electronics (NINO). On the other hand, for the 50μm device, we do observe a constant improvement in coincidence time resolution as a function of threshold voltage, leveling off at 220ps FWHM for the 2x2x10mm^3 and at 142ps FWHM for the 2x2x5mm^3 crystal.

In summary, the 50μm cell type, despite its inferior fill factor compared to its 100μm neighbor, provides the highest CTR and PDE among the three devices tested. This is linked to the lowest DCR found in this cell type hinting at a "higher device maturity" [74] caused by an improving production process. The 100μm neighbor with its higher fill factor we were not able to operate at optimum bias voltages, because of its rapid increase in DCR.

The results obtained substantiate the hypothesis of photo statistics being the dominant cause for limiting the time resolution in a TOF-PET system. Nevertheless as shown in section 5.5 some light propagation modes seem to be beneficial in terms of timing. Direct or back-reflected modes which couple fast into the photodetector are more important than highly delayed scintillation light, e.g. light being reflected on the lateral faces of the crystal. Although this direct modes are important, we always measured a deterioration in time resolution with decreasing light output. We conclude that higher time resolutions can be obtained, if one resorts to brighter crystals, sophisticated light extraction techniques taking the nature of propagation modes into account, and more efficient photodetectors.

For the 25μm and 100μm SPAD sized SiPMs the optimal bias overvoltage values minimizing the CTR values in a TOF-PET like system are comparable to the optimal values deduced if the photodetectors are subject to irradiation with femtosecond laser pulses only (see chapter 4). This outcome gives evidence that for these two SPAD sized SiPM types the DCR is indeed the driving force in the CTR deterioration. This statement is further supported by the rapid increase in DCR

for the 25μm and 100μm. On the other side this correlation between laser and CTR measurements was not observed for the 50μm type SiPM. For this device the DCR is rather low within the applied overvoltages as can be seen in figure 4.2. As a logical consequence we suspect the photopeak selection due to the NINO pulse width energy encoding as the reason for the observed discrepancy. In the following chapter a detailed discussion about this issue will be given.

Chapter 6

TOF-PET towards 100ps resolution with L(Y)SO

6.1. Introduction

In the preceding chapter 5 it was shown that the NINO time-over-threshold energy encoding might be the main reason of deteriorating the CTR for the 50μm type SiPM, if operated at higher bias overvoltages. In this chapter we will discuss in further details the NINO pulse width energy encoding and describe quantitatively certain drawbacks of this method. We will present a newly developed electronics board for SiPM readout which combines the advantages of the NINO leading edge discrimination for the time information and analog readout for the energy information. In the last part of this chapter we will characterize the new developed NINO board and present the refined CTR measurement values following the measurement methods as described in chapter 5. Parts of the content of this chapter were published in [37].

6.2. New electronics for SiPM readout

Despite the advantages of NINO being able to encode time and energy in one single pulse the method has an inherent drawback. Let us consider the SiPM pulse consisting of a single exponential with decay constant τ and amplitude A,

$$y(t) = A \cdot \exp\left(-\frac{t}{\tau}\right) + V_{noise}. \qquad (6.2.1)$$

The term V_{noise} represents the electronic noise as well as noise generated by SiPM dark count events. It is modeled as a Gaussian distribution around the baseline. The NINO output pulse width (PW) as a function of the threshold voltage V_{th} can be calculated by setting equation 6.2.1 equal to V_{th}: $V_{th} = A \cdot exp(-PW/\tau) + V_{noise}$. Figure 3.33 in chapter 3 clarifies this equality. Considering that the amplitude of the SiPM signal is proportional to the gain G, i.e. $A = a \cdot G$, the pulse width can be expressed by equation 6.2.2.

$$PW = \tau \cdot \ln\left(\frac{a}{V_{th} - V_{noise}}\right) + \tau \cdot \ln\left(\frac{G}{V_{th} - V_{noise}}\right).\tag{6.2.2}$$

The first term in equation 6.2.2 is related to the unit gain output a of the SiPM signal. It logarithmically encodes the energy resolution through the signal a and fluctuations of V_{noise}. The gain of a SiPM can be increased by operating the device at higher overvoltages. This however also increases the DCR and thus leads to a higher noise component (V_{noise}). If a linear amplifier were used, the additional noise would be compensated by an increase in SiPM pulse height. On the other hand, equation 6.2.2 shows that in the logarithmic encoding used in NINO, an increase of the gain only leads to an additional constant factor in the pulse width (right term of 6.2.2). Since the fluctuation of V_{noise} also increases with higher overvoltage and is not offset by an increase in gain (left term of formula 6.2.2), the energy resolution degrades. This behavior represents a disadvantage in the photopeak selection process when using the logarithmic energy measurement as compared to a linear one. This statement is supported by the findings in chapter 5 and in [71]. There we find an optimum in CTR around 1.7V overvoltage for the Hamamatsu $50\mu m$ MPPC. At higher bias overvoltages the CTR value degrades from 140ps (at 1.7V overvoltage) to 200ps (at 2.2V overvoltage). This degradation is almost entirely caused by a poor photopeak selection from the NINO pulse width energy measurement.

To further illustrate the time-over-threshold (TOT) encoding we show in figures 6.1 and 6.2 the NINO pulse width histogram and analog SiPM signal amplitude histogram when exciting the scintillator with ^{22}Na. We see that the logarithmic encoding realized in the NINO pulse width leads to an energy resolution degradation making it impossible to clearly separate the 511keV from Compton events, especially for higher bias overvoltages. On the other hand the analog SiPM pulse height amplitude histogram still allows this separation, as can be seen in figure 6.2. As already discussed this behavior leads to the observed CTR deterioration for the Hamamatsu $50\mu m$ type SiPM shown in figure 5.6 and 5.14 in chapter 5. At the applied overvoltages the CTR deterioration cannot be caused by an increase in DCR and crosstalk as for the $50\mu m$ type SiPM these two quantities are still rather low. Another evidence supporting the photopeak selection as the cause for the CTR deterioration with increasing bias overvoltage was discussed in chapter 4. In figure 4.9 and figure 4.12 we observe no minimum in the measured time resolution versus the applied overvoltage if using femtosecond laser pulses.

As discussed the logarithmic encoding of the energy spectrum has inherently a drawback as compared to a linear one. This is especially true if the noise floor is relatively high as it is the case in SiPMs due to the high DCR. By accordingly adjusting the filter between the SiPM and NINO this problem can in principle be mitigated, which to a certain extend was done for the measurements presented in chapter 5. Thus it would be still possible to use the time-over-threshold method and therefore encode energy and time into one pulse. However for reasons like a higher degree of flexibility and to further exploit the full capabilities of the SiPM a new electronics board has been developed using NINO as a low noise high speed leading edge discriminator amplifier delivering the time information and an analog amplifier to access the SiPM pulse directly and thus give the energy information. In the subsequent sections the simplified schematics of the electronics as well

as the printed circuit board is shown.
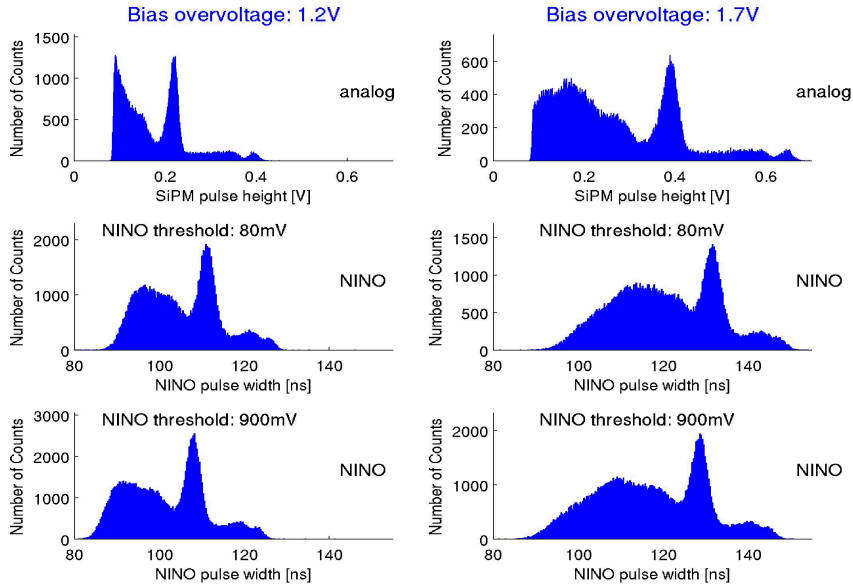
Figure 6.1.: NINO pulse width and analog SiPM pulse height histogram when coupling the SiPM to a LSO type crystal. The 511keV photopeak resolution of the NINO pulse with histogram is worse as compared to the analog pulse height histogram. Measurements are performed at 1.2V and 1.7V SiPM overvoltages. The NINO threshold voltage was set to 80mV and 900mV.
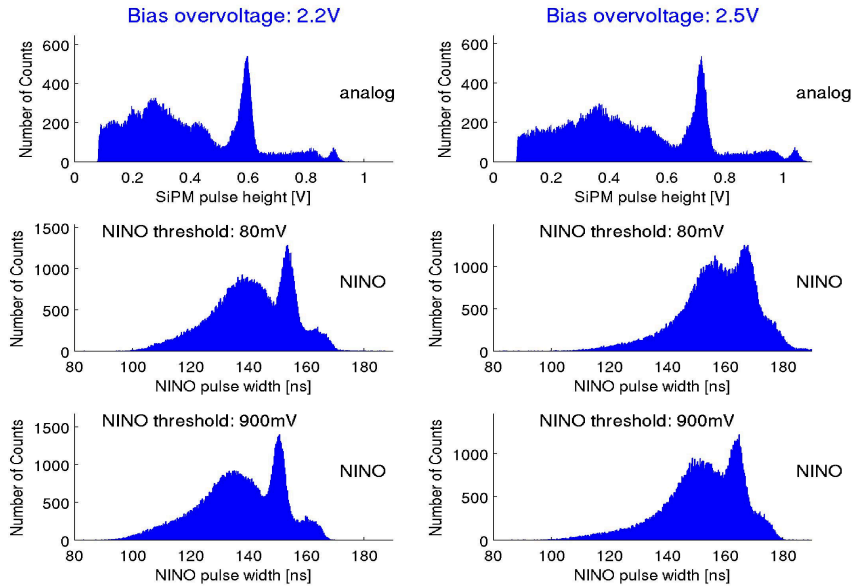

Figure 6.2.: NINO pulse width and analog SiPM pulse height histogram. The time-over-threshold energy resolution degrades drastically with increasing SiPM overvoltage. Measurements are performed at 2.2V and 2.5V SiPM overvoltages. The NINO threshold voltage was set to 80mV and 900mV.

6.2.1. Schematics

In figure 6.3 we show the simplified schematics of the newly developed electronics as used for the subsequent measurements. The full schematics can be found in the appendix A in figure A.1 - figure A.3. As input filter to NINO a 1nF capacitor was chosen as can be seen in figure 6.3. The voltage amplifier has a high resistive input impedance to avoid additional noise at the NINO input.
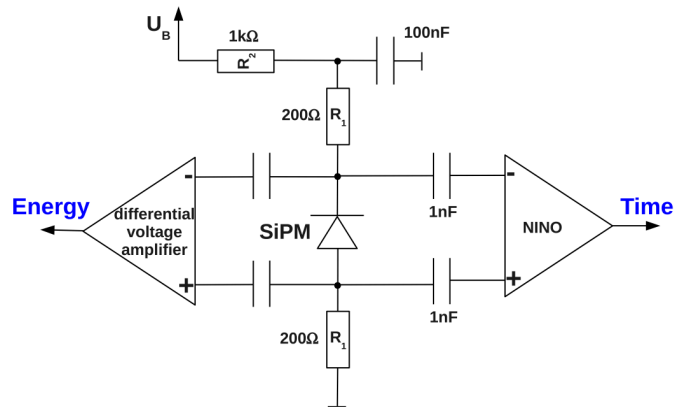
Figure 6.3.: Circuit diagram of the SiPM readout electronics.

6.2.2. Printed circuit board

In figure 6.4 a picture of the assembled printed circuit board can be seen.
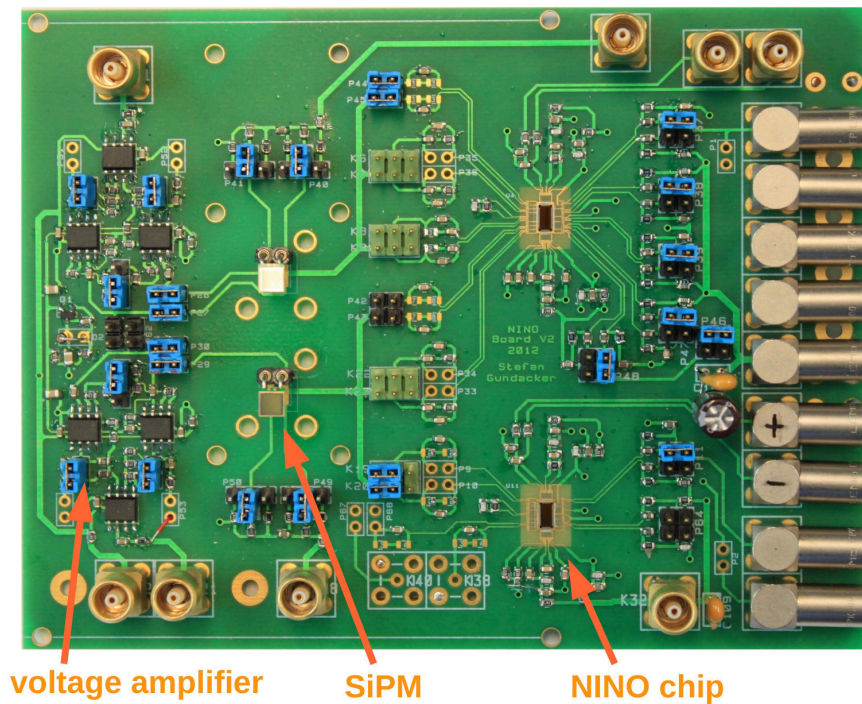
Figure 6.4.: Printed circuit board of the newly developed electronics for SiPM readout.

The board offers the possibility to readout two SiPMs independently. The CTR can thus be measured with a single board that hosts two independent signal chains for a SiPM, NINO and a voltage amplifier. Additionally it is possible to mount a SiPM on each extremities of a crystal in order to study depth of interaction corrections. One SiPM signal can as well be routed into two NINO chips in order to apply two different thresholds on the signal. Each NINO output can be connected differentially to the oscilloscope. The board was designed to have highest flexibility in treating and studying the SiPM output which can be seen in the array of jumpers allowing to guide the signals.

The NINO chip is mounted via wire bond on the PCB. It is as well possible to surface mount the SiPM on a supporting PCB which can be fixed to the PCB via screws as shown in figure 6.4. Holes around the SiPM are intended to mount a crystal holder which allows to position the scintillating crystal at a fixed position on the SiPM. The copper and track vias of the PCB can be seen in more detail in the appendix A.

6.2.3. Characterization with SiPMs

The NINO and amplifier output signals of SiPM dark count events are shown in figure 6.5. Figure 6.5(a) shows the left arm of the coincidence setup. A cascade of afterpulse events can be seen at the analog amplifier output, together with the corresponding NINO signals. In figure 6.5(b) the right branch shows a typical dark count event at 0ns and a crosstalk event at 1000ns. The long fall time observed for the amplifier signals is generated by the 200Ω bias resistors. Due to the coupling capacitor between the SiPM and NINO, leading to a differential input impedance of 40Ω [63], this long fall time is not observed by NINO. It is only sensitive to signal changes in the nanosecond range. This behavior is intended as it corrects baseline shifts.
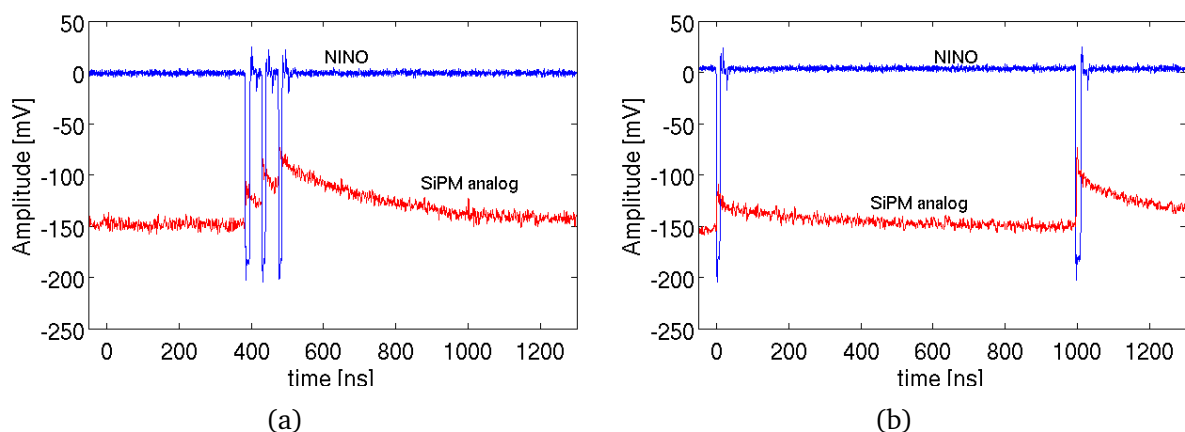
Figure 6.5.: Analog SiPM pulse and response of NINO operating at 60mV threshold coupled to the SiPM operated at 2V overvoltage. (a) left arm and (b) right arm of the coincidence setup

We measured the NINO output pulse slew rate to $dV/dt = 179\,V/\mu s$. Together with the RMS noise floor of the oscilloscope of $\sigma_{noise} = 1.45\,mV$ we can calculate the influence of our acquisition system on the time resolution according to formula 6.2.3. The factor $2 * \sqrt{2 * ln(2)} * \sqrt{2} = 3.33$

converts to coincidence time resolution FWHM.

$$CTR_{acquisition} = \frac{\sigma_{noise}}{dV/dt} * 3.33 = 27ps\,(FWHM) \tag{6.2.3}$$

Table 6.1 summarizes the parameters for the SiPMs from Hamamatsu on this experimental board, including the measured breakdown voltage at a temperature of 20°C.

Table 6.1.: Parameters of the two MPPCs (SiPMs) from the producer Hamamatsu.

branch of setup	MPPC type	active area	number of cells	breakdown voltage @ 20°C	charge gain @ 2V overvoltage
left	S10931-050P	3x3mm^2	3600	70.4V	$1.4 \cdot 10^6$
right	S10931-050P	3x3mm^2	3600	70.5V	$1.4 \cdot 10^6$

6.3. NINO threshold calibration

The calibration of the NINO threshold is necessary to compare measurements with simulations. It relates the NINO threshold value to the SiPM output amplitude, expressed in multiples of single SPAD pulse height. These quantities can be derived from so called staircase plots, produced by measuring the number of triggers in counts per second versus the NINO threshold for different SiPM overvoltages (see figure 6.6). The measurements were performed in a temperature stabilized dark box at a temperature of $20°C$. No crystal was attached to the SiPM.
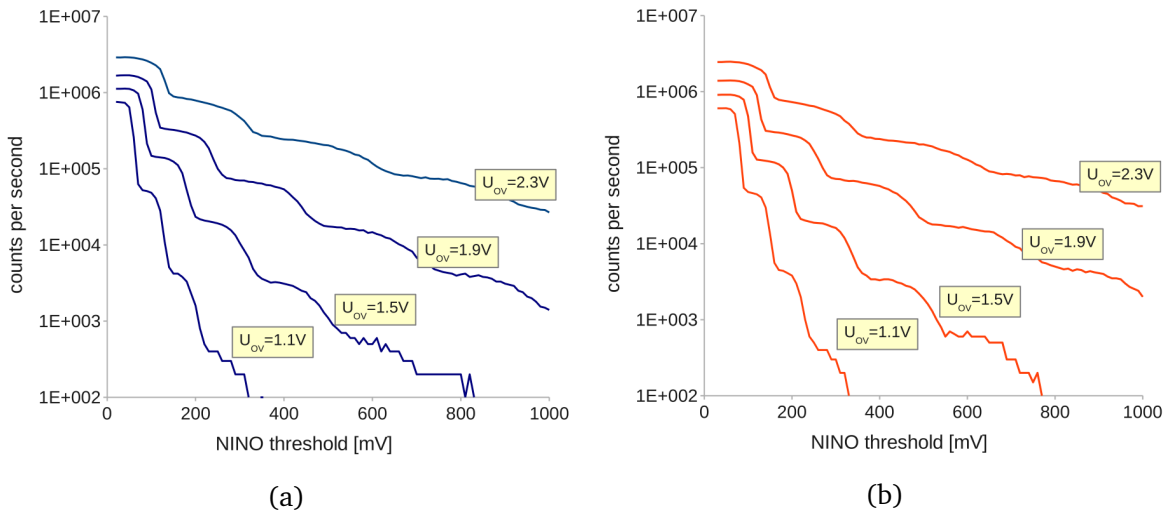
Figure 6.6.: Staircase plots for (a) the left and (b) right arms of the coincidence setup versus NINO threshold for different overvoltages. Measurements at $20°C$.

The first plateau in figure 6.6 shows the DCR and the subsequent plateaus are mainly caused by optical crosstalk in the SiPM. With rising overvoltage the plateau lengths are increasing because

the SiPM is operating at higher gain and thus the threshold in terms of microcell amplitude height is increasing as well. It can be seen in figure 6.6 that for higher overvoltage values the optical crosstalk probability is increased. This is caused by an increasing number of generated secondary photons in the avalanche. The probability of secondary photon production is dependent on the gain and thus on the applied overvoltage (see chapter 3).

Each step in the staircase plot represents the single SPAD amplitude incremented by an integer number [44]. NINO shows a non-linear behavior between its threshold and the equivalent cell amplitude N (see figure 6.7). Superimposed on the expected linear behavior one observes an exponential component in the threshold-to-amplitude response. To account for this non-linearity we calibrate the NINO threshold in terms of the equivalent cell (SPAD) amplitude N with equations 6.3.1-6.3.4, by fitting exponentials to the measurements (see figure 6.7).

$$U_{OV} = 1.1V : \quad Threshold = 61.5 * N * \exp\left[\frac{N}{15.6}\right] \tag{6.3.1}$$

$$U_{OV} = 1.5V : \quad Threshold = 73.6 * N * \exp\left[\frac{N}{7.6}\right] \tag{6.3.2}$$

$$U_{OV} = 1.9V : \quad Threshold = 82.7 * N * \exp\left[\frac{N}{4.9}\right] \tag{6.3.3}$$

$$U_{OV} = 2.3V : \quad Threshold = 113.3 * N * \exp\left[\frac{N}{5.4}\right] \tag{6.3.4}$$
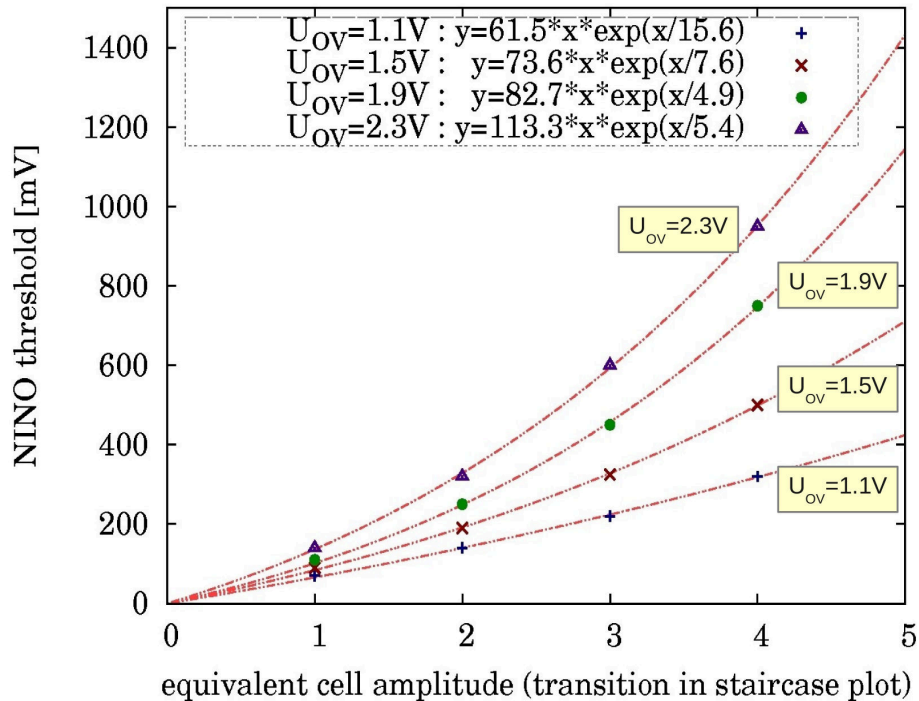
Figure 6.7.: NINO threshold calibration from the shown staircase plots. In addition to the expected linear term we observe an exponential component, that is due to non-linearities of NINO.

6.4. Experimental Methods

In figure 6.8 the schematics of the CTR setup is shown and in figure 6.9 we depict a picture of the printed circuit boards as mounted in the bench used for the timing measurements.
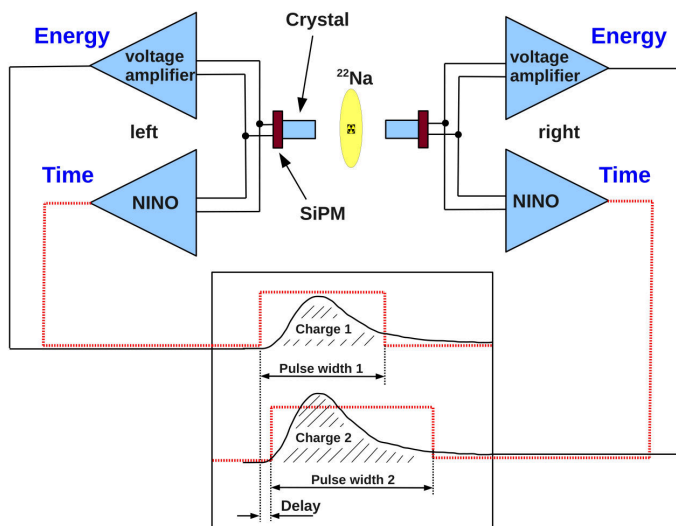
Figure 6.8.: Schematic of the coincidence time measurement setup. In the tests we use NINO for the precise time stamp and a voltage amplifier to determine the output charge and thus the energy.
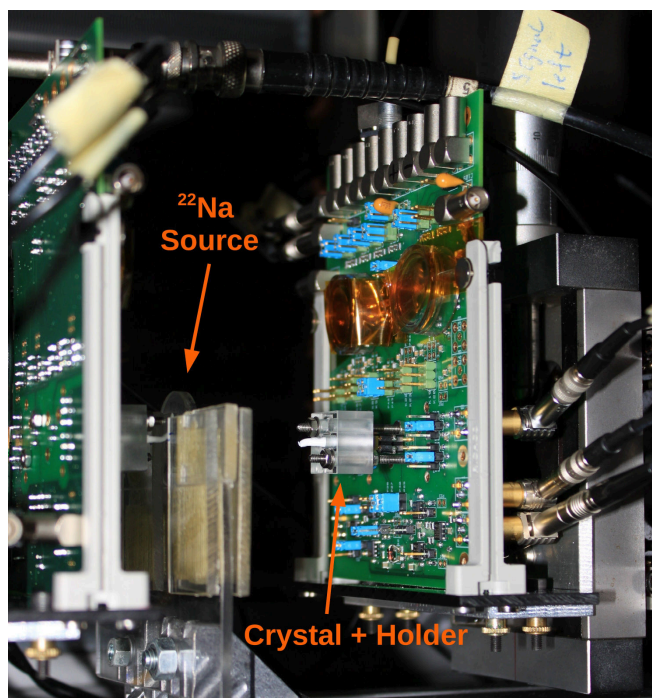

Figure 6.9.: Picture of the newly developed printed circuit board mounted in the CTR setup as used for the timing measurements.

As already discussed in chapter 5 we use a time coincidence setup to test the time resolution of the system. The modified setup can be seen in figure 6.8. We use NINO for the precise time stamp and a voltage amplifier to determine the output charge and thus the energy. In contrary to the measurements in chapter 5 we use in this chapter the output of the linear voltage amplifier to determine the energy information.

6.5. Measured CTR with LSO:Ce codoped 0.4% Ca and 511 keV gammas

The experimental setup for the CTR measurements is shown in figure 6.9. The entire setup is housed in a thermally insulated dark box. The temperature is held stable at 20±0.1°C. This avoids temperature induced gain fluctuations during a single CTR measurement run. The data acquisition is performed with a high sampling rate oscilloscope, LeCroy DDA 735Zi (40GS/s) similar to the method described in chapter 5. The dual pulse heights from the voltage amplifier outputs (operating at an amplification of 1.6) of each branch of the coincidence setup, plus their NINO leading edge delay, were recorded on disk. In the offline data analysis, we histogram the mutual time delay accepting only events from the two photopeaks. In figure 6.10 we show the CTR obtained with the old electronics and 2x2x5mm^3 LSO:Ce codoped 0.4%Ca crystals as already discussed in section 5.4. With the old electronics using the NINO pulse width energy encoding the best CTR value measured was 142±4ps FWHM. The new developed electronics which determines the gamma energy from the analog SiPM pulse is indeed able to improve the measured CTR value to 123±7ps FWHM, as can be seen in figure 6.11. Both measurements were using the same crystals, wrapping, grease and similar SiPMs with identical properties like PDE, SPTR and gain.
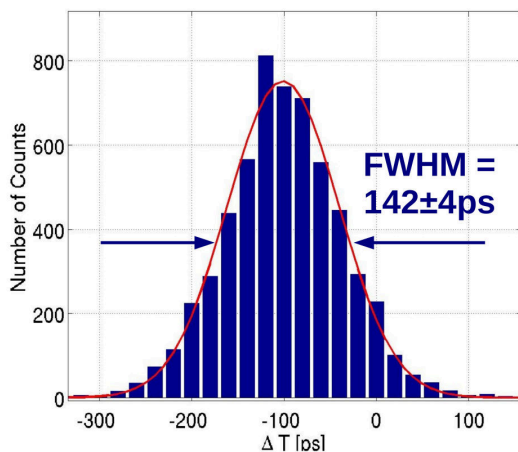

Figure 6.10.: CTR measured with 2x2x5mm^3 LSO:Ce codoped 0.4%Ca crystals and the old electronics with NINO pulse width energy encoding.
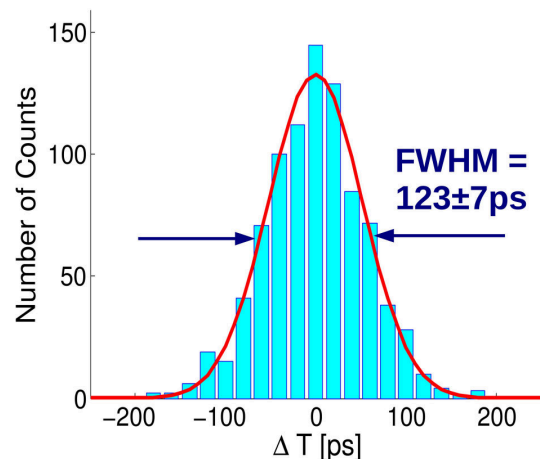
Figure 6.11.: CTR measured with 2x2x5mm^3 LSO:Ce codoped 0.4%Ca crystals and the new electronics with analog energy encoding.

To investigate the limits of the CTR and to further reduce the influence of the crystal dimensions

to the time resolution we tested smaller crystals with dimensions of 2x2x3mm^3. An example of the measured CTR with this type of crystals can be seen in figure 6.12. The crystals with sizes of 2x2x3mm^3, were fully wrapped in Teflon and coupled to the SiPMs with optical grease (Rhodorsil 47V). The crystal face opposite the SiPM is unpolished and all the other faces are polished. We notice that a decrease in crystal length from 5mm to 3mm improves the CTR from 123ps to 108ps. Here this finding will not be discussed further as the influence of the crystal length to the CTR will be explained in full detail in chapter 8.

(a)   (b)
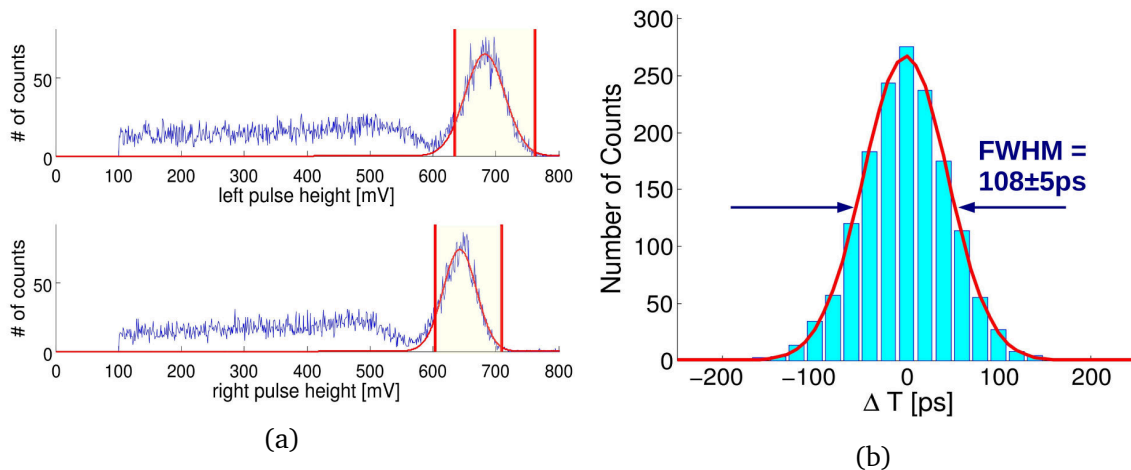
Figure 6.12.: Measurements with 2x2x3mm^3 LSO:Ce codoped 0.4%Ca crystals. We select pulses from the left and right photopeak (a) and plot their delay time histogram (b) from which we determine the CTR.

In figures 6.13 and 6.14 we show the CTR versus the NINO threshold and SiPM bias, respectively. Measurements were performed with 2x2x3mm^3 LSO:Ce codoped 0.4%Ca crystals. The threshold scans show best CTR values of 108ps FWHM at ~80mV, being below the single cell amplitude. SiPM bias scans show a steady improvement of the CTR with increasing overvoltage where the highest resolution (minimum in the plots) is reached at an overvoltage of around 2.2V.

The rise in CTR value for low NINO thresholds (figure 6.13) can be explained by two factors, electronic noise and the SPTR of the SiPM. Due to the single cell signal pile-up the SiPM output signal can be described by a parabolic function, in a first order approximation and for low signal values. Thus the slew rate (dV/dt) is getting smaller for lower NINO thresholds, and consequently the electronic noise starts to dominate the CTR value. Moreover the smearing of the scintillation signal by the photodetector's SPTR causes a significant change to the influence of the photon statistics. Triggering on the first photon emitted by the scintillation will not give the best CTR values anymore. This is mainly caused by the long tails of the SPTR when described by a Gaussian distribution [69]. These two effects are responsible for the rise of the CTR values for low NINO thresholds. We want to mention that these two effects are not independent, for a higher SPTR will as well influence the slew rate of the SiPM output signal.
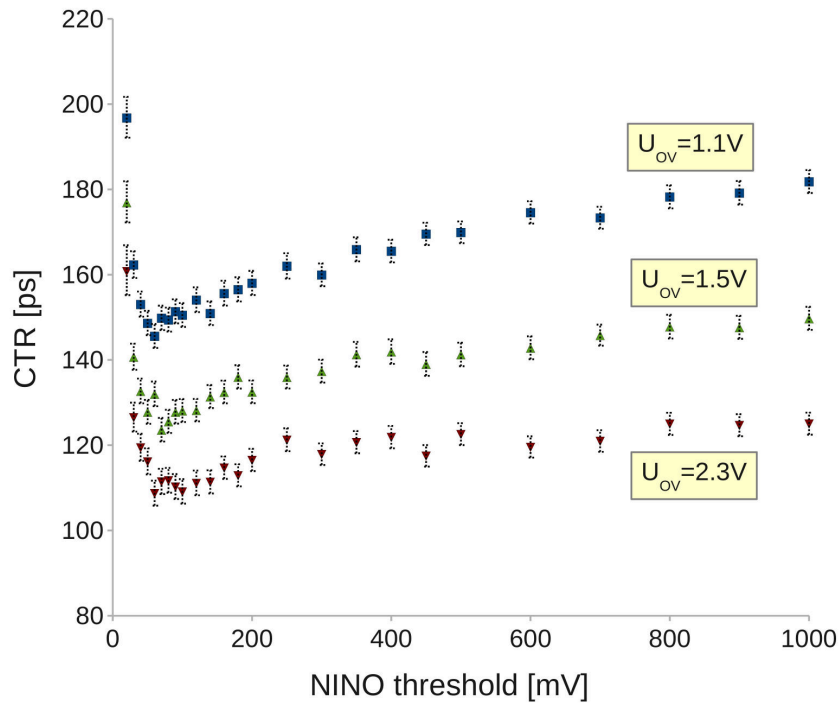
Figure 6.13.: CTR versus NINO threshold. A minimum of the CTR~108ps can be seen at around 80mV for 2.3V bias overvoltage.
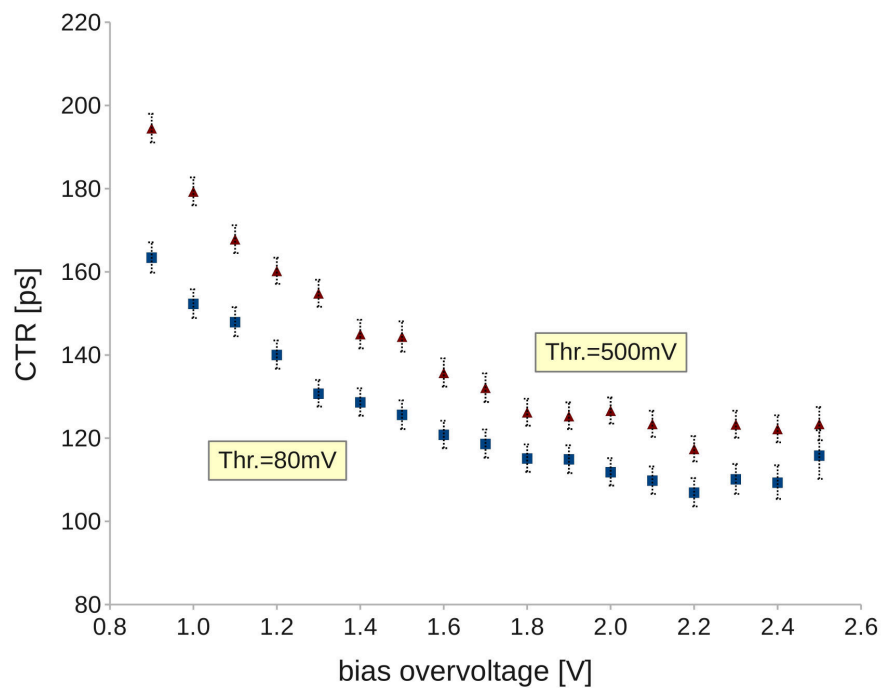

Figure 6.14.: CTR versus the SiPM overvoltage. At 2.2V overvoltage a minimum in the CTR~108ps is obtained with a NINO threshold of 80mV.

The improvement of the CTR values with bias overvoltage (figure 6.14) can be mainly described by an enhancement of the photon detection efficiency (PDE) of the SiPM. The PDE includes the geometrical fill factor, quantum efficiency of the silicon and the probability of triggering an avalanche [44]. With increasing bias voltage the avalanche triggering probability becomes higher, allowing to detect more photons from the scintillation process and thus to improve the timing by higher statistics. The dark count rate and optical crosstalk are increasing with bias overvoltage as well. At a certain bias overvoltage, this increase in DCR and optical crosstalk will begin to deteriorate the time resolution, giving rise to the observed minimum. It should be noted that in comparison to the measurements performed in chapter 5 this minimum is at higher overvoltage values. This illustrates the effect of a better photopeak selection due to the use of the analog SiPM pulse in order to measure the gamma energy.

6.6. Summary and conclusion

We developed new electronics to probe the timing capabilities and limitations of a possible TOF-PET system using LSO crystals. An analog voltage amplifier gives the energy information and the discriminator amplifier NINO the leading edge time information. With LSO:Ce codoped 0.4% Ca scintillators and crystal dimensions of $2x2x3mm^3$ coupled to a commercial MPPC from Hamamatsu (S10931-050P) we measured a CTR of 108±5ps FWHM for gammas with an energy of 511keV. We determined the influence of the data acquisition system to 27±2ps FWHM and thus negligible as compared to the CTR. This shows that L(Y)SO scintillators coupled to SiPM photodetectors are capable of achieving a very good time resolution close to the desired 100ps FWHM for TOF-PET systems. Using the new electronics discussed in section 6.2 we were indeed able to operate the SiPM at higher bias overvoltages as compared to chapter 5. Consequently we could improve the measured time resolution due to a higher PDE of the SiPM. The improvement in PDE at higher overvoltages is mainly caused by a higher avalanche trigger probability [44].

Chapter 7

Simulation of the system time resolution

7.1. Introduction

In chapter 6 it was shown that an optimization of the measurement setup can give excellent time resolutions of 108±5ps FWHM CTR for a 2x2x3mm^3 LSO:Ce codoped 0.4%Ca crystal wrapped in Teflon and coupled with optical grease Rhodorsil 47V to the photodetector. In order to investigate if the measured values are indeed approaching the theoretical limits it is necessary to understand and model all detector components in detail. There were several attempts to model the time resolution of a SiPM based scintillation detector, e.g [82, 83]. To our knowledge however there is still a missing analysis on how to incorporate the crystal geometry into the statistical model, because even for short crystals, e.g. $2x2x3mm^3$, one cannot omit this influence. This is due to the light transfer inefficiency and the photon travel time spread in the crystal in a specific configuration (Teflon wrapping, grease, surface state, ...). The light transfer efficiency is the ratio between the number of photons arriving at the photodetector and the intrinsic light yield, i.e. the total amount of scintillation photons produced. The photon travel time spread is a combination of the light transport time spread of the scintillation photons and the gamma ray interaction point fluctuation in the crystal.

This chapter presents a complete Monte Carlo simulation tool modeling: (1) the scintillation statistics, (2) photon propagation and loss in the crystal (simulated by SLITRANI), (3) photodetector properties like single photon time resolution (SPTR) and detection efficiency, (4) signal pile-up considering the single cell signal of the SiPM, (5) dark count rate and optical crosstalk of the SiPM and (6) the effect of the electronics, i.e. bandwidth limitations and noise. In the second part of this chapter a comparison of the simulation with experimental data is shown. Furthermore the simulation tool will be used to discuss the importance of several parameters to the time resolution, like scintillation rise time, fall time and light yield, as well as single photon time resolution (SPTR) and the photon detection efficiency of the SiPM. As well the influence of properties like electronic noise, DCR and optical crosstalk of the SiPM will be discussed. The content of this chapter was published in [37]

7.2. Model Description

This section gives an overview of the photon statistics to model the scintillation process. It provides a mathematical description of the signal pile-up as well as an overview (flow chart) of a dedicated Monte-Carlo simulation tool.

7.2.1. Scintillation mechanism and photon statistics

The photon emission rate of a scintillation process can be described by bi-exponential functions with one or several rise and fall times [84]. We use this phenomenological model to describe the photon generation process with the following probability density function (PDF):

$$\widehat{f}(t) = \sum_{i=1}^{l} Y_l \frac{\exp\left(-\frac{t-\Delta t}{\tau_{d,i}}\right) - \exp\left(-\frac{t-\Delta t}{\tau_{r,i}}\right)}{\tau_{d,i} - \tau_{r,i}} \Theta(t - \Delta t) \tag{7.2.1}$$

The parameter Δt describes the start of the scintillation process, i.e. the absorption of a gamma in the crystal, and Θ denotes the Heaviside step function. Each contribution in the sum models different energy transfer mechanisms that populate and de-populate the luminescence centers by convolving two exponential functions for each mechanism. Y_l denotes the yield of every single energy transfer mode with $\sum_{i}^{l} Y_l = 1$. The cumulative distribution function (CDF) is then defined in equation 7.2.2 as:

$$\widehat{F}(t) = \int_{-\infty}^{t} \widehat{f}(t')dt' = \sum_{i=1}^{l} Y_l \left\{ 1 - \frac{\tau_{d,i} \cdot \exp\left(-\frac{t-\Delta t}{\tau_{d,i}}\right) - \tau_{r,i} \cdot \exp\left(-\frac{t-\Delta t}{\tau_{r,i}}\right)}{\tau_{d,i} - \tau_{r,i}} \right\} \Theta(t-\Delta t) \tag{7.2.2}$$

The area below $\widehat{f}(t)$ is normalized to one. By multiplying $\widehat{f}(t)$ with the intrinsic light yield n we obtain the average photon rate of the scintillation process $f(t) = n \cdot \widehat{f}(t)$. In the special case of L(Y)SO:Ce crystals we assume equation 7.2.1 and 7.2.2 to be simple bi-exponentials ($l = 1$) [85, 86].

We are able to describe the kth photon's generation time PDF using the average photon rate and a modified binomial distribution [85, 87, 88],

$$p_{k:n}(t) = n\binom{n-1}{k-1}\widehat{f}(t)\widehat{F}(t)^{k-1}(1 - \widehat{F}(t))^{n-k} \tag{7.2.3}$$

with $\widehat{f}(t)$ and $\widehat{F}(t)$ being the probability density function and cumulative density function of the photon generation process, respectively. Equation 7.2.3 describes the probability of the kth photon being emitted in the time interval t and t+dt. To better understand formula 7.2.3 we ask: "What is the probability of a photon y out of n to be the kth one and to be emitted in the time interval t and t+dt? " It is the probability that k-1 photons out of n-1 have already been emitted as described by the binomial distribution $p = \binom{n-1}{k-1}\widehat{F}(t)^{k-1}(1 - \widehat{F}(t))^{n-k}$, multiplied by the probability of photon

emission in the specific time interval t and t+dt, i.e. $\widehat{f}(t)dt$. Since one can repeat this for every photon of n, we apply the factor n in equation 7.2.3. This treatment is valid only if the rate of photon emission is time independent and identically distributed for each event. For $n \cdot \widehat{F}(t)$ reaching a constant value and in the limit of $n \to \infty$, i.e. k being small compared to the total number of photons n, the binomial expression 7.2.3 can be reduced to the Poisson distribution shown in equation 7.2.4. A complete derivation can be found in the appendix B.

$$p_{k:n}(t) \to \frac{F(t)^{k-1}}{(k-1)!} e^{-F(t)} f(t). \tag{7.2.4}$$

With $F(t) = n \cdot \widehat{F}(t)$ and $f(t) = n \cdot \widehat{f}(t)$. Equation 7.2.4 was already used by Post and Schiff [43] to describe the time response of a scintillator coupled to a PMT.

7.2.2. SLITRANI for light ray tracing

LITRANI [89] is a Monte Carlo program based on ROOT [90]. In this work, the newest version of LITRANI, called SLITRANI for "Super LIght TRansmission in ANIsotropic media", was used. Any three dimensional setup that can be described by the TGeo [90] class of ROOT can be used as a setup in SLITRANI. Each volume can be of a different material, and each material can have different optical properties. The optical characteristics of materials can be modeled with a dielectric constant, absorption length and diffusion length. Rayleigh and Compton scattering can also be simulated. Wavelength dependency can be added to most of the parameters. In contrast to other Monte Carlo light ray tracing programs (e.g. GEANT4), LITRANI can handle an anisotropic dielectric constant and absorption length. One has various possibilities to produce photons in SLITRANI: spontaneous emission of photons, photons coming from an optical fiber, photons generated by ionizing particles, photons generated by gamma rays of energy between 0.1 and 1MeV or photons generated by a high energy electromagnetic shower. One can define any volume and material inside the setup as the detector. All photons are tracked until they are absorbed or detected. Most of the transition, reflection and absorption processes can be recorded during the simulation for further analysis. The standard histograms are showing the amount of detected photons, the arrival time, the different wavelengths, materials and volumes where photon absorption or reflection appears. To handle unpolished surfaces and imperfect polishing, we added a self-built function where the roughness can be controlled by a single parameter. It is modeled as a random local surface tilt with the angle described by a Gaussian probability distribution where the roughness parameter equals the standard deviation.

The SLITRANI simulations can be summarized by two important parameters, i.e. the light transfer time spread ξ and the light transfer efficiency η of the scintillation light in the crystal. Both parameters are dependent on the gamma interaction point χ within the crystal. The light transfer time spread describes the variation of the time between the generation of a scintillation photon and the moment it reaches the photodetector. We assume an isotropic emission angle of the photons. The transfer efficiency describes the fraction of photons reaching the photodetector compared to the total number of generated photons. It is dependent on the photon absorption and scattering in the crystal as well as on Teflon wrapping and also on the position of the gamma

interaction point. We can define an average transfer efficiency $\bar{\eta}$, averaging the transfer efficiency η over all possible gamma interaction points.

7.2.3. Organization of the Monte Carlo simulation tool

A multi pixel photon counter (MPPC) or SiPM consists of many micro cells (e.g. 3600 for the Hamamatsu 50μm type). If one of the micro cells or SPADs is fired, they always give rise to the same output signal, no matter how many photons initially triggered the avalanche. The single cell signal is defined by the SiPM's equivalent circuit and the circuitry around the SiPM [91]. In a first order approximation it arises from RC-filters and thus should only have exponential character. The time constants are dependent on the overvoltage, i.e. on the cell capacitance changing with the overvoltage as the depletion zone will change in dimension. However these changes are assumed to be negligible, and to good approximation, we can further assume that the time constants determining the single cell signal are independent of the overvoltage. We model the single cell signal with a bi-exponential function 7.2.5 with τ_{Mr} and τ_{Md} being the rise time and fall time of the signal, respectively. The parameter A denotes the maximum amplitude of the single SPAD signal, and ϵ the moment when each microcell fires determined by equation 7.2.7. Typically the rise time τ_{Mr} is in the order of hundreds of ps and the fall time τ_{Md} in the order of tens of ns. A single cell amplitude jitter caused by gain fluctuations can be modelled by a Gaussian distributed amplitude A, with $\bar{A}$ being the mean value of the cell amplitude and σ_A the standard deviation of the fluctuation. The value $\sigma_A/\bar{A}$ gives the percental gain fluctuation, and the inverse, $\bar{A}/\sigma_A$, will be called $SNR_{gain\,fluctuation}$.

$$s_\epsilon(t) = \frac{A}{b^{\frac{1}{1-b}} - b^{\frac{1}{1/b-1}}} \left(\exp\left[-\frac{t-\epsilon}{\tau_{Md}} \right] - \exp\left[-\frac{t-\epsilon}{\tau_{Mr}} \right] \right) \Theta(t-\epsilon) \quad with \quad b = \frac{\tau_{Md}}{\tau_{Mr}} \quad (7.2.5)$$

Coupling the SiPM to a scintillator with an intrinsic light yield n and a light transfer efficiency η it will give rise to $n \cdot PDE \cdot \eta$ avalanches. Because not all photons generated by the scintillation n will actually produce an avalanche due to absorption in the crystal and limited photo detection efficiency of the SiPM. The probability of one photon emitted by the scintillation to produce an avalanche is $n \cdot PDE \cdot \eta$. This process of losing photons from the scintillation to the production of an avalanche is denoted as random deletion. The output signal of the device can be described as the sum of the single cell signals 7.2.6. Because of the long decay time of a single cell signal this process is often referred to as signal pile-up.

$$S_{SiPM} = \sum_{k=1}^{n} s_{\epsilon(k)}(t) \cdot \Theta\left[PDE \cdot \eta(\chi) - random(1) \right] \qquad (7.2.6)$$

The function "random(1)" generates a random number between 0 and 1 for each k. Thus the Heaviside function $\Theta\left[PDE \cdot \eta(\chi) - random(1) \right]$ represents the random deletion due to the limited detection efficiency of the SiPM (PDE) and the transfer efficiency of the crystal (η). The transfer efficiency $\eta(\chi)$ depends on the scintillation origin in the crystal (χ) and thus changes

with each gamma interaction.

In our simulation $\epsilon(k)$ is a crucial parameter as it models the entire timing behaviour of the system. We identify four contributions to $\epsilon(k)$, i.e. the time Δt from the emission of the 511keV gamma until its absorption in the crystal, the scintillation statistics (see chapter 7.2.1), the light transfer time spread ξ and the detection transit time spread of the SiPM. Supposing that the $T_k(p)$ operator generates a single random time stamp with the PDF p, then $\epsilon(k)$ can be expressed as 7.2.7.

$$\epsilon(k) = \Delta t + T_k(f) + \xi_k(\chi) + T_k(g) \tag{7.2.7}$$

The function $T_k(f)$ gives one time stamp per k^{th} photon of the scintillation process, according to the method described in chapter 7.2.1. The function $\xi_k(\chi)$ gives the random time spread caused by the light transfer in the crystal for the kth photon simulated by SLITRANI (see chapter 7.2.2). It should again be noted that $\xi_k(\chi)$ is dependent on the position of the scintillation origin χ. $T_k(g)$ models the photodetector's transit time spread (see formula 7.2.8) and gives a random time stamp generated by a Gaussian distribution. The sigma of this Gaussian is the single photon time resolution (SPTR) of the SiPM.

$$g(t) = \frac{1}{\sqrt{2\pi}\sigma_{SPTR}} \exp\left[-\frac{(t - \Delta_M)^2}{2(\sigma_{SPTR})^2} \right] \tag{7.2.8}$$

The parameter Δ_M denotes a possible electronic delay and σ_{SPTR} is the single photon time resolution of the SiPM.

The Monte Carlo simulation is organized in the following way:

- Generate a 511keV gamma and calculate the time Δt until it is absorbed in the crystal at the coordinates χ according to the exponential gamma ray absorption law with an absorption length of 11.5mm [31]. The point χ will be the scintillation point of origin.

- At point χ calculate from SLITRANI simulations n random photon transfer time jitters $\xi_1....\xi_n$ based on the light propagation in the crystal. Add to every photon transfer time jitter ξ_k a random time stamp t_k, with k being the photon rank $k \in n$. t_k is subject to the scintillation statistics described in chapter 7.2.1.

- Perform random deletion of photons according to the product of PDE and the photon transfer efficiency of the scintillator (η) simulated by SLITRANI. The transfer efficiency depends on the scintillation origin χ.

- Generate a random noise floor taking into account the DCR and the optical crosstalk of the SiPM.

- With 7.2.6 generate signal pile-up for those photons that have "survived" the random deletion process. This also includes signals from crosstalk which are assumed to be simply

smeared by the SPTR because at this time no model of time evolution of crosstalk events is known to the authors.

- Filter the obtained signal with a first order Butterworth low pass filter with a cut off frequency of 1GHz, matching the bandwidth of NINO.

We wish to note that we did not include any saturation effects of the SiPM in the simulations. Within the first nanosecond approximately 100 avalanches are created at the photodetector and therefore we assume that the used SiPM with a total number of 3600 SPADs will show no signs of saturation. Therefore our method should be a good representation of the SiPM signal in the first few nanoseconds of the scintillation pulse. We then apply leading edge discrimination producing the time stamp of the simulated output pulse. Electronic noise is added by Gaussian distributed white noise on the threshold value. To obtain sufficient statistics we repeat this procedure about 10000 times. A flow chart of the program and processing steps can be seen in figure 7.1.

As a last step we quadratically add $CTR_{acquisition} = 27ps$ FWHM to the simulated CTR value, to account for the time jitter generated by the oscilloscope (see formula 6.2.3 in chapter 6). In the simulation we did not include any fluctuations of the intrinsic light yield, i.e. the intrinsic energy resolution of the crystal.
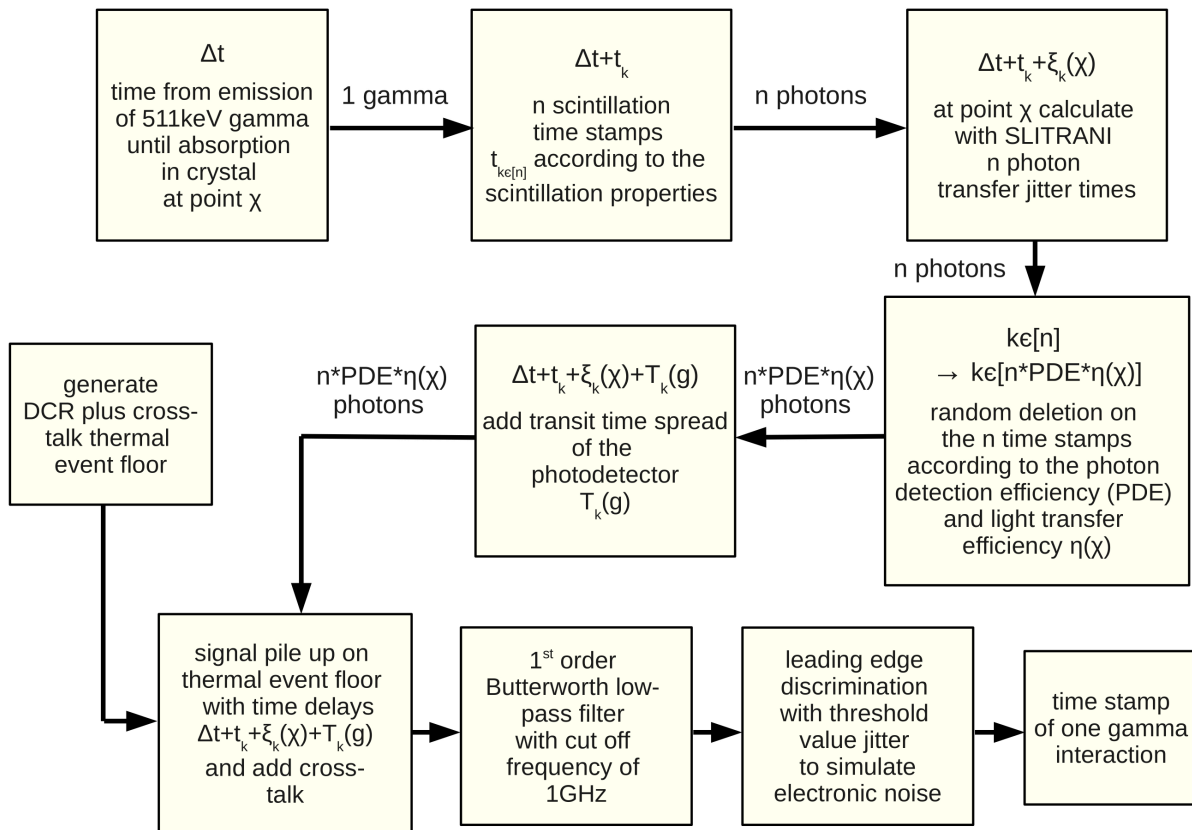
Figure 7.1.: Flow chart of the Monte Carlo program to simulate the time resolution.

7.3. Model Parameters

In this section we describe the different measurements and methods to obtain values for all input parameters necessary for the simulation.

7.3.1. Single cell signal

We model the single cell signal by a bi-exponential function with a single rise time τ_{Mr} and fall time τ_{Md} (equation 7.2.5). Figure 7.2 shows the measurement of a single cell signal coming from the voltage amplifier. The NINO discriminator, although not used here, was nonetheless coupled to the SiPM in order to preserve the same circuit conditions as for real timing measurements.
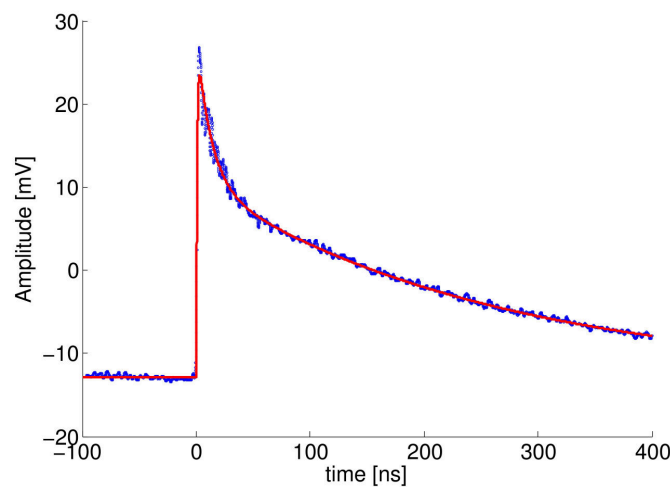
Figure 7.2.: Single cell signal measured at the SiPM with 2V overvoltage when NINO is coupled to the SiPM as well. Measurements are done with the voltage amplifier at an amplification of 88. The fast fall time component represents $\tau_{Md} = 11ns$. Because of the 1nF coupling capacitor in front of NINO, it does not see the long fall time component.

The measured signal is the direct output voltage of the SiPM. We can observe two fall time components. A slow one with 260ns and a fast component with 11ns. The slow 260ns component is generated by the electronics around the SiPM, i.e. the 200Ω resistors (as can be seen in figure 6.3). The fast fall time component is generated by the 1nF coupling capacitor at the front end of NINO and its additional input impedance of 40Ω. It corresponds to the fall time τ_{Md} in equation 7.2.5 which is 11ns. It should be noted that a very small fraction of the slow 260ns-component can still couple into NINO. This fraction however is small enough and will be neglected in our further discussions. In addition we measured the single cell signal with 50Ω bias resistors to determine the SiPM capacitance. The decay time was measured to be 50ns hence corresponding to a SiPM capacitance of 500pF. Compared with the values measured in [91] we suspect a high passive capacitance in our system generated by rather long leads and jumpers used to guide the SiPM signal to NINO. The rise time can be determined to $\tau_{Mr} = (C_D + C_q)R_D$ [92]. It is difficult

to find the proper values for the "micro plasma" resistance R_D, the SPAD capacitance C_D, and the quenching capacitance C_q. Together with the values given in [39] we deduce $\tau_{Mr} = 400ps$ using a value of $R_D = 3k\Omega$ and $C_D + C_q = 130pF$. This value is most probably too high. However, because of the low pass filtering in our simulations, the single cell rise rime t_{Mr} is not a critical parameter. It should be noted that also the exact value of the fall time t_{Md} is not very critical since we are only interested in the pile-up process in the first nanoseconds.

7.3.2. Electronic noise and SiPM gain fluctuation

NINO operates as a current mode amplifier and has a low differential input impedance of 40Ω [63]. A schematic of the SiPM bias circuit can be seen in figure 6.3. It is important to determine the exact electronic noise of the system, in particular when measuring the SPTR. Gain fluctuations of the SiPM have a similar influence on the time resolution as electronic noise. These gain fluctuations can be directly modeled by an amplitude fluctuation of the single cell signal, supposing that the rise and fall times of the single cell signal are independent of SiPM overvoltage and identical within every cell (section 7.2.3). We developed a technique to estimate the electronic noise and the gain fluctuation by means of measurements. With the oscilloscope we measure, at the same time, both the analog SiPM signal from the amplifier and the output pulse of NINO, being operated at a specific threshold. For each dark count event in the SiPM we record the SiPM pulse amplitude and if there was a parallel output signal from NINO or not. In the offline analysis, we select single dark count events using the recorded SiPM amplitude histogram to exclude crosstalk and afterpulsing. We plot the number of events where NINO does not generate a signal versus the threshold (see figure 7.3).
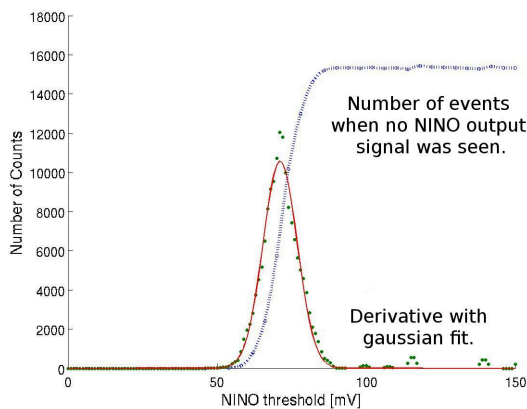
Figure 7.3.: Number of no NINO-output-signal-seen versus the NINO threshold. On the derivative we apply a Gaussian fit which gives the measured SNR.
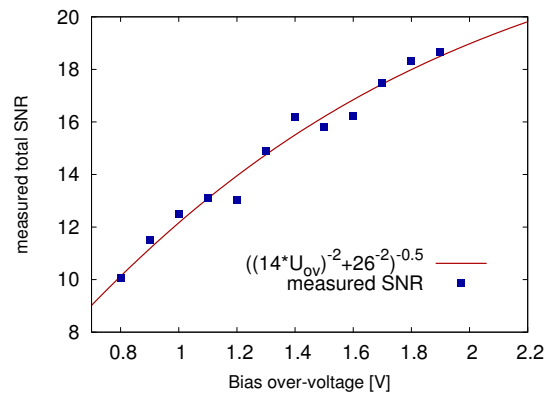
Figure 7.4.: Measured SNR versus bias overvoltage. The fit is parametrized as $SNR_{electronic\ noise} = 14 * U_{ov}$ and $SNR_{gain\ fluctuation} = 26$.

For low thresholds, NINO triggers on every signal, whereas for high thresholds the input signal from a single cell is too low to give rise to a trigger, and thus no signal at the NINO output is seen.

For a perfect input signal with no noise and gain fluctuations this transition should be a sharp step function. In a noisy system, however, this transition is smooth and blurred by electronic noise and amplitude fluctuations. We are able to deduce the combined influence of electronic noise and gain fluctuations by calculating the derivative of this transition and applying a Gaussian fit. The ratio of mean and sigma of the Gaussian fit denotes the measured signal to noise ratio $SNR_{meas} = \frac{\mu}{\sigma}$. It should be noted that throughout this work the signal in the SNR term is always equal to the cell amplitude. This equivalent cell amplitude is changing with bias overvoltage and thus SNR_{meas} as well. We can model the measured SNR as shown in equation 7.3.1.

$$\left(\frac{1}{SNR_{meas}}\right)^2 = \left(\frac{1}{SNR_{electronic\,noise}}\right)^2 + \left(\frac{1}{SNR_{gain\,fluctuation}}\right)^2 \tag{7.3.1}$$

Because the electronic noise is independent of overvoltage in contrast to the single cell amplitude changing linearly with gain and hence with bias overvoltage, $SNR_{electronic\,noise}$ is directly proportional to the overvoltage U_{ov}. We further assume that the gain fluctuations are mainly generated by non-uniformities of the 3600 SPADs of the SiPM. Thus, the relative fluctuation of the gain ($SNR_{gain\,fluctuation}$) should be independent of the bias overvoltage. We model the two contributions in equation 7.3.1 as $SNR_{electronic\,noise} = a \cdot U_{ov}$ and $SNR_{gain\,fluctuation} = b$ with a and b being two constant parameters. In figure 7.4 we show the measured SNR versus the bias overvoltage. Applying a fit according to formula 7.3.1, we can deduce the parameters as: $a = 14/V$ and $b = 26$. Thus the electronic signal to noise ratio is $SNR_{electronic\,noise} = 14 \cdot U_{ov}$, and the gain (single cell amplitude) fluctuation is 3.8%.

7.3.3. Dark count and crosstalk

DCR and optical crosstalk are dependent on the bias overvoltage and can be derived from the staircase plots in chapter 6.3. The first plateau is at thresholds lower than a single SPAD signal and hence corresponds to the dark count rate. The second plateau is generated from a single crosstalk, the third from two simultaneous crosstalk events and so on. In figure 7.5 we plot measured dark count and crosstalk values for four different bias overvoltages. We can fit the DCR and crosstalk rates with exponential functions depending on the overvoltage. The functions are summarized in equations 7.3.2 to 7.3.5.

$$DCR = 183278 * \exp\left[1.15 * U_{OV}\right] \tag{7.3.2}$$

$$1^{st}crosstalk = 4201 * \exp\left[2.26 * U_{OV}\right] \tag{7.3.3}$$

$$2^{nd}crosstalk = 105 * \exp\left[3.39 * U_{OV}\right] \tag{7.3.4}$$

$$3^{rd}crosstalk = 4 * \exp\left[4.33 * U_{OV}\right] \tag{7.3.5}$$

The parameters deduced from these fits are not directly related to physical processes. They rather provide a phenomenological tool to describe DCR and crosstalk in an easy and integral form for our simulations. As such they are a look-up tables in a mathematical description.
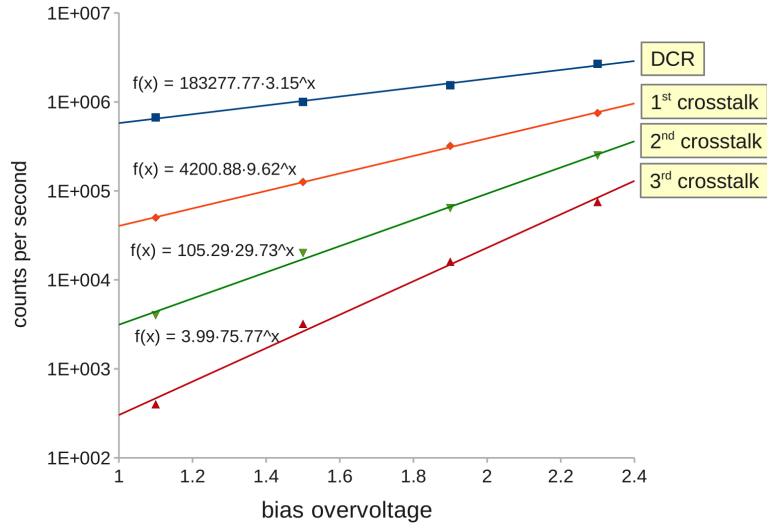
Figure 7.5.: Measured dark count and crosstalk values for different bias voltages deduced from the staircase plots. Data points can be approximated by exponential fits.

7.3.4. Photon detection efficiency

For the photon detection efficiency we used the results published in [80]. In this article measurements of the PDE versus the bias overvoltage at different wavelengths, ranging from 465nm to 870nm, are reported. We are only interested in the measurements for 465nm because of the emission peak at 420nm for LSO:Ce codoped 0.4% Ca.
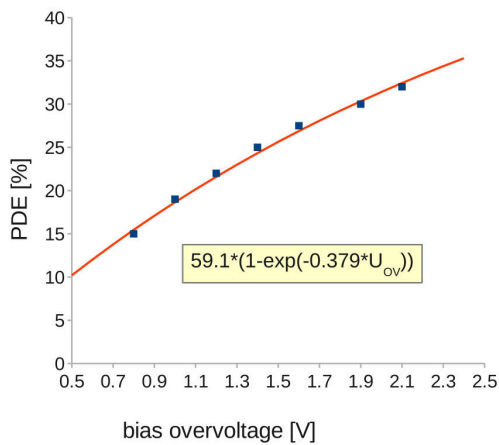
Figure 7.6.: Photon detection efficiency versus bias overvoltage for the Hamamatsu 50μm type, experimental data and fit for 465nm. Data was taken from [80].
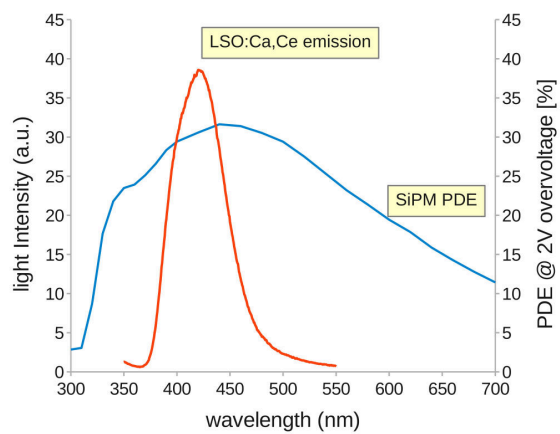
Figure 7.7.: Measured emission spectrum of LSO:Ce codoped 0.4%Ca and the PDE of the SiPM.

We can parametrize the PDE as a function of overvoltage for 465nm with equation 7.3.6 (see figure 7.6).

$$PDE(U_{OV}) = 0.591 * \left(1 - e^{-0.379*U_{OV}}\right) \tag{7.3.6}$$

These parameters only provide a phenomenological description of the data without a direct physical explanation. However, as we can see in figure 7.6, this parametrization of the PDE is a good representation of the experimental data. If we couple the photodetector to a scintillator, we also have to account for the emission spectra of the scintillator. In figure 7.7 we plot the emission spectrum of the used LSO:Ce codoped 0.4%Ca scintillator together with the PDE of the photodetector versus the wavelength. If we normalize the PDE at a wavelength of 465nm we can calculate the weighted integral of the PDE with the emission spectrum which results in a correction factor of 0.96 applied to equation 7.3.6:

$$PDE(U_{OV})^{scint.} = 0.591 * \left(1 - e^{-0.379*U_{OV}}\right) * 0.96 \tag{7.3.7}$$

7.3.5. Single photon time resolution

The single photon time resolution (SPTR) describes the time jitter of the photodetector when detecting single photons and is commonly quoted in sigma, i.e. not in FWHM. The SPTR is influenced by the characteristics of one single pixel, i.e. the avalanche spread in the SPAD, the uniformity of the single cells and the uniformity of the signal transmission to the output. As the signals from the SiPM are small, the electronics plays an important role for the SPTR value. It is therefore important to measure the SPTR with the same electronics used in the CTR measurements. We tested the time response of the SiPM using a femtosecond laser operating at 400nm wavelength and with a pulse width of 200fs presented in chapter 4 [69]. The measured SPTR values can be seen in figure 7.8.
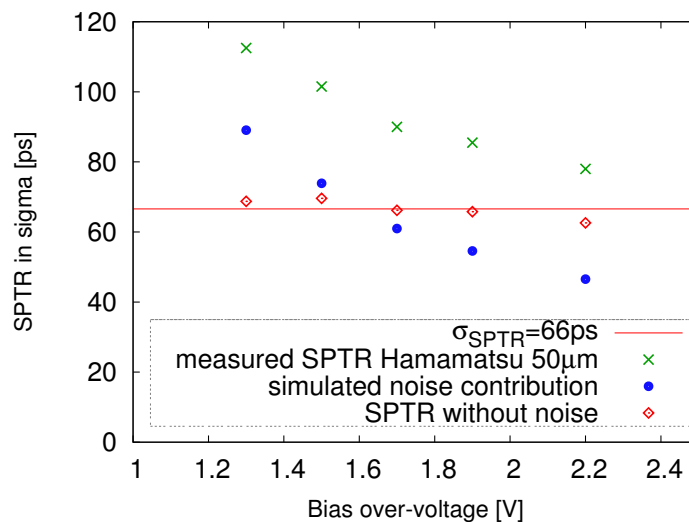
Figure 7.8.: Measured SPTR for the $50\mu m$ SPAD-size Hamamatsu MPPC. Data was taken out of [69]. Subtracting the noise contribution of NINO we obtain an almost constant single photon time resolution $\sigma_{SPTR} = 66ps$.

To get an idea of the influence of the electronic noise and gain fluctuations, we used the values derived in chapter 7.3.2 and simulated the time jitter of the noise contributions taking into account the NINO threshold and its shift in terms of equivalent cell amplitude when changing the bias voltage. Subtracting the noise contribution from the measured SPTR values we obtain an almost constant value of $\sigma_{SPTR} = 66ps$. Although this result is still under investigation, it seems that the SPTR is not strongly dependent on the bias overvoltage. This could be explained by the fact that the SPTR in our MPPC with 3600 SPADs is dominated by uniformity jitter and signal transmission delays. Thus, a device with smaller geometrical dimensions could lead to a better SPTR.

7.3.6. Scintillation rise and fall time

For the scintillation decay time measurement we used the time correlated single photon counting technique originated by Bollinger and Thomas [93]. This way we determined the single fall time of our LSO:Ce codoped 0.4%Ca scintillator to $30.3 \pm 1ns$ (see figure 7.9), in good agreement with the values stated in [94]. To measure the scintillation rise time is more difficult as one needs to deconvolve the impulse response of the measurement apparatus from the intrinsic rise time of the scintillation signal [95]. The rise time values stated in the literature for LSO:Ce range from 0ps to 70ps [86, 95]. In this work we choose a rise time of 70ps, comparable to the value stated in the most recent work [86]. Using equation 7.2.1, we derive the parameters for the PDF of the photon generation process as a single bi-exponential ($l = 1$) with a rise time $\tau_r = 70ps$ and a fall time $\tau_d = 30.3ns$.
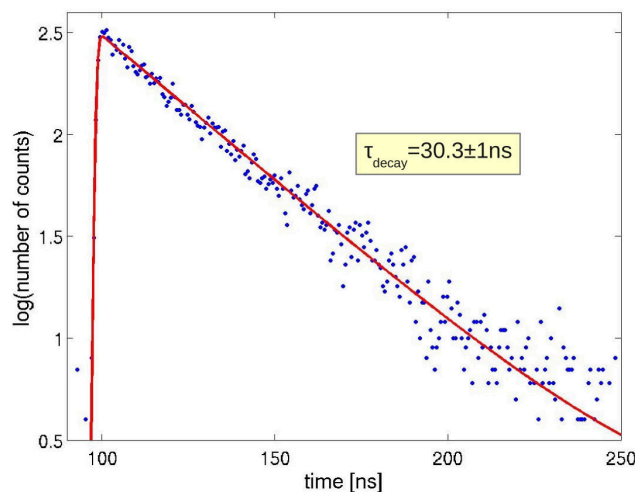
Figure 7.9.: Scintillation decay time measured with the time correlated single photon counting technique.

7.3.7. Light yield measurements for the adaptation of SLITRANI crystal model parameters

The different parts of the SLITRANI setup (crystal, photodetector, wrapping, etc.) are modelled as three dimensional objects that are provided by the ROOT geometry package. In figure 7.10

a schematic of the main parts of the light yield measurement setup can be seen, as well as the different regions of a scintillating crystal which were modeled with different surface roughnesses. The photons in our setup are produced with a ^{137}Cs gamma source. Other parameters necessary for photon generation by gamma excitation, like the photo-electric cross section, the gamma-absorption length, and the emission spectrum, were taken from the work of [18].
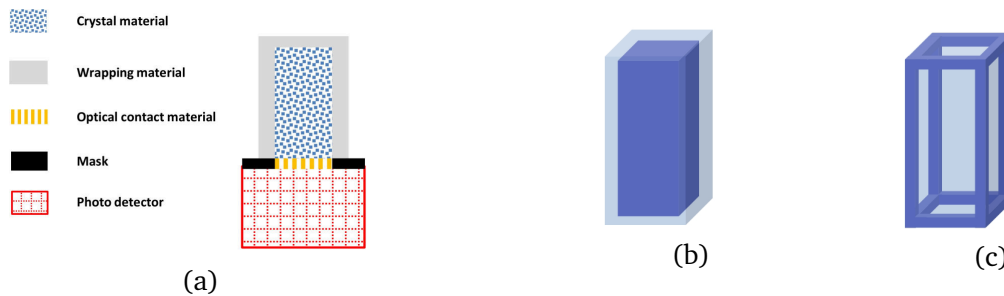
Figure 7.10.: (a): The general setup of a standard light yield measurement using optical glue, diffusive wrapping and a photomultiplier tube. (b) and (c): Schematics of the crystal model. The surface (b) has different material properties than the edges (c); that way the model tries to incorporate the different surface roughness of the different crystal areas.

There are a number of parameters that are well known like the index of refraction of the crystal or of the glue, but there are nonetheless others that change from crystal to crystal and are difficult to measure (e.g. the roughness of surfaces and edges, the diffusion length inside the crystal). Therefore these parameters were fitted to our model using the model-matching technique [96]. In the work of [97] the parameters, like the crystal diffusion and absorption length as well as the surface roughness, were fitted making use of light yield measurements with crystals of differently shaped walls and different contact agents. The parameters for the crystal used in this work were partly imported from the work of [97], but since wrapping was not considered there, some parameters had to be estimated by running another set of simulations as part of a second model-matching technique for this work. Similar to the work of [96,97] the unknown parameters of the setup were adjusted to fit the results of independent measurements with crystals of different size. The unknown parameters for our model were: (1) airgap between wrapping and crystal, (2) roughness of walls and edges (3) absorption and diffusion of the Teflon wrapping and (4) index of refraction of the wrapping. To fit those parameters we made light yield measurements with a crystal with a common $2x2mm^2$ face that is in contact with the photodetector but different lengths of 3, 5, 10 and 20mm. The crystals were wrapped in Teflon, and optical glue was used for the coupling to the photodetector. The fitted parameters together with parameters taken from other references can be seen in table 7.1 and table 7.2.

In table 7.3 we summarize the measured light yield and the simulated light transfer efficiencies for different crystal configurations. The light yield was measured with a Photonis XP2020Q PMT. The values are corrected for the quantum efficiency of the PMT and given in photons per MeV. We measured the light yield in different configurations, i.e. with 5 (5FP) or 6 polished faces (6FP) and different crystal lengths. The configuration "5 faces polished" means that only the side opposite to the SiPM is unpolished. The crystal was always wrapped in Teflon, 0.075mm thick and with at

least 5 layers, and coupled to the photodetector with optical grease: Rhodorsil 47V.

Table 7.1.: Parameters used in our SLITRANI simulation setup. Parameters were taken from the work of [97] and [18].

Table 7.2.: Parameters used in our SLITRANI simulation setup. Parameters fitted to the light yield results of the crystals used in this work.

Crystal diffusion length	70cm
Thickness of the glue layer	10-20μm
Crystal absorption length @ 420nm	30cm
Index of refraction of the crystal	1.82
Index of refraction of the glue	1.41

Roughness sidewalls standard deviation	σ=0.5°
Roughness edges standard deviation	σ=5°
Diffusion of the wrapping	98%
Airgap between crystal/wrapping	No
Index of refraction of the wrapping	1.37
Absorption of the wrapping	2%

Table 7.3.: Light yield values of the used LSO:Ce codoped 0.4%Ca crystals in photons/MeV, measured with a Photonis XP2020Q photomultiplier. Averaged photon transfer efficiency $\bar{\eta}$ as simulated by SLITRANI is shown as well. The crystals were fully wrapped in Teflon and the square 2x2mm^2 side was coupled to the PMT with optical grease. The surface opposite the PMT was either unpolished (5FP) or polished (6FP).

configuration	measured light yield [ph/MeV] (5% error)	average light transfer efficiency $\bar{\eta}$ [%]	intrinsic light yield [ph/MeV]
3mm / grease / 5FP	26200	0.682	38420
5mm / grease / 5FP	23950	0.617	38820
10mm / grease / 5FP	21400	0.497	43060
5mm / grease / 6FP	23200	0.589	39390
10mm / grease / 6FP	19900	0.480	41460
20mm / grease / 6FP	14800	0.386	38340

The measured light yield uncertainty was estimated to be about 5%, including uncertainties in quantum efficiency and collection efficiency of the PMT. This number also includes handling uncertainties caused by the mounting of the samples onto the PMT with possible misalignment and the use of optical grease. The computed intrinsic light yield in table 7.3 is fluctuating by ∼10%. These fluctuations are higher than the measured light yield uncertainties and are caused by deficiencies in the SLITRANI model. If we suppose that the measured light yield and SLITRANI errors are mainly of statistical nature we can define a global light yield, averaging the intrinsic light yield in table 7.3, which should give the most reliable value. We determine this global intrinsic light yield to 39920 ph/MeV.

7.4. Model Validation

In this section we compare the simulated CTR values with the measured ones. In table 7.4 we summarize the input parameters describing the scintillation process and the SiPM. We emphasize that the simulation parameters were not deduced from any fit of the measured CTR. Thus the simulation outcome is pure prediction without incorporating any prior knowledge of the CTR

measurements.

Table 7.4.: Summary of the scintillation and SiPM input parameter values used for the Monte Carlo simulation tool.

scintillation rise time	$\tau_r = 70ps$
scintillation fall time	$\tau_d = 30.3ns$
intrinsic light yield of the scintillation	39920 ph/MeV
single cell pulse rise time	$\tau_{Mr} = 400ps$
single cell pulse fall time	$\tau_{Md} = 11ns$
cell-to-cell amplitude fluctuation ratio	$SNR_{gain\,fluctuation} = 26$
cell signal to noise ratio	$SNR_{electronic\,noise} = 14 * U_{ov}$
single photon time resolution	$\sigma_{SPTR} = 66ps$
photon detection efficiency for LSO:Ce,Ca	$PDE(U_{OV})^{scint.} = 0.591 * \left(1 - e^{-0.379*U_{ov}}\right) * 0.96$
dark count rate	$DCR = 183278 * \exp\left[1.15 * U_{OV}\right]$
first crosstalk rate	$1xtalk = 4201 * \exp\left[2.26 * U_{OV}\right]$
second crosstalk rate	$2xtalk = 105 * \exp\left[3.39 * U_{OV}\right]$
third crosstalk rate	$3xtalk = 4 * \exp\left[4.33 * U_{OV}\right]$

7.4.1. Special Case: Timing of the SiPM using a femtosecond laser

An important special case is the simulation of the time response of the SiPM plus the accompanying readout electronics alone without the scintillation mechanism and light transfer. Measurements were done at different light levels with a femtosecond laser operating at 400nm wavelength and 200fs pulse width [69], see as well chapter 4.
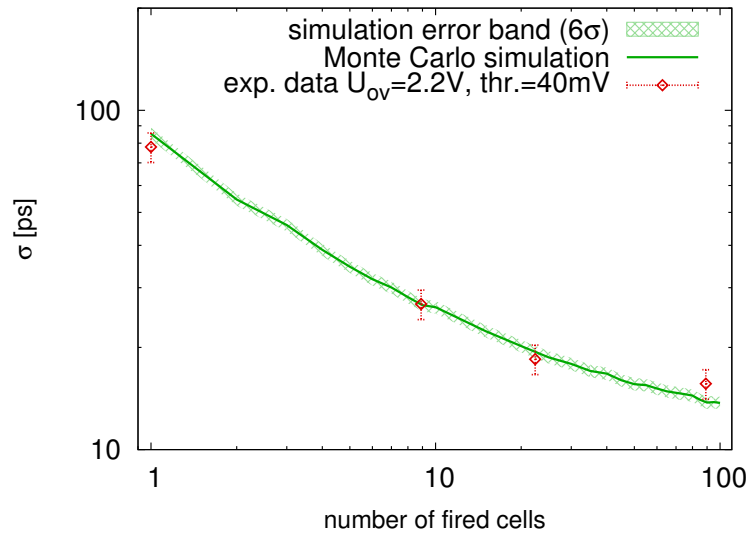
Figure 7.11.: Time resolution of the SiPM for different light levels and comparison with simulation. Experimental data was taken from [69].

Figure 7.11 shows the measured time response of a Hamamatsu 50μm SPAD size MPPC versus the number of fired cells or photo-electrons. The SiPM was operated at an overvoltage of 2.2V. We compare the experimental data with simulations described in section 7.2.3. For that purpose we "switched off" the scintillation and crystal influence. The simulation thus represents the interplay of the signal pile-up with the SPTR jitter and the leading edge discrimination. The solid line shows the simulation with its associated 99.7% confidence interval. These error bars comprise only the statistical Monte Carlo fluctuation since we have not yet incorporated the uncertainties of the input parameters.

7.4.2. CTR as a function of SiPM Bias and NINO threshold

We compare the Monte Carlo simulation results with measured data. In the following plots (figure 7.12 and 7.13) the solid lines show the simulation with a 99.7% statistical confidence level (no parameter uncertainties are incorporated) different shaped points are the data points from different CTR measurements, e.g. CTR versus bias overvoltage and CTR versus NINO threshold voltage (see in chapter 6 figure 6.14 and figure 6.13). For the shown simulations and measurements the crystals were LSO:Ce codoped 0.4%Ca with a size of 2x2x3mm^3 fully wrapped in Teflon and coupled with optical grease Rhodorsil 47V to the SiPM.

Figure 7.12 shows the CTR versus the SiPM bias overvoltage. Points show the experimental data at a NINO threshold of 80mV. We achieved best CTR values for all SiPM overvoltages around this threshold value. The simulation is in good agreement with the experimental data. The decrease of the plot (which corresponds to an improvement in CTR) as a function of SiPM overvoltage is almost perfectly matched by the corresponding increase in PDE, as we modeled the SPTR to be constant with bias voltage. For higher bias overvoltages the experiment shows a higher saturation or even a degradation in CTR when compared to simulations. One possible explanation can be the neglect of an additional time smearing of the crosstalk events, which we had assumed to be prompt. We also neglected afterpulsing and its time distribution. However we do not believe that afterpulses influence the time resolution to a high degree as these events happen relatively late compared to the avalanches triggered by the relatively high scintillation photon rate ($\sim$10 avalanches per 100ps).

In figure 7.13 the CTR versus the NINO threshold for different bias voltages can be seen. For low bias overvoltage (1.1V) the simulation predicts around 5ps lower values of CTR than measured. This could be an indication that the approximation of the SPTR being independent of the bias overvoltage is not absolutely true. By looking more closely at picture 7.8 in section 7.3.5 we can even see a slight dependence of the SPTR on the bias voltage. Furthermore for 1.1V overvoltage we have no measured SPTR value available, and thus the simulation for this bias overvoltage region is simple extrapolation. Figure 7.13 shows an interesting behavior at low threshold values. As we had noted in chapter 6.5 the rise in the CTR value at low threshold values is caused by the SPTR and electronic noise. The fact that, in this low threshold region, the MC simulation predicts consistently lower CTR values than the measured data could be explained by a deficiency in the model of the single cell signal. An additional parabolic component at the beginning of the

single cell signal could lead to a lower slew rate of the signal at low threshold values. Because of electronic noise this would lead to a deterioration of the measured CTR values as compared to the simulation, where we assumed a simple bi-exponentially shaped single cell signal.
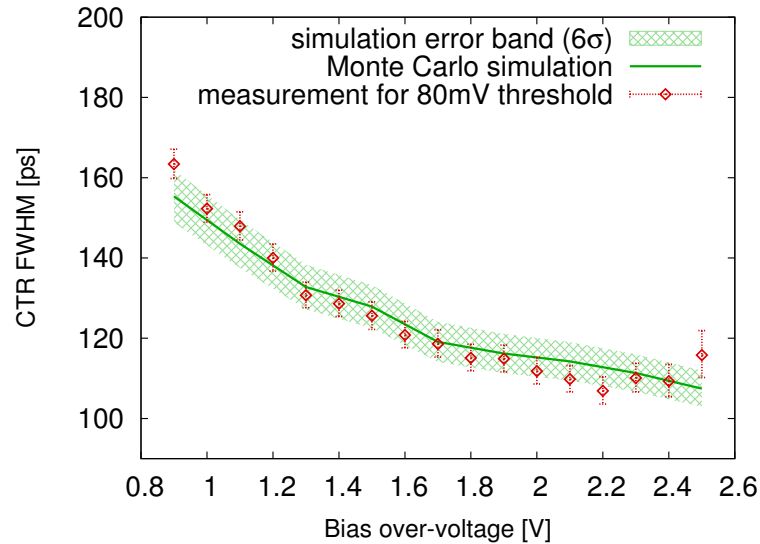
Figure 7.12.: Comparison of CTR values derived from the Monte Carlo simulation tool versus experimental data as a function of the bias overvoltage. Good agreement with experimental data can be seen.
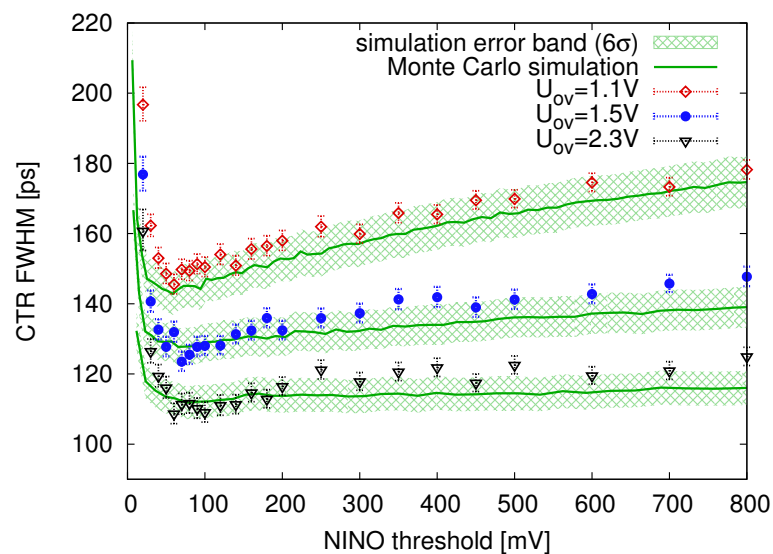
Figure 7.13.: Comparison of simulated CTR values with experimental ones as a function of the NINO threshold for three different bias overvoltages.

The deviation of the measurement from the simulation is in the range of the measurement error plus the statistical fluctuations of the Monte Carlo simulation. In view of the fact that no fits were

made to the experimental CTR data, the agreement between simulation and measurement is quite good.

7.5. Discussion

In the previous paragraph we showed that for the used 2x2x3mm^3 LSO:Ce codoped 0.4%Ca crystal the developed Monte Carlo simulation tool is in good agreement with experimental data. This gives us confidence to correctly quantify the different model input parameters to the CTR. We change one input parameter of the simulation, e.g. light yield, scintillation rise-, fall time, PDE or SPTR while keeping the others constant. In figure 7.14 we depict the minimum simulated CTR values versus the normalized parameter value as can be seen in table 7.4, i.e. the model input parameter under investigation multiplied by a factor ranging from 0.1 to 10.
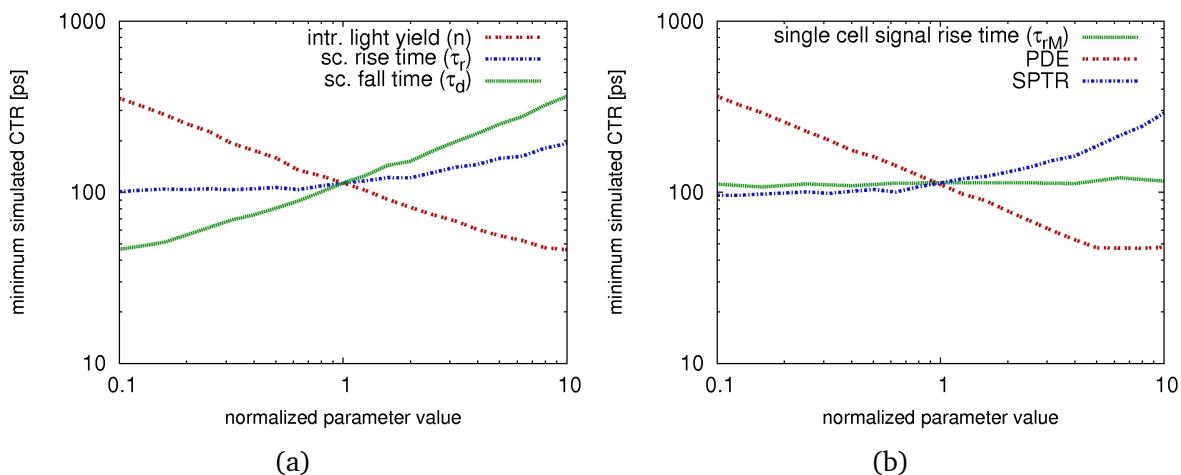
Figure 7.14.: Minimum simulated CTR when scanning one parameter by a multiplicative factor ranging from 0.1 to 10, whilst holding the other parameters constant. (a): scans for intrinsic light yield (n), scintillation rise time (τ_r) and scintillation fall time (τ_d). (b): scans for single cell signal rise time (τ_{Mr}), PDE and SPTR

The CTR is dependent on the square root of the intrinsic light yield (n), the scintillation fall time (τ_d) and the SiPM photon detection efficiency (PDE), i.e. $CTR \propto \sqrt{\tau_d/(n \cdot PDE)}$. This is in agreement with the findings of [82] and [98]. In the conditions given in table 7.4, a lower scintillation rise time (τ_r) than 70ps seems to improve the CTR only marginally. This outcome is also in agreement with [82]. For the minimum CTR values we calculate the number of photoelectrons already piled-up, until the SiPM signal reaches the leading edge threshold, to approximately 10. Because of the electronic noise and the SPTR, triggering on the first photon will not necessarily lead to the best CTR values. This also explains why the scintillation rise time seems to have only little influence on the CTR. If we could reach lower threshold values we might then expect a behavior like $CTR \propto \sqrt{\tau_r}$ as predicted by photon statistics. For the SPTR we observe a similar behavior as for the scintillation rise time: a decrease of the measured SPTR value of 66ps by a factor of 10 only leads to a CTR improvement by $\sim$ 10ps. The single cell signal rise time has almost no influence on

the CTR (see figure 7.14(b)). This is because of the bandwidth limitation of NINO together with the low electronic noise and gain fluctuation in our system.

In figure 7.15 we show the minimum simulated CTR versus bias overvoltage and the simulated CTR versus threshold expressed in terms of equivalent single cell amplitude at an overvoltage of 2.3V. In these graphs we successively eliminate the contributions of electronic noise and gain fluctuations, the dark count and crosstalk probability, the SPTR and finally the light transfer time spread and gamma conversion jitter in the crystal. The light transfer time spread is denoted as $\xi_k(\chi)$ and the gamma conversion jitter as Δt in equation 7.2.7. We always keep the PDE and the photon transfer efficiency of the crystal constant. We can see that electronic noise and gain fluctuations have almost no influence on the final time resolution. We notice an improvement only for very low bias and equivalent cell amplitude values if we set these two terms to zero. If additionally we also set the dark count and crosstalk probabilities to zero, we notice an improvement by ~5-10ps at 2.3V overvoltage. This improvement is mostly due to the absence of crosstalk. Setting additionally the SPTR to zero leads to an further improvement of around 20ps. The improvement is larger as compared to the one obtained in figure 7.14(b), because the influence of dark count, crosstalk and electronic noise is already subtracted. In figure 7.15(b) we see that the CTR changes significantly as a function of the equivalent cell amplitude. Because of the zero SPTR, a minimum in the CTR plot at very low threshold values is observed, meaning that Poisson-photostatistics gain in influence. If we only consider Poisson-photostatistics triggering on the first photon would then lead to the best CTR, which in our system occurs only at very low thresholds. The last test is to set the influence of the light transfer time spread and gamma conversion jitter in the crystal to zero. An additional improvement of approximately 25ps can be seen in figure 7.15, manifesting the importance of the crystal dimensions on time resolution, and this even for small crystals with dimensions of only $2x2x3mm^3$. We want to mention that for these tests we kept the PDE and photon transfer efficiency constant.
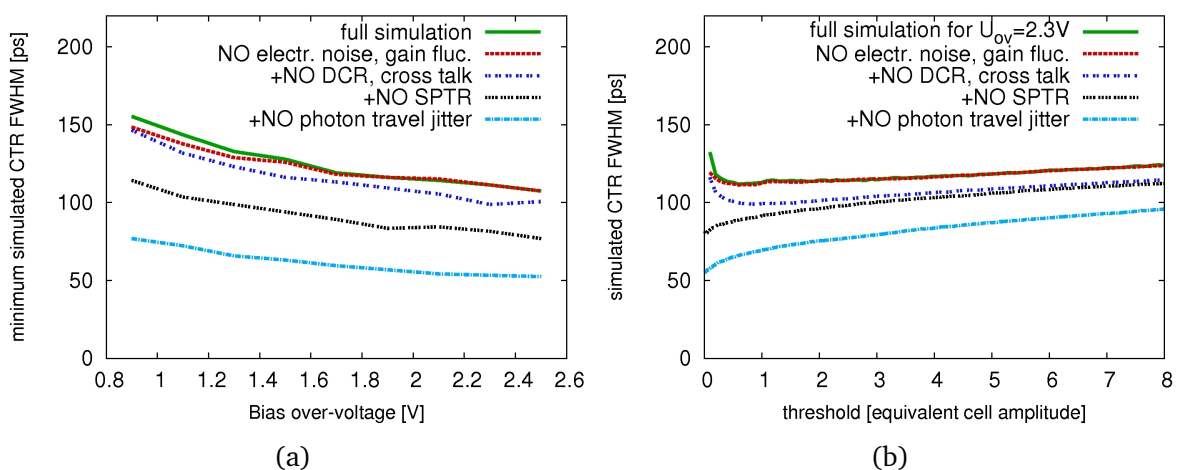
Figure 7.15.: Subtracting consecutively: electronic noise and gain fluctuation, DCR and crosstalk, SPTR, light transfer time spread and gamma conversion jitter (a): minimum simulated CTR versus bias overvoltage and (b): CTR versus threshold for 2.3V bias overvoltage

In figure 7.16 we show the improvement of the CTR if we only set the light transfer time spread plus the gamma conversion jitter to zero and leave all other parameters unchanged. Even in this case we see an improvement of around 20ps. The improvement is smaller because other factors like SPTR, DCR and crosstalk are deteriorating the CTR. We can estimate the influence of the light transfer time spread plus the gamma conversion jitter to the CTR to $\sqrt{(110ps^2 - 90ps^2)} = 63ps$. According to [39] we can determine the gamma conversion jitter for a $2x2x3mm^3$ size crystal to approximately 6ps FWHM CTR and thus negligible if compared to 63ps.

To understand the rather dramatic influence of the crystal size on the CTR we show the light transfer time spread histogram in figure 7.17. For this histogram we simulated random photon emissions in the crystal according to the SLITRANI model also used for the CTR simulations (section 7.3.7).
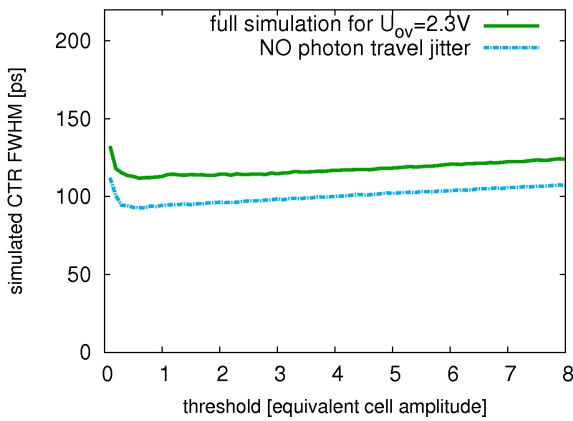
Figure 7.16.: Simulated CTR versus leading edge discrimination threshold in equivalent cell amplitude at an overvoltage of 2.3V. Switching off only the light transfer time spread and gamma conversion jitter in the model leads to an CTR improvement of around 20ps. The PDE and light transfer efficiency (η) of the crystal remain untouched.
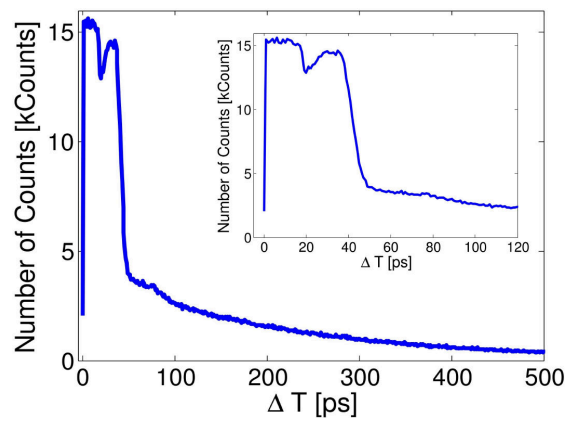
Figure 7.17.: Light transfer time spread in the crystal with a geometry of $2x2x3mm^3$. The left peak stems from directly emitted photons towards the photodetector and the second peak from back-reflected ones. The tail is caused by totally reflected photons due to scattering and surface impurities.

The time from the emission of the photon until it reaches the face of the crystal next to the photodetector is recorded and plotted in the histogram. We can see two initial peaks, the earlier one correspond to direct photons and the later one to reflected photons. The direct photons are the ones emitted directly towards the photodetector, whereas the reflected ones are emitted in the opposite direction and thus have to undergo at least one reflection at the back end of the crystal in order to reach the front face. In addition we observe a rather long exponential-like tail. This tail is caused by photons that are not in a mode to exit the crystal directly. These photons undergo several reflections in the crystal and eventually exit due to surface roughness and scattering in the crystal. It is still under investigation how this tail influences the CTR, as the total number of photons in this tail is not negligible. From figure 7.17 we determine the influence

of the intrinsic light transfer time spread ($\xi_k(\chi)$) to 40ps. This value is smaller than the value of 63ps as calculated from the CTR simulations and gives a first hint on how the tail in figure 7.17 might influence the time resolution.

7.6. Summary and conclusion

To understand the measured CTR values in detail we developed a comprehensive Monte Carlo simulation tool to model the scintillation process and the detector chain, i.e. the light transfer in the crystal, the SiPM properties and the electronics. We took special care of deducing the input parameters for the Monte Carlo simulation without fitting to measured CTR values. Our simulations show very good agreement with the experimental CTRs as a function of both bias overvoltage and NINO threshold. In addition we were able to give a good description of the intrinsic time response of the SiPM when exposed solely to femtosecond laser pulses with different light intensities.

In our system the CTR is strongly dependent on the scintillator's light yield, on the scintillation fall time and the PDE of the SiPM. Due to the interplay of the single cell signal pile-up with the SPTR and the electronic noise we were unable to trigger on the first photon emitted in the scintillation process. Moreover it was shown that because of the SPTR, triggering on the first photon will not automatically lead to the best CTR values. This is a direct consequence when the photon emission rate is smeared by a Gaussian distribution. Consequently the scintillation rise time gives a smaller contribution to the CTR. In addition the assumed rise time of 70ps is low compared to the achieved CTR of 108ps. We used commercial SiPMs from Hamamatsu with a maximum PDE of 33%, a rather modest value. Increasing the PDE of the SiPMs would be a plausible and effective way to improve the time resolution. Also an increase in the scintillation light yield and a faster decay time would both lead to similar improvements.

With the developed model we determined the photon travel spread in the crystal influencing the time resolution to a high degree. If we artificially set the photon travel spread for the used $2x2x3mm^3$ geometry to zero we would obtain a CTR improvement of 20ps. For PET systems, crystals of 20mm length and longer are needed to achieve an acceptable conversion efficiency of the 511keV gamma rays. Thus the influence of the photon travel spread will be more significant and consequently a potential problem, if a CTR of 100ps FWHM is to be achieved. Techniques like double-sided readout with travel spread corrections could be a possible solution in that case which will be described in chapter 9.

Chapter 8

Time resolution in dependence on crystal length

8.1. Introduction

In chapter 6 we have shown that with 2x2x3mm^3 LSO:Ce codoped 0.4%Ca crystals coupled to commercially available SiPMS (Hamamatsu S10931-050P MPPC) a CTR of 108±5ps FWHM can be achieved. At this high time resolution, the time spread due to photon transport within the crystal turns out to be non-negligible to the overall time resolution [10, 11]. Already for crystals with lengths of 3mm this influence is relatively high, i.e. setting for a 2x2x3mm^3 crystal the influence of the photon travel spread (PTS) to zero, would lead to an improvement of 20ps (from 108ps FWHM CTR to 90ps FWHM CTR) as discussed in chapter 7. The degradation in CTR with increasing crystal length is caused by the photon travel spread (PTS) and light transfer efficiency (LTE) loss in the crystal. Throughout this chapter we will define the PTS as the combined influence of the gamma interaction point fluctuation in the crystal (given by its absorption characteristics) and the scintillation light transfer time spread (LTTS). The LTTS is the time fluctuation of a scintillation photon from the time of its production to impinging on the photodetector assuming an isotropic angle of emission. Hence the LTTS is dependent on the gamma interaction point (scintillation origin) in the crystal. In a TOF-PET system crystal lengths of 20mm and longer are necessary to achieve adequate detection efficiency of the 511keV gamma. Hence, it is necessary to study the CTR dependence as a function of the crystal length. In a further step the influence of the PTS and LTE to the CTR has to be understood, both as a function of the crystal length.

This chapter is organized in three main sections; first we present measurements for different crystal lengths of 3mm, 5mm, 10mm and 20mm. The second part compares the predicted CTR values of the developed Monte Carlo simulation tool, as discussed in chapter 7, with the measurements. And the third part models the different contributions to the time resolution such as the photon travel spread (PTS) and the light transfer efficiency (LTE), i.e. the ratio of photons reaching the photodetector to the total amount of photons generated by the scintillation. The content of this chapter was published in [99].

8.2. CTR and light output measurements for different crystal lengths

The time resolution was determined for different crystal lengths in the same coincidence config-
uration as shown in figure 6.8 in chapter 6. A summary of the measured CTR and corresponding
light output values can be seen in table 8.1. In figure 8.1 we depict the CTR versus the SiPM
bias overvoltage for these different crystal lengths, always measured at a NINO threshold of 80mV
(this is equivalent to approximately half a single MPPC cell amplitude height). A minimum of
the CTR as a function of overvoltage can be seen at ~2.2V for all crystal lengths. Examples of
delay time histograms with best CTR values achieved are shown in figure 8.3, i.e. for 5mm and
20mm lengths. In figure 8.2 we depict the CTR versus the NINO threshold for the different crystal
lengths, measured at a SiPM overvoltage of 2.3V. The minimum CTR value can be seen at ~80mV
threshold similar for all crystal lengths.

Table 8.1.: Geometrical properties, CTR configuration, measured light output [37] and measured CTR of
the used crystals. The term "5FP" refers to the $2x2mm^2$ face opposite to the SiPM being unpolished.
Whereas "6FP" means that all crystal faces are polished. Crystals were fully wrapped in Teflon and coupled
to the photodetector with optical grease (Rhodorsil 47V).

size $[mm^3]$	configuration surface state	averaged light output [kph/MeV]	CTR [ps]
2x2x3	5FPvs5FP	26.2±1.3	108±5
2x2x5	5FPvs5FP	24.0±1.2	123±7
2x2x10	5FPvs6FP	20.7±1.0	143±7
2x2x20	6FPvs6FP	14.8±0.7	176±7

We always measured two crystals in coincidence, however with different surface state configu-
rations as can be seen in column two of table 8.1. The term "5FP" means that the $2x2mm^2$ face
opposite to the SiPM is unpolished, whereas "6FP" denotes that all faces of the crystal are polished.
This work mainly aims at the comparison between MC simulation and experimental data. Hence
the use of different surface configurations is not a problem as long as this circumstance is taken
into account in all MC simulations and calculations. The light output values are taken from [37],
similar to the ones stated in table 7.3 in chapter 7. For the 10mm crystal length configuration
we account for the different surface states by averaging the light output value over the 5FP and
6FP cases as for this particular crystal length we used a 5FP versus 6FP configuration in the CTR
setup (see table 8.1). In addition we want to mention that the LY difference between 5FP and 6FP
crystals with same length is small, of the order of a few percent (as can be seen in table 7.3). This
further justifies the use of crystals with different surface finishings.
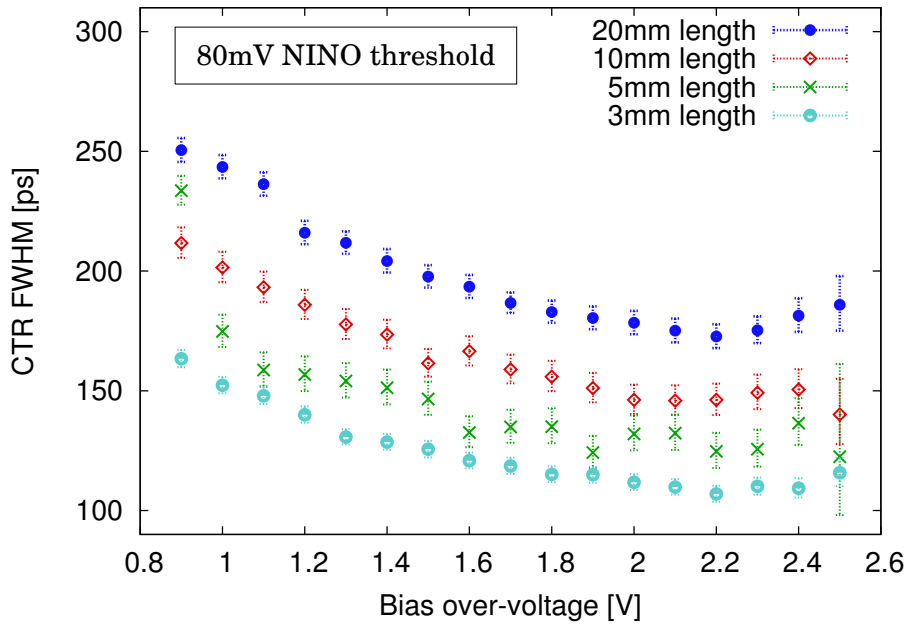
Figure 8.1.: Measured CTR as a function of SiPM bias overvoltage for different crystal lengths at a NINO threshold of 80mV. An optimum in CTR can be seen at approximately 2.2V overvoltage similar for all crystal lengths.
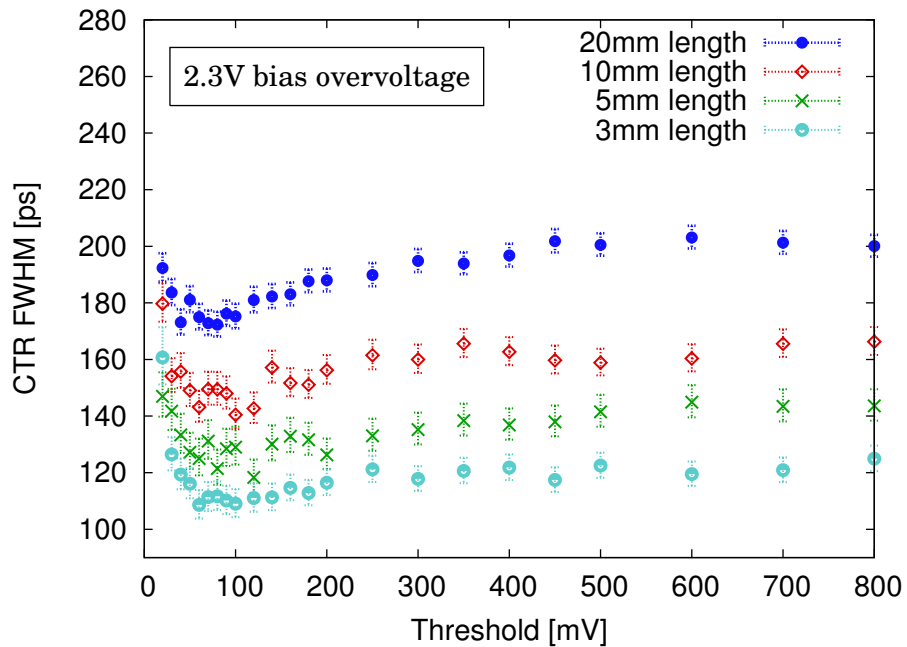
Figure 8.2.: Measured CTR as a function of NINO threshold voltage for different crystal lengths at a SiPM bias overvoltage of 2.3V. An optimum in CTR can be seen at approximately 80mV threshold for all crystal lengths.
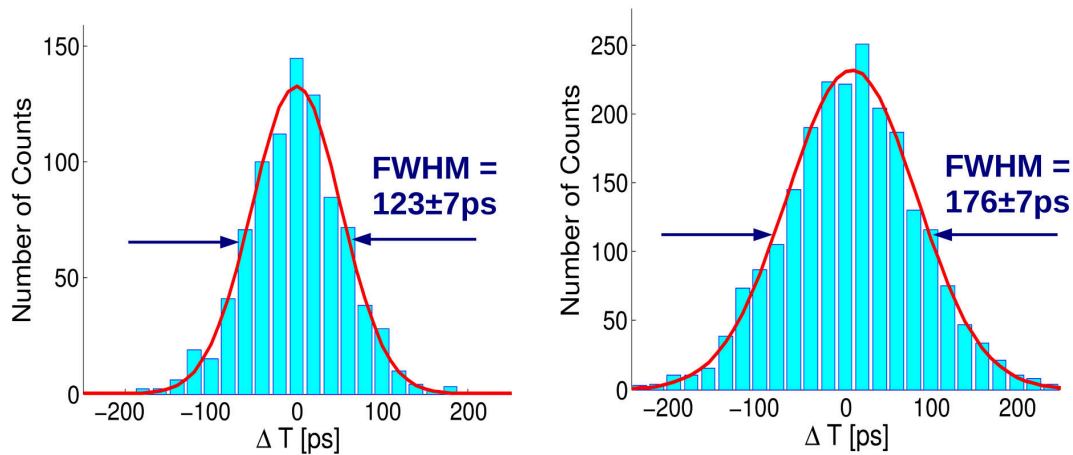
Figure 8.3.: Measurements for LSO:Ce codoped 0.4%Ca with dimensions of $2x2x5mm^3$ and $2x2x20mm^3$ yield a CTR of 123±7ps and 176±7ps, respectively.

In figure 8.4 we show the best CTR measured versus the crystal length (crystals were wrapped in Teflon and coupled with optical grease to the SiPM) and the CTR corrected for the light output as shown in figure 8.5. The light output (LO) was measured with a Photonis XP2020Q photomultiplier tube and not with the MPPC itself for the following reason: LY measurements in a SiPM are prone to nonlinearities arising from optical crosstalk, the DCR (dark count rate) and photon pileup due to the limited number of SPADs in the chosen device. These shortcomings are not present in PMTs, notably the Photonis XP2020Q where we applied for the LY only a wavelength-dependent correction to the quantum efficiency.
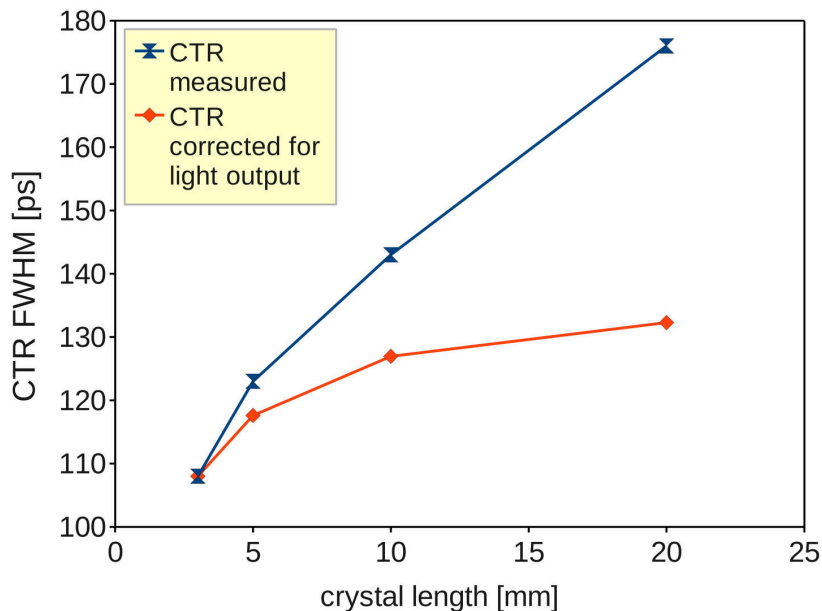
Figure 8.4.: CTR measured for different crystal lengths and CTR corrected for the light output. The bias overvoltage was set to 2.3V for the CTR measurements.

The light output correction to the CTR accounts for the photon statistics and therefore is done with the square root of the relative light output (normalized to the 3mm case) $CTR_{corrected} = CTR_{measured} \cdot \sqrt{LO_{measured}/LO_{3mm}}$ [98]. Even by applying this correction, an increase in CTR value with crystal length still remains (see figure 8.4). This increase is caused by the LTTS plus the gamma interaction point fluctuation in the crystal. Looking at figure 8.4 we notice that for longer crystals the light output correction has a larger effect and that the deterioration in CTR caused by the PTS seems to level off. This asymptotic behavior can be explained by the gamma interaction probability in the crystal which is highest near the gamma entrance of the crystal opposite the SiPM and decreases exponentially with an interaction length of ∼12mm in LSO [31]. Thus, for long crystals the density of gamma interactions along the crystal axis decreases rapidly making the contribution of gamma interactions close to the photodetector less important. A possible consequence is that for long crystals (>10mm-20mm) the LTE begins to dominate the CTR in contrast to the PTS.
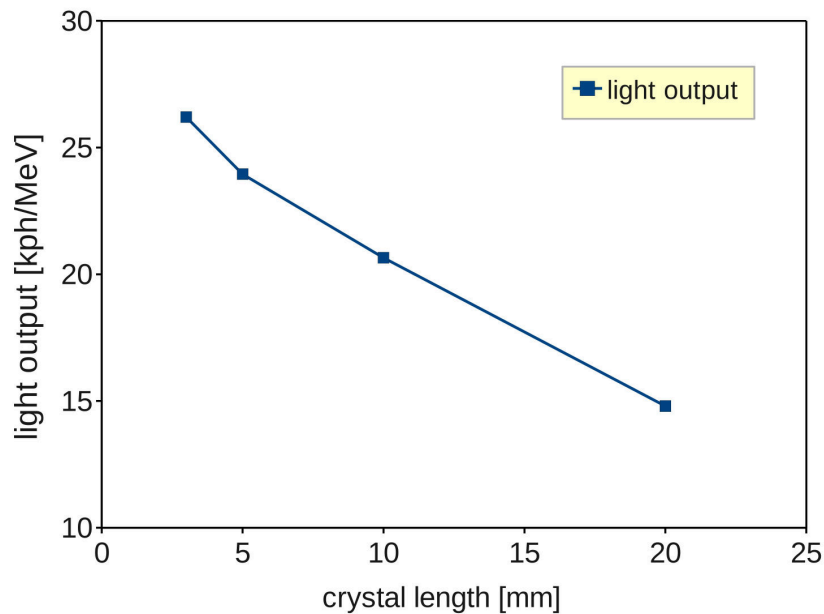
Figure 8.5.: Light output versus crystal length. Measured with a Photonis XP2020Q photo multiplier tube (PMT), values taken from [37]

8.3. Monte Carlo simulation framework

To predict the CTR measurements and to get a reliable time model we developed a Monte Carlo (MC) simulation program that includes the light ray tracing simulations from SLITRANI [37] as described in chapter 7. For convenience to the reader we again give a short overview of the model. Figure 8.6 shows a schematic describing the components taken into account in the Monte Carlo simulation.

In the MC simulation we recorded the time Δt from the generation of the gamma until its absorption in the crystal. At the point of gamma absorption 20400 photons/511keV are emitted

isotropically [37]. For the utilized LSO:Ce codoped 0.4%Ca crystal the emission of the k-th scintillation photon $t_{Scintillation}(k)$ is modeled by a bi-exponential with a rise time of 70ps and a fall time of 30ns [37]. Every k-th scintillation photon is subject to light ray tracing in SLITRANI. With the light ray tracing program we thus calculate the LTTS and the LTE. The LTTS gives rise to a time jitter of every k-th photon which is described by $t_{light\,transfer}(k)$ in equation 8.3.1. It should be noted that the LTTS and LTE are dependent on the gamma interaction point in the crystal. The timing properties of the photodetector are accounted for by adding an additional time event t_{SPTR} that is Gaussian distributed describing the single photon time resolution (SPTR) expressed as standard deviation.
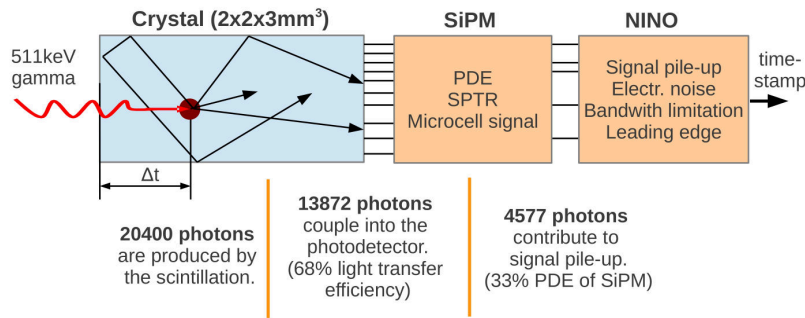
Figure 8.6.: Flow diagram of the photon conversion and propagation in the radiation detector. Shown is the special case of a 3mm long crystal (5FP).

We then overlap the microcell signal responses of the detected photons with the proper time delay, according to equation 8.3.1.

$$t_{k-thphoton} = \Delta t + t_{Scintillation}(k) + t_{light\,transfer}(k) + t_{SPTR}(k) \qquad (8.3.1)$$

As can be seen in figure 8.6, detected photons had to undergo absorption in the crystal and detection by the SiPM expressed by the LTE and the photon detection efficiency (PDE), respectively. On the resulting signal we apply leading edge discrimination taking also into account noise and bandwidth limitations of the electronics (see figure 8.7). A more detailed description and definition of the MC input parameters can be found in [37] and in chapter 7.
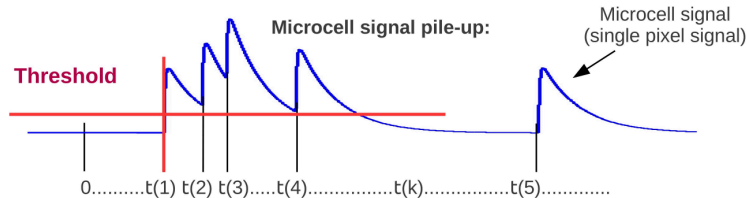
Figure 8.7.: Illustration of the microcell signal pile-up. Each microcell signal is added with the proper delay. Applying a threshold on the summed signal gives the time stamp for one 511keV gamma. In reality pile-up is so rapid that the subsequent cell-signals already sum up on the rising edge of the first cell-signal.

8.4. Comparison of simulations with measurements

In this section we compare the CTR measurements with the Monte Carlo simulations for different crystal lengths. It should be noted that in our simulation we deduced all MC input parameters from CTR-independent measurements [37] so as to avoid bias to the calculated CTR values as much as possible. In figure 8.8 - figure 8.11 we show the measured CTR versus bias overvoltage and CTR versus the NINO threshold. The simulations are overlaid as solid lines with their corresponding error "bands".
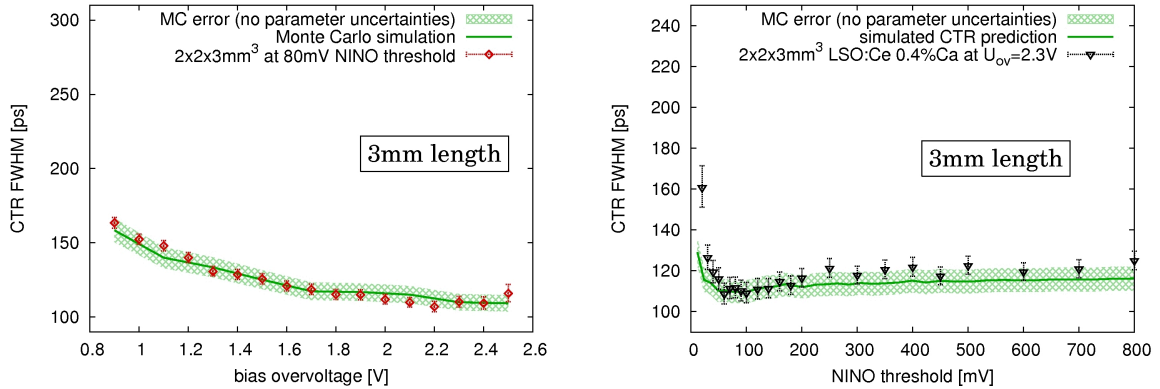
Figure 8.8.: Measurements for LSO:Ce codoped 0.4%Ca with dimensions of $2x2x3mm^3$ yielding a minimum CTR of 108±5ps.
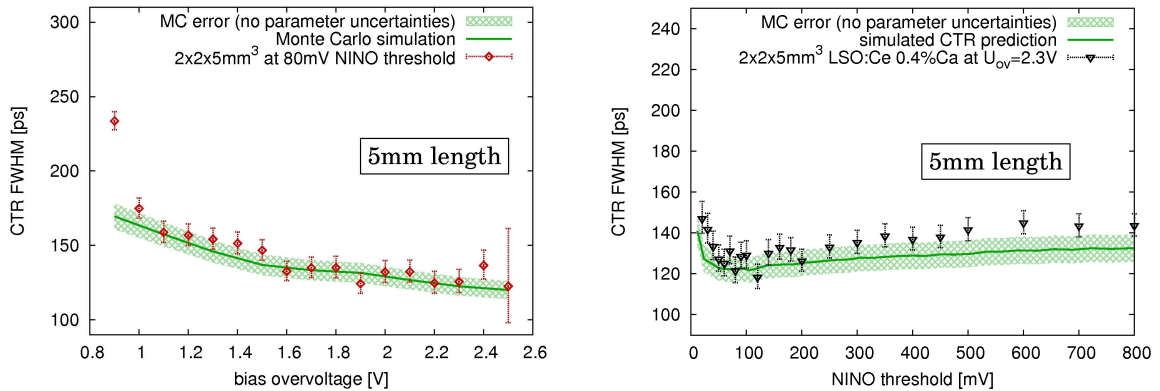
Figure 8.9.: Measurements for LSO:Ce codoped 0.4%Ca with dimensions of $2x2x5mm^3$ yielding a minimum CTR of 123±7ps.

The figures 8.8 - 8.11 show that our simulation tool is in good agreement with the CTR measurements in terms of the SiPM bias overvoltage and NINO threshold scans. This was already presented in [37] and chapter 7. The MC tool also closely predicts the deterioration of the CTR with increasing crystal length. However, for longer crystals we notice a systematic underestimation of the predicted CTR values as compared to the measurements. This could be a hint that our simulation underrates the LTTS for longer crystals. A possible reason is an additional time

117

smearing caused by random delays of photons scattered by the Teflon reflector. Another explanation could be a poor polished surface state of the lateral faces, which we observed for the 20mm case. This would cause additional light loss during the transfer and thus explains the observed deviations for the longer crystal cases.
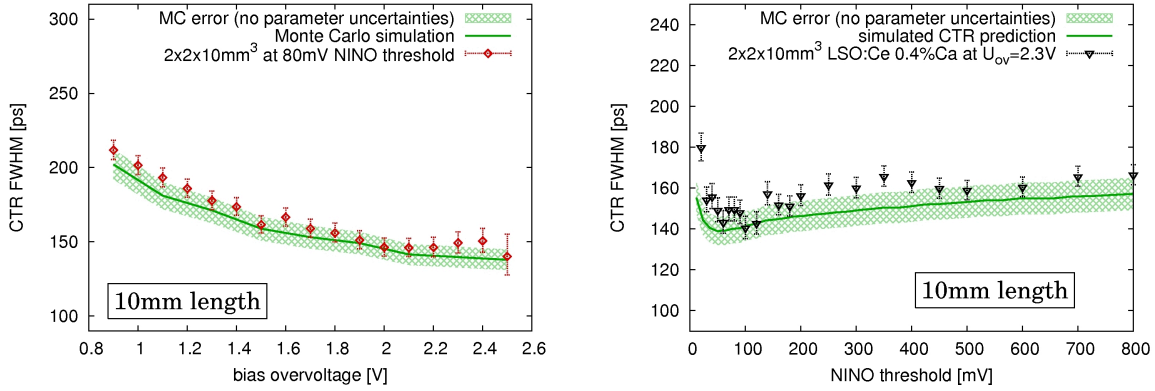
Figure 8.10.: Measurements for LSO:Ce codoped 0.4%Ca with dimensions of $2x2x10mm^3$ yielding a minimum CTR of 143±7ps.
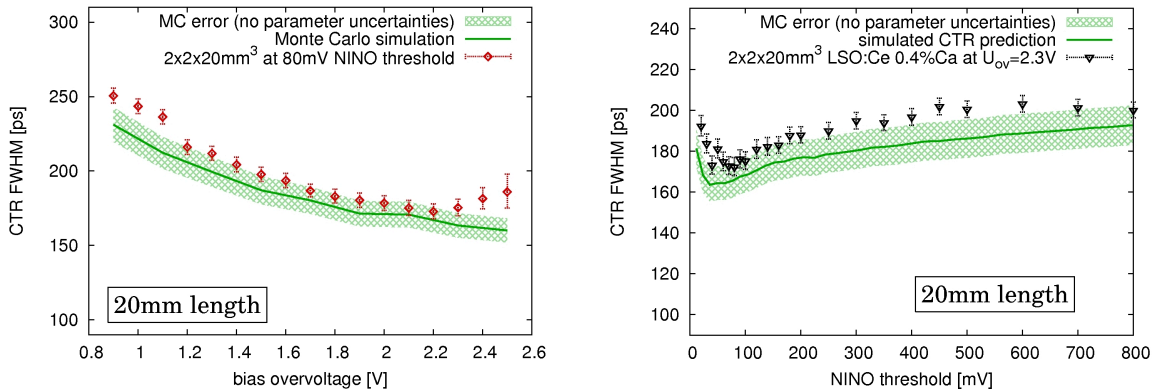
Figure 8.11.: Measurements for LSO:Ce codoped 0.4%Ca with dimensions of $2x2x20mm^3$ yielding a minimum CTR of 176±7ps.

The simulations are able to represent our measurements within the combined errors of the experiment and simulations. The MC simulation error takes into account only the uncertainty due to the limited number of simulated gamma interactions, namely 5000 (purely statistical error). Thus, we have not yet incorporated the uncertainties of the individual input parameters, which would increase the MC errors.

8.5. Discussion

All simulations were performed with an intrinsic light yield of 39920±4000ph/MeV (see section 7.3.7 in chapter 7), which we determined for our LSO:Ce codoped 0.4%Ca scintillators from the

work of [37]. The deterioration of the CTR values with increasing length is a combined effect of LTE and PTS, as we can describe the SLITRANI light ray tracing results by only these two terms. The MC simulation predicts the measured CTR very well, justifying to investigate the influence of the LTE and PTS to the CTR in more detail. In figure 8.12 we show the best measured CTR values for different crystal lengths compared with the standard Monte Carlo simulation, i.e. taking all factors into account in order to simulate the measurement setup. As already mentioned the simulation underestimates the CTR values for larger crystal lengths. This behavior is still under investigation but can be an indication that in our simulation we systematically underestimate the LTTS. We also show the CTR versus the crystal length if the LTE is kept constant. figure 8.12 shows two cases, LTE corresponding to the case of 2x2x3mm^3 size and LTE set to one. These curves demonstrate the influence of the PTS to the overall time resolution. We only see a slight deterioration of the CTR with increasing crystal length, i.e. for LTE=1 from 93ps at 3mm to 107ps at 20mm. On the other hand, if we set the PTS to zero the degradation in CTR with increasing length is more pronounced, i.e. from 90ps at 3mm to 125ps at 20mm. Thus, the MC simulation forecasts that for increasing crystal length the PTS contributes less than the LTE. This behavior was already observed in figure 8.4, were we corrected the measured CTR for the measured light output. Although the PTS influence increases only marginally with increasing crystal length its overall influence is noticeable. Turning off the PTS for the 2x2x3mm^3 size improves the CTR from 110ps to 90ps, for the 2x2x20mm^3 size from 166ps to 125ps.
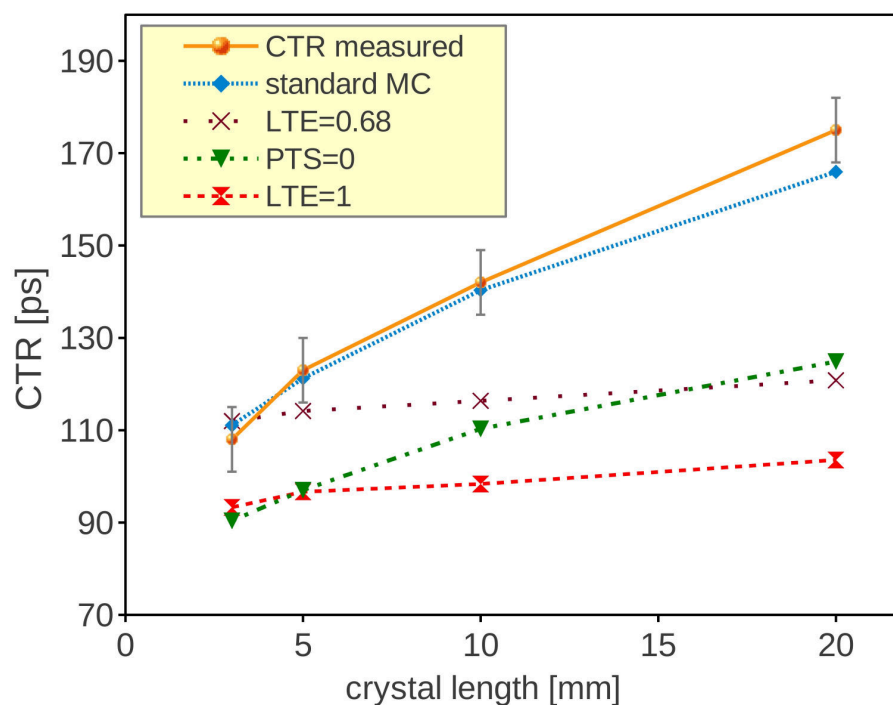
Figure 8.12.: Measured CTR compared with the standard MC simulation, with simulated constant LTE and zero PTS. If the LTE is held constant at a value of one and equal to that of the 3mm case (LTE=0.68), only a small deterioration with increasing crystal length is seen. If the PTS is set to zero the deterioration is more pronounced.

To understand the MC simulation in more detail we show in figure 8.13 and 8.14 the histogram of the LTTS, the weighted LTTS and the weighted PTS for a 2x2x3mm^3 and 2x2x20mm^3 crystal, respectively. The LTTS, shown as solid line, represents the time from the emission of a scintillation photon to reach the photodetector, with equal emission probability at every position in the crystal. In figure 8.13 the LTTS shows two peaks, the first one is caused by photons being emitted towards the SiPM (direct photons) whereas the photons in the second peak had to undergo at least one reflection on the "back" face opposite to the SiPM until reaching the photodetector. The tail seen at larger times is caused by photons that cannot escape the crystal directly and thus are subject to scattering, e.g. in the crystal bulk, at the surface or wrapping. We show as "weighted LTTS" the LTTS weighted by the gamma absorption in the crystal with an absorption length of 12mm. For longer crystals (see figure 8.14) the weighted LTTS histogram is squeezed in time as compared to the LTTS, which is caused by a higher probability of emission of scintillation photons at the opposite side of the SiPM, where gamma events are being absorbed with a higher probability. If in addition we account for the travel time of the gamma in the crystal we define the weighted PTS. The weighted PTS histogram is even more squeezed in time than the weighted LTTS, giving evidence that the gamma interaction in the crystal is able to offset at least partly the LTTS. This type of offset is only valid if the gamma enters the crystal opposite to the SiPM. Thus, a later conversion of the gamma (deeper penetration into the crystal) entails a shorter distance for scintillating photons directly emitted to the SiPM. Hence, the gamma absorption in the crystal plays an important role in reducing the effect of the scintillation light transfer time spread, becoming more relevant for increasing crystal length.
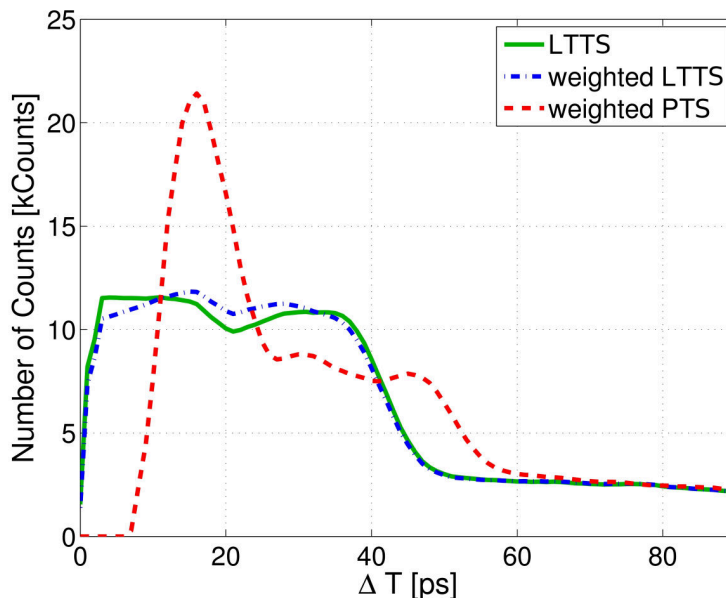
Figure 8.13.: Histogram of LTTS, weighted LTTS and weighted PTS for a 2x2x3mm^3 crystal. Weighted LTTS accounts for the absorption length of the gamma photon and weighted PTS in addition for the travel time of the gamma in the crystal.
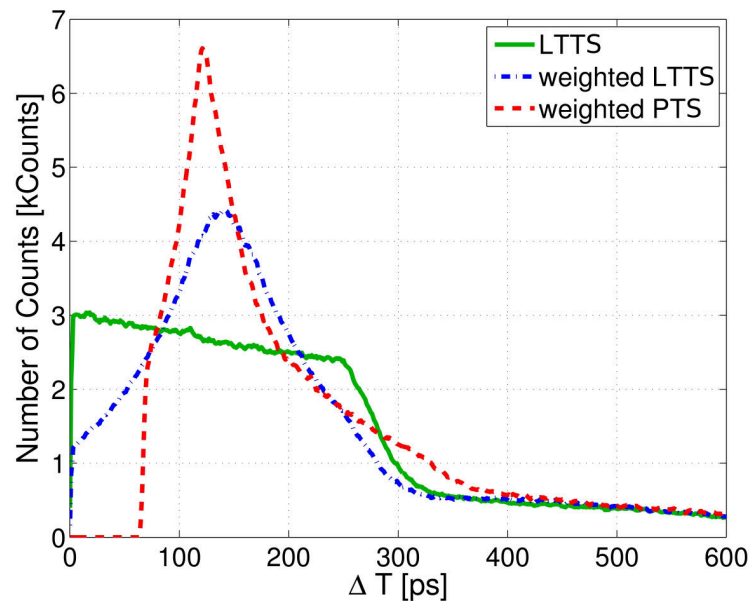
Figure 8.14.: Histogram of LTTS, weighted LTTS and weighted PTS for a 2x2x20mm³ crystal. Weighted LTTS accounts for the absorption length of the gamma photon and weighted PTS in addition for the travel time of the gamma in the crystal.

In figure 8.15 and 8.16 we show the LTTS as a function of the depth of interaction (DOI) for 3mm and 20mm crystal lengths, respectively. In figure 8.16, for example (while same arguments also hold for figure 8.15), three different DOI configurations for a 20mm long crystal are shown. DOI=20mm denotes a gamma interaction taking place in a 2x2x0.5mm³ slice adjacent to the SiPM. Two light peaks can be seen, a first one at 0ps stemming from photons emitted directly to the SiPM and a second peak at 280ps originating from photons emitted to the other side of the crystal and thus reflected at the crystal surface opposite to the SiPM. DOI=0mm, on the other hand, describes the case where the gamma interaction was at the entrance face of the crystal, i.e. opposite to the SiPM. Consequently both the reflected and direct photons need approximately the same time to reach the photodetector. This then shows up as a single peak in both figures.

If for a 20mm long crystal the gamma interaction takes place close to the SiPM (DOI=20mm), the back-reflected photons undergo a large delay of ∼280ps as can be seen in figure 8.16. Whether these delayed photons contribute to the CTR or not, will be explained as follows: In the MC simulation for the 2x2x20mm³ crystal we force the gamma interactions to be close to the SiPM (DOI=20mm), i.e. in a small slice adjacent to the SiPM. In this specially prepared simulation we estimate the average time lag from the instant of gamma conversion to the point where the signal crosses the threshold to ∼250ps. The threshold value was set as such to reach the highest CTR. Therefore, combining the results in figure 8.16 (DOI=20mm) with this outcome shows that reflected photons from a 20mm long crystal simply arrive too late at the photodetector to contribute to the CTR that had already reached its optimum value ∼30ps prior from the directly emitted photons. This fact would also explain why in longer crystals the LTTS has less of an influence on the CTR with increasing crystal length.
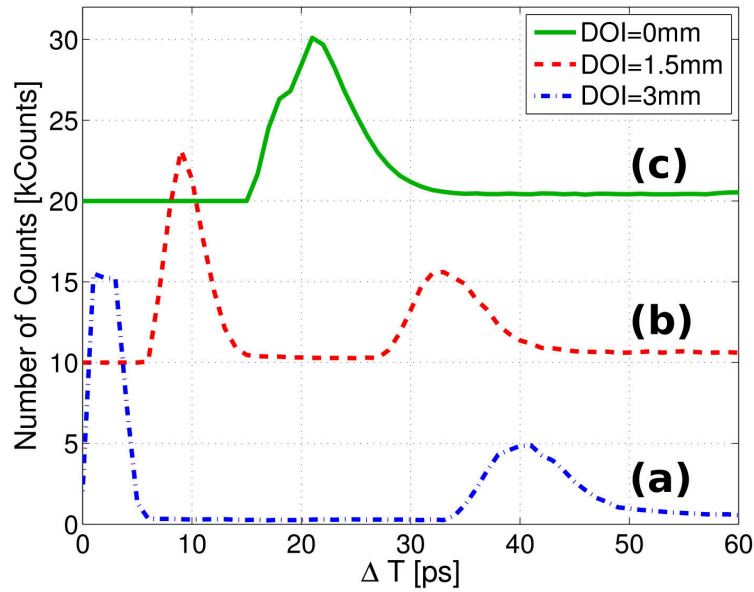
Figure 8.15.: LTTS at fixed DOI for a 3mm long crystal: (a) gamma interaction near the SiPM (DOI=3mm), (b) in the middle of the crystal (DOI=1.5mm) and (c) opposite to the SiPM near the crystal surface (DOI=0mm)
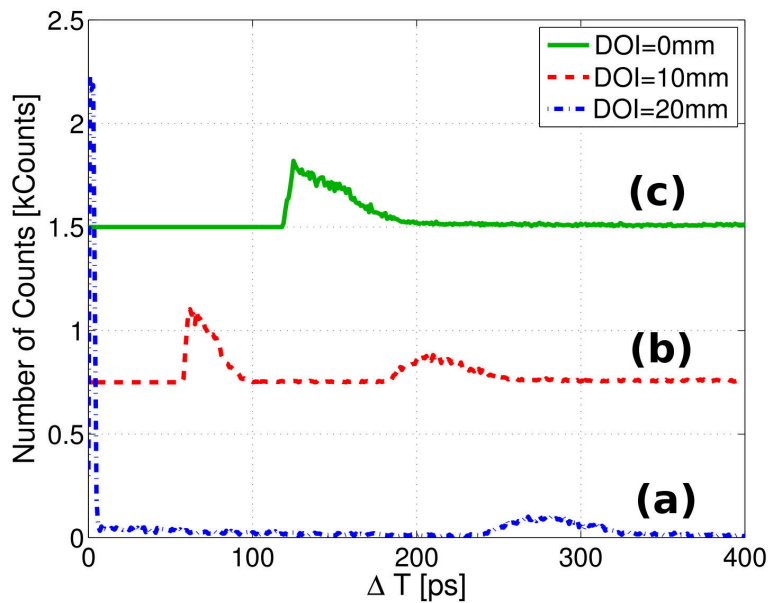
Figure 8.16.: LTTS at fixed DOI for a 20mm long crystal: (a) gamma interaction near the SiPM (DOI=20mm), (b) in the middle of the crystal (DOI=10mm) and (c) opposite to the SiPM near the crystal surface (DOI=0mm)

To investigate the influence of the crystal cross section to the CTR we simulated different configurations as shown in table 8.2. In this simulation we kept the SiPM's active area constant at 3x3mm^2 and varied only the crystals' cross section of a 20mm long crystal from 0.5x0.5mm^2 to

3x3mm^2. As the results show, the simulated CTR does not change significantly as a function of the chosen crystal cross sections. Small deteriorations in CTR can only be seen for 0.5x0.5mm^2 and 3x3mm^2 sections. For the 0.5x0.5mm^2 case the absorption of scintillation light increases (expressed by a lower LTE) due to an increase in the number of reflections from the Teflon shield, giving rise to a slight deterioration in CTR. On the other hand in crystals with 3x3mm^2 cross section, a small loss in scintillation light and thus in photostatistics is caused by photons that may escape through the sidewalls of the 0.5mm thick silicon resin layer protecting the SiPM surface. We therefore conclude that the crystals cross section plays only a small role in the achievable timing performance, which is supported by measurements presented in [10] and in chapter 5 in table 5.4.

Table 8.2.: Simulated coincidence time resolution as a function of the crystal cross section. The active area of the SiPM is 3x3mm^2. Crystals are wrapped in Teflon and polished on all sides.

Scintillator cross section [mm^2]	LTE [%]	CTR [ps]
0.5x0.5	29	176±9
1x1	34	166±8
2x2	37	165±8
3x3	32	178±9

8.6. Summary and conclusion

In a TOF-PET system a crystal length of 20mm or longer is necessary to achieve adequate detection efficiency for the 511keV gammas. Measurements were performed using NINO for the leading edge time information and an analog amplifier for the energy information. We achieve CTR values of 108ps FWHM for 2x2x3mm^3, 123ps FWHM for 2x2x5mm^3, 143ps FWHM for 2x2x10mm^3 and 176ps FWHM for 2x2x20mm^3 LSO:Ce codoped 0.4%Ca crystals. Correcting the measured CTR for the measured light output of the crystal with various lengths we could show that the influence of the photon travel spread (PTS) levels off with increasing length. We identified three mechanisms responsible for this behavior, (a) the absorption of the gamma in the crystal with its characteristic absorption length of 12mm reducing the effective sampling of the crystal, (b) the time delay of the gamma entering the crystal until being absorbed, which acts as an offset to the light transfer time spread (LTTS) and (c) highly delayed scintillation photons (e.g. back-reflected photons) that will likely not contribute to the time stamp derived from photoelectron pile-up with leading edge discrimination.

To analyze the measurements in more detail we developed a Monte Carlo simulation tool dedicated to model the complete chain from the gamma ray conversion, scintillation light production and transport in the crystal, light extraction and conversion in the SiPM photodetector to the electronic readout, taking also into account single photon time resolution (SPTR), electronic noise and bandwidth limitations of the electronics. The MC simulation predicts and matches well the

measured CTR values as a function of SiPM bias overvoltage and NINO threshold. In addition, the MC tool is also able to affirm the deterioration of the CTR with increasing crystal length. From the simulation it appears that the PTS plays an inferior role to the CTR deterioration with increasing crystal length than the LTE, which is in good agreement with the measurements (see figure 8.4). Despite the fact that in our simulation the PTS does not increase significantly with increasing length, its overall influence still seems to be quite high. If in the simulation we "turn off" the PTS contribution for the 2x2x3mm^3 crystal size the CTR would improve from 108ps to 90ps and for the 2x2x20mm^3 size from 166ps to 125ps. Setting, in contrast to the above, the LTE in our simulation to one would improve the CTR from 108ps to 93ps for a 2x2x3mm^3 sized crystal and from 166ps to 104ps for a 2x2x20mm^3 sized crystal. It should be noted that the latter improvement (from 166ps to 104ps) is most likely overestimated since our simulation systematically underestimates the LTTS for longer crystals, e.g. the 20mm case.

Our MC simulation also comprised an investigation of the influence of crystal cross section on CTR. Within the framework of the studied cases, shown in Section 8.5, and in agreement with [10], the CTR changes only insignificantly with respect to the scintillator cross section.

To achieve a CTR of 100ps FWHM using crystals with lengths necessary for TOF-PET systems, i.e. 15-30mm, one has to account for both the LTE and PTS. The scintillation light transfer in the crystal has to be understood in more detail, in particular the influence of wrapping. Also a better extraction of the scintillation light into the photodetector must be achieved. Photonic crystals are an interesting approach to meet this challenge [100]. Concepts of employing a double sided readout of the crystal that incorporates the depth of interaction information is also expected to improve the CTR.

Chapter 9

Double sided readout of crystals

9.1. Introduction

Using double sided readout of a long aspect ratio crystal can improve the time resolution via improving the light output and minimizing the photon travel spread (PTS) in the crystal. In chapter 8 it was shown that in a TOF-PET system the achievable coincidence time resolution (CTR) value is increasing for longer crystals. This deterioration of the CTR with increasing crystal length is mainly caused by the increasing absorption of scintillation light and the consequent loss in photostatistics. On the other hand, it was shown in chapter 8 that the PTS in the crystal increases only marginally with increasing crystal length. Consequently a system employing double sided readout is expected to improve the CTR mainly via the increased light output. In this chapter we will discuss the double sided readout of crystals in terms of its possibilities to improve the CTR.

9.2. Light output difference between double sided and single sided readout

This section gives a theoretical analysis of the total light output using either double sided or single sided readout. In figure 9.1 a scheme of the crystal readout either double sided or single sided is shown.
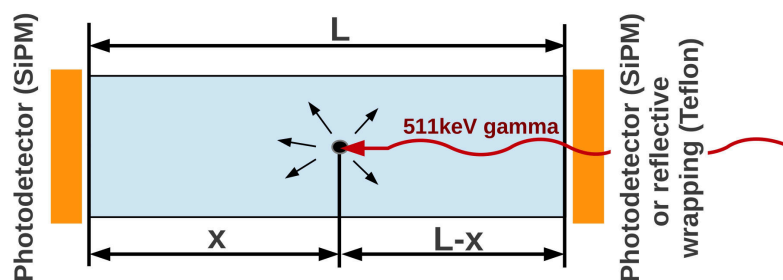
Figure 9.1.: The crystal is either readout on both extremities or readout single sided.

If the 2x2x20mm^3 sized crystal is readout single sided then the SiPM is placed at the crystal extremity which is farthest away from the ^{22}Na source (on the left hand side in figure 9.1). The remaining crystal surfaces are wrapped in Teflon. In the case of double sided readout the two SiPMs are coupled to the 2x2mm^2 faces of the crystal and the remaining lateral faces are wrapped in Teflon.

The photoelectron intensity $i_L^S(x, \tau)$ (see formula 9.2.1) describes the light output of a single sided readout crystal for a gamma event taking place at the DOI position $(L-x)$. The parameter τ is the effective attenuation length in the crystal. It includes all effects causing loss of scintillation photons, e.g. absorption in the bulk or wrapping, scattering on the surface or wrapping. I_0 denotes the total number of photoelectrons which could be detected without any absorption.

$$i_L^S(x, \tau) = \frac{I_0}{2} \exp\left(-\frac{x}{\tau}\right) + \frac{I_0}{2} \exp\left(-\frac{2L-x}{\tau}\right) \tag{9.2.1}$$

The intensity $i_{L'}^D(x, \tau)$ describes the combined light output of a double sided readout crystal, i.e. equation 9.2.2 sums up the light output of both photodetectors coupled to the two extremities of the crystal.

$$i_{L'}^D(x, \tau) = \frac{I_0}{2} \exp\left(-\frac{x}{\tau}\right) + \frac{I_0}{2} \exp\left(-\frac{L'-x}{\tau}\right) \tag{9.2.2}$$

In figure 9.2 the photoelectron intensity $i_{L'}^D(x, \tau)$ of a double sided readout crystal with 20mm length is shown. We notice a minimum of the light output at a DOI position $(L-x)$ of 10mm which corresponds to gamma interactions in the middle of the crystal. If the effective attenuation length τ is decreased this minimum is getting more pronounced.
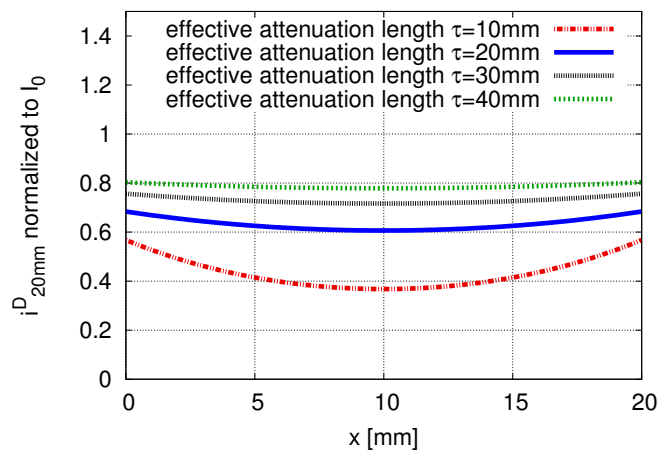
Figure 9.2.: Combined light output $i_{L'}^D(x, \tau)$ of a 20mm long crystal readout on both extremities as a function of gamma interaction point x and effective attenuation length τ.

In equation 9.2.1 and 9.2.2 we describe the light output as a function of a single gamma event in the crystal at position x. If the probability of gamma interactions in the crystal would be uniformly distributed we immediately notice that the light output of a 10mm long crystal readout single sided

is the same as the combined light output of a 20mm long crystal readout on both extremities. However in the experimental conditions we irradiate the crystal with gamma photons along the crystal axis and we have to take into account the 511keV gamma attenuation in the crystal. The averaged intensity supposing a gamma interaction length τ_γ of 11.4mm is described in equation 9.2.3 and 9.2.4 for single sided readout $\overline{I^S_L}(\tau)$ and double sided readout $\overline{I^D_{L'}}(\tau)$, respectively.

$$
\overline{I^S_L}(\tau) = \frac{\int_0^L i^S_L(x,\tau) \exp\left[-\frac{L-x}{\tau_\gamma}\right] dx}{\int_0^{L'} \exp\left[-\frac{L-x}{\tau_\gamma}\right] dx} =
$$

$$
= \frac{\frac{I_0}{2} \exp[-L/\tau_\gamma] \left\{ \frac{\tau_\gamma \tau}{\tau-\tau_\gamma} \left(\exp\left[L \frac{\tau-\tau_\gamma}{\tau \tau_\gamma}\right] - 1 \right) + \exp[-2L/\tau] \frac{\tau \tau_\gamma}{\tau+\tau_\gamma} \left(\exp\left[L \frac{\tau+\tau_\gamma}{\tau \tau_\gamma}\right] - 1 \right) \right\}}{\tau_\gamma \left(1 - \exp\left[-L/\tau_\gamma\right] \right)}
$$

(9.2.3)

$$
\overline{I^D_{L'}}(\tau) = \frac{\int_0^{L'} i^D_{L'}(x,\tau) \exp\left[-\frac{L'-x}{\tau_\gamma}\right] dx}{\int_0^{L'} \exp\left[-\frac{L'-x}{\tau_\gamma}\right] dx} =
$$

$$
= \frac{\frac{I_0}{2} \exp[-L'/\tau_\gamma] \left\{ \frac{\tau_\gamma \tau}{\tau-\tau_\gamma} \left(\exp\left[L' \frac{\tau-\tau_\gamma}{\tau \tau_\gamma}\right] - 1 \right) + \exp[-L'/\tau] \frac{\tau \tau_\gamma}{\tau+\tau_\gamma} \left(\exp\left[L' \frac{\tau+\tau_\gamma}{\tau \tau_\gamma}\right] - 1 \right) \right\}}{\tau_\gamma \left(1 - \exp\left[-L'/\tau_\gamma\right] \right)}
$$

(9.2.4)

In figure 9.3 the effective attenuation length is estimated for the used LSO:Ce codoped 0.4% Ca crystals with a cross section of 2x2mm^2.
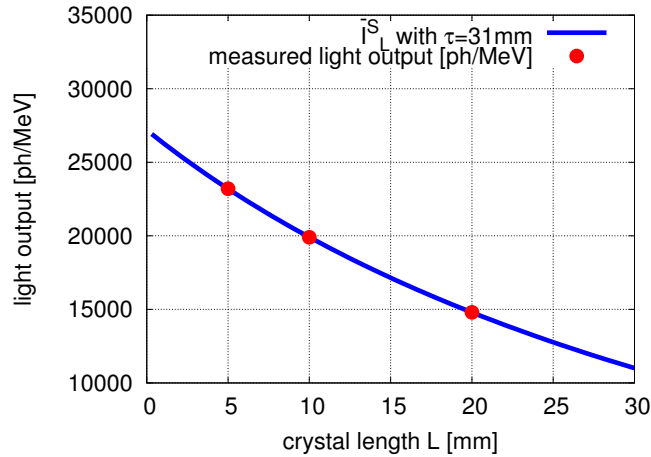
Figure 9.3.: Measured light output in dependence of crystal length (L) with a 2x2mm^2 cross section. Overlaid is the function $\overline{I^S_L}(\tau)$ with a fitted effective attenuation length of $31mm$.

We measured the light output of three different crystal lengths as shown in table 7.3 in chapter

7. The crystals are readout single sided, on the 2x2mm^2 face opposite to the gamma entrance, fully polished, wrapped in Teflon and coupled to the photodetector with optical grease Rhodorsil 47V. Fitting $\overline{I_L^S}(\tau)$ in equation 9.2.3 to the measured light output we can determine the effective attenuation length τ to approximately 31mm (see figure 9.3). This attenuation length should not be confused with the bulk absorption in the crystal [97] as the effective attenuation length τ in addition includes surface properties, e.g. wrapping, surface roughness, and the composition of the detected propagation modes [101].

The quotient $\overline{I_L^S}(\tau)/\overline{I_{L'}^D}(\tau)$ gives the amount of light output loss when a single sided readout configuration is compared to a double sided readout configuration. In figure 9.4 we show this quotient for a crystal of length $L = 10$mm single sided readout and a crystal of length $L' = 20$mm double sided readout. We can see that a crystal of 20mm length which is readout on both extremities gives a better combined light output than a single sided readout crystal of 10mm length, if the gamma enters the crystal opposite the SiPM. However, for an effective attenuation length $\tau = 31$mm we determine the light output of a 20mm long crystal readout double sided almost equal to a 10mm long crystal readout single sided.
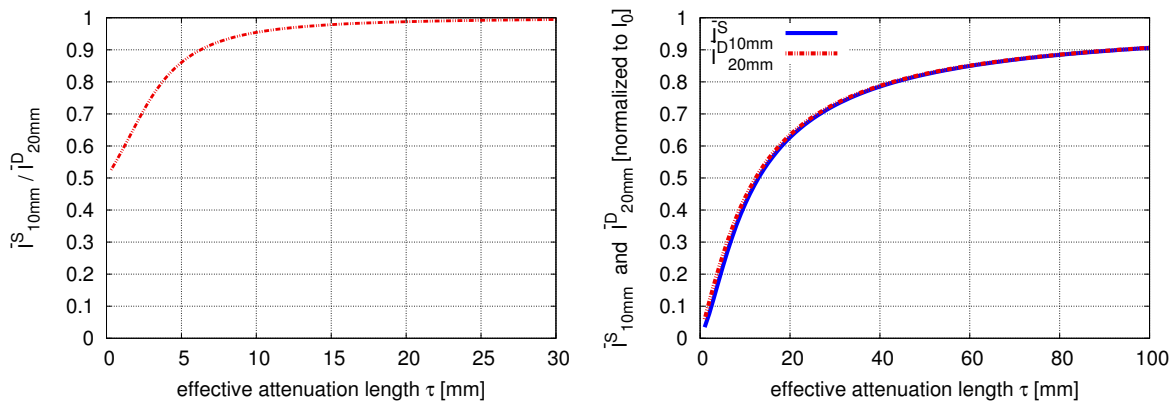
Figure 9.4.: Comparing the light output of a 10mm long crystal single sided readout and a 20mm long crystal double sided readout. Assuming the ^{22}Na source positioned opposite the SiPM in the single sided readout configuration shows that double sided readout gives a higher light output for all attenuation lengths τ.

9.3. Experimental methods and data analysis

The measurement setup consists of a 2x2x20mm^3 LSO:Ce codoped 0.4%Ca crystal readout on both extremities as shown in figure 9.5. The bias voltages of the used SiPMs were set to 2.2V overvoltage according to the best operational point determined in chapter 6. The time resolution is measured versus a 2x2x5mm^3 reference which we determined to have a single time resolution of 85ps FWHM corresponding to 120ps FWHM CTR. For every coincidence event detected we measure two time delays D_1 and D_2. The time delay D_1 is defined as the difference between the time stamp T_1 measured on the left extremity (SiPM 1) of the 20mm crystal and the time stamp of

the reference T_R, i.e. $D_1 = T_1 - T_R$. The time delay D_2 describes the difference between the time stamp T_2 of the right extremity (SiPM 2) versus the reference T_R, i.e. $D_2 = T_2 - T_R$.

In addition to the time delays D_1 and D_2 we as well measure the number of photoelectrons (p.e.) detected by SiPM 1 and SiPM 2, i.e. N_1 and N_2. In figure 9.6 we show the scatter plot of the photoelectrons measured on the right extremity (SiPM 2) versus the photoelectrons detected on the left extremity (SiPM 1). At values around 0.4 and 0.7 for both axis the 511keV and the 1274keV gamma emission peaks of the ^{22}Na source can be seen, respectively. The correlation of the light output can be used to determine the depth of interaction (DOI), i.e. where in the crystal the 511keV gamma was absorbed.
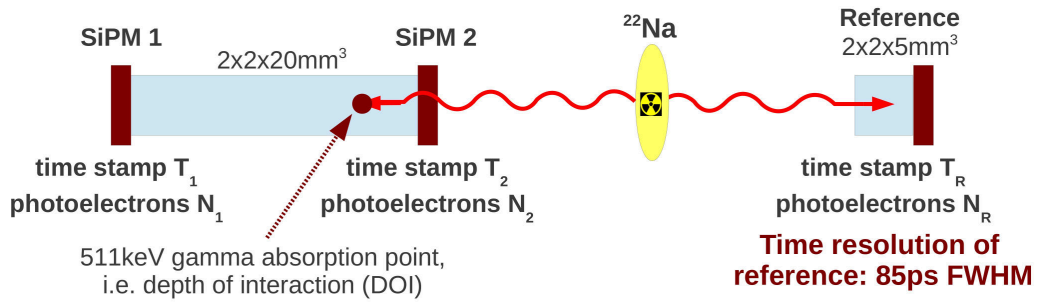
Figure 9.5.: Coincidence time resolution measurement setup as used for the tests employing double sided readout.
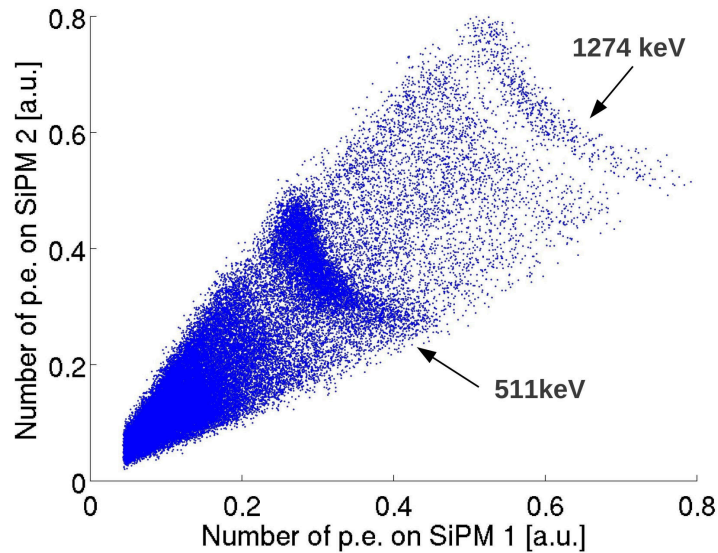
Figure 9.6.: Scatter plot of photoelectrons detected at SiPM 2 versus photoelectrons detected at SiPM 1. The anti-correlation between these two signals makes it possible to determine the depth of interaction.

We will use the DOI information to correct the time delays D_1 and D_2 in such a way as if they were independent on the gamma absorption point. Thus, the idea is to minimize the photon travel

spread in the crystal to a minimum by using this DOI information. Applying a correction factor $S_{D_1}(N_1, N_2)$ for the time delay D_1 and a correction factor $S_{D_2}(N_1, N_2)$ for the time delay D_2 we can express the corrected time delay D as stated in equation 9.3.1. The time delay D is defined as the average of the corrected time delay $D_1 - S_{D_1}(N_1, N_2)$ and the corrected time delay $D_2 - S_{D_2}(N_1, N_2)$ which combines the photostatistics of the left and right extremity (SiPM1 and SiPM2) of the 20mm long crystal. On the right hand side of equation 9.3.1 we simplify the expression to use only one correction factor $S(N_1, N_2)$. The system matrix $S(N_1, N_2)$ describes the propagation time of a 511keV gamma in the crystal until its absorption as a function of the DOI position, expressed by the detected photoelectrons N_1 and N_2. Hence, the full system information is given by $S(N_1, N_2)$ which can be determined in a single calibration measurement.

$$D = \frac{D_1 - S_{D_1}(N_1, N_2) + D_2 - S_{D_2}(N_1, N_2)}{2} = \frac{D_1 + D_2}{2} - S(N_1, N_2) \qquad (9.3.1)$$

It should be noted that the average $(D_1 + D_2)/2$ corrects intrinsically for the scintillation light transfer time spread, i.e. the average propagation time delay of the scintillation photons in dependence of the DOI. As already mentioned the correction $S(N_1, N_2)$ used in equation 9.3.1 does only account for the gamma interaction fluctuation in the crystal.

9.4. Measured CTR with double sided readout

For the CTR measurements we used the setup shown in figure 9.5. In a first step the measurement system was calibrated, i.e. we determined the system matrix $S(N_1, N_2)$. This was done by acquiring a lot of data and calculating the centroid of the term $(D_1 + D_2)/2$ as a function of the photoelectron yield N_1 and N_2. Having determined $S(N_1, N_2)$ we performed a second measurement applying equation 9.3.1 to each coincidence event detected in the crystals in order to calculate the combined and corrected time delay D. In figure 9.7 we show the corrected delay time histogram for all acquired coincidence events. The Gaussian fit gives a time resolution of 138ps FWHM measured against the reference. The single time resolution of the reference was determined to 85ps FWHM in a separate measurement run.

To be able to compare with the standard measurements stated in CTR FWHM we transform the value measured against the reference according to equation 9.4.1. We obtain an equivalent CTR of 154ps FWHM when applying double sided readout of a 2x2x20mm^3 LSO:Ce codoped 0.4%Ca crystal.

$$CTR_{double} = \sqrt{138^2 - 85^2} * \sqrt{2} = 154ps\, FWHM \qquad (9.4.1)$$

In figure 9.8 we directly compare the measured CTR of single sided readout crystals with 10mm and 20mm length to a double sided readout crystal of 20mm length. We are able to achieve a CTR of 176ps FWHM with a 20mm long crystal readout single sided. In contrast double sided readout of the same 20mm long crystal is able to improve the CTR to a value of 154ps FWHM CTR. On the other hand it is interesting to notice that a 10mm long crystal readout single sided shows a slightly better performance of 142ps FWHM CTR as can be seen in figure 9.8.
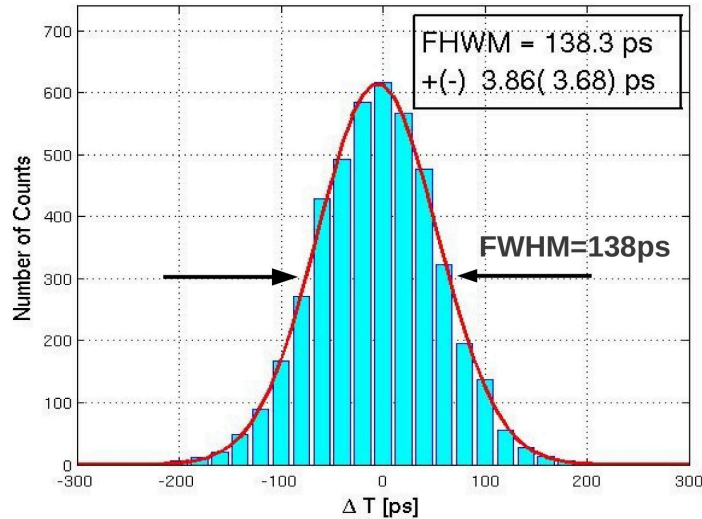
Figure 9.7.: Measured time resolution with double sided readout of a 20mm long crystal versus the reference gives 138ps FWHM. The single time resolution of the reference was determined to be 85ps FWHM. Thus we can express the coincidence time resolution of a double sided readout system to $CTR_{double} = \sqrt{138^2 - 85^2} * \sqrt{2} = 154ps$ FWHM.

Figure 9.8.: Comparing single sided readout with double sided readout. The standard single sided readout measurements give 176ps FWHM CTR for 20mm long crystals. Whereas the time resolution improves to 154ps by using double sided readout of the same 20mm long crystal. In comparison 10mm long crystals readout single sided give a CTR of 143ps FWHM.

The amount of collected photoelectrons of a single sided readout crystal of 10mm length is about the same then the summed light collection of a double sided readout crystal of 20mm length as described in section 9.2. Consequently the time resolution of a 20mm long crystal readout double sided should be compared with the time resolution of a 10mm long crystal readout single sided. The measured value of 154ps FWHM for a 20mm long crystal readout double sided is close to

the achieved coincidence time resolution value of 143ps for a 10mm long crystal readout single sided. However, it is surprising that the double sided readout cannot benefit to a full amount of the higher light output. This may be a hint that the applied formalism is not representing the optimum and could be further improved. On the other hand the concept of single sided and double sided readout are fundamentally different in view of collecting the scintillation light. As described in chapter 8 there are several mechanism mitigating the influence of the photon travel spread in the crystal when readout single sided with the SiPM placed on the extremity opposite the gamma entrance. In such a single sided readout system the light transfer time jitter is partly minimized by the gamma propagation time in the crystal and together with the disregard of highly delayed scintillation photons in the determination of the time stamp effectively mitigates the influence of the photon travel spread. In contrast the corrections applied for a double sided readout system do not include these effects, which may explain the slightly worse time resolution for the 20mm long crystal readout double sided if compared with a 10mm long crystal readout single sided, as shown in figure 9.8.

9.5. Moving the source of positron emission

To prove the formalism described in equation 9.3.1 we moved the source of positron emission along the crystal axis as can be seen in figure 9.9.
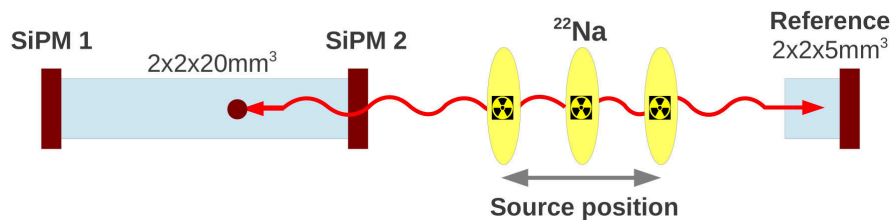
Figure 9.9.: In order to test in more detail the applied procedure for double sided readout we changed the position of the ^{22}Na source in the setup.

In figure 9.10 the corrected combined delay time histogram of the double sided readout 20mm long crystal versus the reference can be seen for three different source positions, i.e. 0cm, 2cm and 4cm. If the ^{22}Na source is moved by 2cm it causes that the source is moved 2cm away from one detector and 2cm towards the other detector. Thus moving the source by 2cm translates to a delay shift of 4cm or equivalent to 133ps which can be seen in figure 9.10.

In figure 9.11 we depict the centroid of the Gaussian fit of the DOI corrected delay time histogram as a function of the ^{22}Na source position. Fitting a straight line to the data we determine a slope of 66ps/cm, representing two times the speed of light in vacuum. Thus the stated formalism in equation 9.3.1 is indeed unbiased against translations of the positron emission point, as it was constructed to be.

Source position: 0cm   2cm   4cm
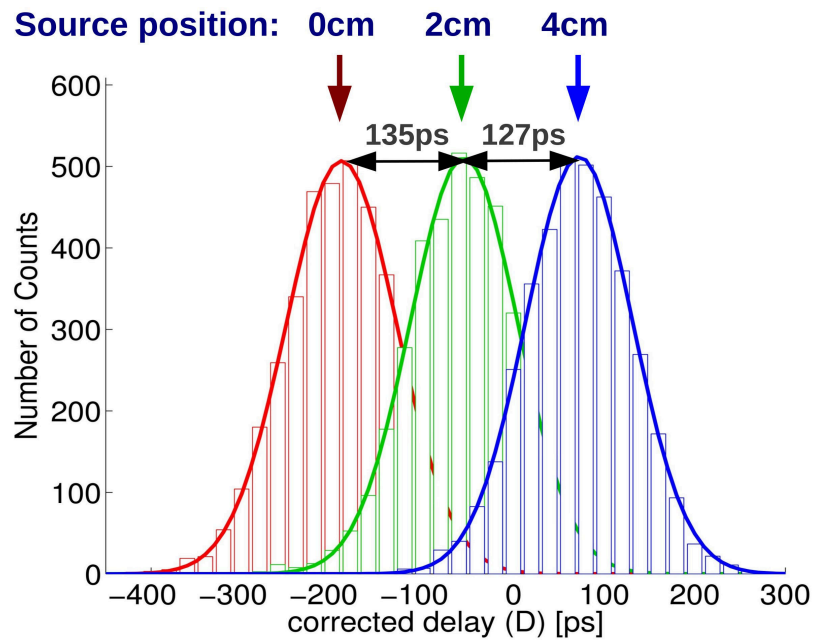
Figure 9.10.: Moving the position of the ^{22}Na source by 2cm results in a Gaussian centroid movement of about 133ps, representing twice the speed of light in vacuum. DOI corrections are applied to all three Gaussian plots. The values stated of 135ps and 127ps are well within the measurement error of ∼10ps.

66ps/cm => two times
speed of light in vacuum

f(x) = 66.0x - 190.5
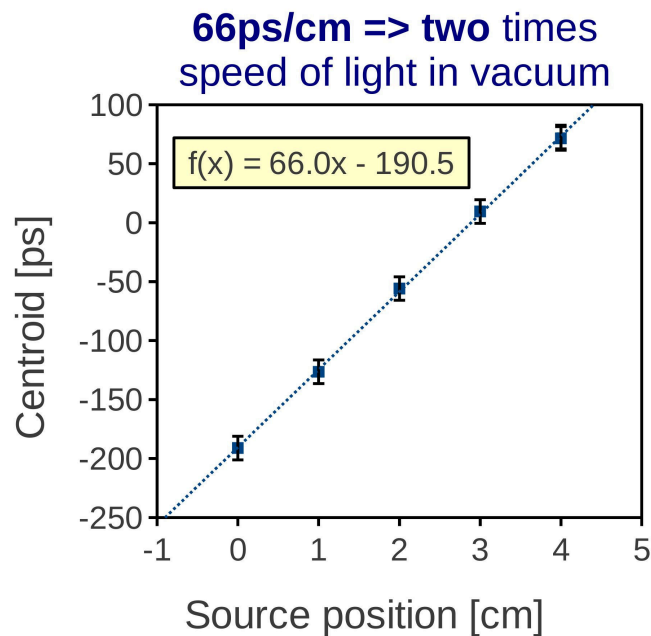
Figure 9.11.: Centroid of the delay time histogram as a function of the source position. The slope of the curve is 66ps per one cm source movement, representing twice the speed of light in vacuum because 1cm of source movement translates to 2cm delay time movement.

9.6. Parallax effects

In a full body PET parallax effects are observed if the positron emission is taking place not in the center of the PET ring, as was already discussed in chapter 2. These parallax effects get more pronounced the further away the emission point is from the PET ring center. Additionally to the known and discussed deterioration in determining the exact location of the positron emission point the time resolution of a TOF-PET system is as well influenced by parallax. To demonstrate this influence we measure the CTR of a 2x2x20mm^3 LSO:Ce codoped 0.4%Ca crystal readout single and double sided versus a reference, as can be seen in figure 9.12. The measurements are performed in two different rotational positions of the 20mm long crystal: (a) the crystal axis is in line with the 511keV gamma trace, i.e. 0° rotation and (b) the crystal axis is rotated by 45°, i.e. representing a positron emission off-centered in a whole body PET. The single sided readout is always performed with the SiPM placed opposite to the positron emitter.
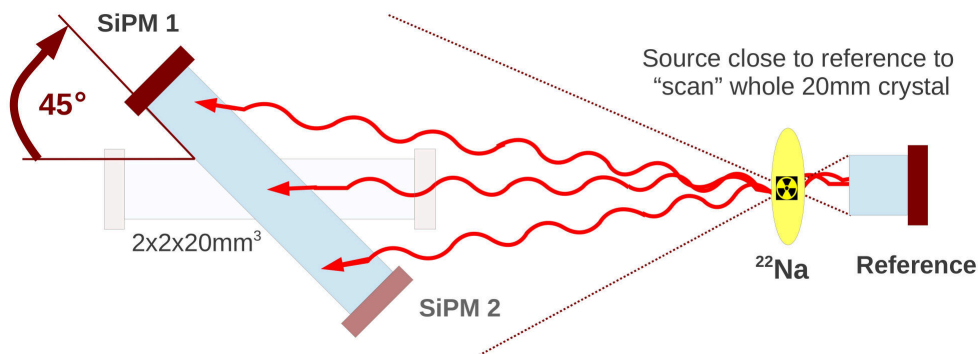
Figure 9.12.: Experimental setup to test the influence of parallax as observed in a full body PET system. A 2x2x20mm^3 LSO:Ce codoped 0.4%Ca crystal is readout either single or double sided. The time resolution is measured versus a reference as a function of rotation of the 20mm long crystal. Two angles are measured: 0° corresponding to the crystal in line with the gamma trace and 45° rotated. The single time resolution of the reference was determined to be 85ps FWHM.

In figure 9.13 we show an overview of the measured results. If the crystal axis is in line with the 511keV gamma path (0° rotation) and is only readout single sided a CTR of 176ps FWHM is measured. If in the same configuration the 20mm long crystal is rotated by 45° the time resolution deteriorates to 200ps FWHM CTR. This deterioration is mainly caused by a change in the gamma absorption probability in the crystal. The 511keV gamma photons have a characteristic absorption length of approximately 12mm in LSO, thus by placing the 20mm long crystal with 0° rotation the main part of the gamma photons are absorbed in the head of the crystal opposite the SiPM. If in contrary the crystal is turned by 45° the 511keV gamma are absorbed more uniformly in the crystal causing an additional time jitter component and thus deteriorating the overall time resolution. However, it should be noted, that this is necessarily not true for a PET ring (shown in chapter 2) where the geometry of the surrounding crystals provoke an average absorption in the head of the crystals even for off-centered coincidence events. If we apply double sided readout

of the crystal it seems that the time resolution is almost not influenced by these parallax effects. For a rotation of 0° we measure a time resolution of 154ps FWHM CTR which degrades only marginally to 157ps FWHM CTR if the 20mm long crystal is rotated by 45°. It should be noted that time resolution related parallax effects are expected to get more pronounced for higher time resolutions in the domain of 100ps FWHM CTR.

Single sided readout 20mm:

CTR(0°)=176±7ps FWHM

CTR(45°)=200±10ps FWHM

Double sided readout 20mm:

CTR(0°)=154±10ps FWHM

CTR(45°)=157±10ps FWHM
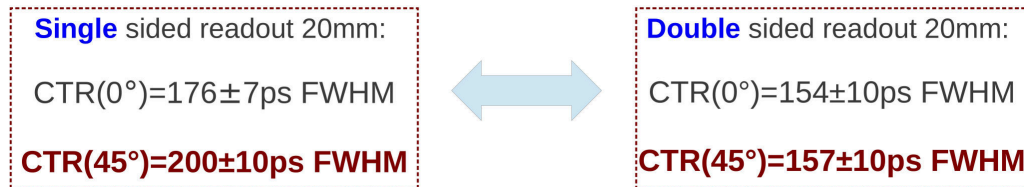
Figure 9.13.: If the crystal is readout single sided a CTR deterioration from 176ps FWHM at 0° to 200ps FWHM at 45° rotation is measured. In contrast, double sided readout seems to be only marginally influenced by parallax effects.

9.7. Summary and conclusion

Using double sided readout of a 2x2x20mm^3 LSO:Ce codoped 0.4%Ca crystal we are able to obtain a coincidence time resolution of 154±10ps FWHM. Single sided readout of the same crystal gives a coincidence time resolution of 176±7ps FWHM, if the photodetector is positioned opposite the surface where the 511keV gammas enter the crystal. In contrary, the CTR would be worse if the SiPM is positioned at the side where the gamma enters the crystal. The time resolution improvement of a system using double sided readout is mostly driven by the gain in light output and thus in photostatistics. We found that the amount of collected scintillation photons of a single sided readout crystal of 10mm length is about the same as the summed light collection of a double sided readout crystal of 20mm length. Consequently the time resolution of a 2x2x20mm^3 crystal using double sided readout should be compared with the time resolution of a 2x2x10mm^3 crystal single sided readout. The measured values of 154±10ps FWHM for a 2x2x20mm^3 crystal double sided readout are close to the achieved coincidence time resolution values of 143±7ps for a 2x2x10mm^3 crystal single sided readout. That the time resolution of a single sided readout 10mm long crystal is still slightly better than the time resolution of a double sided readout crystal of 20mm length could be explained by the gamma interaction and its interplay with the LTTS. In chapter 8 we described that the gamma interaction delay naturally offsets the influence of the LTTS in the crystal. Here we point out two effects minimizing the PTS in a single sided readout configuration: (a) the gamma absorption in the crystal with an absorption length of 12mm in LSO provoking that the majority of gamma interactions take place in the "head" of the crystal, close to the positron emitter and (b) the time Δt of the 511keV gamma entering the crystal until being absorbed. In fact the time Δt effectively minimizes the influence of the LTTS, when the crystal is readout single sided. Another factor intensifying this minimization of the LTTS influence is that highly delayed scintillation photons, e.g. back reflected light, does not

contribute to the time stamp derived in a single sided readout system. These various aspects could provoke that the time resolution of double sided readout with 20mm long crystals is slightly worse than the achievable time resolution of a 10mm long crystal single sided readout, despite having approximately the same light collection and thus photostatistics. However double sided readout gives valuable time resolution improvements. Another important feature of a system employing double sided readout is its higher independence of parallax effects. This is important because in whole body PET scanners most of the line of responses (LORs) are not in axis with the crystal, because the positron emission took not place in the center of the PET ring. We have shown that single sided readout degrades the time resolution if the crystal is misaligned to the LOR. Double sided readout gives a higher independence on these effects and thus could achieve constant CTR performance independent on the point of emission in the bore of an actual whole body PET scanner.

Chapter 10

Limits of the time resolution

10.1. Introduction

In the preceding chapters we discussed the influence of various entities to the time resolution. The developed MC simulation tool gave insight on the nature of the light transfer in the crystal, SiPM properties like dark count and crosstalk as well as the influence of electronic noise. Within these simulations we estimated the limits of the CTR, only considering scintillation statistics and light loss in the crystal, to be around 50ps FWHM for LSO:Ce codoped 0.4%Ca scintillators with an intrinsic light yield of 40 000 photons/MeV, scintillation decay time of 30ns and rise time of 70ps. This estimate took only the influence of the scintillation statistics into account without any time smearing of the photodetector and photon travel spread (PTS). Further we used a PDE of 33% and a LTE of 68% for this estimate.

In this chapter the discussion should be extended to mathematical methods, investigating more in detail the limits of the best achievable time resolution. For the purpose of finding the best achievable time resolution we will use the Fisher information and the Cramér-Rao lower bound as already discussed by S. Seifert et al. in [102]. In statistics the Fisher information measures the information that the observable random variable $\vec{x}$ carries about an unknown parameter θ on which the probability of $\vec{x}$ depends on. The inverse of the Fisher information describes the minimum variance of an unbiased estimator of the unknown parameter θ and is called the Cramér-Rao lower bound. In our case θ denotes the time of positron anihilation in the PET system, which we want to determine, and $\vec{x}$ describes the measured photon detection times of the cascade of scintillation photons detected. Using the Cramér-Rao lower bound we can determine the minimum variance of θ under the assumption of a fully efficient estimator and thus the limit of the best time resolution possibly achievable. We will compare the lower bound of the CTR with the best values obtained by the MC simulations. The MC simulation describes an analog photon detection system with single cell signal pile-up, as shown in chapter 7. The comparison between MC simulation and Cramér-Rao lower bound will give insight in the efficiency of an analog system in order to reach the best CTR possible.

We as well will discuss simulations of CTR with the so called digital SiPM. This type of SiPM gives a single time stamp for each detected photon as described in section 3.3. For this purpose we

will use the same MC program, but modified to give single time stamps for each detected photon, i.e. changing the readout strategy in the program. Within the digital approach we will investigate maximum likelihood (MLH) estimators and their capabilities to improve the coincidence time resolution. This MLH time estimators will be compared to the analog single cell signal pile-up with leading edge discrimination for different cases, e.g. different crystal lengths.

10.2. Limits deduced from the analog MC simulation

In this section we discuss the influence of the scintillation parameters to the simulated coincidence time resolution, i.e. the scintillation rise time (τ_r), the scintillation fall time (τ_d) and the intrinsic light yield or total number of scintillation photons produced (n). We further analyse the influence of the most important SiPM parameters, i.e. photon detection efficiency (PDE) and single photon time resolution (SPTR). The CTR values determined by the MC simulations in this section do not account for the contribution of the acquisition system (oscilloscope) of 27ps FWHM CTR (see equation 6.2.3), which is in contrary to the stated simulated CTR values in chapter 7 and chapter 8. For the simulations we used a crystal geometry of 2x2x3mm^2 with a light transfer efficiency (LTE) of 68% and photon travel spread (PTS) of ∼60ps, see chapter 7. In figure 10.1 and figure 10.2 we show the simulated CTR values for the standard MC as a function of the normalized parameter values as stated in table 7.4. Each curve in the figures represents the calculated CTR values as a function of a single MC input parameter change, i.e τ_r normalized to 70ps, τ_d normalized to 30.3ns, n normalized to 20400ph/511keV, SPTR normalized to 66ps and PDE normalized to 33%.
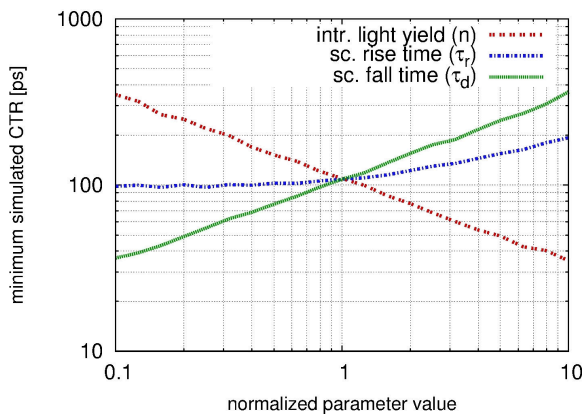
Figure 10.1.: Standard MC simulation with scintillation rise time normalized to $\tau_r = 70ps$, scintillation fall time normalized to $\tau_d = 30.3ns$ and intrinsic light yield (total number of scintillation photons produced by the scintillation) normalized to $n = 20400ph/511keV$. The simulated CTR is ∼108ps FWHM CTR for normalized parameter values one.
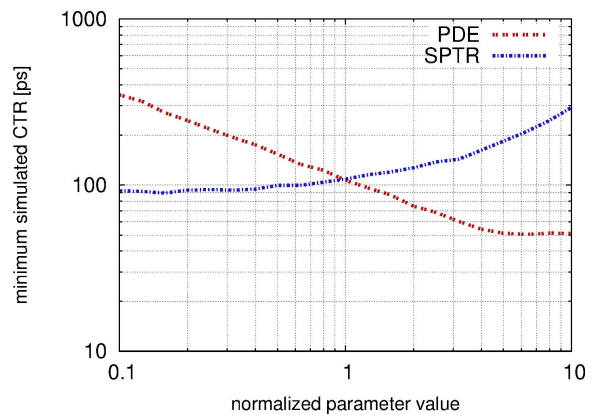
Figure 10.2.: Standard MC simulation with single photon time resolution normalized to $SPTR = 66ps$ and photon detection efficiency of the SiPM normalized to $PDE = 33\%$. For the simulations we used a 2x2x3mm^3 crystal with a light transfer efficiency of $LTE = 68\%$.

We observe that the time resolution is inversely proportional to the square root of the pho-

toelectron yield and proportional to the square root of the scintillation decay time, i.e. $CTR \sim \sqrt{\tau_d/(PDE*n)}$. The LTE describes the scintillation light transfer efficiency of the crystal, i.e. the fraction of scintillation photons arriving at the photodetector to the total amount of photons produced by the scintillation. If all scintillation light would be converted at the photodetector ($LTE*PDE = 100\%$) a CTR of 51ps FWHM could be achieved, as can be seen in figure 10.2. A decrease in τ_r and SPTR does not improve the CTR to a noticeable amount. This can be explained by the PTS in the crystal being in the same order of magnitude like the SPTR. Further the convolution of a zero rise time photon-emission rate with the PTS would cause an artificial rise time being again in the order of 70ps.

In figure 10.3 and figure 10.4 we show the standard MC simulation if we set to zero the dark count rate (DCR), optical crosstalk probability and gain fluctuation of the SiPM as well as the electronic noise. We notice an improvement of the CTR of ~5ps-10ps as already discussed in chapter 7 which is mainly due to the influence of the optical crosstalk of the SiPM.
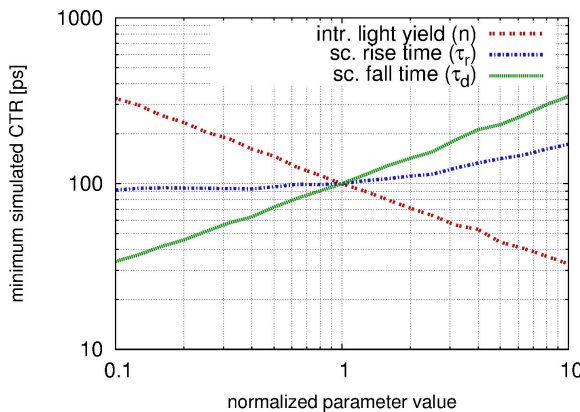

Figure 10.3.: Setting in the standard MC simulation to zero the DCR, crosstalk and electronic noise. The scintillation rise time is normalized to $\tau_r = 70ps$, fall time to $\tau_d = 30.3ns$ and intrinsic light yield to $n = 20400ph/511keV$. The simulated CTR is ~100ps FWHM CTR for normalized parameter values one.
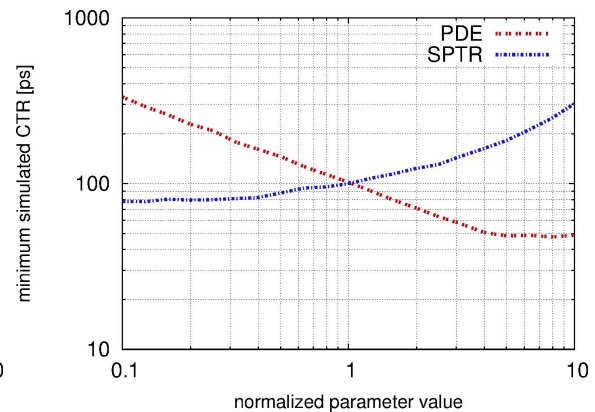
Figure 10.4.: Setting in the standard MC simulation to zero the DCR, crosstalk and electronic noise. The single photon time resolution is normalized to $SPTR = 66ps$ and photon detection efficiency of the SiPM to $PDE = 33\%$. For the simulations we used a 2x2x3mm^3 crystal with a light transfer efficiency of $LTE = 68\%$.

In figure 10.5 and figure 10.6 we in addition set to zero the influence of the photon travel spread in the 2x2x3mm^3 LSO:Ce codoped 0.4%Ca crystal. A further improvement of ~20ps FWHM CTR can be seen, i.e. at normalized parameter values one we simulate a CTR of 81ps FWHM. In these conditions (PTS=0) we observe that a lower SPTR value would improve the CTR to a noticeable amount, as can be seen in figure 10.6.

In figure 10.7 and in figure 10.8 we set to zero the SPTR, DCR, optical crosstalk, gain fluctuation and electronic noise. In these conditions we simulate a CTR of ~76ps FWHM at normalized parameter values of one. In figure 10.7 we notice a more pronounced CTR dependence on the scintillation rise time τ_r. If we decrease τ_r to almost zero we would obtain a CTR improvement of ~25ps FWHM. Showing that a faster scintillation rise time can improve the CTR if the SiPM

would be perfect, i.e. SPTR=0, no crosstalk and dark count.
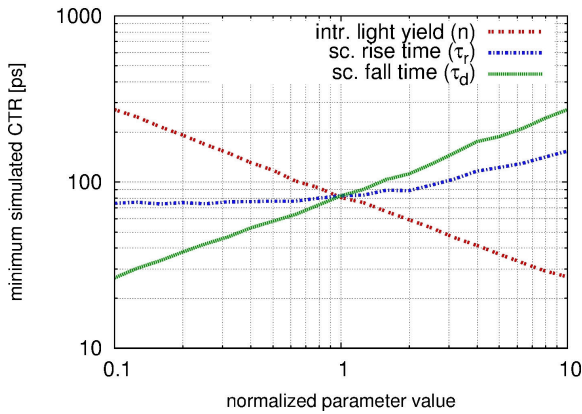
Figure 10.5.: Setting in the MC simulation to zero the PTS, DCR, crosstalk and electronic noise. The scintillation rise time is normalized to $\tau_r = 70ps$, fall time to $\tau_d = 30.3ns$ and intrinsic light yield to $n = 20400ph/511keV$. The simulated CTR is ∼81ps FWHM CTR for normalized parameter values one.
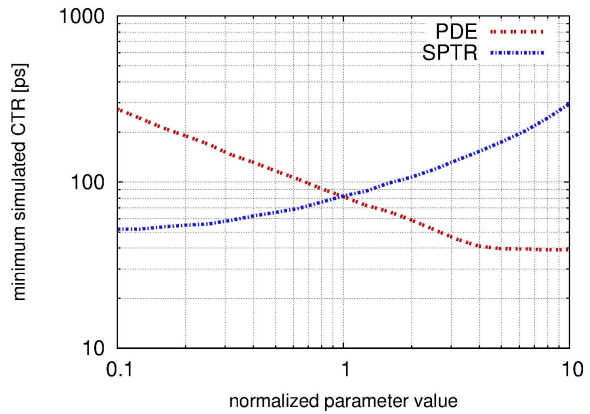
Figure 10.6.: Setting in the MC simulation to zero the PTS, DCR, crosstalk and electronic noise. The single photon time resolution is normalized to $SPTR = 66ps$ and photon detection efficiency of the SiPM to $PDE = 33\%$. For the simulations we used a 2x2x3mm³ crystal with a light transfer efficiency of $LTE = 68\%$.
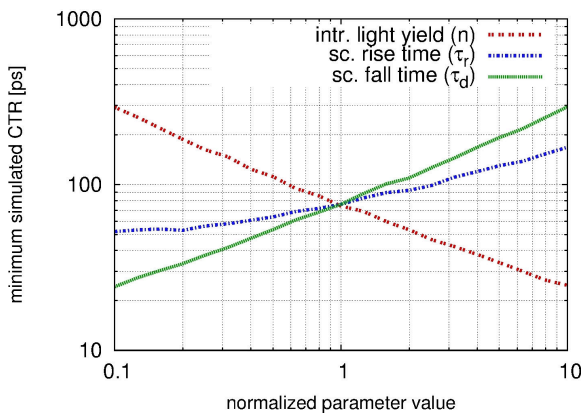
Figure 10.7.: Setting in the MC simulation to zero the SPTR, DCR, crosstalk and electronic noise. The scintillation rise time is normalized to $\tau_r = 70ps$, fall time to $\tau_d = 30.3ns$ and intrinsic light yield to $n = 20400ph/511keV$. The simulated CTR is ∼76ps FWHM CTR for normalized parameter values one.
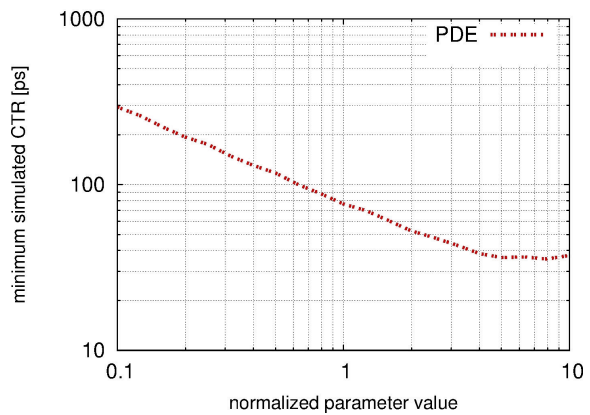
Figure 10.8.: Setting in the MC simulation to zero the SPTR, DCR, crosstalk and electronic noise. The photon detection efficiency of the SiPM is normalized to $PDE = 33\%$. For the simulations we used a 2x2x3mm³ crystal with a light transfer efficiency of $LTE = 68\%$.

In figure 10.9 and in figure 10.10 we show simulated CTR values if we set to zero the PTS, SPTR, DCR, crosstalk, gain fluctuation and electronic noise. As a consequence these simulations represent only the scintillation statistics with a light transfer efficiency kept at 68% and a photon detection efficiency of the SiPM at 33%. At normalized parameter values of one we simulate a

CTR of 48ps FWHM. If in this case the LTE and PDE are 100% the time resolution would become 21ps FWHM CTR. This value represents the limits of the time resolution given by the scintillation process with a rise time of $\tau_r = 70ps$, fall time of $\tau_d = 30.3ns$ and intrinsic light yield of $n = 20400ph/511keV$. In figure 10.9 a pronounced dependence of the CTR on the scintillation rise time τ_r can be seen. Stating that, if only the scintillation statistic is considered, the rise time is important in order to achieve highest CTR. However it should be noted that the CTR dependency on the scintillation rise time τ_r is not as strong as for the scintillation decay time τ_d or intrinsic light yield n.
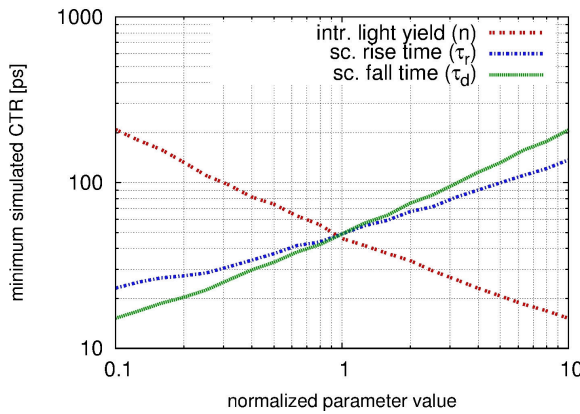
Figure 10.9.: Setting in the MC simulation to zero the SPTR, PTS, DCR, crosstalk and electronic noise. The scintillation rise time is normalized to $\tau_r = 70ps$, fall time to $\tau_d = 30.3ns$ and intrinsic light yield to $n = 20400ph/511keV$. The simulated CTR is ~48ps FWHM CTR for normalized parameter values one.
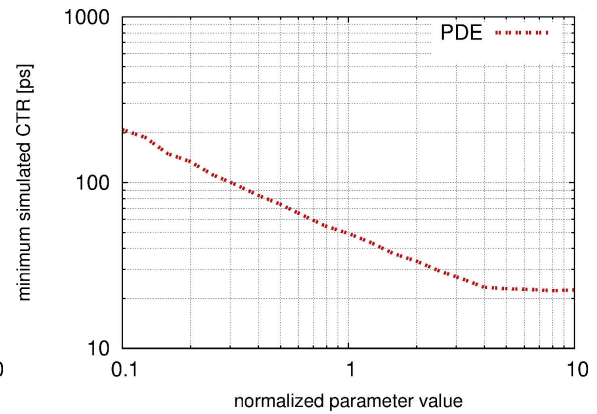
Figure 10.10.: Setting in the MC simulation to zero the SPTR, PTS, DCR, crosstalk and electronic noise. The photon detection efficiency of the SiPM is normalized to $PDE = 33\%$. For the simulations we used a 2x2x3mm³ crystal with a light transfer efficiency of $LTE = 68\%$.

In table 10.1 we summarize the simulated CTR as a function of DCR, crosstalk, electronic noise, SPTR and PTS.

Table 10.1.: Simulated CTR values as a function of DCR, crosstalk, electronic noise, SPTR and PTS. Other MC input parameters are held constant at $\tau_r = 70ps$, $\tau_d = 30.3ns$, $n = 20400ph/511keV$, $PDE = 33\%$ and $LTE = 68\%$.

dark counts	crosstalk	electronic noise	SPTR	PTS	CTR
yes	yes	yes	66ps	yes	~108ps
no	no	no	66ps	yes	~100ps
no	no	no	66ps	no	~81ps
no	no	no	0ps	yes	~76ps
no	no	no	0ps	no	~48ps

In table 3.2 in chapter 3.2 a simple expression of the CTR based on the first emitted photon was discussed. The equation shown can in a similar form be used for photons detected. With n'=4577, τ_r=70ps and τ_d=30.3ns a coincidence time resolution of CTR=47ps can be calculated. This value is very close to the one found in the MC simulations without the influence of DCR, crosstalk, electronic noise, SPTR and PTS as can be seen in table 10.1, in figure 10.9 and in figure 10.10.

10.3. Fisher information and Cramér-Rao lower bound

This chapter describes the Cramér-Rao lower bound of the time resolution as introduced in the work of [102]. This lower bound is derived by pure statistical considerations and gives the intrinsic limit of the CTR. For simplification we consider the crystal to be zero in dimensions, i.e. setting the photon travel spread (PTS) to zero, however still considering a LTE of 68%.

In chapter 3.2 the photon emission rate of the scintillation was introduced to be a bi-exponential with one or several rise and fall time components. In equation 10.3.1 we state the simplified probability density function (PDF) of the scintillation photon emission rate with only one rise time constant (τ_r) and one fall time constant (τ_d). Here the time θ denotes the start of the scintillation.

$$\widehat{f}(t|\theta) = \frac{\exp\left(-\frac{t-\theta}{\tau_d}\right) - \exp\left(-\frac{t-\theta}{\tau_r}\right)}{\tau_d - \tau_r} \, \Theta(t-\theta) \tag{10.3.1}$$

Every photon detected by the SiPM undergoes a certain time smearing due to the transit time spread in the SiPM. This can be modeled by a Gaussian with the variance expressed by the single photon time resolution (SPTR) as shown in equation 10.3.2. It should be noted that this smearing could be extended to contain the PTS in the crystal. The parameter Δ_M expresses a possible electronic delay.

$$g(t) = \frac{1}{\sqrt{2\pi}\sigma_{SPTR}} \exp\left[-\frac{(t-\Delta_M)^2}{2(\sigma_{SPTR})^2}\right] \tag{10.3.2}$$

The likelihood function of photon detection given a certain gamma impact time θ can be expressed by equation 10.3.3. It is the convolution of the scintillation photon emission rate (see equation 10.3.1) with the time smearing of the SiPM photodetector (see equation 10.3.2).

$$\widehat{f}_g(t|\theta) = \widehat{f}(t,\theta) * g(t) = \int_{-\infty}^{\infty} \widehat{f}(t'|\theta)\, g(t-t')dt' \tag{10.3.3}$$

As explained in [102] the convolution in equation 10.3.3 can be done (semi-)analytically, using the error-function with the following properties: $erf(\pm\infty) = \pm 1$ and $erf(0) = 0$. We obtain the result as shown in equation 10.3.4.

$$\widehat{f_g}(t|\theta) = \frac{1}{2(\tau_d - \tau_r)} e^{\frac{2\tau_d(\Delta_M + \theta - t) + \sigma_{SPTR}^2}{2\tau_d^2}} \left(1 - erf\left[\frac{\tau_d(\Delta_M + \theta - t) + \sigma_{SPTR}^2}{\sqrt{2}\,\sigma_{SPTR}\,\tau_d} \right] \right) + \dots$$
$$\dots + \frac{1}{2(\tau_d - \tau_r)} e^{\frac{2\tau_r(\Delta_M + \theta - t) + \sigma_{SPTR}^2}{2\tau_r^2}} \left(1 - erf\left[\frac{\tau_r(\Delta_M + \theta - t) + \sigma_{SPTR}^2}{\sqrt{2}\,\sigma_{SPTR}\,\tau_r} \right] \right) \tag{10.3.4}$$

In equation 10.3.4 the limit $\sigma_{SPTR} \to 0$ gives the scintillation photon emission rate $\widehat{f}(t|\theta)$, although moved by Δ_M which represents the electronic delay in equation 10.3.2.

The Fisher information $I(\theta)$ is the expectation value of the score $\frac{\partial}{\partial\theta} \log \widehat{f_g}(t|\theta)$ squared, as can be seen in equation 10.3.5 and being defined in [102].

$$I(\theta) = E\left[\left(\frac{\partial}{\partial\theta} \log \widehat{f_g}(t|\theta) \right)^2 \Big| \theta \right] = \int_{-\infty}^{\infty} \frac{1}{\widehat{f_g}(t|\theta)} \left(\frac{\partial \widehat{f_g}(t|\theta)}{\partial\theta} \right)^2 d\theta \tag{10.3.5}$$

Supposing an unbiased estimator the Cramér-Rao lower bound can be expressed as the inverse of the Fisher information [102] (see equation 10.3.6). If we suppose that the likelihood is independent and identically distributed (iid) for each of the photons, i.e. according to equation 10.3.4, then the Fisher information is additive. In that case we can account for the integral number of photons detected ($n' = n \cdot PDE \cdot LTE$) by adding the term n' in equation 10.3.6. The term $2 \cdot \sqrt{2 \cdot ln(2)} \cdot \sqrt{2} = 3.33$ converts to coincidence time resolution in FWHM.

$$CTR_{LB} = 3.33 \cdot \sqrt{\frac{1}{n' \cdot I(\theta)}} \tag{10.3.6}$$

Equation 10.3.6 tells that the CTR is inversely proportional to the square root of the photons detected. If the photon emission is independent and identically distributed, the inverse square root dependence of the CTR value on the number of scintillation photons detected (n') can be understood as a fundamental principle.

In the following figures we use the Cramér-Rao lower bound to calculate the limits of the CTR as described by equation 10.3.6. In these calculations we only account for the SPTR of the SiPM and neglect the photon travel time spread in the crystal. We will assume a PDE of 33% and a LTE of 68% in order to be comparable to the MC simulations discussed previously (see figure 10.5). We will discuss the influence of the scintillation rise time, scintillation fall time and SPTR of the SiPM to the CTR.

In figure 10.11 we plot CTR values obtained by the Cramér-Rao lower bound (equation 10.3.6) as a function of the scintillation rise time and SPTR of the SiPM. For better visibility we as well show the CTR expressed in contour lines in the same plot. The x-axis and y-axis show the "normalized parameter value", i.e. the scintillation rise time of 70ps and SPTR of 66ps multiplied by a factor ranging from 0.01 to 100, respectively. We chose the values of 70ps for the scintillation rise time and 66ps for the SPTR similar to the ones deduced in chapter 7 (table 7.4). This was done

in order to be as close as possible to the experimental setup described in chapter 6. Additionally we chose the number of detected photons n' equal 4577, which represents the use of a 2x2x3mm^3 LSO:Ce codoped 0.4%Ca crystal with an LTE of 68%. The PDE of the SiPM is set to 33% which represents an operational overvoltage of 2.3V of the Hamamatsu 50μm SPAD sized MPPC. The scintillation decay time was set to 30.3ns as measured for the LSO:Ce codoped 0.4%Ca scintillator shown in chapter 7.
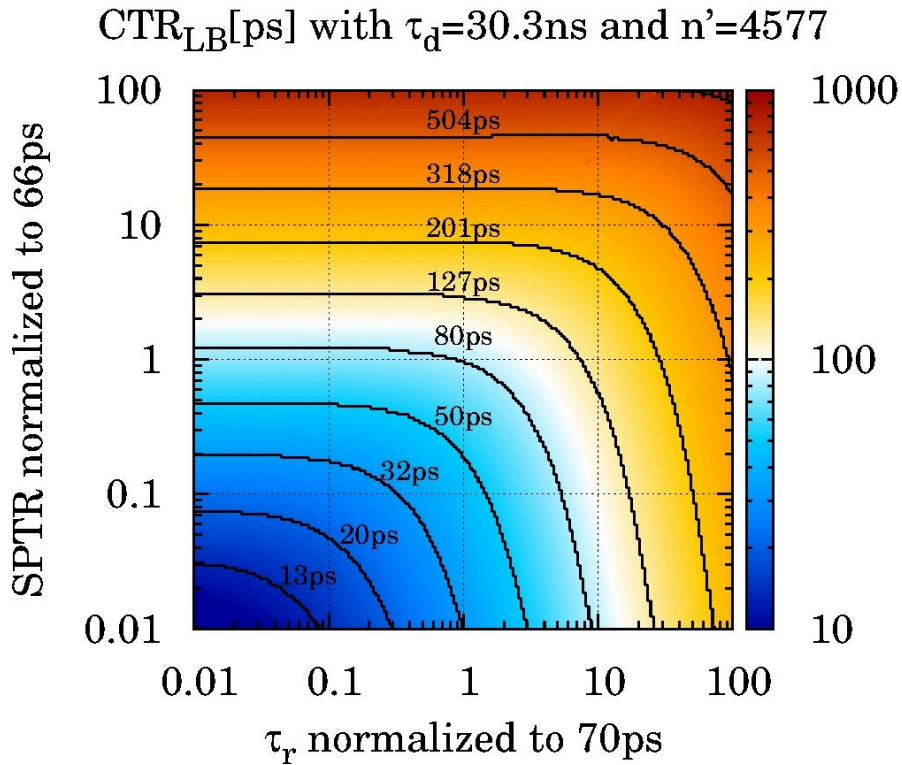
Figure 10.11.: Calculated lower bound of the CTR. The standard scintillation rise time of 70ps (determined for our experimental setup with LSO:Ce codoped 0.4%Ca) and SPTR of 66ps (determined for the used Hamamatsu 50μm SPAD sized MPPC) are multiplied with a factor between 0.01 and 100. Colors encode the CTR in ps.

The lower bound of the CTR for $\tau_r = 70ps$, $\tau_d = 30.3ns$, $n' = 4577$ and $SPTR = 66ps$ is $CTR_{LB} = 81ps$ FWHM. This value is the same as the minimum CTR deduced from the analog MC simulations with the same input parameters as shown in figure 10.5 and in table 10.1. It seems that the analog microcell signal pile-up with leading edge discrimination is in principle able to deliver time resolution values which are comparable to the calculated lower bound in the same conditions. For this comparison we only took into account the scintillation photon emission rate, photon detection efficiency and time smearing by the SiPM. If we would extent the model to include optical crosstalk of the SiPM this comparison would be not valid anymore, simply because optical crosstalk events appear to be time correlated with the primary detected photon. Figure 10.11 further shows that for a constant SPTR=66ps a decrease in the rise time τ_r to values around zero would only marginally improve the CTR. This behavior was already observed in the analog

MC simulations as can be seen figure 10.5. The reason can be evaluated by equation 10.3.4, even in the case of a zero rise time $\tau_r = 0$ a non-zero SPTR would cause an artificial rise time term in equation 10.3.4 and vice versa. It should be noted that a non zero photon travel spread (PTS), which is unavoidable in a real crystal, can be compared to the influence of a non-zero SPTR. However, if we only consider the scintillation statistics by setting the SPTR to zero we can see in figure 10.11, that in this case, a rise time improvement would indeed improve the CTR to a noticeable amount.

In figure 10.12 we show the CTR as a function of the detected scintillation photons $n' = n \cdot PDE \cdot LTE$ and the scintillation fall time τ_d. The CTR value isolines show a linear dependence between n' and τ_d implying $CTR_{LB} \sim \sqrt{\tau_d/n'}$.
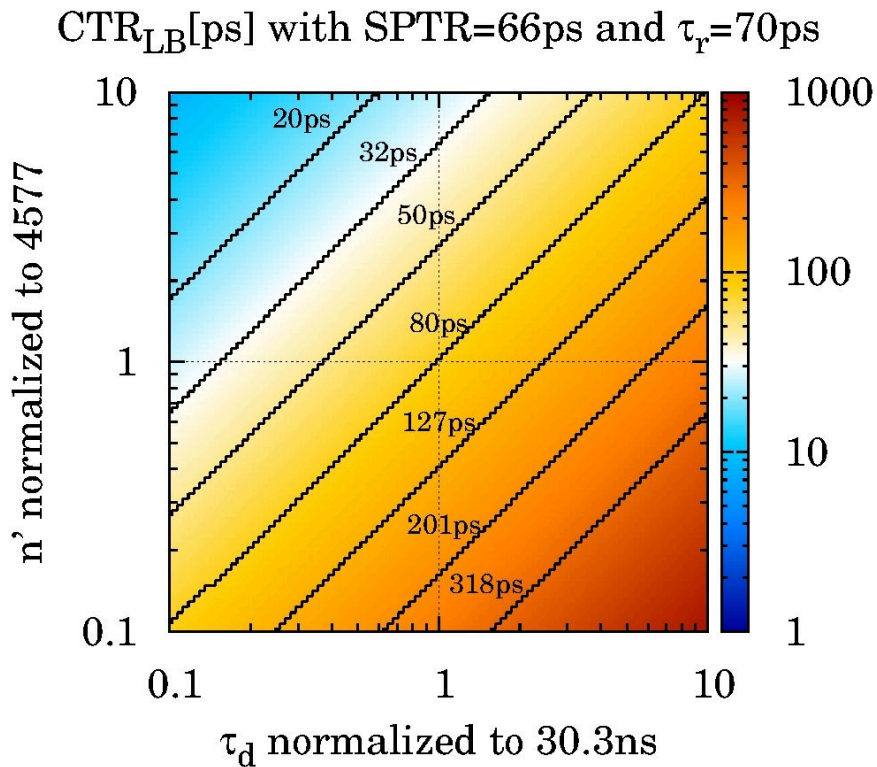
Figure 10.12.: Lower bound of the CTR as function of detected scintillation photons n' and fall time τ_d. Colors encode the CTR in ps.

Figures 10.13 show in more detail the influence of the scintillation rise time τ_r and SPTR of the SiPM to the CTR. Decreasing the scintillation rise time (τ_r) value causes a saturation in the CTR, i.e. at a certain point a further decrease in τ_r does not lead to any CTR improvement anymore. This observation holds for any possible combinations of photons detected n' and scintillation fall times τ_d. The same behavior can be observed if we decrease the SPTR value, however the saturation does not appear as pronounced. As already discussed this can be explained by the interplay of rise time τ_r with the single photon time resolution of the SiPM in equation 10.3.4. Decreasing τ_r will after some point provoke the SPTR to dominate the rising edge of the the photon detec-

tion likelihood function described in equation 10.3.4. The same reasoning holds for decreasing the SPTR value, where after a certain point the scintillation rise time will dominate the photon detection rate.
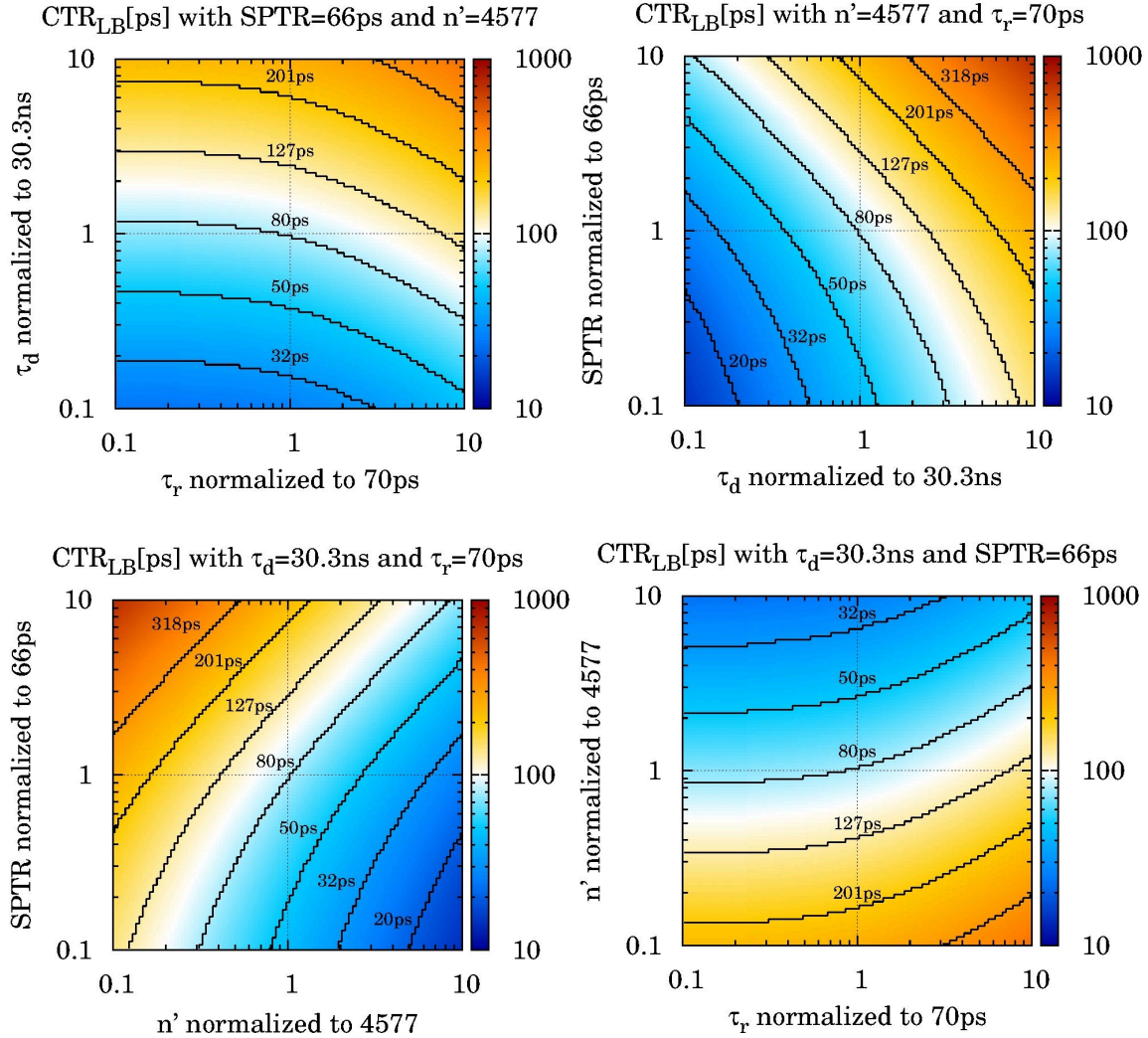
Figure 10.13.: Calculated lower bound of the CTR. Colors encode the CTR in ps.

In figures 10.14 - 10.17 we show the calculated lower bound of the CTR if either the scintillation rise time τ_r or the SPTR of the SiPM is set to zero. We observe that in the case of zero rise time $\tau_r = 0ps$ the CTR is dependent on the square root of the SPTR, i.e. $CTR \sim \sqrt{SPTR}$ (see figure 10.14 and figure 10.15). Setting the SPTR to zero we observe in figure 10.17 that the CTR becomes almost proportional to the square root of the scintillation rise time. Even in this case we can observe a slight saturation in the improvement of the CTR if decreasing τ_r, which was as well observed in the analog MC simulations (see figure 10.9). In general we conclude that an improvement in the scintillation rise time, starting from a value of $\tau_r = 70ps$, improves the CTR only if additional time smearing is set to zero, i.e. SPTR=0ps. Additionally the CTR improvement will not be as pronounced as improving other parameters determining the time resolution, e.g.

the number of photons detected n', scintillation decay time τ_d and even the SPTR of the SiPM.
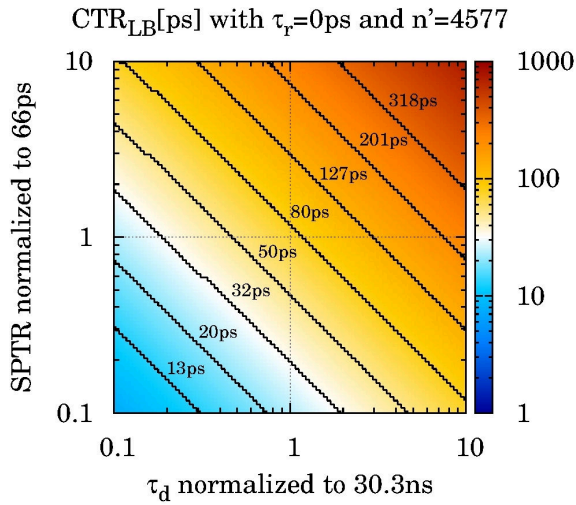
Figure 10.14.: Lower bound of the CTR as function of SPTR and fall time τ_d when the rise time τ_r is set to zero.
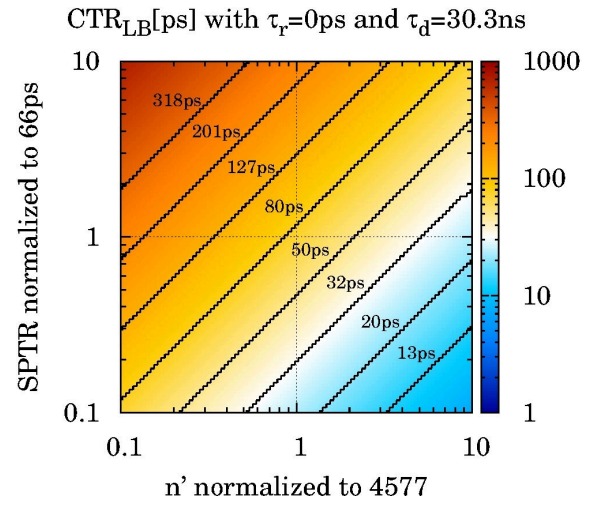
Figure 10.15.: Lower bound of the CTR as function of SPTR and detected photons n' when the rise time τ_r is set to zero.
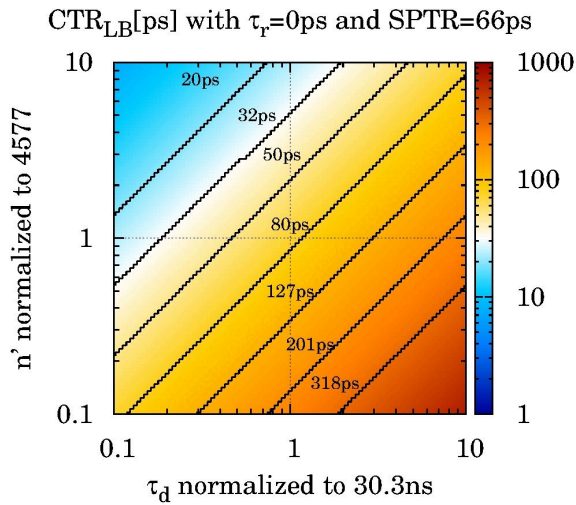
Figure 10.16.: Lower bound of the CTR as function of detected photons n' and fall time τ_d when the rise time τ_r is set to zero.
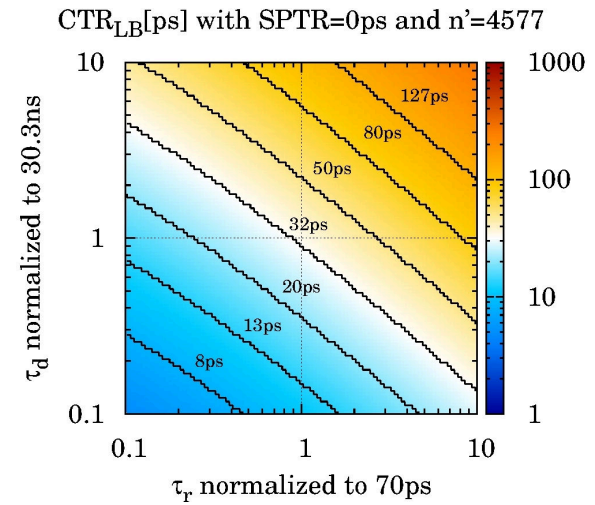
Figure 10.17.: Lower bound of the CTR as function of fall time τ_d and rise time τ_r when the SPTR is set to zero.

10.4. Photon counting and maximum likelihood

In chapter 3 the digital SiPM was introduced. In this type of photodetector every photon detected N_i is associated with a time stamp T_i. In the coincidence setup discussed in chapter 5 time measurements are always defined by measuring the time difference of one detector arm against the other. Thus in practice an absolute time stamp per incident photon cannot be given and we have

to resort on time differences D_{ij} shown in equation 10.4.1.

$$D_{ij} = T_i^{detector\,1} - T_j^{detector\,2} \tag{10.4.1}$$

In equation 10.4.1 the absolute time stamp for the ith photon detected at the left side in the co-incidence setup is denoted $T_i^{detector\,1}$ and the jth photoelectron at the right arm of the coincidence setup $T_j^{detector\,2}$. As already mentioned, in an experiment only the time lag matrix D_{ij} can be measured with i and j being the photon rank of the respective detectors, which are defined from one to the maximum number of photons detected. In the following we will simplify the analysis and use only delay times D_{kk} with $i = j = k$, i.e. only time differences of photons detected with the same rank. Each time difference D_{kk} carries a certain amount of information regarding the positron annihilation time θ, i.e. time of emission of the two 511keV gammas. The easiest time estimator would be to combine all time differences D_{kk} by taking the mean. This approach will be referred to as "simple average" and is defined in equation 10.4.2 with $\widehat{\theta}_{sa}(K)$ describing the most likely time of positron annihilation for a given number K of averaged time differences D_{ii}.

$$\widehat{\theta}_{sa}(K) = \frac{1}{K} \sum_{i=1}^{K} D_{ii} \tag{10.4.2}$$

Another method is to estimate the most likely time of positron annihilation $\widehat{\theta}$ with a maximum likelihood (MLH) approach. In a first approximation we neglect cross-correlations, i.e. $Cov(D_{ii}, D_{jj}) = 0 \; for \; i \neq j$. We define the probability density function $P(\theta|D_{11}, D_{22}, ..., D_{KK})$ as in equation 10.4.3. It gives the probability of a certain gamma emission time θ under the condition of a measured delay time data set $D_{11}, D_{22}, ..., D_{KK}$. The maximum of the function $P(\theta|D_{11}, D_{22}, ..., D_{KK})$ will give the most likely positron annihilation time $\widehat{\theta}_{MLH}$. This method will be denoted as MLH estimator.

$$P(\theta|D_{11}, D_{22}, ..., D_{KK}) = \frac{P(D_{11}, D_{22}, ..., D_{KK}|\theta) \cdot P(\theta)}{P(D_{11}, D_{22}, ..., D_{KK})} \tag{10.4.3}$$

The right hand side in equation 10.4.3 was obtained by using Bayes' theorem. The term $P(D_{11}, D_{22}, ..., D_{KK}|\theta)$ is the likelihood function shown in equation 10.4.4. It is the probability of observing a set of time delays $D_{11}, D_{22}, ..., D_{KK}$ under the condition of a certain gamma emission time θ. The likelihood function is given by the measurement setup and can be obtained by a calibration run. In other words, the probability density functions p_{ii} are determined by collecting a lot of D_{ii} measurements, histogramming and fitting an appropriate function to the data for easier numerical treatment.

$$P(D_{11}, D_{22}, ..., D_{KK}|\theta) = p_{11}(D_{11} - \theta) \cdot p_{22}(D_{22} - \theta) \cdot ... \cdot p_{KK}(D_{KK} - \theta) \tag{10.4.4}$$

The normalization $P(D_{11}, D_{22}, ..., D_{KK})$ is of less importance as it is only dependent on the photon detection probability density functions and not on the gamma emission time θ. As it is a constant independent on θ it will not influence the maximum of $P(\theta|D_{11}, D_{22}, ..., D_{KK})$. We choose the normalization somehow arbitrary as the maximum possible probability:

$$P(D_{11}, D_{22}, ..., D_{KK}) = max(p_{11}) \cdot max(p_{22}) \cdot ... \cdot max(p_{KK}) \tag{10.4.5}$$

The prior $P(\theta)$ we define as unity, meaning that we assume no prior knowledge about the positron emission time.

$$P(\theta) = 1 \tag{10.4.6}$$

As already mentioned we search for the time $\widehat{\theta}_{MLH}$ which maximizes the probability density function $P(\theta|D_{11}, D_{22}, ..., D_{KK})$.

In figure 10.18 we show Monte Carlo simulations applying digital readout of the SiPM. The MC simulation was described in chapter 7. In the digital readout scheme we do not perform microcell signal pile-up but extract the time of each firing microcell directly. The input parameters of the simulations are: scintillation rise time $\tau_r = 70ps$, scintillation fall time $\tau_d = 30.3ns$, the total number of photons detected $n' = 4577$ and the $SPTR = 66ps$ of the SiPM. We set to zero the optical crosstalk, DCR and afterpulse in the SiPM as well as electronic noise and the photon travel spread in the crystal $PTS = 0$. The light transfer efficiency is equal to a 3mm long crystal, i.e. LTE=0.68. We show the time resolution calculated with the simple average method (see equation 10.4.2) and the maximum likelihood estimator (see equation 10.4.3) as a function of included time ranks K. In other words, the estimators combine the time information of photons detected until the rank K, at which the calculated value is plotted.
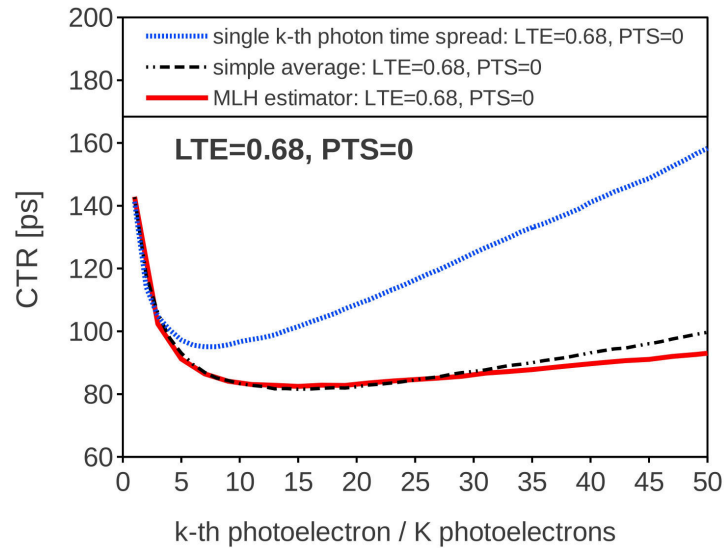

Figure 10.18.: CTR simulation of a fully digital SiPM. Shown is the single $k - th$ photon time spread given in CTR and the CTR value if combining the preceding K time stamps. Two different cases of time estimators are illustrated: a simple average of the preceding K time stamp values and a maximum likelihood estimator with disregarded cross-correlations of the covariance matrix.

For comparison we as well show the single $k - th$ photon time spread in figure 10.18. It gives the CTR of each single photon detected with rank k. We see that the simple average method

is indeed able to combine the different photon ranks in order to improve the time resolution if compared to the single $k - th$ photon time spread. The minimum value of 82ps FWHM CTR can be identified at around k=17 photons. The maximum likelihood estimator performs a little bit better at higher numbers of delay time stamps D_{kk} combined. However shows the same minimum of 82ps at around k=17 photons. The simulations presented in figure 10.18 are performed with the same input settings as the lower bound calculations in figure 10.11. The direct comparison shows that within simulation errors which are in the range of 5% the simple average and MLH methods achieve already the lower bound of the time resolution. Furthermore the analog MC simulation with the same input parameters summarized in table 10.1 shows the same CTR value of 81ps FWHM.

In figure 10.18 we see that the CTR value for the simple average and MLH estimator rises after a certain number of included photon ranks. The disregard of cross-correlations in the former approaches of the time estimator seems not to be justified and is responsible for the observed increase in CTR value with increasing number of included photon ranks. One possibility is to extend the MLH method to contain the full covariance matrix. The idea is to approximate the likelihood function $P(\vec{D}|\theta)$ in equation 10.4.4 with the multivariate normal distribution shown in equation 10.4.7.

$$P(\vec{D}|\theta) = \frac{1}{\sqrt{(2\pi)^K |\mathbf{C}|}} \exp\left[-\frac{1}{2}\left(\vec{D} - \vec{\mathbb{1}}\theta\right)^T \mathbf{C}^{-1}\left(\vec{D} - \vec{\mathbb{1}}\theta\right)\right] \qquad (10.4.7)$$

The approximation of the likelihood function with the multivariate normal distribution is justified since the $p_{ii}(D_{ii} - \theta)$ in equation 10.4.4 are very well described by a Gaussian. The next step is to maximize the probability density function $P(\theta|\vec{D})$ which can be done by using Bayes' theorem and setting the derivative to zero. A complete derivation can be found in the appendix C. Within this procedure we can express the best positron emission time estimator $\widehat{\theta}_{GM}$ as in equation 10.4.8. The vector $\vec{W}^T$ solves the constraints of $E[\widehat{\theta}_{GM}] = \theta$ and minimizes $E[(\widehat{\theta}_{GM} - \theta)^2]$ with $E[]$ denoting the expectation value. Hence the estimator $\widehat{\theta}_{GM}$, including the full covariance matrix $\mathbf{C}$, being unbiased and of minimum variance.

$$\widehat{\theta}_{GM} = \vec{W}^T \vec{D} = \left(\vec{\mathbb{1}}^T \mathbf{C}^{-1} \vec{\mathbb{1}}\right)^{-1} \vec{\mathbb{1}}^T \mathbf{C}^{-1} \vec{D} \qquad (10.4.8)$$

In equation 10.4.8 the observation vector is denoted as $\vec{D}$, i.e. the measured time differences D_{ii}. The term $\left(\vec{\mathbb{1}}^T \mathbf{C}^{-1} \vec{\mathbb{1}}\right)$ represents the normalization with $\vec{\mathbb{1}}$ being the unity vector, a vector filled with ones and of length K. $\mathbf{C}$ is the covariance matrix defined in equation 10.4.9 with $N_{samples}$ the number of calibration measurements or simulation runs. $\mathbf{C}^{-1}$ is the inverse of the covariance matrix. The covariance matrix can be determined in a calibration run which then gives the input for the positron emission time estimation $\widehat{\theta}_{GM}$ for the following independent measurements of $\vec{D}$.

$$C_{ij} = \frac{1}{N_{samples} - 1} \sum_{n=1}^{N_{samples}} (D_{nii} - \overline{D_{ii}})(D_{njj} - \overline{D_{jj}}) \qquad (10.4.9)$$

The estimated time of positron emission $\widehat{\theta}_{GM}$ described in equation 10.4.8 has already been

used in literature [103, 104]. It can as well be calculated by the generalized least squares method and is linked to the Gauss-Markov theorem. In the following discussions we will denote the time estimator $\widehat{\theta}_{GM}$ as "Gauss-Markov" estimation.

In figure 10.19 we use the same MC input parameters as for figure 10.18, i.e. scintillation rise time $\tau_r = 70ps$, scintillation fall time $\tau_d = 30.3ns$ and the total number of photons detected $n' = 4577$. The photon travel spread was set to zero ($PTS = 0$) and the light transfer efficiency is equal to a 3mm long crystal ($LTE = 0.68$). The Gauss-Markov time estimator gives improved time resolution values with increasing number of incorporated photoelectrons and is leveling off at a coincidence time resolution of 80ps FWHM. In comparison to the simple average estimator or MLH estimator shown in figure 10.18 the CTR value does not increase for higher order of included photoelectrons K. This is a direct consequence of including cross correlations in the time estimator $\widehat{\theta}_{GM}$ via the use of the full covariance matrix **C**. If we set the off-diagonal elements in **C** to zero and apply the same formalism for $\widehat{\theta}_{GM}$ we see that the CTR value shows a minimum in figure 10.19. However, the CTR deterioration with increasing number of incorporated photoelectrons K is lower as compared to the simple average time estimator. It is interesting to notice that the Gauss-Markov estimator with zero cross-correlations is giving exactly the same CTR values as obtained with the MLH estimator shown in figure 10.18, where cross-correlations were neglected as well.
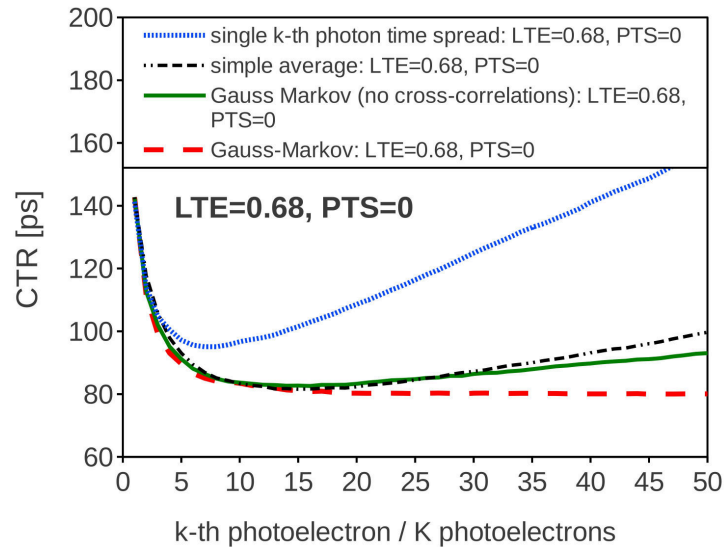
Figure 10.19.: CTR simulation of a fully digital SiPM. Shown is the single $k - th$ photon time spread given in CTR and the CTR value if combining the preceding K time stamps. Different methods are depicted: the simple average estimator, Gauss-Markov estimator with zero off-diagonal elements in the covariance matrix and Gauss-Markov estimator including the full covariance matrix. If the full covariance matrix is used the CTR improves steadily, leveling at a constant value of 80ps after $K = 20$ photoelectrons included.

In the following we will compare the Gauss-Markov and the simple average time estimators in the fully digital SiPM with the analog MC simulation introduced in chapter 7. The comparison is done for different crystal lengths with similar MC input parameters for all lengths. We chose the parameters equal to the ones used in the preceding discussions for the case of a LSO:Ce

codoped 0.4%Ca scintillator with a rise time of $\tau_r = 70ps$, a fall time of $\tau_d = 30.3ns$ and a total number of scintillation photons produced $n = 20400$ per 511keV gamma. The SPTR of the SiPM is set to 66ps and the PDE to 33%, similar for the digital and analog simulations. We in addition set to zero optical crosstalk, afterpulse and DCR in the SiPM as well as electronic noise of the readout electronics. In the digital MC simulation we extract the time stamps of the cascade of photons detected in the SiPM which represent the input for calculating the different time estimators presented. In the analog simulation these time stamps provoke microcell signals which are added to form an analog signal on which the time estimator is given by a leading edge discrimination. Both MC simulations are exactly similar with the only difference in the readout strategy, which makes it possible to directly compare the CTR results.

The first simulation run was already partly presented in figure 10.18 and 10.19. In these simulations we set to zero the photon travel spread in the crystal (PTS=0). In addition the light transfer efficiency was held constant at 68% (LTE=0.68) which gives a total number of 4577 photoelectrons detected per 511keV gamma. The MC input parameters are chosen similar to the parameters used for calculating the lower bound shown in figure 10.11. For the input parameters of $\tau_r = 70ps$, $\tau_d = 30.3ns$, $n' = 4577$ and $SPTR = 66ps$ we calculated a lower bound of 81ps FWHM CTR. In figure 10.20 the simulated digital readout is shown.
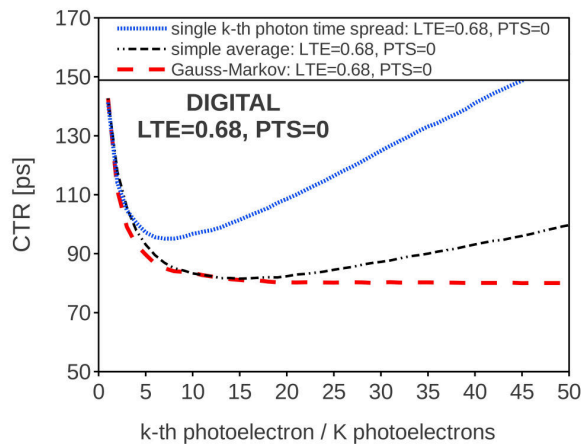
Figure 10.20.: Digital readout of a SiPM. Shown is the single $k-th$ photon time spread and different time estimators combining the time information of the preceding K photons. In the simulation the photon travel spread was set to zero (PTS=0) and the light transfer efficiency to 68% (LTE=0.68).
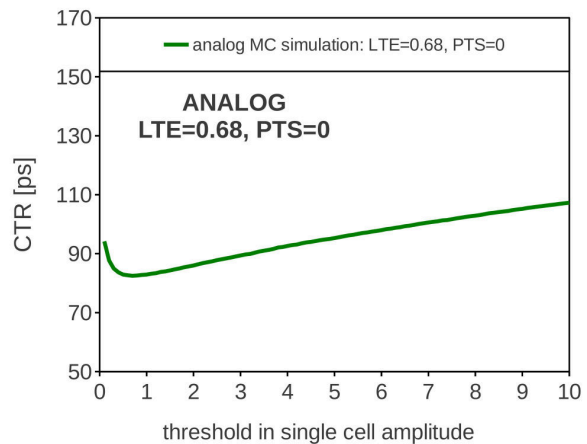
Figure 10.21.: Analog readout of a SiPM with leading edge discrimination. In the simulation the photon travel spread was set to zero (PTS=0) and the light transfer efficiency to 68% (LTE=0.68).

With the simple average time estimator we obtain a CTR value of 82ps whereas the Gauss-Markov estimator saturates at a time resolution of 80ps FWHM CTR, as can be seen in figure 10.20. The statistical error of the simulated values is in the order of a few percent. Meaning that both the simple average and Gauss-Markov time estimator are able to reach the intrinsic limit of the time resolution. In figure 10.21 we show the same MC simulation in the analog SiPM case.

The best CTR value at optimized threshold is 82ps FWHM CTR, which is equal to the lower bound of the time resolution. According to our simulations it seems that both ways of SiPM readout, either digital or analog, are in principle able to reach the intrinsic limit of the time resolution. This is a direct consequence of the fact that the simple average time estimator leads to almost the same values as the more complex Gauss-Markov approach.

In the following figures 10.22 - 10.29 similar comparisons are shown for simulations including the light transport in the crystal for sizes of 2x2x3mm^3, 2x2x5mm^3, 2x2x10mm^3 and 2x2x20mm^3.
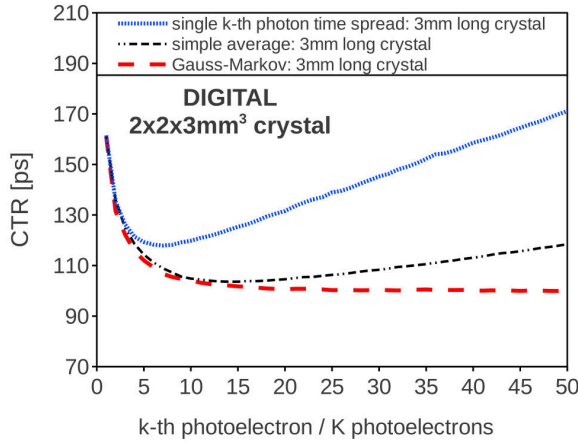
Figure 10.22.: Digital readout of a SiPM. Shown is the single $k - th$ photon time spread and different time estimators combining the time information of the preceding K photoelectrons for a crystal of 2x2x3mm^3 size.
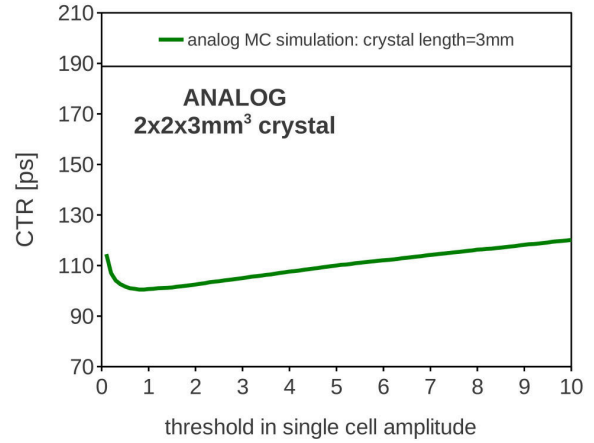
Figure 10.23.: Analog readout of a SiPM with leading edge discrimination for crystal dimensions of 2x2x3mm^3.
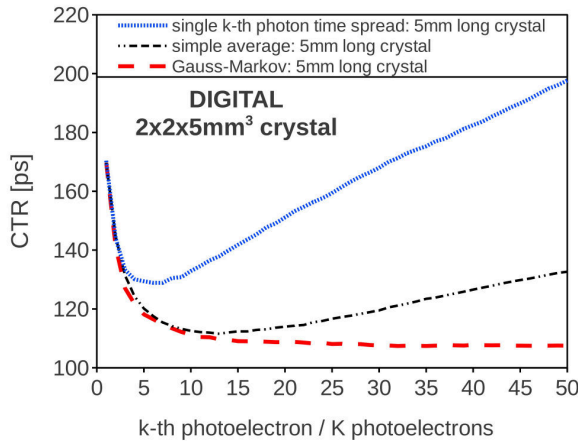
Figure 10.24.: Digital readout of a SiPM. Shown is the single $k - th$ photon time spread and different time estimators combining the time information of the preceding K photoelectrons for a crystal of 2x2x5mm^3 size.
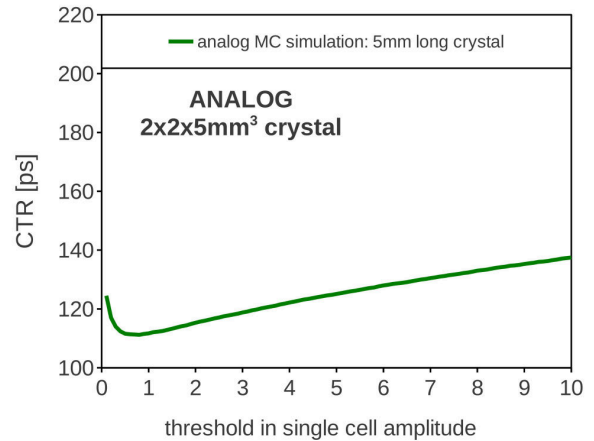
Figure 10.25.: Analog readout of a SiPM with leading edge discrimination for crystal dimensions of 2x2x5mm^3.
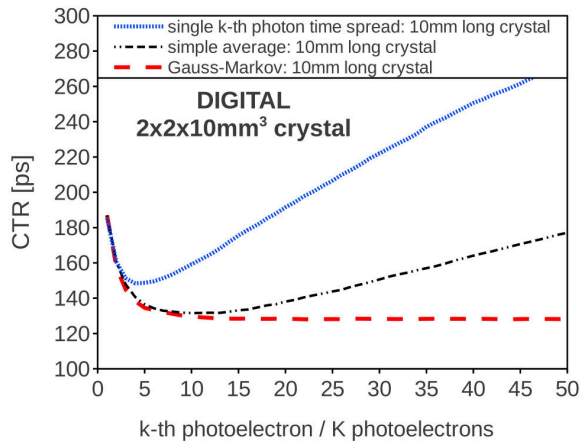
Figure 10.26.: Digital readout of a SiPM. Shown is the single $k-th$ photon time spread and different time estimators combining the time information of the preceding K photoelectrons for a crystal of 2x2x10mm^3 size.
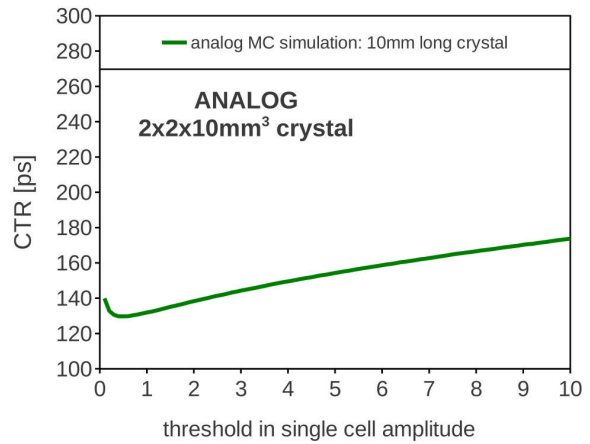
Figure 10.27.: Analog readout of a SiPM with leading edge discrimination for crystal dimensions of 2x2x10mm^3.
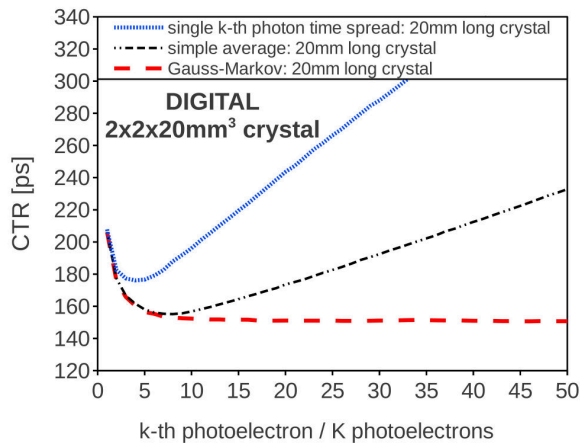
Figure 10.28.: Digital readout of a SiPM. Shown is the single $k-th$ photon time spread and different time estimators combining the time information of the preceding K photoelectrons for a crystal of 2x2x20mm^3 size.
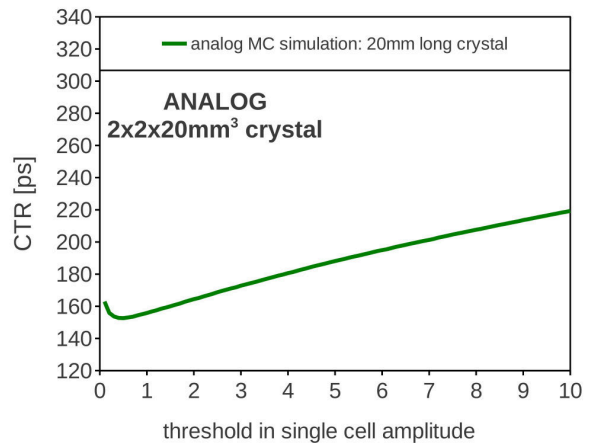
Figure 10.29.: Analog readout of a SiPM with leading edge discrimination for crystal dimensions of 2x2x20mm^3.

In all plots it can be seen that the digital readout of the SiPM with the use of the Gauss-Markov time estimator gives CTR values which are similar to the minimum CTR deduced in an analog SiPM with microcell signal pile-up and leading edge discrimination. In table 10.2 we summarize the best CTR values simulated as a function of crystal length using either analog or digital readout of the SiPM. The shown simulations do not include optical crosstalk and DCR of the SiPM neither electronic noise of the readout electronics.

Table 10.2.: Direct comparison of the digital SiPM and analog SiPM in terms of their theoretical timing performance for different crystal lengths. In the case of digital readout a full incorporation of covariances (Gauss-Markov estimator) leads to the same minimum CTR values as compared to microcell signal pile-up with leading edge discrimination in the analog SiPM. The mean simulation error of the stated values is about 5%.

configuration	digital SiPM k-th time spread	digital SiPM simple average	digital SiPM Gauss-Markov	analog SiPM leading edge
LTE=0.68, PTS=0	95ps	82ps	80ps	82ps
2x2x3mm^3	118ps	104ps	100ps	100ps
2x2x5mm^3	129ps	112ps	108ps	111ps
2x2x10mm^3	149ps	132ps	128ps	130ps
2x2x20mm^3	176ps	155ps	151ps	152ps

It seems that the digital readout scheme of a SiPM with Gauss-Markov time estimator performs equal to the analog readout of a SiPM with leading edge discrimination. Even for different crystal lengths this equality in terms of timing holds for the digital and analog readout of a SiPM. However, in an analog system the best achievable time resolution is very sensitive to the threshold settings which might be a disadvantage in a practical system. In contrary the fully digital readout shows a constant time resolution if the number of included time stamps exceeds a value of about 20. This could make the digital readout more stable against instrumental noise. The simulations in this chapter were performed without optical crosstalk and DCR of the SiPM. If these noise sources would be included, then the digital readout may show further advantages over the analog readout. However this must be carefully balanced with the more complex fabrication processes of a fully digital SiPM compared to an analog SiPM. Moreover, in the digital SiPM, disadvantages like a lower PDE due to the electronic structures occupying photosensitive area have to be taken into account as well.

10.5. Summary and conclusion

In this chapter we discussed the limits of the time resolution deduced by Monte Carlo simulations for the analog and digital SiPM. Further we used the Cramér-Rao lower bound to calculate the intrinsic limit of the time resolution and compared the obtained values with the analog and digital SiPM simulations. Using the Cramér-Rao lower bound we calculated an intrinsic CTR limit of 81ps FWHM for a scintillation photon emission rate with a rise time $\tau_r = 70ps$, a fall time $\tau_d = 30.3ns$ and a total number of detected photons $n' = 4577$. The single photon time resolution of the SiPM was 66ps ($SPTR = 66ps$) and the PTS in the crystal was set to zero ($PTS = 0ps$). With the same input parameters we simulated the best CTR value to be 81ps for the analog SiPM and 80ps for the fully digital SiPM using a refined time estimator. This means that both approaches of SiPM readout, either analog or digital, are able to reach the intrinsic CTR deduced by pure statistical considerations. In this analysis we did not include SiPM noise like dark counts, optical crosstalk or

afterpulsing. For an analog SiPM the best CTR value is observed around a small threshold window. This makes the analog SiPM more vulnerable in terms of instrumental noise. In contrary the fully digital SiPM readout shows a CTR which is stable after the inclusion of about 20 photoelectrons in the time estimator. It can be expected that this feature of the fully digital readout leads to a higher stability against SiPM noise like crosstalk, DCR and afterpulsing.

We further investigated the influence of the scintillation rise time τ_r, fall time τ_d and the number of photons detected n'. It was found that the time resolution is proportional to the square root of the scintillation fall time and inversely proportional to the square root of the number of photons detected, i.e. $CTR \propto \sqrt{\tau_d/n'}$. This directly leads to the conclusion that a higher PDE of the SiPM as well as a higher intrinsic light yield of the scintillator and a better light transfer efficiency in the crystal would lead always to an improvement in the time resolution. In addition a faster scintillation decay time will give similar improvements.

If we set to zero the PTS, the SPTR, optical crosstalk, DCR and electronic noise in the analog SiPM Monte Carlo simulations we obtain a CTR of 48ps FWHM. This value is only determined by the scintillation statistics and considers a light transfer efficiency of 68% and a PDE of 33%. Especially the PDE of 33% is a rather low value, which constantly improves for commercially available SiPMs. If all scintillation light would be detected, i.e. $LTE * PDE = 1$, then the best achievable coincidence time resolution in the analog system would be 21ps FWHM. Because of the zero Gaussian smearing of the photon emission rate (PTS=0 and SPTR=0) the necessary threshold values are very low. This is because in that case the first photoelectrons detected give the best time estimator. Meaning that for these optimal case of zero PTS and SPTR a fully digital readout may show advantages over the analog leading edge discrimination.

The scintillation rise time τ_r was assumed to be very fast with a value of 70ps. In this case it was shown that the scintillation rise time influences the CTR to a lower amount, if the PTS and SPTR are non-zero and in the order of 60ps each. This is a direct consequence of the convolution of the photon emission rate with the transfer time spread of the scintillator and SiPM. A non-zero PTS or SPTR can be seen to provoke an artificial rise time in the photon emission rate. The same arguments hold as well for a non zero scintillation rise time preventing an improvement in CTR when the SPTR or PTS is lowered. If we set the PTS and SPTR to zero then we start to notice the importance of the scintillation rise time which then would influence the CTR proportionally to its square root, i.e. $CTR \propto \sqrt{\tau_r}$. For a zero rise time and PTS we as well see the same proportionality for the SPTR, i.e. $CTR \propto \sqrt{SPTR}$. Hence, the scintillation rise time, the SPTR and the PTS are strongly correlated with each other. Consequently the photon travel time spread in the crystal has to be considered, as it is in the range of 60ps, even for very small crystals with dimensions of 2x2x3mm^3. At this time being there are no means to reduce the PTS in the crystal, which partly negates any improvement in the SPTR and scintillation rise time.

The performed analysis leads again to the conclusion that brighter crystals, faster scintillation decay times, better photon detection efficiencies, improved light transport and coupling to the photodetector would improve the time resolution most effectively.

Chapter 11

Summary and outlook

This thesis investigated the time resolution of a scintillator based detector for applications in time of flight positron emission tomography. The detector consists of a scintillating crystal, a photodetector and the readout electronics. As scintillator we used Lutetium oxyorthosilicate (LSO) doped with cerium and calcium. This scintillator is particularly suited for PET because of its high photoelectric absorption cross section, which leads to a high detection efficiency of the 511keV gammas. In addition it is well suited for time of flight applications because of its large intrinsic light yield of about 40000 photons produced per MeV and fast decay time of $\tau_d = 30ns$. As photodetector we used commercial SiPMs from Hamamatsu (the S10931 MPPC series). The tested SiPMs had all a common active area of 3x3mm^2 but different microcell sizes, i.e. 25μm, 50μm and 100μm. We found that the 50μm cell size type shows the best performance in terms of highest time resolution. This is explained by the fact that the 50μm type can be operated at fairly high bias overvoltages without a critical increase in DCR and optical crosstalk. Contrary to this type and despite a more favourable geometrical fill factor of the 100μm type we were not able to operate the 100μm device at optimal bias overvoltages because of a drastic increase in DCR and optical crosstalk with rising bias overvoltages. Using the 50μm type SiPM and the ultrafast amplifier-discriminator NINO for the readout of the SiPM signals we measured a CTR of 142±4ps FWHM with 2x2x5mm^3 LSO:Ce codoped 0.4% Ca crystals. We showed that the time-over-threshold energy encoding from NINO became inaccurate for higher bias overvoltages, because of the exponential decay of the SiPM signal together with the increasing DCR of the SiPM. This makes it nearly impossible to separate Compton events from photoelectric events and therefore leads to a deterioration of the measured CTR at higher bias overvoltages. To overcome this problem we had developed a new electronics board where we used NINO only as a low noise and fast leading edge discriminator for the timing information, and separately an analog amplifier to give the energy information. With this new board we were able to improve the measured CTR to 123±7ps FHWM using the same 2x2x5mm^3 LSO:Ce codoped 0.4% Ca crystals, an improvement of 15% compared to the old NINO board with its own time-over-threshold energy determination. The improvement stems from the possibility of operating the SiPM at higher bias overvoltages. Furthermore, we tested the timing performance of the new electronics as well with 2x2x3mm^3 LSO:Ce codoped 0.4%Ca crystals and obtained a value of 108±5ps FWHM. Hence, within the framework of these tests we could show that the

scintillation process can provide excellent coincidence time resolutions close to 100ps FWHM.

To understand and evaluate the measured values we had developed a Monte Carlo simulation tool in MATLAB in which we modelled the whole detection chain from the gamma ray conversion in the crystal, scintillation light production and transport in the crystal, light extraction and conversion in the SiPM photodetector to the electronic readout, taking also into account the single photon time resolution (SPTR), electronic noise and bandwidth limitations of the electronics. The input parameters of the simulation were determined by CTR independent measurements. This MC tool is able to model the CTR with high precision encouraging us to probe the individual contributions to the CTR in more detail. The summary of these studies can be seen in figure 11.1.
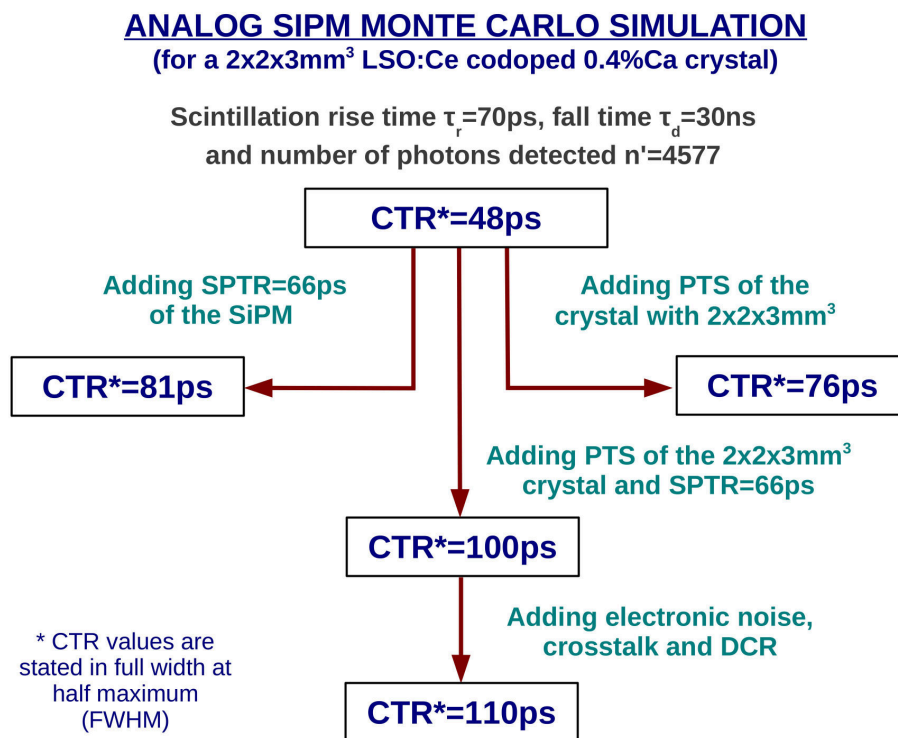
Figure 11.1.: Build-up of the measured CTR in the analog SiPM. The photon travel spread in the $2\text{x}2\text{x}3\text{mm}^3$ crystal plays a similar role as the SPTR of 66ps in the SiPM. In the shown simulations the PDE of the SiPM is set to 33% (2.3V overvoltage) and the LTE of the $2\text{x}2\text{x}3\text{mm}^3$ crystal is 68%.

In the analog SiPM the best achievable coincidence time resolution is about 48ps FWHM. This value includes only the scintillation properties of the LSO:Ce codoped 0.4%Ca crystal, the PDE of the SiPM with 33% and the light transfer efficiency of the crystal of 68%, which is the calculated value for a $2\text{x}2\text{x}3\text{mm}^3$ sized crystal wrapped in Teflon and coupled to the SiPM with optical grease Rhodorsil 47V (see figure 11.1). Other influences like the photon travel spread in the crystal, DCR and crosstalk, as well as SPTR of the SiPM, and electronic noise are not taken into account. If, in addition, we account for the PTS in the $2\text{x}2\text{x}3\text{mm}^3$ crystal, the CTR will degrade to 76ps FWHM.

If we only add the SPTR of the SiPM (SPTR=66ps) a similar degradation to 81ps FWHM can be observed. Accounting for both the PTS and SPTR would then degrade the CTR to 100ps FWHM. This value will further increase to 110ps FWHM if we include also optical crosstalk and the DCR of the SiPM, as well as electronic noise.

We further showed that a shorter scintillation decay time τ_d, a higher number of photons produced by the scintillation n and a higher PDE and LTE would improve the CTR like $CTR \propto \sqrt{\tau_d/(PDE * LTE * n)}$. From figure 11.1 we can deduce that the PTS of the crystal has a large influence on the CTR, and this already for rather small dimensions of only 2x2x3mm^3. This implies that the CTR improves less from a lower SPTR value of the SiPM than from an increased number of detected photons and/or a shorter scintillation decay time. A similar argumentation as for the SPTR holds as well for the scintillation rise time, where the CTR would benefit less from a faster rise time.

In PET crystal lengths of 20mm or longer are necessary to detect the 511keV gamma with a high probability and thus to increase the sensitivity of the PET system. Therefore we had studied the influence of the crystal length to the CTR in more detail. We measured the time resolution for different crystal lengths and found a clear dependence of the CTR on the length. For a 2x2x3mm^3 crystal we were able to measure 108±5ps FWHM. If we increase the length to 5mm the CTR deteriorates to 123±7ps FWHM, at 10mm the CTR is 143±7ps and at 20mm 176±7ps FWHM. We compared the measurements with our MC simulations and found good agreements for the various crystal lengths. The simulations also showed that the CTR deterioration is mainly limited by the light transfer efficiency in the crystal, i.e. being due to a higher attenuation factor arising from more frequent photon reflections with longer crystals. The simulations further illustrated that the influence of photon travel time spread is high, however does not seem to play too large a role with increasing crystal length. An improvement in CTR for longer crystals could be achieved, for example, by improving the light coupling to the photodetector. The simulations pointed out that scintillator wrapping and surface quality play an important role and thus have to be considered to a greater extent in future work.

An interesting way to improve time resolution and minimize parallax errors in PET is to read-out the crystal on both sides. We tested this double sided readout on a 2x2x20mm^3 crystal and achieved a CTR of 154±10ps FWHM. This is an improvement of 14% over the single sided readout of the same crystal with a CTR of 176±7ps FWHM. We showed that the CTR improvement from double sided readout is almost entirely explained by better light collection. This is in line with our simulation results showing that the PTS contribution is not increasing significantly with increasing crystal lengths.

Another important feature of our MC simulation was to enable us to give insight in the operation of the fully digital SiPM. We could show that the best achievable CTR in the analog SiPM with microcell signal pile-up and leading edge discrimination is comparable to the best achievable CTR

in the digital SiPM with a generalized least squares time estimator (Gauss-Markov estimator). This similarity of both SiPM types in terms of timing holds also for different crystal lengths as shown in table 11.1. Both types of SiPMs (digital and analog) are even able to achieve the CTR predicted by the Cramér-Rao lower bound with zero PTS in the crystal. Hence, there is no preference in choosing either the digital or analog SiPM in terms of reaching the best CTR. However it should be noted that the digital SiPM seems to be more stable against instrumental and SiPM noise.

Table 11.1.: Measured CTR as a function of crystal length. According analog SiPM simulations with and without instrumental and SiPM noise. The best achieved CTR for the analog SiPM is compared with the fully digital SiPM in MC simulations with zero crosstalk, zero DCR and zero electronic noise.

crystal length: (2x2mm^2 cross-section)	**measured CTR**	Monte Carlo simulation:		digital SiPM **Gauss-Markov** (WITHOUT crosstalk, DCR and electr. noise)
		analog SiPM		
		(WITH crosstalk, DCR, electr. noise)	(WITHOUT crosstalk, DCR, electr. noise)	
0mm (LTE=0.68 & PTS=0)		90ps	82ps	80ps
3mm	108±5ps	110ps	100ps	100ps
5mm	123±7ps	121ps	111ps	108ps
10mm	143±7ps	140ps	130ps	128ps
20mm	176±7ps	166ps	152ps	151ps

Future outlook: Surface effects in crystals with dimensions used for PET seem to play a crucial role in the scintillation light transport. In this domain further efforts have to be made in the modeling of the wrapping and surface finishing of the crystal.

In addition new measurements give hints that LSO:Ce codoped 0.4%Ca shows two decay components, a short one with $\tau_{d1} \sim 8ns$ and $\sim$8% abundance Y_1 (see equation 7.2.1) and a long one with $\tau_{d2} \sim 33ns$ and $\sim$92% abundance Y_2. The consequence of these two decay components would be that the MC simulation values given in chapter 7 and chapter 8 would improve by about 10% for all crystal lengths. Hence the simulated CTR values would be lower than the measured ones, which would give room to implement additional photon travel time spread caused by scattering in the Teflon. Such an additional jitter would increase the CTR values for all crystal lengths, however due to the higher number of reflections in longer crystals the deterioration of the CTR is expected to be more pronounced. This might explain the deviation of simulation from measurement in table 11.1 with increasing crystal length.

In the best case we could only extract 68% of the scintillation photons produced in a 2x2x3mm^3 crystal. Therefore improvements in light extraction should be envisaged in the future, especially for long crystals where the LTE can drop to 40%.

In summary, we have shown that SPTR, scintillation rise time and PTS are correlated having a joint effect on the CTR. Hence these three quantities must be improved concurrently in order to improve the CTR noticeably. The biggest challenge, however, is to reduce the PTS in the crystal being of the order of tens to hundreds of picoseconds, e.g. $\sim$60ps for crystals of only 2x2x3mm^3.

The principal conclusion of the performed work is that a 100ps TOF-PET system is feasible in the near future. An improvement of the SiPM-PDE by a factor of two would already put this goal in reach. Indeed companies like Hamamatsu K.K., FBK, Ketek, Sensl and others are pushing their developments into this direction. PDE values of about 50% have already been reported recently [105]. Increasing the intrinsic light yield of crystals and decreasing the scintillation decay time would bring similar improvements.

Appendix A

Schematics and printed circuit board of the new electronics

<u>Schematics:</u>

Here the complete schematics of the newly developed NINO Board is shown. In figure A.1 as well as in figure A.3 the NINO chip with external circuitry can be seen.

In figure A.2 the circuit diagram of the analog amplifier can be seen. The SiPMs can be found in this figure as well. Both NINO and the amplifier can be decoupled from the SiPM in order to be able to perform measurements without mutual influence.

The amplification of the amplifier can be adjusted in a wide range in order to measure single SiPM cell (microcell or SPAD) signals of several hundreds of microvolts up to several volts of input delivered by the SiPM if coupled to a scintillator. The bandwidth of the amplifier is around 300MHz with a noise floor lower than 0.1mV at highest gain.

The three figures have to be read as one. On the right hand side in figure A.1 three wires can be seen which will be continued in figure A.2 on the left. Whereas in figure A.2 on the right four open wires can be seen, and figure A.3 is the continuation of figure A.2.

Figure A.1.: Schematics first part of the newly developed NINO Board. Shown is NINO with its surrounding circuitry.
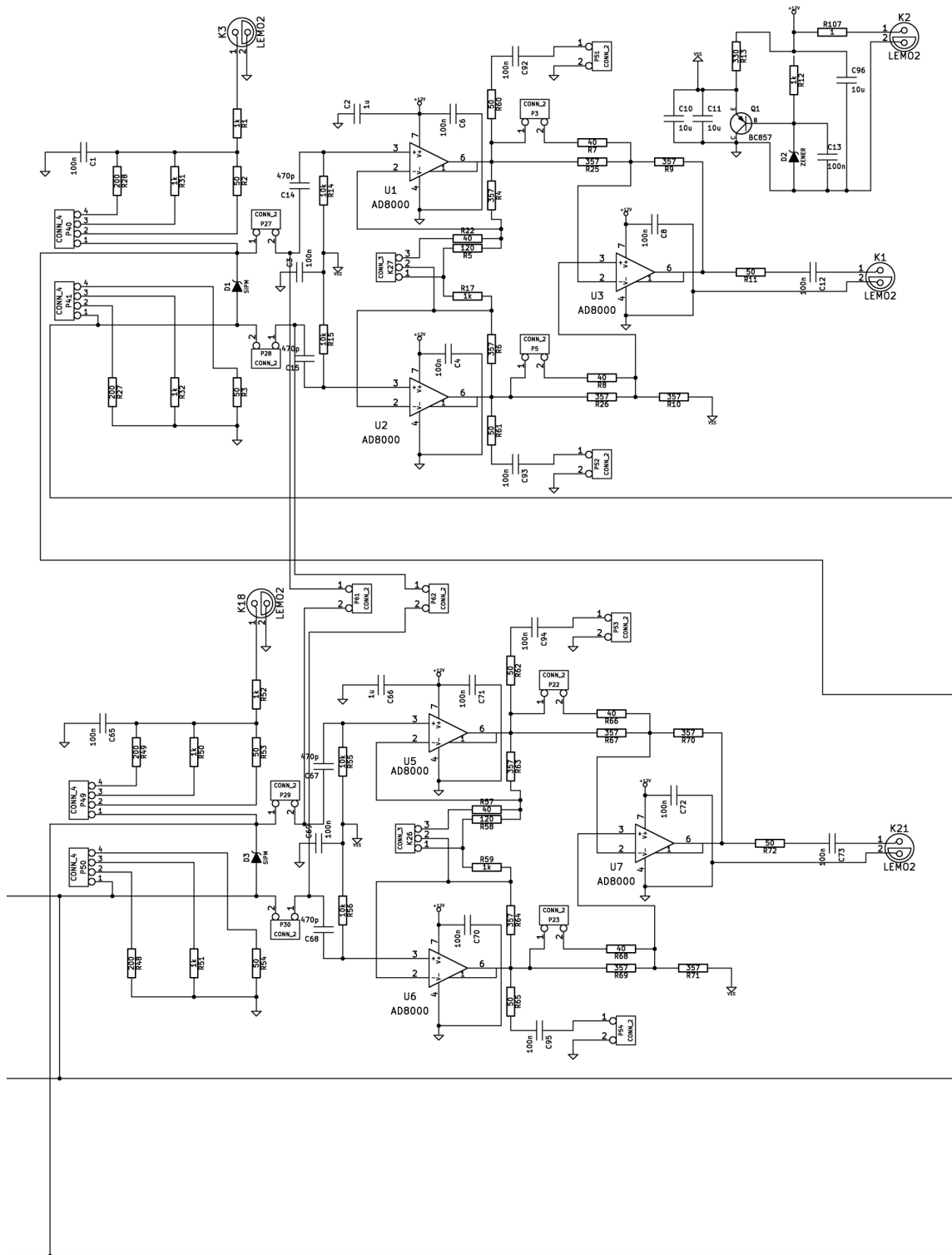
Figure A.2.: Schematics second part of the newly developed NINO Board. Shown is the analog voltage amplifier and the SiPM biasing circuitry.

Figure A.3.: Schematics third part of the newly developed NINO Board. Shown is NINO with its surrounding circuitry.

Printed circuit board:

The printed circuit board layout with the wire routing can be seen in figure A.4. Figure A.5 and figure A.6 show the printed circuit boards of the new developed electronics in more detail. In figure A.5 the component tracks of the PCB can be seen and in figure A.6 the copper tracks with copper ground plates.
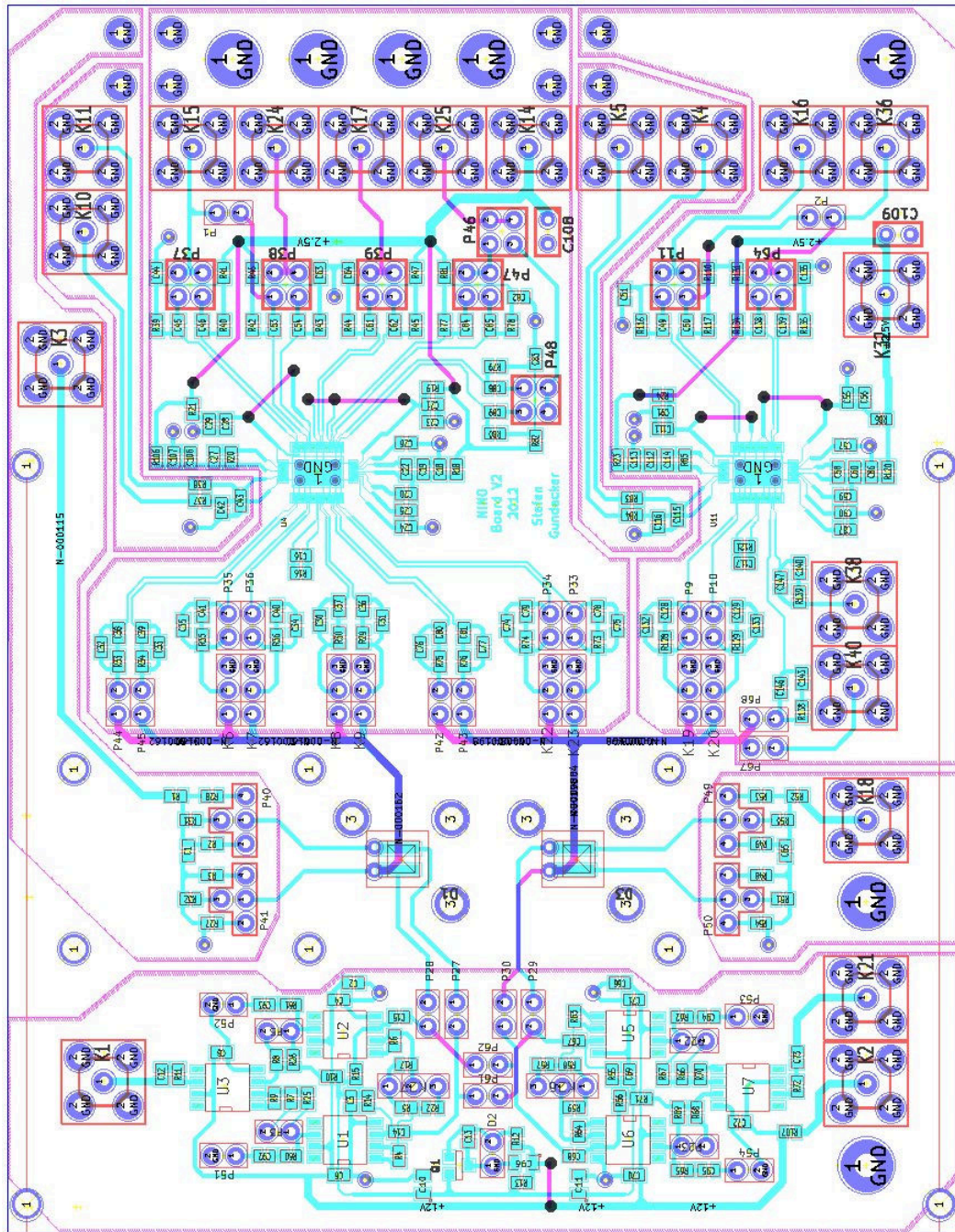
Figure A.4.: Layout of the developed printed circuit board in order to study SiPMs in terms of timing.
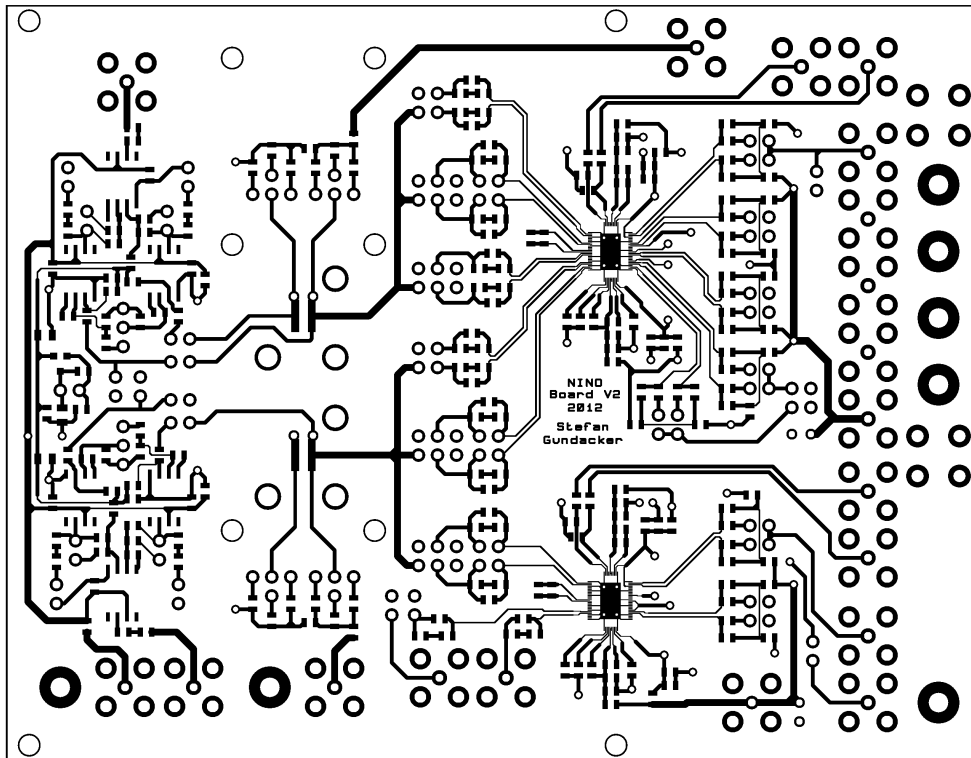
Figure A.5.: Component tracks of the PCB. Drill holes and SMD pads can be seen as well.
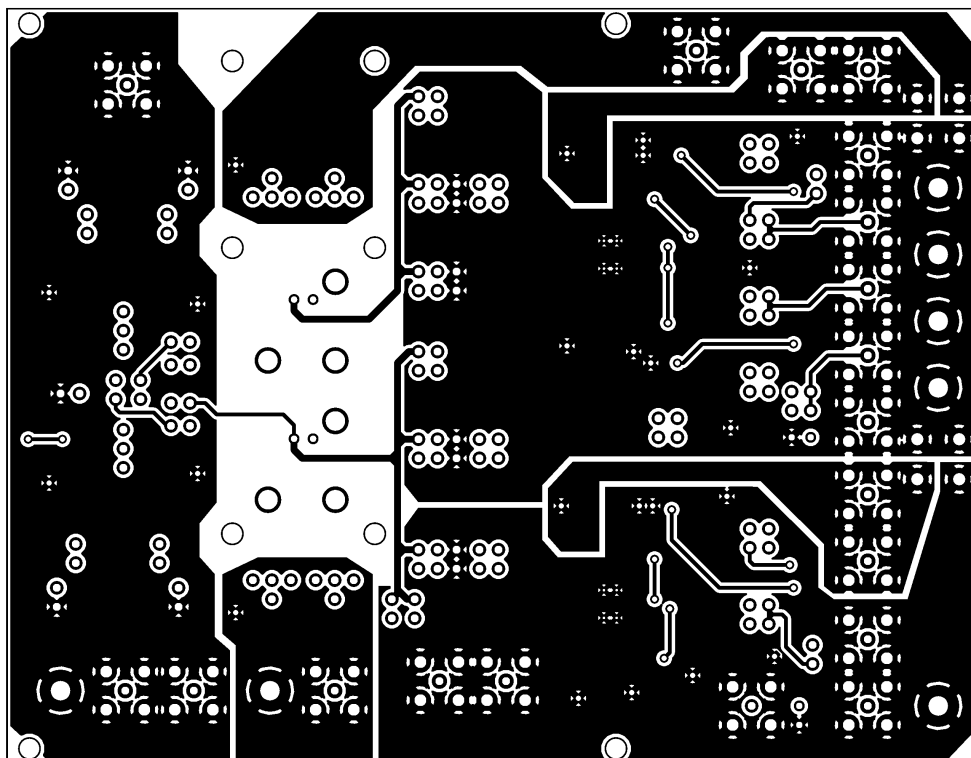
Figure A.6.: Copper tracks of the PCB and copper ground plates. Drill holes can be seen as well.

Appendix B

Mathematical description of the photon emission

We start with the kth photon's generation time PDF in equation 2.0.1.

$$p_{k:n}(t) = n \binom{n-1}{k-1} \widehat{f}(t)\widehat{F}(t)^{k-1}(1-\widehat{F}(t))^{n-k} \tag{2.0.1}$$

Equation 2.0.1 we rewrite to obtain equation 2.0.2.

$$
\begin{aligned}
p_{k:n}(t) &= \frac{n(n-1)!}{(n-1-k+1)!\,(k-1)!} \widehat{f}(t)\widehat{F}(t)^{k-1}(1-\widehat{F}(t))^{n-k}\frac{\widehat{F}(t)}{\widehat{F}(t)} \\
&= \frac{n(n-1)!}{(n-k)!\,k!}\widehat{F}(t)^k (1-\widehat{F}(t))^{n-k} \cdot k \cdot \frac{\widehat{f}(t)}{\widehat{F}(t)}
\end{aligned}
\tag{2.0.2}
$$

We can identify the standard binomial distribution in equation 2.0.2:

$$B_{k:n} = \binom{n}{k}\widehat{F}(t)^k(1-\widehat{F}(t))^{n-k}, \tag{2.0.3}$$

which can be approximated by the Poisson distribution if $\widehat{F}(t) \cdot n$ approaches a constant value for $n \to \infty$ and $\widehat{F}(t) \to 0$. This condition is equal to the emission of the first photons in the photon emission rate. With $f(t) = n \cdot \widehat{f}(t)$ and $F(t) = n \cdot \widehat{F}(t)$ we arrive at the approximation in 2.0.4.

$$
\begin{aligned}
B_{k:n}(t) &= \frac{n!}{(n-k)!\,k!}\widehat{F}(t)^k (1-\widehat{F}(t))^{n-k} \\
&= \frac{n(n-1)(n-2)\cdots(n-k+1)}{k!}\left(\frac{F(t)}{n}\right)^k\left(1-\frac{F(t)}{n}\right)^{n-k} \\
&= \left(1-\frac{1}{n}\right)\left(1-\frac{2}{n}\right)\cdots\left(1-\frac{k-1}{n}\right)\left(1-\frac{F(t)}{n}\right)^{n-k}\frac{F(t)^k}{k!} \\
&\to \frac{F(t)^k}{k!}e^{-F(t)}
\end{aligned}
\tag{2.0.4}
$$

In equation 2.0.4 we used the limit definition of the exponential: $\exp(x) = \lim_{n\to\infty}(1 + x/n)^n$. With the derived approximation in 2.0.4 we can express the binomial distribution in equation 2.0.2 by the Poisson distribution for the kth photon emission probability in equation 2.0.5.

$$p_{k:n}(t) \to \frac{F(t)^k}{k!}e^{-F(t)} \cdot k \cdot \frac{\widehat{f}(t)}{\widehat{F}(t)} = \frac{F(t)^{k-1}}{(k-1)!}e^{-F(t)}f(t) \tag{2.0.5}$$

Appendix C

Derivation of the "Gauss-Markov" time estimator

In order to obtain the most probable time of positron emission $\widehat{\theta}_{GM}$ we have to maximize the probability density function $P(\theta|\vec{D})$, which gives the probability of a certain positron emission time θ under the condition of a measured data set $\vec{D}$. The data set $\vec{D}$ is the vector of measured time stamps with length K. Using Bayes' theorem we can express $P(\theta|\vec{D})$ with the likelihood function $P(\vec{D}|\theta)$ as can be seen in equation 3.0.1.

$$P(\theta|\vec{D}) = \frac{P(\theta) \cdot P(\vec{D}|\theta)}{P(\vec{D})} \tag{3.0.1}$$

The term $P(\theta)$ in equation 3.0.1 denotes the prior which we define to be one, i.e. $P(\theta) = 1$. Meaning that we suppose to have no prior knowledge of the positron emission time and thus being unbiased. The likelihood function $P(\vec{D}|\theta)$ we express by the multivariate normal distribution, as can be seen in equation 3.0.2.

$$P(\vec{D}|\theta) = \frac{1}{\sqrt{(2\pi)^K |\mathbf{C}|}} \exp\left[-\frac{1}{2}\left(\vec{D} - \vec{\mathbb{1}}\theta\right)^T \mathbf{C}^{-1}\left(\vec{D} - \vec{\mathbb{1}}\theta\right)\right] \tag{3.0.2}$$

In the equation 3.0.2 $\mathbf{C}$ denotes the full covariance matrix of the measured data set. It should be noted that the covariance matrix can be determined by a calibration run and subsequently be used to calculate the best time estimator for independently measured data sets $\vec{D}$.

The maximum of the probability density function $P(\theta|\vec{D})$ can be found by setting its derivative to zero, i.e. $\frac{dP(\theta|\vec{D})}{d\theta} = 0$. Because of the unity prior $P(\theta) = 1$ the maximum of the probability density function $P(\theta|\vec{D})$ is equal to the minimum of the argument of the exponential of the likelihood function $\left[\left(\vec{D} - \vec{\mathbb{1}}\theta\right)^T \mathbf{C}^{-1}\left(\vec{D} - \vec{\mathbb{1}}\theta\right)\right]$. Hence, the here discussed maximum likelihood approach links to the generalized least squares method. In equation 3.0.3 the derivation of the best positron emission time estimator $\widehat{\theta}_{GM}$ maximizing $P(\theta|\vec{D})$ can be found.

$$0 = \frac{dP(\theta|\vec{D})}{d\theta}$$

$$0 = \frac{d}{d\theta} \left[-\frac{1}{2} \left(\vec{D} - \mathbb{1}\theta \right)^T \mathbf{C}^{-1} \left(\vec{D} - \mathbb{1}\theta \right) \right]$$

$$0 = \frac{1}{2} \vec{\mathbb{1}}^T \mathbf{C}^{-1} \left(\vec{D} - \mathbb{1}\theta \right) + \frac{1}{2} \left(\vec{D} - \mathbb{1}\theta \right)^T \mathbf{C}^{-1} \vec{\mathbb{1}} \qquad (3.0.3)$$

$$0 = \vec{\mathbb{1}}^T \mathbf{C}^{-1} \left(\vec{D} - \mathbb{1}\theta \right)$$

$$\Rightarrow \widehat{\theta}_{GM} = \frac{\vec{\mathbb{1}}^T \mathbf{C}^{-1} \vec{D}}{\vec{\mathbb{1}}^T \mathbf{C}^{-1} \vec{\mathbb{1}}}$$

In the last steps we used the product rule and the transpose of the matrix multiplication $(\mathbf{AB})^T = \mathbf{B}^T\mathbf{A}^T$ (see equation 3.0.4), together with the property of $\mathbf{C}$ being symmetric and thus $\mathbf{C}^{-1}$ being symmetric as well, i.e. $\left(C^{-1} \right)^T = C^{-1}$.

$$\left[\left(\vec{D} - \mathbb{1}\theta \right)^T \mathbf{C}^{-1} \vec{\mathbb{1}} \right]^T = \vec{\mathbb{1}}^T \mathbf{C}^{-1} \left(\vec{D} - \mathbb{1}\theta \right) \qquad (3.0.4)$$

Bibliography

[1] M. Conti, "Focus on time-of-flight PET: the benefits of improved time resolution," Eur. J. Nucl. Med. Mol. Imaging, vol. 38, pp. 1147–1157, 2011.

[2] M. Conti, "State of the art and challenges of time-of-flight PET," Physica Medica, vol. 25, pp. 1–11, 2009.

[3] B. W. Jakoby, Y. Bercier, M. Conti, M. E. Casey, B. Bendriem, and D. W. Townsend, "Physical and clinical performance of the mCT time-of-flight PET/CT scanner," Physics in Medicine and Biology, vol. 56, pp. 2375–2389, April 2011.

[4] V. Bettinardi, L. Presotto, E. Rapisarda, M. Picchio, L. Gianolli, and M. C. Gilardi, "Physical performance of the new hybrid PET/CT discovery-690," Medical Physics, vol. 38, no. 10, pp. 5394–5411, 2011.

[5] S. Surti, A. Kuhn, M. E. Werner, A. E. Perkins, J. Kolthammer, and J. S. Karp, "Performance of philips gemini TOF PET/CT scanner with special consideration for its time-of-flight imaging capabilities," J. Nucl. Med., vol. 48, pp. 471–480, March 2007.

[6] "EndoTOFPET-US Proposal: Novel multimodal endoscopic probes for simultaneous PET/ultrasound imaging for image-guided interventions," European Union 7th Framework Program (FP7/2007-2013) under Grant Agreement No. 256984, Health- 2010.1.2-1.

[7] C. Kim, G. Wang, and S. Dolinsky, "Multi-pixel photon counters for TOF-PET detectors and its challenges," IEEE Trans. Nucl. Sci., vol. 56, pp. 2580–2585, October 2009.

[8] R. Vinke, H. Löhner, D. Schaart, H. van Dam, S. Seifert, F. Beekman, and P. Dendooven, "Optimizing the timing resolution of SiPM sensors for use in TOF-PET detectors," Nucl. Instrum. Methods Phys. Res. A, vol. 610, pp. 188–191, 2009.

[9] J. Y. Yeom, R. Vinke, and C. S. Levin, "Optimizing timing performance of silicon photomultiplier-based scintillation detectors," Phys. Med. Biol., vol. 58, pp. 1207–1220, 2013.

[10] E. Auffray, B. Frisch, F. Geraci, A. Ghezzi, S. Gundacker, H. Hillemanns, P. Jaron, T. Meyer, M. Paganoni, K. Pauwels, M. Pizzichemi, and P. Lecoq, "A comprehensive & systematic study of coincidence time resolution and light yield using scintillators of different size, wrapping and doping," IEEE Trans. Nucl. Sci., vol. 60, pp. 3163–3171, October 2013.

[11] W. Moses and S. Derenzo, "Prospects for Time-of-Flight PET using LSO Scintillator," <u>IEEE Trans. Nucl. Sci.</u>, no. NS-46, pp. 474–478, 1999.

[12] T. F. Budinger, K. M. Brennan, W. W. Moses, and S. E. Derenzo, "Advances in positron tomography for oncology," <u>Nuclear Medicine and Biology</u>, vol. 23, pp. 659–667, August 1996.

[13] A. Selmin, A. Nuri, O. Ahmet, and O. M. Ali, "Abnormal 18F-FDG Uptake Detected with Positron Emission Tomography in a Patient with Breast Cancer: A Case of Sarcoidosis and Review of Literature," <u>Case Reports in Medicine</u>, vol. 2009, 2009.

[14] B. Frisch, "Development of a combined positron emission mammograph and ultrasound scanner," <u>PhD thesis, Vienna University of Technology</u>, 2012.

[15] J. L. Humm, A. Rosenfeld, and A. D. Guerra, "From PET detectors to PET scanners," <u>Eur. J. Nucl. Med. Mol. Imaging</u>, vol. 30, pp. 1574–1597, November 2003.

[16] M. Lubberink, R. Boellaard, A. P. van der Weerdt, F. C. Visser, and A. A. Lammertsma, "Quantitative Comparison of Analytic and Iterative Reconstruction Methods in 2- and 3-Dimensional Dynamic Cardiac ^{18}F-FDG PET," <u>J. Nucl. Med.</u>, vol. 45, pp. 2008–2015, December 2004.

[17] Y. Vardi, L. A. Shepp, and L. Kaufman, "A statistical model of positron emission tomography," <u>Journal of the American Statistical Association</u>, vol. 80, pp. 8–20, March 1985.

[18] M. Kronberger, "Optimization of the light extraction from heavy inorganic scintillators," <u>PhD thesis, Vienna University of Technology</u>, June 2008.

[19] H. Zaidi and K. Koral, "Scatter modelling and compensation in emission tomography," <u>Eur. J. Nucl. Med. Mol. Imaging</u>, vol. 31, no. 5, pp. 761–782, 2004.

[20] P. Lecoq and J. Varela, "Clear-PEM a dedicated PET camera for mammography," <u>Nucl. Instrum. Methods Phys. Res. A</u>, vol. 486, pp. 1–6, June 2002.

[21] E. Auffray, P. Bruyndonckx, O. Devroede, A. Fedorov, U. Heinrichs, M. Korjik, M. Krieguer, C. Kuntner, C. Lartizien, P. Lecoq, S. Leonard, C. Morel, J. Mosset, C. Pedrini, A. Petrosian, U. Pietrzyk, M. Rey, S. Saladino, D. Sappey-Marinier, L. Simon, M. Streun, S. Tavernier, J. Vieira, and K. Ziemons, "The ClearPET project," <u>Nucl. Instrum. Methods Phys. Res. A</u>, vol. 527, pp. 171–174, July 2004.

[22] K. Ziemons, E. Auffray, R. Barbier, G. Brandenburg, P. Bruyndonckx, Y. Choi, D. Christ, N. Costes, Y. Declais, O. Devroede, C. Dujardin, A. Fedorovd, U. Heinrichs, M. Korjik, M. Krieguer, C. Kuntner, G. Largeron, C. Lartizien, H. Larue, P. Lecoq, S. Leonard, J. Marteau, C. Morel, J. Mosset, C. Parl, C. Pedrini, A. Petrosyan, U. Pietrzyk, M. Rey, S. Saladino, D. Sappey-Marinier, L. Simon, M. Streun, S. Tavernier, and J. Vieira, "The ClearPET^{TM} project: development of a 2nd generation high-performance small animal PET scanner," <u>Nucl. Instrum. Methods Phys. Res. A</u>, vol. 537, pp. 307–311, January 2005.

[23] C. Casella, M. Heller, C. Joram, and T. Schneider, "A high resolution TOF-PET concept with axial geometry and digital SiPM readout," <u>Nucl. Instrum. Methods Phys. Res. A</u>, vol. 736, pp. 161–168, 2014.

[24] J. S. Karp, S. Surti, M. E. Daube-Witherspoon, and G. Muehllehner, "Benefit of time-of-flight in PET: Experimental and clinical results," <u>J. Nucl. Med.</u>, vol. 49, no. 3, pp. 462–470, 2008.

[25] E. van Loef, P. Dorenbos, C. van Eijk, K. Kramer, and H. Gudel, "High-energy-resolution scintillator: Ce^{3+} activated $LaBr_3$," <u>Appl. Phys. Letters</u>, vol. 79, no. 10, pp. 1573–1575, 2001.

[26] R. Lecomte, "Novel detector technology for clinical PET," <u>Eur. J. Nucl. Med. Mol. Imaging</u>, vol. 36, no. 1, pp. 69–85, 2009.

[27] G. F. Knoll, <u>Radiation Detection and Measurement</u>. John Wiley & Sons, Inc., 3 ed., 1999.

[28] C. L. Melcher and J. S. Schweitzer, "Cerium-doped Lutetium Oxyorthosilicate: A Fast, Efficient New Scintillator," <u>IEEE Trans. Nucl. Sci</u>, vol. 39, no. 4, p. 502, 1992.

[29] R. Evans and A. Noyau, <u>The atomic nucleus</u>. McGraw-Hill, 1955.

[30] G. Nelson and D. Reilly, "Gamma-ray interactions with matter," <u>Passive Nondestructive Analysis of Nuclear Materials, Los Alamos National Laboratory, NUREG/CR-5550, LAUR-90-732</u>, pp. 27–42, 1991.

[31] M. Berger, J. Hubbell, S. Seltzer, J. Chang, J. Coursey, R. Sukumar, D. Zucker, and K. Olsen, "XCOM: Photon cross section database," `http://www.nist.gov/pml/data/xcom/index.cfm`.

[32] B. Shleien, L. Slaback, and B. Birky, <u>Handbook of Health Physics and Radiological Health</u>. Baltimore: Lippincott Williams & Wilkins, January 1998.

[33] C. Pédrini, "Scintillation mechanisms and limiting factors on each step of relaxation of electronic excitation," <u>Phys. Solid State</u>, vol. 47, pp. 1359–1363, 2005.

[34] M. Weber, "Scintillation: mechanisms and new crystals," <u>Nucl. Instrum. Methods Phys. Res. A</u>, vol. 527, pp. 9–14, 2004.

[35] P. Lecoq, A. Annenkov, A. Gektin, M. Korzhik, and C. Pedrini, <u>Inorganic Scintillators for Detector Systems. Physical Principles and Crystal Engineering.</u> Berlin: Springer, 2006.

[36] A. Lempicki, A. Wojtowicz, and E. Berman, "Fundamental limits of scintillator performance," <u>Nucl. Instrum. Methods Phys. Res. A</u>, vol. 333, no. 2-3, pp. 304–311, 1993.

[37] S. Gundacker, E. Auffray, B. Frisch, P. Jarron, A. Knapitsch, T. Meyer, M. Pizzichemi, and P. Lecoq, "Time of flight positron emission tomography towards 100ps resolution with L(Y)SO: an experimental and theoretical analysis," <u>JINST</u>, August 2013. JINST 8 P07014.

[38] J. Birks, <u>The theory and practice of scintillation counting</u>. New York: Pergamon Press, 1964.

[39] F. Powolny, E. Auffray, S. Brunner, E. Garutti, M. Goettlich, H. Hillemanns, P. Jarron, P. Lecoq, T. Meyer, H. Schultz-Couloun, W. Shen, and M. Williams, "Time-Based Readout of a Scilicon Photomultiplier (SiPM) for Time of Flight Positron Emission Tomography (TOF-PET)," <u>IEEE Trans. Nucl. Sci.</u>, vol. 58, pp. 597–604, June 2011.

[40] M. Moszynski, J. Zalipska, M. Balcerzyk, M. Kapusta, W. Mengesha, and J. Valentine, "Intrinsic energy resolution of NaI(Tl)," <u>Nucl. Instrum. Methods Phys. Res. A</u>, vol. 484, no. 1-3, pp. 259–269, 2002.

[41] P. Dorenbos, J. de Haas, and C. van Eijk, "Non-proportionality in the scintillation response and the energy resolution obtainable with scintillation crystals," <u>IEEE Trans. Nucl. Sci.</u>, vol. 42, pp. 2190–2202, December 1995.

[42] P. Dorenbos, "Light output and energy resolution of Ce^{3+}-doped scintillators," <u>Nucl. Instrum. Methods Phys. Res. A</u>, vol. 486, pp. 208–213, 2002.

[43] R. Post and L. Schiff, "Statistical limitations on the resolving time of a scintillation counter," <u>Phys. Rev.</u>, vol. 80, p. 1113, December 1950.

[44] D. Renker and E. Lorenz, "Advances in solid state photon detectors," <u>JINST</u>, April 2009. JINST 4 P04004.

[45] F. Powolny, "Characterisation of time resolved photodetector systems for Positron Emission Tomography," <u>PhD thesis, Universite de Neuchatel</u>, May 2009.

[46] A. Otte, "Observation of VHE Gamma-Rays from the Vicinity of magnetized Neutron Stars and Development of new Photon-Detectors for Future Ground based Gamma-Ray Detectors," <u>PhD thesis, Technische Universität München</u>, 2007.

[47] R. McIntyre, "Theory of microplasma instability in silicon," <u>J. Appl. Phys.</u>, vol. 32, pp. 983–995, June 1961.

[48] R. Haitz, "Model for the electrical behavior of a microplasma," <u>J. Appl. Phys.</u>, vol. 35, p. 1380, May 1964.

[49] V. Golovin, "Avalanche Photodetector," <u>Russian Agency for Patents and Trademarks, Patent No. Ru 2142175</u>, 1998.

[50] Z. Sadygov, "Avalanche Detector," <u>Russian Agency for Patents and Trademarks, Patent No. RU 2102820</u>, 1998.

[51] B. Dolgoshein, L. Filatov, P. Buzhan, A. Ilyin, V. Kantzerov, V. Kaplin, A. Karakash, F. Kayumov, S. Klemin, E. Popova, and S. Smirnov, "Silicon photomultiplier and its possible applications," <u>Nucl. Instrum. Methods Phys. Res. A</u>, vol. 504, pp. 48–52, May 2003.

[52] M. Lesser, "Antireflection coatings for silicon charge-coupled devices," <u>Optic. Eng.</u>, vol. 26, September 1987.

[53] G. Hurkx, D. Klaassen, and M. Knuvers, "A new recombination model for device simulation including tunneling," <u>IEEE Trans. Electron. Dev</u>, vol. 39, pp. 331–338, February 1992.

[54] G. Hurkx, H. de Graaff, W. Kloosterman, and M. Knuvers, "A new analytical diode model including tunneling and avalanche breakdown," <u>IEEE Trans. Electron. Dev.</u>, vol. 39, pp. 2090–2098, September 1992.

[55] L. Lacaita, F. Zappa, S. Bigliardi, and M. Manfredi, "On the bremsstrahlung origin of hot-carrier-induced photons in silicon devices," <u>IEEE Trans. Electron. Dev.</u>, vol. 40, pp. 577–582, March 1993.

[56] P. Buzhan, B. Dolgoshein, L. Filatov, A. Ilyin, V. Kaplin, A. Karakash, S. Klemin, R. Mirzoyan, A. Otte, E. Popova, V. Sosnovtsev, and M. Teshim, "Large area silicon photomultipliers: performance and applications," <u>Nucl. Instrum. Methods Phys. Res. A</u>, vol. 567, pp. 78–82, June 2006.

[57] H. Otono, S. Yamashita, T. Yoshioka, H. Oide, T. Suehiro, and H. Hano, "Study of MPPC at liquid nitrogen temperature," <u>Proceedings of Science PoS(PD07)007</u>, 2007.

[58] W. Oldham, R. Samuelson, and P. Antognetti, "Triggering phenomena in avalanche diodes," <u>IEEE Trans. Electron. Dev.</u>, vol. 19, pp. 1056–1060, September 1972.

[59] T. Frach, G. Prescher, C. Degenhardt, R. Gruyter, A. Schmitz, and R. Ballizany, "The digital silicon photomultiplier principle of operation and intrinsic detector performance," <u>IEEE Nuclear Science Symp. Conf.</u>, pp. 1959–1965, 2009.

[60] S. Mandai, V. Jain, and E. Charbon, "A Fully-Integrated 780x800μm^2 Multi-Digital Silicon Photomultiplier With Column-parallel Time-to-Digital Converter," <u>Proceedings of ESSCIRC</u>, pp. 89–92, September 2012.

[61] Y. Haemisch, T. Frach, C. Degenhardt, and A. Thon, "Fully Digital Arrays of Silicon Photomultipliers (dSiPM) - a Scalable Alternative to Vacuum Photomultiplier Tubes (PMT)," <u>Physics Procedia</u>, vol. 37, pp. 1546–1560, 2012.

[62] B. Frisch, "Combining endoscopic ultrasound with Time-Of-Flight PET: The EndoTOFPET-US Project," <u>Nucl. Instrum. Methods Phys. Res. A</u>, vol. 732, pp. 577–580, 2013. On behalf of the EndoTOFPET-US Collaboration.

[63] F. Anghinolfi, P. Jarron, F. Krummenacher, E. Usenko, and M. Williams, "NINO: An ultrafast low-power front-end amplifier discriminator for the time-of-flight detector in the ALICE experiment," <u>IEEE Trans. Nucl. Sci.</u>, vol. 51, pp. 1974–1978, October 2004.

[64] P. Jarron, E. Auffray, S. Brunner, M. Despeisse, E. Garutti, M. Goettlich, H. Hillemanns, P. Lecoq, T. Meyer, F. Powolny, W. Shen, H. Schultz-Coulon, and M. Williams, "Time based

readout of a silicon photomultiplier (SiPM) for time of flight positron emission tomography (TOF-PET)," Nuclear Science Symposium Conference record (NSS/MIC), pp. 1212–1219, 2009.

[65] W. W. Moses, "Time of flight in PET revisited," IEEE Trans. Nucl. Sci., vol. 50, pp. 1325–1330, October 2003.

[66] M. Moszynski, M. Kapusta, A. Nassalski, T. Szczesniak, D. Wolski, L. Eriksson, and C. L.Melcher, "New prospects for time-of-flight PET with LSO scintillators," IEEE Trans. Nucl. Sci., vol. 53, pp. 2484–2488, October 2006.

[67] T. Szczesniak, M. Moszynski, L. Swiderski, A. Nassalski, P. Lavoute, and M. Kapusta, "Fast photomultipliers for TOF PET," IEEE Trans. Nucl. Sci., vol. 56, pp. 173–181, February 2009.

[68] T. Szczesniak, M. Moszynski, M. Grodzicka, D.Wolski, L. Swiderski, M. Szawlowski, and M. Kapusta, "Time resolution of scintillation detectors based on SiPM in comparison to photomultipliers," IEEE NSS/MIC Conf. Rec., pp. 1728–1735, October 2010.

[69] S. Gundacker, E. Auffray, N. D. Vara, B. Frisch, H. Hillemanns, P. Jarron, B. Lang, T. Meyer, S. Mosquera-Vazquez, E. Vauthey, and P. Lecoq, "SiPM time resolution: From single photon to saturation," Nucl. Instrum. Methods Phys. Res. A, vol. 718, pp. 569–572, August 2013.

[70] S. Gundacker, E. Auffray, B. Frisch, H. Hillemanns, P. Jarron, T. Meyer, K. Pauwels, and P. Lecoq, "A Systematic Study to Optimize SiPM Photodetectors for Highest Time Resolution in PET," IEEE Trans. Nucl. Sci., vol. 59, pp. 1798–1804, October 2012.

[71] S. Gundacker, E. Auffray, B. Frisch, T. Meyer, P. Jarron, and P. Lecoq, "SiPM photodetectors for highest time resolution in PET," Proceedings of Science PoS(PhotoDet 2012)016, June 2012. LAL Orsay, France.

[72] F. Powolny, E. Auffray, H. Hillemanns, P. Jarron, P. Lecoq, T. Meyer, and D. Moraes, "A novel time-based readout scheme for a combined PET-CT detector using APDs," IEEE Trans. Nucl. Sci., vol. 55, pp. 2465–2474, October 2008.

[73] R. Mirzoyan, B. Dolgoshein, P. Holl, S. Klemin, C. Merck, H. G. Moser, A. N. Otte, J. Ninkovic, E. Popova, R. Richter, and M. Teshima, "SiPM and APD as advanced detectors for astro-particle physics," Nucl. Instrum. Methods Phys. Res. A, vol. 572, pp. 493–494, 2007.

[74] D. Henseler, R. Grazioso, N. Zhang, and M. Schmand, "SiPM performance in PET applications: An experimental and theoretical analysis," IEEE NSS/MIC Conf. Rec., pp. 1941–1948, October 2009.

[75] M. Spurrier, P. Szupryczynski, K. Yany, A. Carey, and C. Melcher, "Effects of Ca^{2+} co-doping on the scintillation properties of LSO:Ce," IEEE Trans. Nucl. Sci., vol. 55, pp. 1178–1182, June 2008.

[76] M. Janecek and W. Moses, "Optical reflectance measurements for commonly used reflectors," IEEE Trans. Nucl. Sci., vol. 55, pp. 2432–2437, August 2008.

[77] "3M Vikuiti Enhanced Specular Reflector (ESR)," `http://www.3m.com/product/information/Vikuiti-Enhanced-Specular-Reflector.html`.

[78] J. Hanlon, Handbook of Package Engineering, vol. 1. Lancaster, PA, USA: Technomic Publishing, 1992. Chapter 3, Films and Foils.

[79] B. Dolgoshein, V. Balagura, P. Buzhan, M. Danilov, L. Filatov, E. Garutti, M. Groll, A. Ilyin, V. Kantserov, V. Kaplin, A. Karakash, F. Kayumov, S. Klemin, V. Korbel, H. Meyer, R. Mizuk, V. Morgunov, E. Novikov, P. Pakhlov, E. Popova, V. Rusinov, F. Sefkow, E. Tarkovsky, and I. Tikhomirov, "Status report on silicon photomultiplier development and its applications," Nucl. Instrum. Methods Phys. Res. A, vol. 563, pp. 368–376, 2006. Calice/SiPM Collaboration.

[80] P. Eckert, H. Schultz-Coulon, W. Shen, R. Stamen, and A. Tadday, "Characterisation studies of silicon photomultipliers," Nucl. Instrum. Methods Phys. Res. A, vol. 620, pp. 217–226, 2010.

[81] M. A.Ward and A. Vacheret, "Impact of after-pulse, pixel crosstalk and recovery time in multi-pixel photon counter response," Nucl. Instrum. Methods Phys. Res. A, vol. 610, pp. 370–373, 2009.

[82] S. Seifert, H. van Dam, R. Vinke, P. Dendooven, H. Löhner, F. Beekman, and D. Schaart, "A Comprehensive Model to Predict the Timing Resolution of SiPM-Based Scintillation Detectors: Theory and Experimental Validation," IEEE Trans. Nucl. Sci., vol. 59, February 2012.

[83] V. Spanoudaki and C. Levin, "Investigating the temporal resolution limits of scintillation detection from pixellated elements: comparison between experiment and simulation," Phys. Med. Biol., vol. 56, pp. 735–756, 2011.

[84] Y. Shao, "A new timing model for calculating the intrinsic timing resolution of a scintillator detector," Phys. Med. Biol., vol. 52, no. 4, p. 1103, 2007.

[85] M.W.Fishburn and E. Charbon, "System Tradeoffs in Gamma-Ray Detection Utilizing SPAD Arrays and Scintillator," IEEE Trans. Nucl. Sci., vol. 57, October 2010.

[86] S. Seifert, J. Steenbergen, H. van Dam, and D. Shaart, "Accurate measurement of the rise and decay times of fast scintillators with solid state photon counters," JINST, July 2012. JINST 7 P09004.

[87] B. Arnold, A First Course in Order Statistics. New York: Wiley-Interscience, 1992.

[88] H. David, Order Statistics. New York: Wiley, 1989.

[89] F. Gentit, "Litrani: a General Purpose Monte-Carlo Program Simulating Light Propagation In Isotropic or Anisotropic Media," CMS-NOTE-2001-044, October 2001.

[90] R. Brun and F. Rademakers, "ROOT - An Object Oriented Data Analysis Framework," <u>Nucl. Instrum. Methods Phys. Res. A</u>, vol. 389, pp. 81–86, 1997.

[91] P. Avella, A. Santo, A. Lohstroha, M. Sajjada, and P. Sellina, "A study of timing properties of Silicon Photomultipliers," <u>Nucl. Instrum. Methods Phys. Res. A</u>, vol. 695, p. 257, 2011.

[92] S. Seifert, H. van Dam, J. Huizenga, R. Vinke, P. Dendooven, H. Löhner, and D. R. Schaart, "Simulation of Silicon Photomultiplier Signals," <u>IEEE Trans. Nucl. Sci.</u>, vol. 56, pp. 3726–3733, December 2009.

[93] L. Bollinger and G. Thomas, "Measurement of the time dependence of sintillation intensity by a delayed-coincidence method," <u>Rev. Sientif. Instrum.</u>, vol. 32, no. 9, pp. 1044–1050, 1961.

[94] K. Yang, C. Melcher, P. Rack, and L. Eriksson, "Effects of Calcium Codoping on Charge Traps in LSO:Ce Crystals," <u>IEEE Trans. Nucl. Sci.</u>, vol. 56, pp. 2960–2965, October 2009.

[95] S. Derenzo, M. Weber, W. Moses, and C. Dujardin, "Measurement of the Intrinsic Rise Times of Common Inorganic Scintillators," <u>IEEE Trans. Nucl. Sci.</u>, vol. 47, pp. 860–864, June 2000.

[96] D. Wahl, V. Mikhailik, and H. Kraus, "The monte-carlo refractive index matching technique for determining the input parameters for simulation of the light collection in scintillating crystals," <u>Nucl. Instrum. Methods Phys. Res. A</u>, vol. 570, no. 3, p. 529 535, 2007.

[97] A. Knapitsch, "Photonic Crystals: Enhancing the Light Output of Scintillation Based Detectors," <u>PhD thesis, Vienna University of Technology</u>, 2012.

[98] L. Hyman, R. Schwarcz, and R. Schluter, "Study of high speed photomultiplier systems," <u>Rev. Sci. Instrum.</u>, vol. 35, no. 3, pp. 393–406, 1964.

[99] S. Gundacker, A. Knapitsch, E. Auffray, P. Jarron, T. Meyer, and P. Lecoq, "Time resolution deterioration with increasing crystal length in a TOF-PET system," <u>Nucl. Instrum. Methods Phys. Res. A</u>, vol. 737, pp. 92–100, February 2014.

[100] A. Knapitsch, E. Auffray, C. Fabjan, J. Leclercq, X. Letartre, R. Mazurczyk, and P. Lecoq, "Results of Photonic Crystal Enhanced Light Extraction on Heavy Inorganic Scintillators," <u>IEEE Trans. Nucl. Sci.</u>, vol. 59, pp. 2334–2339, October 2012.

[101] K. Pauwels, C. Dujardin, S. Gundacker, K. Lebbou, P. Lecoq, M. Lucchini, F. Moretti, A. Petrosyan, X. Xub, and E. Auffray, "Single crystalline LuAG fibers for homogeneous dual-readout calorimeters," <u>JINST</u>, August 2013. JINST 8 P09019.

[102] S. Seifert, H. T. van Dam, and D. R. Schaart, "The lower bound on the timing resolution of scintillation detectors," <u>Phys. Med. Biol.</u>, vol. 57, pp. 1797–1714, 2012.

[103] C. Herzet, V. Ramon, L. Vundendorpe, and M. Moeneclaey, "An iterative soft decision directed linear timing estimator," <u>4th IEEE Workshop on Signal Processing</u>, pp. 55–59, June 2003.

[104] E. Venialgo, S. Mandai, and E. Charbon, "Time mark estimators for MD-SiPM and impact of system parameters," <u>Nuclear Science Symposium Conference record (NSS/MIC)</u>, November 2013.

[105] Y. Musienko, "private communication," January 2014.

List of Figures

List of Tables

Stefan Gundacker

CERN
European Organization for Nuclear Research
PH-CMX-DS

Route de Meyrin 23	Phone: (+41) 2276-74623
1211 Geneve	Mobile: (+43) 680-3013895
Switzerland	E-mail: stefan.gundacker@cern.ch

Personal information

Surname / First Name: Gundacker Stefan

Date and place of birth: 03.04.1984, Zwettl, Austria

Citizenship: Austria

Mother tongue: German

Education

Sep. 2010 – Feb. 2014: PhD at CERN: "Time resolution in scintillator based detectors for positron emission tomography"

13.01.2010: Graduation in Technical Physics passed with distinction, Diploma thesis at the Institute of Atomic and Subatomic Physics of the Austrian Universities in the field of nuclear physics: „Quality of nuclear reaction models for data evaluation in the calcium – copper region"

Oct. 2003 – Jan. 2010: Studies of Technical Physics at Vienna University of Technology, Austria

Oct. 2007 – July 2008: Stay abroad, Erasmus at the UGR (Universidad de Granada), Faculty of Sciences, Physics, Granada, Spain

20.06.2003: School leaving examination, Thesis in the field of analogue and digital technology with the title „Hochstabiler Referenzoszillator für Sat-Uplink" (High stable reference oscillator for sat-uplink)

1998 - 2003:	HTL (higher technical education institute) in communications engineering, St.Pölten, Austria
1994 - 1998:	Hauptschule in Langschlag, Austria
1990 – 1994:	Volksschule in Langschlag, Austria

Professional experience

Feb. 2014 – now:	Post-Doc (Fellow) position at CERN
Sep. 2010 – Jan. 2014:	Full time researcher at CERN (PhD)
Jan. 2010 – Aug. 2010:	Scientific assistant at the Institute of Atomic and Subatomic Physics at Vienna University of Technology
Oct. 2006 – Feb. 2007:	Tutor at Vienna University of Technology, "Numerical exercises in experimental physics III"
August 2006:	Voest Alpine, Division Stahl (blast-furnace) in Linz
July 2005:	Voest Alpine, Division Stahl (blast-furnace) in Linz
July 2004:	Voest Alpine, Division Stahl (blast-furnace) in Linz
August 2003:	Sawmill Roman Zwölfer
July 2003:	Marktgemeinde Langschlag
July 2001:	Practical training as communication engineer, Siemens AG Austria, location: ICN S CAR WN Service Carrier Wireline Networks
July 2000:	Practical training as electrician, Rentenberger Franz & Co KG

Competences

Computer:	Word Processing (MS-Office, OpenOffice, Latex) Operating Systems (Linux, MS Windows) Programming (C/C++, Fortran, VHDL , Visual Basic)

	User programs (Mathcad, Matlab, Mathematica, Corel Draw,...)
Languages:	German mother tongue
	English fluent
	Spanish advanced
	French basic
Additional:	Driving licence ABF
Hobbies:	Skiing, snowboarding, backpacking, photographing, constructing electrical systems

---

Communication

October 2013:	"Time Resolution Deterioration with Increasing Crystal Length in a TOF-PET System and Concepts for Improvements", Talk at IEEE NSS/MIC 2013, Seoul (Korea), 27.10.2013 – 02.11.2013
April 2013:	"Time of flight positron emission tomography towards 100ps resolution with L(Y)SO, an experimental and theoretical analysis", Talk at SCINT 2013, Shanghai (China), 15.04.2013 – 19.04.2013
June 2012:	"Photodetectors for highest time resolution in PET", Talk at PhotoDet 2012, International workshop on new photon-detectors, LAL, Orsay (France), 13.06.2012 – 15.06.2012
May 2012:	"SiPM time resolution: from single photon to saturation", Poster at XII Pisa Meeting on advanced detectors, La Biodola, Isola d'Elba (Italy), 20.05.2012 – 26.05.2012
July 2011:	"A systematic study to optimize SiPM photodetectors for highest time resolution in PET", Poster at NDIP, 6th

	international conference on new developments in photodetection, Lyon (France), 04.07.2011–08.07.2011
September 2009:	„Model defects for nuclear data evaluation", Talk at the EFNUDAT workshop at the Institute of Isotopes, Budapest (Hungary), 23.09.2009 – 25.09.2009

Selection of most important publications

Gundacker, S., Knapitsch, A., Auffray, E., Jarron, P., Meyer, T., & Lecoq, P. (2014). "*Time resolution deterioration with increasing crystal length in a TOF-PET system*", *Nuclear Instruments and Methods in Physics Research Section A: Accelerators, Spectrometers, Detectors and Associated Equipment*, *737*, 92-100.

Gundacker, S., Auffray, E., Frisch, B., Jarron, P., Knapitsch, A., Meyer, T., ... & Lecoq, P. (2013). "*Time of flight positron emission tomography towards 100ps resolution with L(Y)SO: an experimental and theoretical analysis*", *Journal of Instrumentation*, *8*(07), P07014.

Gundacker, S., Auffray, E., Frisch, B., Hillemanns, H., Jarron, P., Meyer, T., ... & Lecoq, P. (2012), "*A Systematic Study to Optimize SiPM Photo-Detectors for Highest Time Resolution in PET*", IEEE Trans. Nucl. Sci. 59 (2012) 1798

Gundacker, S., Auffray, E., Di Vara, N., Frisch, B., Hillemanns, H., Jarron, P., ... & Lecoq, P. (2013), "*SiPM time resolution: From single photon to saturation*", *Nuclear Instruments and Methods in Physics Nucl. Instrum. Meth. Phys. A 718 (2013) 569*

Gundacker, S., Auffray, E., Frisch, B., Meyer, T., Jarron, P., & Lecoq, P. (2012, June), "*SiPM Photodetectors for Highest Time Resolution in PET*", PoS(PhotoDet 2012)016, June 13-15, LAL Orsay, France

Honors and awards

Best poster award at the 3rd EIROforum School on Instrumentation, Geneva 30th May 2013, "Time Resolution in scintillator based detectors for positron emission tomography"

John Elias Memorial Award for the best poster at the 12th Pisa Meeting on advanced detectors. La Biodola, Isola d'Elba (Italy), "SiPM time resolution: from single photon to saturation"

Geneva, 23/03/2014